Time Resolved Broadband Spectroscopy from UV to NIR

Beneficial Use of the Coherent Artifact and Pyrene Dynamics

Bastian Baudisch

Dissertation

München 2017

Time Resolved Broadband Spectroscopy from UV to NIR

Beneficial Use of the Coherent Artifact and Pyrene Dynamics

Bastian Baudisch

Dissertation
an der Fakultät für Physik
der Ludwig-Maximilians-Universität
München

vorgelegt von
Bastian Baudisch
aus Baden-Baden

München, im Dezember 2017

Erstgutachter: Prof. Dr. Eberhard Riedle
Zweitgutachter: Prof. Dr. Matthias Kling

Tag der mündlichen Prüfung: 26.02.2018
Tag der Abgabe: 20.12.2017

Kurzfassung

Die transiente Absorptionsspektroskopie (TA) nutzt kurze Lichtimpulse, um die photoinduzierte Dynamik von Molekülen zu untersuchen. Gewöhnlich regt dabei ein kurzer Anregeimpuls die Proben an und ein verzögerter Abfrageimpuls liefert transiente Absorptionsspektren der Probe zu ausgewählten Verzögerungszeiten. Gängig sind Verzögerungen vom Femto- (fs) bis zum Millisekunden-Regime, wo Relaxationsprozesse und schnelle chemische Reaktionen ablaufen.

Der erste Teil dieser Arbeit konzentriert sich auf kurze Verzögerungszeiten, wo sich Anrege- und Abfrageimpuls zeitlich überlappen. Die Interaktion der beiden Impulse im Probenmedium führt im ultravioletten (UV), sichtbaren (VIS) und nahinfraroten (NIR) Spektralbereich häufig zum sogenannten „kohärenten Artefakt“ (CA). Je nach Chirp des Abfrageimpulses kann das CA Signale bis zu Verzögerungen von mehreren 100 fs überlappen. Nur durch genaueste Modellierung des CA können in diesem Bereich Informationen über die Moleküldynamik extrahiert werden. Bei der Erzeugung des CA dominiert im UV Zwei-Photonen-Absorption, während im VIS/NIR Kreuzphasenmodulation (XPM) vorherrscht. Simulationen zeigen, dass für typische, gechirpte Abfrageimpulse der kürzeste Anregeimpuls nicht zum kürzesten CA führt. Im Gegenteil sind für stärker gechirpte Abfrageimpulse längere Anregeimpulse besser geeignet. Da Simulationen und Experimente zu stark variierenden Artefaktformen führen, wird eine neue Parametrisierung entwickelt, mit der sich das CA in allen beobachteten Fällen gut apassen und korregieren lässt.

Man kann das CA nutzen, um Beschichtungen dielektrischer Spiegel zu charakterisieren. Die Methode wird an maßgefertigten, dispersionskompensierten CMUV08 und PC5-L Spiegeln im UV und VIS/NIR getestet, und auf den neuartigen Balzers DIFLEX® Ultrabreitbandspiegel angewandt. Direkte Messungen der Gruppenverzögerung verschiedener Beschichtungen ergeben eine Genauigkeit von unter ±1 fs. Diese neue Technik wird etablierte interferometrische Verfahren nicht ersetzen, führt aber zu vergleichbaren Ergebnissen und funktioniert problemlos im UV.

Im zweiten Teil dieser Arbeit zeigen die Überlappenden Signaturen des Pyren, dass Breitbanddetektion oft notwendig ist, um ein vollständiges Bild der Moleküldynamik zu erhalten. Pyren gilt als möglicher Baustein für funktionalisierte Materialien in der organischen Elektronik, doch trotz häufiger Nutzung als Fluoreszenzmarker und Lehrbuch-Beispiel sind die Reversibilität der Excimerbildung und die Rolle des Triplettzustands noch unklar. Pyren und ausgewählte Derivate werden hier systematisch vom Femtosekunden- bis zum Mikrosekundenregime untersucht. Dank globaler Analysemethoden und spektraler Zerlegung werden Widersprüche in bisherigen Modellen aufgeklärt. Entgegen früher Modelle ist die Excimerbildung bei Raumtemperatur nicht reversibel. Multiexponentielle Zerfälle der Monomerfluoreszenz sind auf einen Überlapp mit der Excimer Fluoreszenzbande zurückzuführen. Der meist vernachlässigte transiente Beitrag zur Diffusionsrate beeinflusst die Dynamik zunehmend bei Konzentrationen > 1 mM. Ein vereinfachtes Ratenmodell wird vorgestellt, das sowohl die Dynamik des Pyren also auch die verbrückter Dimere beschreibt. Absorptionsspektren der S_1-, Excimer- und Triplettzustände werden bestimmt. Trotz minimierung der O_2-Konzentration in der Lösung ist Sauerstoffquenchen des Singlettzustands verantwortlich für einen Großteil der beobachteten Tripletts. Nach Abzug des Sauerstoffbeitrags liegt die Quantenausbeute für das Excimer in 10 mM Lösung bei 98%. Hiervon gehen 3% in einen Triplettzustand über, dessen Signatur dem Monomer-Triplett stark ähnelt. Eine direkte Verknüpfung zweier Pyrene an der 1-Position beschleunigt die Relaxation drastisch. Kandidaten für die Materialforschung sind an der 4-Position verbrückte Verbindungen, da diese auch nach Polymerisierung eine langlebige Fluoreszenz aufweisen.

Summary

Transient absorption (TA) spectroscopy utilizes short laser pulses to probe photo induced molecular dynamics. Commonly samples are excited by a short 'pump' pulse and a delayed 'probe' pulse monitors the sample's absorption change at selected pump probe delays. Transient spectra are recorded from the femtosecond (fs) to the millisecond regime, where intramolecular relaxation processes and fast chemical reactions take place.

The first part of this thesis focuses on the shortest delays, where pump and probe pulses overlap in time. In the visible (VIS) and ultraviolet (UV) spectral range the interaction of pump and probe in the sample often leads to the observation of the 'coherent artifact' (CA). Depending on the probe chirp it can obscure molecular dynamics up to a few hundred femtoseconds. Only accurate modeling facilitates extraction of molecular information in this range. While in the UV two-photon absorption is the dominant process, cross phase modulation (XPM) is determined to be most relevant in the VIS and near infrared (NIR). Simulations of XPM induced CAs show that in the most common scenario of a chirped probe, the shortest pump pulse does not yield the shortest CA. Instead, for increasingly chirped probe pulses longer pump pulses are preferable. As a series of simulations and experiments yields strongly varying shapes and widths, a novel parameterization is developed, allowing accurate fit and subtraction of the CA in all observed cases.

The CA can be used to characterize the group delay (GD) of dielectric mirror coatings from the UV to the NIR. With recent advances in broadband coating technology, performance testing will become increasingly important. This novel technique will likely not replace established interferometric techniques, but provides comparable results and overcomes technical limitations in the UV. The method is tested on custom, dispersion compensated CMUV08 UV and PC5-L VIS/NIR mirrors and applied to novel Balzers DIFLEX® utrabroadband mirrors. An overall GD accuracy of better than ±1 fs was achieved.

In the second part of this thesis the overlapping excited state signatures of pyrene exemplify that spectrally resolved broadband detection is often necessary to acquire a 'full picture' of the molecular dynamics. Recently pyrene has been considered as a building block for functionalized materials in organic electronics. Despite many applications as a fluorescence marker and multiple use as a textbook example, the oft proposed reversibility of the excimer formation as well as the role of the triplet state are still debated. The dynamics of pyrene and selected derivatives are systematically reevaluated from the fs to the µs timescale using state-of-the-art broadband detection. Taking advantage of spectral domain fitting and global analysis techniques, ambiguities in the current models are resolved. In contrast to earlier claims, the pyrene excimer formation is not reversible at room temperature. Double exponential decays of the 'monomer' fluorescence are due to overlapping monomer and excimer fluorescence bands. Commonly neglected transient effects of diffusion increasingly impact the fitted rate constants at concentrations > 1 mM. A simplified rate model is proposed, describing the dynamics of pyrene as well as linked pyrene dimers. TA studies yield transient spectra of the S_1-, excimer and triplet states. Despite efforts to minimize the oxygen concentration in the solution, oxygen quenching of the singlet state proved to be the source of most of the observed triplets. Correcting for oxygen quenching leads to 98% quantum yield for the excimer at 10 mM, of which 3% form triplet states whose signatures closely resemble that of the triplet formed from the monomer. In pyrene dimers a direct link at the 1-position drastically accelerates the dynamics. Units linked at the 4-position are candidates for advanced materials, featuring a long-lived fluorescence even after polymerization.

Publications

The following publications have been produced in the scope of this thesis:

1 **On the Edge: Characterizing Broadband Dielectric Mirrors from UV to NIR Using a Pump-Probe Technique**
B. Baudisch, F. Habel, V. Pervak, and E. Riedle
International Conference on Ultrafast Phenomena, OSA Technical Digest (online), Optical Society of America (2016).

2 **Pyrene Dynamics: Covalently Linked Dimers Accelerate the Kinetics from ns to ps and Produce Excimers**
B. Baudisch, A. Keerthi, A. Reiner, J. Reschauer, K. Müllen, and E. Riedle
International Conference on Ultrafast Phenomena, OSA Technical Digest (online), Optical Society of America (2016).

3 **Characterizing Broadband Dielectric Mirrors from UV to NIR Using a Pump-Probe Technique**
B. Baudisch, F. Habel, V. Pervak, and E. Riedle
To be submitted to Optics Express.

4 **Irreversible Excimer Formation in Pyrene: Impact of Band Overlap and Time Dependent Rates**
B. Baudisch, R.-J. Kutta, and E. Riedle
In preparation.

5 **Linker Position Dramatically Affects Properties of Pyrene Dimers**
B. Baudisch, A. Keerthi, A. Reiner, R.-J. Kutta, K. Müllen and E. Riedle
In preparation.

Contents

1 Introduction

Since the development of the first lasers in the late 1950's and 60's, the availability of shorter and shorter light pulses has stimulated the study of light-matter interaction on the shortest timescales [Tow58, Gou59, Mai60]. Molecular dynamics span a wide range of timescales between femtoseconds (10^{-15} s) and seconds. Transient absorption spectroscopy utilizes short laser pulses to probe dynamic absorption changes from the femtosecond to the millisecond regime, where intramolecular relaxation processes and fast chemical reactions take place. A common approach is to excite a sample with a short 'pump' pulse and use a delayed 'probe' pulse to monitor the sample's response at selected delay times Δt. On the path to resolve ever faster dynamics, spectroscopists are moving to ever shorter pump pulses. Today, this approach is even extended to the sub-femtosecond regime, probing attosecond electron motion in atoms [Wir11, Pab12].

Chapters 2 and 3 of this thesis focus on the very shortest pump probe delays, where the pump and probe pulses overlap in time due to their finite duration. In the visible and ultraviolet spectral range the interaction of pump and probe in the sample leads to the observation of the 'coherent artifact'. The coherent artifact often obscures early time molecular dynamics and only accurate modeling facilitates extraction of meaningful molecular information in the first tens of femtoseconds. A novel parameterization is presented that allows for accurate fit and subtraction of the artifact signal. Simulations reveal that the shortest pump pulse does not necessarily produce the shortest artifact in the most common parameter range.

Yet, this unwanted perturbation can be put to good use in the characterization of dielectric mirrors designed for femtosecond applications. Chapter 3 reports direct measurement of the group delay with femtosecond precision using the coherent artifact from the ultraviolet to the near-infrared. Thanks to advances in coating technology over the past decade, the use of tailored dielectric mirrors with defined group delay characteristics has become customary for a wide range of applications, from chirped mirror compression of femtosecond pulses to efficient propagation of ever larger bandwidths. Consequently, the accurate characterization of such coatings is of utmost importance and with recent advances in broadband coating technology, this will become increasingly interesting as exact specifications are often kept a secret by vendors for fear of plagiarism.

While results from Chapters 2 and 3 push the short end of the observable delay range, the final chapter exemplifies that in order to acquire a 'full picture' of the molecular dynamics

spectrally resolved broadband detection is often necessary. Despite its many applications as a fluorescence marker and extensive use as a textbook example [Bir70, Tur91, Dyk98, Kla09, Tur10], relevant aspects of the excimer dynamics of pyrene and linked pyrene dimers are still debated. A likely cause for apparent inconsistencies in the models are pyrene's overlapping excited state signatures. In the 1960's, fluorescence dynamics were most often probed using a combination of bandpass filters to select a portion of the spectrum for detection [Bir63]. Similar single-line techniques are still employed today [Han13]. Pyrene has sparked increasing interest recently, representing a potential building block for functionalized materials in organic electronic devices such as organic light emitting diodes (OLEDs), organic photovoltaics, organic field-effect transistors (OFETs), as well as lasers [Fig11, Jia04, Zha07, Mog06, Wan06, Lee11]. Therefore, now is the time to systematically reevaluate the dynamics of pyrene and selected derivatives from the femtosecond to the microsecond timescale using state-of-the-art broadband detection. Taking advantage of spectral domain fitting and global analysis techniques, this work addresses the much discussed reversibility of the excimer formation, often proposed to explain a multiexponential decay of the monomer's fluorescence [Bir63, Zac76, Zac78, Zac84, Zac85, Zac85a, Sie87, Zac88, Sie89, Rey90, Zac91a, Win93, Tsu95]. While the excimer formation is widely believed to be diffusion limited, a simulation sheds light on previously neglected transient effects. Finally, the role of the triplet state in the excimer dynamics is clarified via transient absorption measurements and a simplified model for the excimer dynamics is proposed, which is consistently applied to both pyrene and linked pyrene dimers.

2 Managing Varying Artifact Shapes in Chirped Probe Transient Absorption Spectroscopy

Transient absorption (TA) spectroscopy utilizes femtosecond (fs) laser pulses to probe molecular dynamics from the fs to the millisecond (ms) timescales. TA signatures often span bandwidths of several hundreds of nanometers, making very broadband 'white light' probe pulses a necessity if a complete picture of the dynamics is desired. Very stable white light pulses can be generated from bulk solid state substrates. Probe pulses obtained in this way usually carry a significant chirp. In TA experiments using chirped probe pulses, dynamics recorded at different probe wavelengths originate from different pump probe delays. The accurate determination of the time origin for each probe wavelength is of paramount importance for chirp correction and consistent analysis of the signal's time evolution [Meg09]. In the ultraviolet (UV), visible (VIS) and near infrared (NIR) spectral range the coherent artifact (CA) can be observed around zero pump probe delay. The CA originates from the interaction of a strong pump pulse with the probe pulse during their temporal overlap in the sample. It obscures early time molecular dynamics and is therefore an undesired perturbation. When the CA is modeled with sufficient accuracy, the time origin $\Delta t_0(\lambda)$ and the approximate width of the instrumental response function (IRF) can be extracted from the fit [Tok96, Kov99, Mac00, Ras01, Zio01, Lor02, Meg09, Lap11]. To obtain $\Delta t_0(\lambda)$ and the shape of the CA without any overlapping molecular dynamics, a chirp reference measurement is often performed either in a cuvette holding pure solvent or in a thin solid substrate [Wil11]. The CA's contribution to the time traces can then be subtracted from the dynamics in post processing [Sla15]. CA also carry information about pulse parameters such as the group delay (GD) and the pump and probe pulse durations. For this reason, models for the CA are constantly being improved to date [Wah16].

On the path to resolve ever faster dynamics, spectroscopists are moving to ever shorter pump pulses. As pump pulses become very short compared to the chirped probe, artifact shapes change dramatically due to spectral interference caused by cross phase modulation. The most common fitting models cannot reproduce these shapes. In this chapter current models are reviewed and a novel parameterization is introduced, facilitating a fit of the CA with sub-fs accuracy in the fitted $\Delta t_0(\lambda)$ and accurately reproducing their varying shapes over a wide range of parameters. This is demonstrated by application to simulated and experimental data.

2.1 An Introduction to the Coherent Artifact

Coherent artifacts are observed using a TA system featuring a white light probe pulse covering a spectral range from 290 nm to 700 nm. The probe is generated in 5 mm CaF_2 at a 1 kHz repetition rate. Mechanically delayed pump pulses with durations of $\tau_{pump} \approx 25$ fs are employed, generated by a noncollinear optical parametric amplifier (NOPA). For each pump probe delay (also 'delay time') Δt the probe is spectrally dispersed by a prism spectrograph and detected on a CCD array. The observable is the pump induced change in the transmission $T(\lambda, \Delta t)$ of the probe pulse through a sample. The signal $S(\lambda, \Delta t)$ is obtained by dividing $T(\lambda, \Delta t)$ by the transmission when the pump is blocked by a chopper wheel $T_0(\lambda, \Delta t)$ and averaging over 200 pulse pairs. $S(\lambda, \Delta t)$ is commonly expressed in units of optical density (OD). A detailed description of the setup can be found in [Meg09]. Part of the probe light is sent to a second prism spectrograph for referencing without traversing the sample [Bra14].

Figure 2.1 shows an example of a TA dataset obtained from a 1 mm flow cuvette containing a 1 mM solution of pyrene (Fig. 2.1c) in cyclohexane. The recorded change in optical density ΔOD is shown in false color representation in Fig. 2.1b. Color coded cursors indicate probe wavelengths and delay times corresponding to the line outs in Fig. 2.1a and 2.1d.

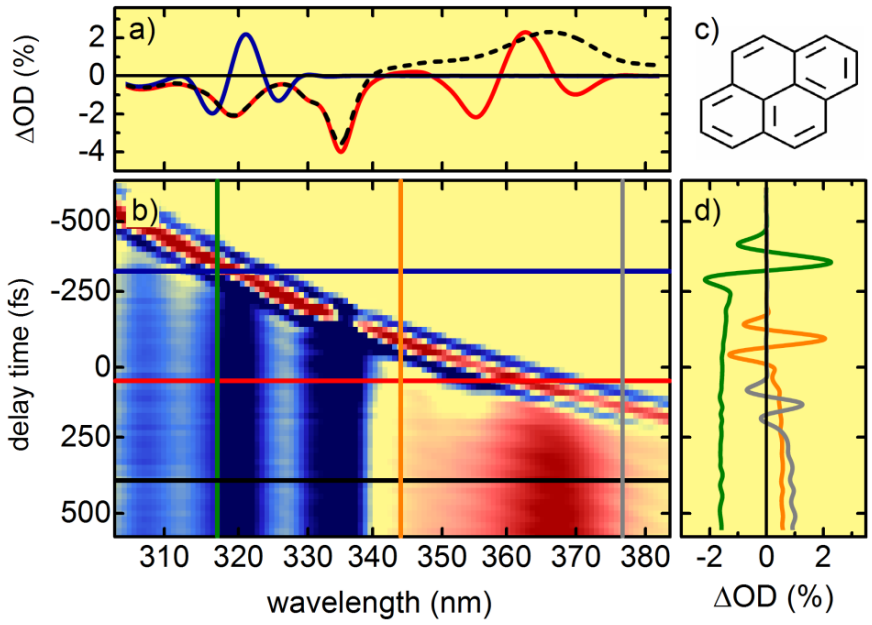

Fig.2.1: Section of a TA dataset of 1 mM Pyrene in Cyclohexane, excited in a 1mm flow cuvette using 100 nJ at $\lambda_{pump} = 334$ nm. (a) TA spectra at selected delay times, (b) TA signal in false color representation, red (blue) indicates positive (negative) contributions. (c) pyrene structure, (d) time traces at selected wavelengths.

Due to its generation in bulk CaF_2, the probe white light is positively chirped. For this reason Figs. 2.1a and 2.1b show the artifact occurring at different delay times for different probe wavelengths: at negative delay the positively chirped probe precedes the pump. As the pump probe delay is scanned towards positive delay, the artifact moves from the blue to the red part of the recorded spectrum. The blue line in Fig. 2.1a shows only the CA. Probe spectral components around 320 nm overlap the pump pulse inside the sample and become modulated due to absorption as well as nonlinear effects induced by the pump (cf. Section 2.3). Spectral components at longer wavelengths precede the pump pulse and therefore do not contribute to the transient signal. The red line shows the transient spectrum at a later delay time, where the artifact has moved to a spectral interval around 365 nm. Probe spectral components at smaller wavelengths interact with the sample after the pump pulse. Hence, the probe spectrum in that range is modulated by the excited molecules and a negative ground state bleach signal is observed below 340 nm. At even later delay times (black dashes) the artifact has moved outside the spectral range shown and a positive excited state absorption (ESA) has appeared around 365 nm. For details on the dynamics of pyrene, refer to Chapter 4 of this thesis.

In the delay time domain the CA modulates the signal around the respective time origin for the wavelength under consideration (Fig. 2.1d), obstructing the early time molecular dynamics. For an undisturbed look at the CA it makes sense to use samples that do not exhibit significant transient absorption or emission dynamics in the spectral range observed, e.g. a cuvette filled with pure solvent or a solid substrate of the same thickness. The artifact shape observed in a time trace taken at a given detection wavelength can depend on a number of factors, including but not limited to the material, the pump wavelength, duration and intensity, the probe spectrum and chirp as well as the detector design [Kov99, Lap11, Wah16, Die07]. Figure 2.2 shows typical delay time domain signals obtained using the setup detailed above in thin, plain parallel solid substrates. In Fig. 2.2a normalized signals at 470 nm detection wavelength for 12 nJ and 1000 nJ pump energy are shown. Most commonly, a positive central peak is accompanied by two distinct and not necessarily symmetric negative ‘wings’. No significant change in signal shape is observed when the pump energy is increased. A comparison of traces at a wide range of pump energies confirms this observation. It can be concluded that in HOYA L42 glass none of the contributing effects saturates and no new effects come into play within the pump energy range used. This is also true for Schott B270 glass.

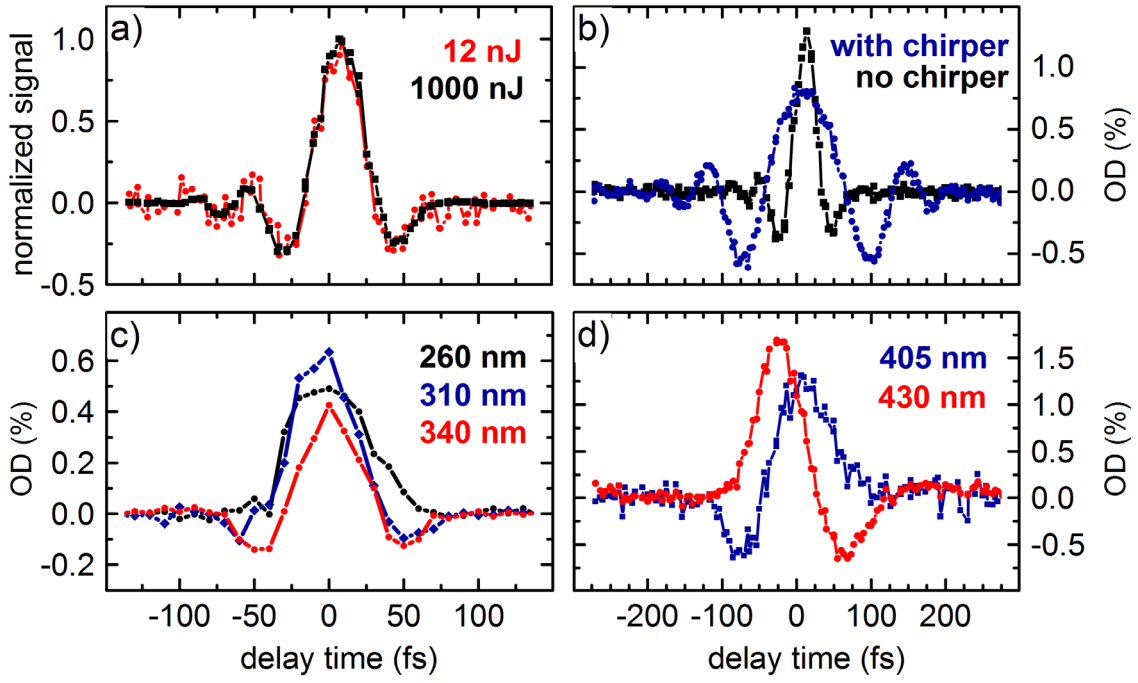

Fig. 2.2: (a) Coherent artifact in 775 nm pumped CaF_2 white light at λ_{probe} = 470 nm for pump pulses of different energies at λ_{pump} = 500 nm, τ_{pump} = 22 fs in 217 µm HOYA L42 glass. (b) Black: same as (a) with white light additionally chirped by transmission through a 14.5 mm Schott BK7 block (blue). (c) Coherent artifact in 50 µm sapphire using 180 nJ pump at λ_{pump} = 230 nm and UV white light generated by the frequency doubled CPA at 389 nm in CaF_2. (d) Coherent artifact at selected probe wavelengths in 100 µm α-BBO induced by a 27 fs, 600 nJ pump at λ_{pump} = 270 nm, probed by a 25 fs NOPA pulse at λ_{probe} = 420 nm.

Figure 2.2b illustrates the significant shape change when the white light probe chirp is increased by adding a 14.5 mm BK7 block. The amplitude decreases while the artifact broadens significantly as its negative 'wings' turn into periodic fringes. In most measurements to date such prominent fringes have not been observed (with exception of reference [Wah16]) and commonly used fitting models cannot reproduce them. Highly chirped probe pulses occur in the deep UV, where dispersion compensation is challenging, and will also play a role in Chapter 3. Simulations will show that the same effect occurs when instead of increasing the probe chirp, the pump pulse duration is decreased (cf. Section 2.3.2), so artifact fringes will likely be observed more frequently in the future. Figure 2.2c illustrates CAs generated in sapphire in the UV spectral range. As the probe wavelength increases, the CA turns from an all positive shape reminiscent of a Gaussian (black) into a shape comparable to those in Fig. 2.2a (red). In Fig. 2.2d the effect of negligible probe chirp is

shown. Here, instead of a chirped white light, a compressed pulse from a NOPA was used for probing, resulting in a sinusoidal shape. The signal is inverted at the central wavelength of the probe pulse (420 nm). Note that the delay time Δt is a relative quantity. Here the absolute values were chosen such that the pump interacts with the respective λ_{probe} around $\Delta t = 0\,fs$.

2.2 Effects Contributing to the Coherent Artifact

The main effects that need to be considered for the experiments presented in this work are two photon absorption (TPA) and cross phase modulation (XPM) which will be covered in detail in the following sections. Other effects such as impulsive stimulated Raman scattering (ISRS) in the solvent as well as perturbed free induction decay (PFID) can also contribute to the coherent artifact. While ISRS manifests as an oscillation at positive delay [Sil85, Pol07, Kov99, Meg09], Fig. 2.2a shows a slight oscillation at negative delay that could be due to PFID [Ham95, Nue09, Yan11].

2.2.1 Two Photon Absorption (TPA)

First predicted by Göppert-Mayer et al. in 1931, TPA occurs when the combined energy of two coinciding photons exceeds the material's bandgap, even though their individual photon energies are too small to be directly absorbed [Göp31]. When one pump and one probe photon are absorbed, a measurable change in transmission is induced in the spectral component of the broadband probe that temporally overlaps the pump pulse. TPA creates a purely Gaussian signal for Gaussian pump and probe pulses in a thin medium, when they are not broadened significantly by group velocity dispersion (GVD). For detailed derivations refer to [Mac00, Ras01, Lor02, Hom11]. For example, signals shown in Fig. 2.2c are clearly dominated by TPA. The delay time origin $\Delta t_0(\lambda)$ can then be easily extracted. The instrumental response function (IRF) for a given wavelength is a Gaussian with the width of the cross correlation between pump and probe and can be directly inferred from the fit.

Experimental TPA coefficients for HOYA L42 and Schott B270 are not reported for the wavelengths used. A value of $\beta_{TPA} = 4.33 \cdot 10^{-3}\,cm/GW$ is given for B270 in [Mog10] using two 800 nm photons and a 5 mm thick substrate. Using this value, the change in transmission due to TPA is estimated to ~12 mOD for a peak intensity of 300 GW/cm^2 [Hom11]. Utilizing referenced detection, the setup is sensitive to changes in transmission down to 0.02 mOD [Bra14], so a signal on this scale is readily detectable, especially since β_{TPA} tends to increase towards smaller wavelengths approaching the bandgap [Hom11].

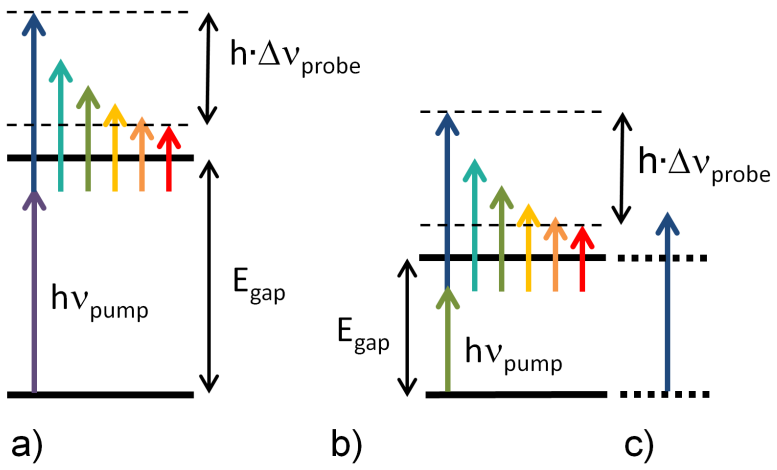

Fig. 2.3: Energy diagram for two photon absorption of one pump and one probe photon. (a) UV pump: the pump photon energy is large compared to probe photon energies. (b) VIS pump: pump photon energy comparable to probe photon energies, bandgap must be carefully matched to allow TPA but avoid single photon absorption of the high energy probe photons. (c) Direct absorption of highest energy probe photon.

In a medium with a bandgap energy E_{gap} the condition

$$\frac{h \cdot c}{\lambda_{pump}} + \frac{h \cdot c}{\lambda_{probe}} > E_{gap} > \frac{h \cdot c}{\lambda_{probe}} \tag{2.1}$$

has to be fulfilled for TPA to occur while the medium is transparent for the individual probe photons. In practice the combined photon energies of pump and probe must exceed the bandgap significantly to obtain a reasonable signal. In 389 nm pumped UV white light this can be done using sapphire, α-BBO or Schott B270 glass. For more materials refer to [Hom11]. With a UV pump, the pump photon energy is large compared to the energy difference between the photons in the broadband probe (see Fig. 2.3a). Conversely, in the VIS/NIR spectral range appropriate materials must be selected carefully: when using a visible pump pulse, pump and probe photon energies are comparable and the bandgap has to be carefully matched in order to allow TPA but avoid single photon absorption of the bluest probe photons (Fig. 2.3b,c). In practice there is no single material that fulfills this condition for the whole visible spectral range, so several media with appropriate bandgaps are required. When a TPA induced artifact is to be obtained throughout the VIS/NIR, measurements in different materials must be stitched together. This increases complexity and measurement time and can lead to errors due to temperature and other fluctuations in the laboratory.

Moreover, the two photon absorption edges do not always coincide with half the energy of the one photon edge, so finding a suitable set of materials is often trial and error. For example, HOYA L42 glass was initially considered because its bandgap should facilitate TPA throughout most of the visible spectral range. Unfortunately it features an excited state absorption at just above 400 nm that has to be included in modeling and is not transparent below 400 nm. Schott B270 glass is a candidate transparent throughout the entire spectral range probed, but cannot sustain TPA for longer probe wavelengths. Even at moderate pump energies, both glasses show features deviating from a 'clean' Gaussian.

2.2.2 Cross Phase Modulation (XPM)

Most commonly, the artifact's negative 'wings' are attributed to cross phase modulation (cf. Fig. 2.2a). First observed in 1986 by Alfano et al. [Alf86], XPM is a redistribution of spectral components of the probe due to a change in the refractive index n of a medium induced by the intense pump pulse:

$$n(t, \Delta t) = n_0 + n_2 \cdot I_{pump}(t) . \tag{2.2}$$

Here n_2 is the nonlinear refractive index and $I_{pump}(t)$ the temporal envelope of the pump intensity. When the probe pulse temporally overlaps the pump in the medium, the modulated refractive index causes a redistribution of spectral intensity. This leads to a detectable change in probe transmission for a given spectral component, even though no net absorption of the probe light has taken place.

Defining the total electric field of two copropagating plane wave packets as

$$E(z,t) = \mathrm{Re}\left[A_1(z,t) \cdot e^{i(k_1 z - \omega_1 t)} + A_2(z,t) \cdot e^{i(k_2 z - \omega_2 t)} \right], \tag{2.3}$$

with amplitudes A_i, central angular frequencies ω_i and wave vectors k_i. The coupled amplitude equations in a nonabsorbing medium can be derived using the slowly varying amplitude approximation [Alf89, Agr89, Kry05]:

$$i\left(\frac{\partial A_1}{\partial z} + \frac{1}{v_1}\frac{\partial A_1}{\partial t} \right) + \frac{\omega_1 \cdot n_{2,1}}{c}\left(|A_1|^2 \cdot A_1 + 2|A_2|^2 \cdot A_1 \right) = 0 , \tag{2.4a}$$

$$i\left(\frac{\partial A_2}{\partial z} + \frac{1}{v_2}\frac{\partial A_2}{\partial t} \right) + \frac{\omega_2 \cdot n_{2,2}}{c}\left(|A_2|^2 \cdot A_2 + 2|A_1|^2 \cdot A_2 \right) = 0 . \tag{2.4b}$$

Here v_1 and v_2 are the group velocities and $n_{2,1}, n_{2,2}$ the nonlinear refractive indices corresponding to the pump (index 1) and probe (index 2) pulses, respectively. z is the coordinate in propagation direction. Amplitudes A_i are defined such that $|A_1|^2 = I_{pump}$. Group velocity dispersion for the individual waves has been neglected here.

In a coordinate frame moving alongside the probe pulse the time derivative in Eq. 2.4b vanishes, leaving only the z dependence. A solution to this wave equation at the output of a medium of length $z = L$ is

$$A_2(L,T) = A_2(0,T) \cdot \exp[\,i\Phi_{XPM}\,], \tag{2.5}$$

with

$$\Phi_{XPM} = \frac{\omega_2 \cdot n_2}{c}\left(L\,|A_2(0,T)|^2 + 2 \cdot \int_0^L |A_1(0, T + z \cdot d)|^2\, dz \right), \tag{2.6}$$

where $T = t - z/v_2$ is the time in the comoving frame and $d = (v_2 - v_1)/(v_1 \cdot v_2)$ the group velocity mismatch (GVM). The first summand in Eq. 2.6 describes self phase modulation, which will be neglected for the weak probe pulse from this point on. The second summand describes the buildup of the phase acquired due to cross phase modulation along z.

An approximate but intuitive expression can be inferred from Eq. 2.6 when neglecting the GVM and defining a fixed pump probe delay Δt instead. The integral then reduces to a multiplication with the substrate length and the XPM induced phase is

$$\Phi_{XPM}(t,\Delta t) = 2\frac{n_2 \cdot \omega_2 \cdot L}{c} I_{pump}(t,\Delta t)\,. \tag{2.7}$$

This simplified expression will be used later on to simulate XPM induced CAs. The pump induced modulation of the probe's instantaneous frequency is then [Agr89, Alf89, Lor02]

$$\Delta\omega(t,\Delta t) = -\frac{\partial}{\partial t}\Phi_{XPM} = -2\frac{n_2 \cdot \omega_2 \cdot L}{c}\frac{\partial}{\partial t} I_{pump}(t,\Delta t)\,, \tag{2.8}$$

where ω_2 is the central frequency of the probe pulse. Figure 2.4a illustrates the frequency modulation of a linearly chirped probe pulse modulated by an intense Gaussian pump pulse.

When the pump pulse travels with a significantly different group velocity due to the dispersion of the material's linear refractive index, its position with respect to the probe will change along the medium, causing the modulated interval to broaden as indicated in Fig. 2.4b.

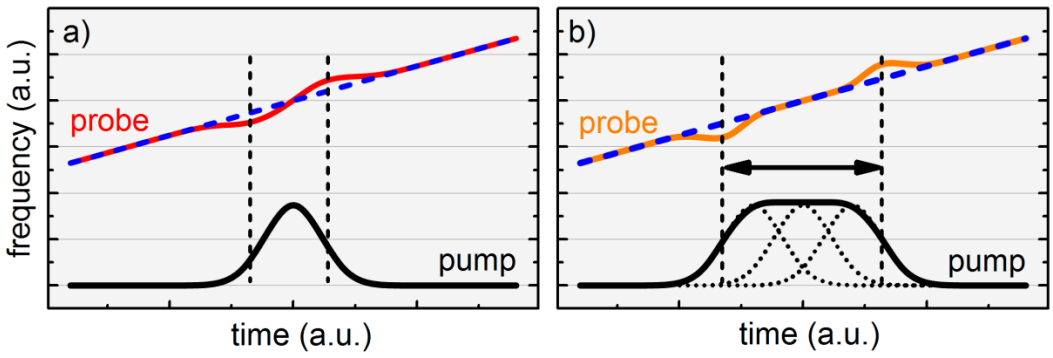

Fig. 2.4: Schematic illustration of the modulation (red) of a linear probe chirp (blue) by a Gaussian pump pulse (black), (a) neglecting and (b) including the effect of group velocity mismatch. Modulations are drawn untypically large for clarity. Figure adapted from [Lor02].

At a peak intensity of 330 GW/cm^2, the maximum frequency shift in the probe induced by XPM can be estimated using Eq. 2.7 with L = 200 µm and the nonlinear refractive index $n_2 = 2.06 \cdot 10^{-7}\,\mathrm{cm}^2/\mathrm{GW}$ given for B270 glass in [Mog10]. The estimated maximum frequency shift corresponds to ±1.6 nm at 300 nm and ±3.7 nm at 700 nm. The spectral resolution of the setup used is ~2.25 THz in the VIS [Meg09]. At 300 nm one CCD pixel corresponds to 0.7 nm, while at 700 nm a shift by 3.7 nm is needed to move spectral intensity to the next pixel. XPM is therefore expected to yield a detectable contribution to the signal in the UV/VIS.

Signal shapes resulting from cross phase modulation vary significantly depending on the duration of the pump and the chirp of the probe pulse (cf. Fig. 2.2b). This will be investigated in detail in the following section.

2.3 Simulating Cross Phase Modulation

In the following the signal contribution due to XPM that is expected in a typical TA experiment is simulated in PTC Mathcad Prime 3.1 using equation 2.7. Using this approximate model, the dependence of the signal on pulse parameters is explored and finally the simulated data is compared to experimental data.

TA measurements monitor the delay time dependent change in the probe spectrum after transmission through the sample. Neglecting propagation effects like GVM, the total temporal phase imprinted on the probe pulse due to XPM in the sample can be approximated by $\Phi_{XPM}(t, \Delta t)$ as given in Eq. 2.7. A Gaussian pump pulse with an intensity of 300 GW/cm^2 and FWHM pulse duration τ_1 of 25 fs will be assumed, modulating the refractive index of a medium with $n_2 = 2.06 \cdot 10^{-7}$ cm^2/GW and a thickness of L = 200 µm. The simulation first computes the discrete Fourier transformation (DFT) of an input probe spectrum $E_2(\omega)$ with a predefined phase to obtain the electric field $\tilde{E}_2(t)$. The electric field is then modulated in the time domain by the phase $\Phi_{XPM}(t, \Delta t)$. This is done for a range of pump probe delays Δt in 3 fs steps, resulting in a matrix of modulated electric fields $\tilde{E}_{2,XPM}(t, \Delta t)$.

$$\tilde{E}_{2,XPM}(t, \Delta t) = \tilde{E}_2(t) \cdot \exp[i \cdot \Phi_{XPM}(t, \Delta t)] \tag{2.9}$$

Subsequently the modulated fields are transformed back into the spectral domain via the inverse DFT, resulting in a matrix of transmission spectra $T(\lambda, \Delta t)$. These correspond to the XPM modulated TA spectra that would be observed by the CCD camera in the experiment. Just as in the experiment, $T(\lambda, \Delta t)$ is divided by the transmission without pump (i.e. the input spectrum) and the negative logarithm is taken to yield the TA signal $S(\lambda, \Delta t)$ in OD.

In practice the white light probe carries a nonlinear chirp due to its generation in CaF_2 and its spectrum is modulated. Around the CPA fundamental wavelength at 778 nm, which is used to generate the probe white light, the probe light is suppressed by a dielectric filter to avoid overexposure of the CCD (cf. Fig. 2.5). The employed dielectric also slightly modulates the spectral intensity throughout the VIS. For an introduction to the signal shapes and their dependence on the pulse parameters, two assumptions will be made in the following. Firstly, the probe spectrum is approximated by a flattop envelope centered at 530 nm with a FWHM width of 180 nm (cf. Fig. 2.5). Secondly, the probe chirp is assumed to be linear in the frequency domain. Hence, the probe is defined in the frequency domain via its spectrum S_2 and a quadratic phase.

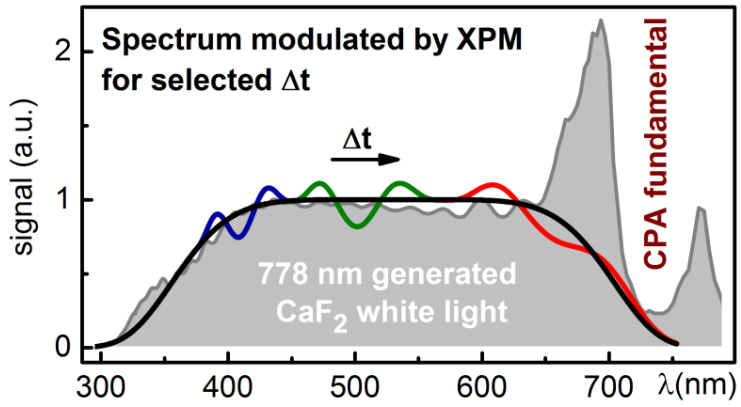

Fig. 2.5: Experimental probe spectrum generated using the CPA fundamental at 778 nm in 5 mm CaF_2 (gray), approximated by a flattop spectrum centered at 530 nm (black). Colored lines: simulated modulation by XPM for increasing delay time using a chirp factor $\beta = 10^{-2}$ 1/fs^2.

$$E_2(\omega) = \sqrt{S_2(\omega)} \cdot \exp\left[\tfrac{i}{2} \cdot \beta_\omega \cdot (\omega - \omega_2)^2 \right] \tag{2.10}$$

Here ω_2 is the probe's central frequency and β_ω a frequency domain chirp factor. The more commonly used slope β of the instantaneous frequency

$$\omega(t) = \omega_2 + \beta \cdot t \tag{2.11}$$

with the units 1/fs^2 is given by $\beta_\omega = 1/\beta$ as a consequence of the similarity theorem. Typical values for β range between 10^{-2} and 10^{-3} 1/fs^2. Note that in this convention a small chirp rate β means a strongly chirped pulse and vice versa. The modulations shown in Fig. 2.5 were calculated using a chirp factor $\beta = 10^{-2}$ 1/fs^2.

2.3.1 Dependence on Probe Chirp

Figures 2.6a and 2.6c show simulated signals produced by linearly chirped probe pulses carrying moderate ($\beta = 10 \cdot 10^{-3}$ 1/fs^2) and strong chirp ($\beta = 2 \cdot 10^{-3}$ 1/fs^2). For comparability with experimental data, signals are plotted vs. detection wavelength. As the chirp is assumed linear in the frequency domain, the signals vs. wavelength are not straight lines. Insets show the calculated time domain probe pulses (blue) compared to the assumed pump pulses (red). Most commonly, the moderately chirped case is observed in chirped pulse TA measurements. Obviously, higher chirp causes an increase in the observed slope, as the same frequency interval is stretched over a longer probe pulse duration.

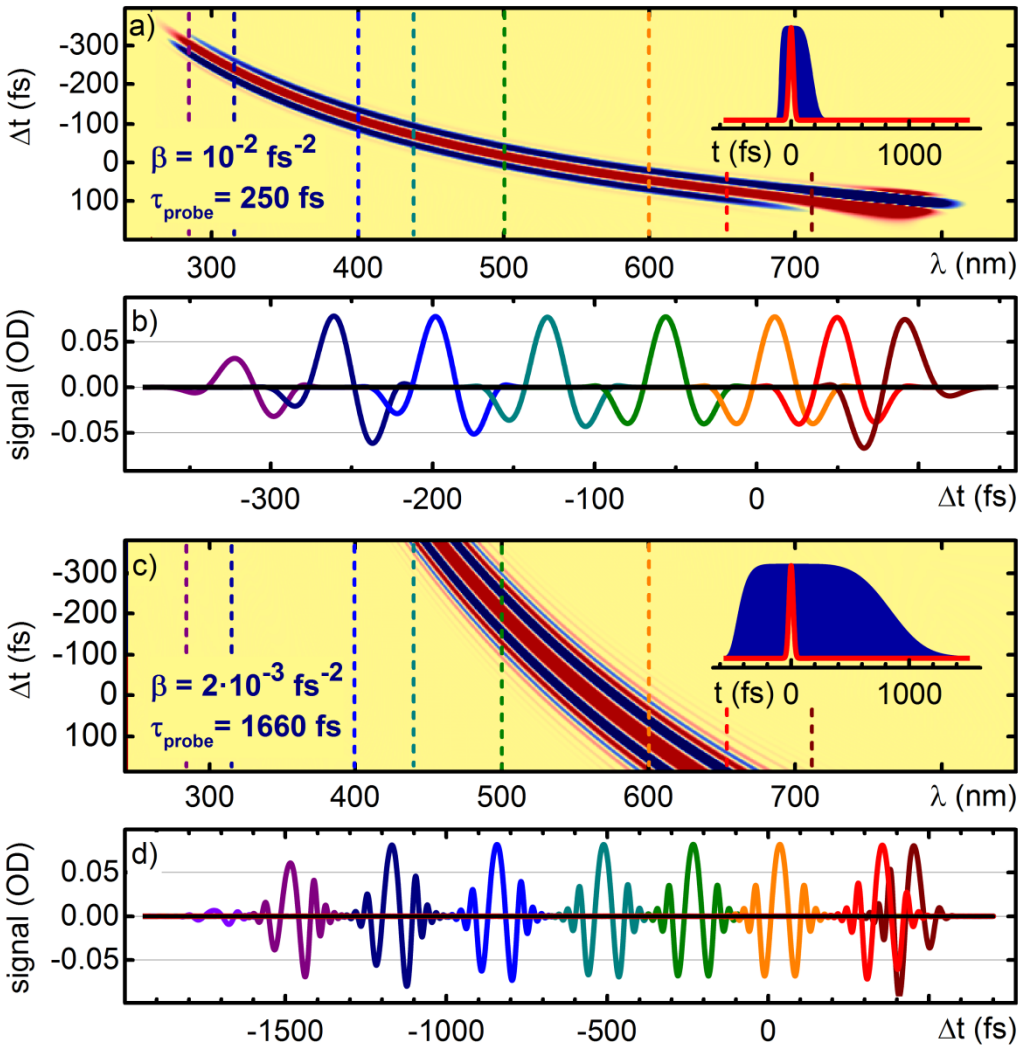

Fig. 2.6: Simulated signals due to XPM of moderately (a) and strongly chirped (c) white light probe in false color representation. $\tau_{pump} = 25\,fs$. Red (blue) indicates positive (negative) signal. Insets show calculated time domain pump (red) and probe pulses (blue). (b,d) delay time domain traces for selected wavelengths correspond to color coded cursors in (a) and (c).

For comparability only a section of the strongly chirped dataset is shown in Fig. 2.6c. Panels 2.6b and 2.6d show delay time domain signals for selected wavelengths spanning the entire probe range, leading to several crucial observations. First, $\Delta t = 0$ coincides with the probe's central wavelength at 530 nm. Second, delay time domain signals are perfectly symmetric around their respective $\Delta t_0(\lambda)$ as long as the probe spectrum is constant. Third, signals become increasingly asymmetric at the edges of the probe spectrum. A direct dependence of the signals symmetry on the probe spectrum's slope is confirmed when the probe spectrum is changed from a flat top to a Gaussian.

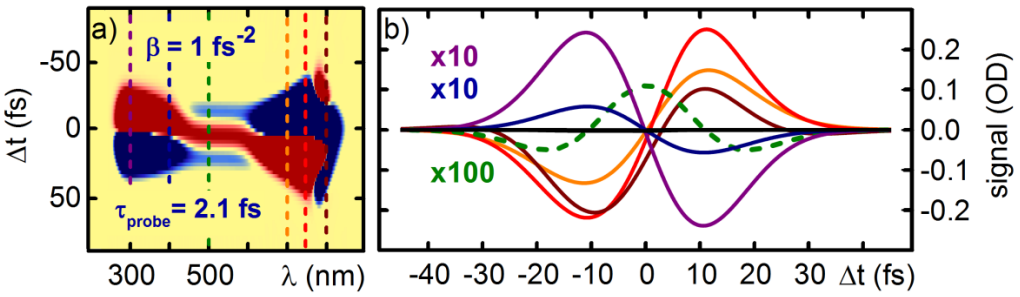

Fig. 2.7: (a) Simulated signal due to XPM of white light probe with very little chirp in false color representation. $\tau_{pump} = 25$ fs. Red (blue) indicates positive (negative) signal. (b) Delay time domain traces for selected wavelengths correspond to color coded cursors. Amplitudes of selected curves were increased for better visibility.

In this case only the time trace at the central wavelength is symmetric. Furthermore, at the red edge of the spectrum the asymmetry is stronger, leading to strongly distorted signals above 700 nm. This can be easily explained: the probe spectrum was assumed as a flat top when plotted vs. wavelength. In the frequency domain, where the XPM modulation is computed, the intensity drop on the red edge of the spectrum is much steeper than that on the blue edge. This is also reflected by the computed time domain pulse shapes, which exhibit a steepened leading edge. Finally, the experimentally observed broadening of the delay time domain signal as well as the change from two negative 'wings' to multiple fringes is well reproduced by the simulation. When the chirp is negative, the detected signal simply flips, i.e. peaks become dips and vice versa.

In the extreme case of an (almost) unchirped probe ($\beta = 1/\text{fs}^2$), the entire probe spectrum is modulated at the same time (cf. Fig. 2.7). The probe pulse is now significantly shorter than the pump. The CA is still symmetric in the center of the spectrum, but its amplitude is reduced by a factor of 10 compared to the chirped case. The large asymmetries can again be attributed to the spectral shape. For a Gaussian pump, the symmetric central section vanishes.

2.3.2 Dependence on Pump Pulse Duration

The dependence of the delay time domain signal on pump pulse duration τ_{pump} is illustrated in Fig. 2.8a. Here the symmetric signal at the probe's central wavelength was computed assuming the most common moderately chirped case with $\beta = 10 \cdot 10^{-3}$ $1/\text{fs}^2$. The delay time step size was reduced to 0.25 fs for this study.

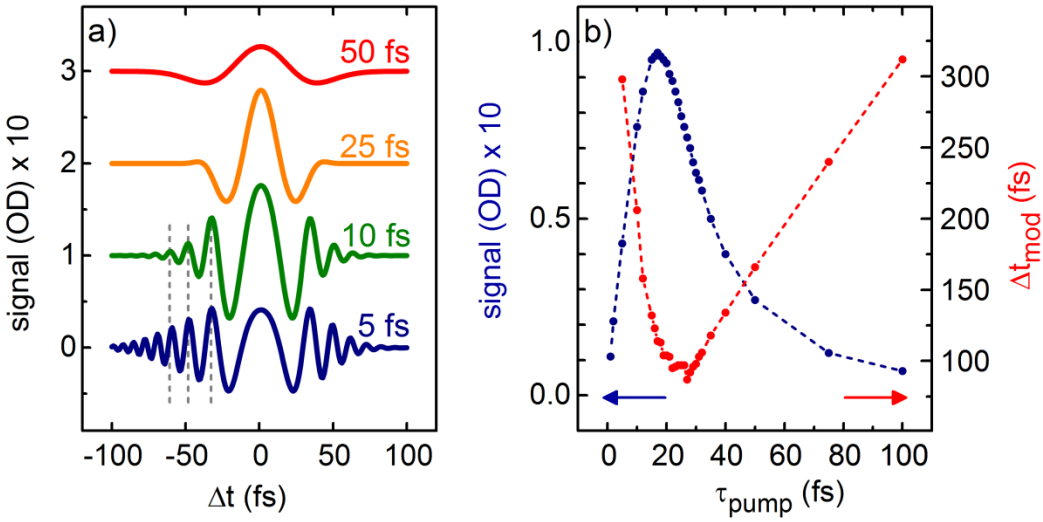

Fig. 2.8: (a) Simulated signal at $\beta = 10 \cdot 10^{-3}$ 1/fs^2 for different pump pulse durations τ_{pump}. Gray cursors illustrate increasing modulation frequency toward the sides (b) Coherent artifact amplitude (blue) and total width of modulated delay time interval Δt_{mod} (red) vs. τ_{pump}.

Figure 2.8b illustrates the signal amplitudes and widths of the delay time interval modulated by the artifact. Exact fitting will be discussed later in this chapter. At this point, a metric independent of a specific fit function is used: the modulated interval Δt_{mod} is defined as the range where the modulation's amplitude is at least 1/1000 of its maximum. Surprisingly, the shortest pump pulse does not yield the shortest CA. Around 25 fs a minimum is reached. This is due to the appearance of artifact fringes at short pump pulse durations. Recognizing that this is the same effect observed when increasing the probe pulse duration by chirping, one can conclude that the observed artifact fringes are not a direct result of the chirp, but arise from the large ratio between the two pulse durations. It follows that the fringes observed in chirped white light should be suppressed when using a longer pump pulse. This was confirmed by the simulation. The amplitude of the central peak does drop considerably as the modulated interval broadens, but the optimum configuration for the smallest and at the same time shortest artifact is assumed at a width of Δt_{mod} = 87 fs using a 27 fs FWHM pump pulse. The conclusion is that if one is to obtain the shortest possible XPM induced CA for a given probe chirp, it does not make sense to shorten the pump pulse beyond a certain limit. Fortunately, 27 fs pump pulses are routinely available in our setup. Yet, already at this optimum pulse duration XPM should be taken into account by the fitting model used.

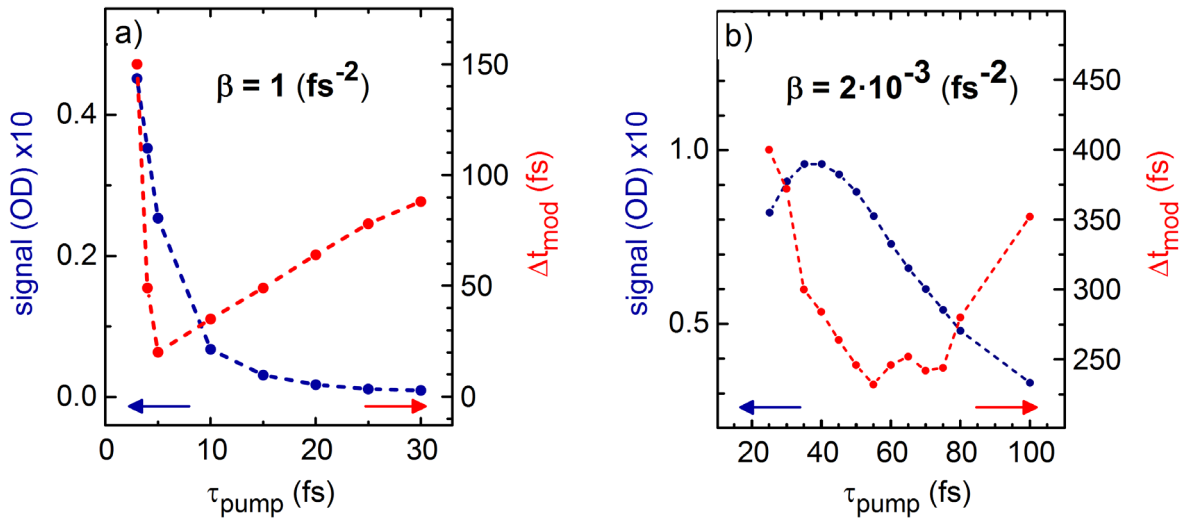

Fig. 2.9: Coherent artifact amplitude (blue) and total width of modulated delay time interval Δt_{mod} (red) vs. pump pulse duration for white light carrying (a) negligible and (b) high linear chirp, $\beta = 1$ 1/fs^2 and $\beta = 2 \cdot 10^{-3}$ 1/fs^2, respectively.

A similar systematic can be observed in (almost) unchirped and highly chirped white light, as illustrated in Fig. 2.9a and 2.9b. respectively. While for (almost) unchirped white light the minimal modulated interval could be shortened to 20 fs assuming a 5 fs pump pulse, at high chirp the minimum width was reached at a pump pulse duration of ca. 230 fs.

Hence, in order to obtain a temporally short artifact, both pump and probe pulses should be compressed whenever possible. Compression of a chirped white light generated in bulk material is cumbersome, as its nonlinear chirp can't be fully compensated by a simple prism compressor. This requires tailored chirped mirrors. Recently, direct generation of (almost) unchirped white light in thin solid substrates has been envisioned [Wit15].

Making use of this effect, in principle one can optimize the pump compression without the need of an additional pulse characterization device: in linearly chirped white light, the spectral signatures exhibit the same features as their delay time domain counterparts (cf. Fig 2.5). While observing a transient spectrum recorded by the CCD camera at a fixed delay time, one can tune the pump compression either to obtain the maximum number of fringes, which corresponds to the shortest pump pulse, or instead optimize for a narrow artifact.

2.3.3 The Origin of Artifact Fringes

The broadening of the artifact with increasing white light chirp seems unintuitive at first: for a larger chirp (i.e. a smaller chirp rate β) the pump is interacting with a spectrally narrower part of the probe. For a linearly chirped probe the wavelength interacting with the pump at a given delay time can be calculated via equation 2.11, assuming the probe central wavelength λ_0 coincides with the pump at $\Delta t = 0$.

$$\lambda_{mod}(\Delta t) = 2\pi \cdot c \cdot (\omega_2 + \beta \cdot \Delta t)^{-1} \tag{2.12}$$

An estimate for the spectral interval directly modulated by the pump is then

$$\Delta\lambda_{mod} = \lambda_{mod}(\Delta t - \tau_{pump}/2) - \lambda_{mod}(\Delta t + \tau_{pump}/2). \tag{2.13}$$

For $\beta = 10^{-2}$ 1/fs^2 and $\lambda_0 = 530$ nm, $\Delta\lambda_{mod}$ is ca. 15 nm for a 10 fs pump pulse.

Artifact fringes can be understood as a spectral interference phenomenon [Wan99, Wah16]. Spectral components within the bandwidth perturbed can interfere with the unperturbed ones. When the pump pulse is much shorter than the probe, only a very narrow part of the probe spectrum is phase shifted at a given delay time. As a consequence, interference fringes appear in the spectrum over a range significantly broader than the perturbed interval. These are recorded by the CCD camera and inevitably translate into the delay time domain signal.

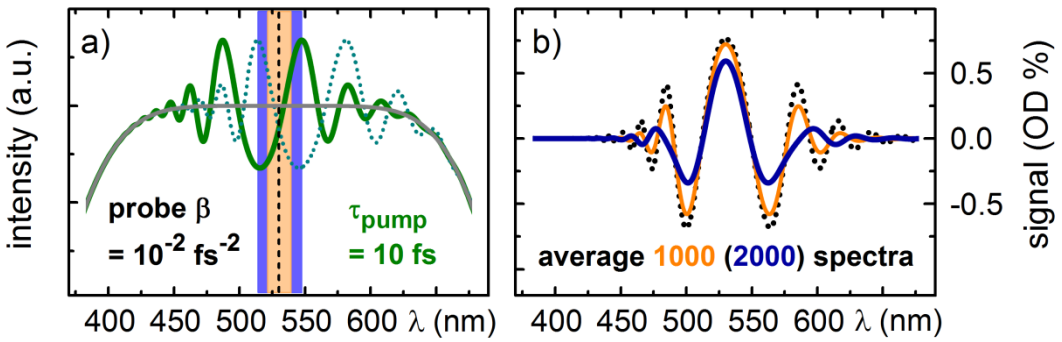

Fig 2.10: Spectral interference of signals produced by increasingly shifted 10 fs pump pulses. (a) Unmodulated probe spectrum (gray) and individual spectra produced by first and last 10 fs pump pulse (green). Colored areas mark scanned Δt intervals. (b) Resulting signal for a single pump pulse (black dots) and the average over signals from 1000 (orange) and 2000 (blue) pump pulses delayed in steps of 0.01 fs, centered around 530 nm. Signal amplitudes scaled for comparability.

When a broad spectral interval is modulated, this interference cancels out due to the superposition of signals. To illustrate this, the average over signals induced by increasingly delayed 10 fs pump pulses was calculated (cf. Fig. 2.10a). The delay time interval was chosen centered around $\Delta t = 0$ with a fine step size of 0.01 fs. As the scanned interval is increased from ±0 fs to ±10 fs, the fringes in the averaged signal wash out (cf. Fig. 2.10b) and the amplitude of the main peak slightly decreases. The same effect occurs when instead of the sum of many short pump pulses, one longer pulse is used (cf. Fig. 2.8). The period of the fringes shortens with increasing distance to the central peak. In the delay time domain this translates into a faster modulation with increasing distance to $\Delta t_0(\lambda)$. Wahlstrand et al. make use of this interference to reconstruct the spectral phase of the probe pulse [Wah16]. Therein an analytical expression is derived that features a cosine with quadratic frequency dependence.

2.3.4 Comparison to Experimental Data

Finally it stands to be determined how closely the simulation can reproduce experimentally obtained data. In the following, experimentally obtained probe spectra will be used as input spectra in the simulation. The spectral phase reflecting the nonlinear chirp of the CaF_2 white light can also be obtained from the experimental data. The spectral phase can be approximated by a Taylor expansion around the probe's central wavelength [Die96].

$$\Phi_s = \sum_0^n \Phi_{s0}(\omega_c) + \Phi_{s1}(\omega_c)(\omega - \omega_c) + \frac{1}{2}\Phi_{s2}(\omega_c)(\omega - \omega_c)^2 + \ldots, \qquad (2.14)$$

where $\Phi_{s1}(\omega)$ and $\Phi_{s2}(\omega)$ represent the first and second derivatives of the spectral phase $\Phi_s(\omega)$ with respect to ω. In the time domain $\Phi_{s0}(\omega)$ will merely result in a shift of the carrier envelope phase without affecting the pulse shape and delay, $\Phi_{s1}(\omega)$ is a frequency dependent shift of the temporal pulse envelope, the group delay (GD), measured in fs. The second derivative represents the group delay dispersion (GDD), measured in fs^2. By determining the $\Delta t_0(\lambda)$ from the experimental time traces using the fitting model derived in the following section, the white light's GD is obtained [Wah16]. Numerically integrating the fitted GD yields the spectral phase up to a constant corresponding to a temporal shift of the entire pulse. Absolute time shifts are irrelevant here, as the pump probe delay Δt is defined relative to the probe pulse. In the simulation the delay at which the pump interacts with the probe's central frequency is defined as $\Delta t = 0$. The central frequency of the experimentally used white light is not a priori clear, especially since the spectrum's long wavelength edge is truncated using a filter and therefore heavily structured. Hence, $\Delta t = 0$ is chosen such that the

coherent artifact manifests in the central part of the spectrum, but this choice is arbitrary.

Three experimental datasets have been selected for comparison. For Dataset A white light generated from the CPA fundamental in 5 mm CaF_2 and a visible 475 nm pump pulse with 24 fs FWHM pulse duration were overlapped in a 200 μm thick Schott BK7 substrate. Dataset B was recorded with increased probe chirp. This was implemented by introducing a 14.5 mm Schott BK7 glass block into the white light's beam path. To exemplify very small chirp, Dataset C was recorded in a nondegenerate NOPA pump NOPA probe experiment. The pump pulse was a 27 fs pulse from a NOPA at 270 nm and 600 nJ pulse energy, while the probe was obtained from the strongly attenuated output of a second NOPA tuned to 420 nm and compressed to 25 fs. The sample was a 100 μm thick α-BBO crystal.

Figure 2.11 juxtaposes the experimentally obtained Dataset A with the simulation. The experimentally obtained probe spectrum and GD are illustrated in Fig. 2.11a. Fitting the GD close to the fundamental is cumbersome, so the curve was extrapolated in the red to cover the entire spectrum used (dashes). This is obviously not the whole truth, since the actual white light spectrum reaches significantly further into the NIR, past the fundamental at 778 nm, but these spectral components are usually not recorded by the CCD camera. Also, it is not a priori clear that the bulk generated white light can be viewed as a single linearly chirped pulse.

Using just the observed part of the spectrum, Fourier transformation yields the time domain pulse shape illustrated in Fig. 2.11b. The structured red part of the spectrum is concentrated in the front of the pulse, since the GD is small in that spectral region. The blue components are delayed by up to about 1.2 ps. This perfectly matches the scanning range needed in the experiment to have the pump pulse interact with the entire probe spectrum, so even though not the whole spectrum was taken into account and the GD was fitted and extrapolated, the obtained probe pulse duration is realistic.

Qualitatively, experimental and simulated TA signals illustrated in Fig. 2.11c and 2.11d look very similar. Even at the structured red edge the features are reproduced surprisingly well. Upon quantitative examination, some differences in the obtained time traces are found. Firstly, signals produced by the simulation are generally a factor of five larger than the experimental ones. Simulation shows that the amplitude of the artifact is directly proportional to the magnitude of the pump induced phase shift Φ_{XPM}.

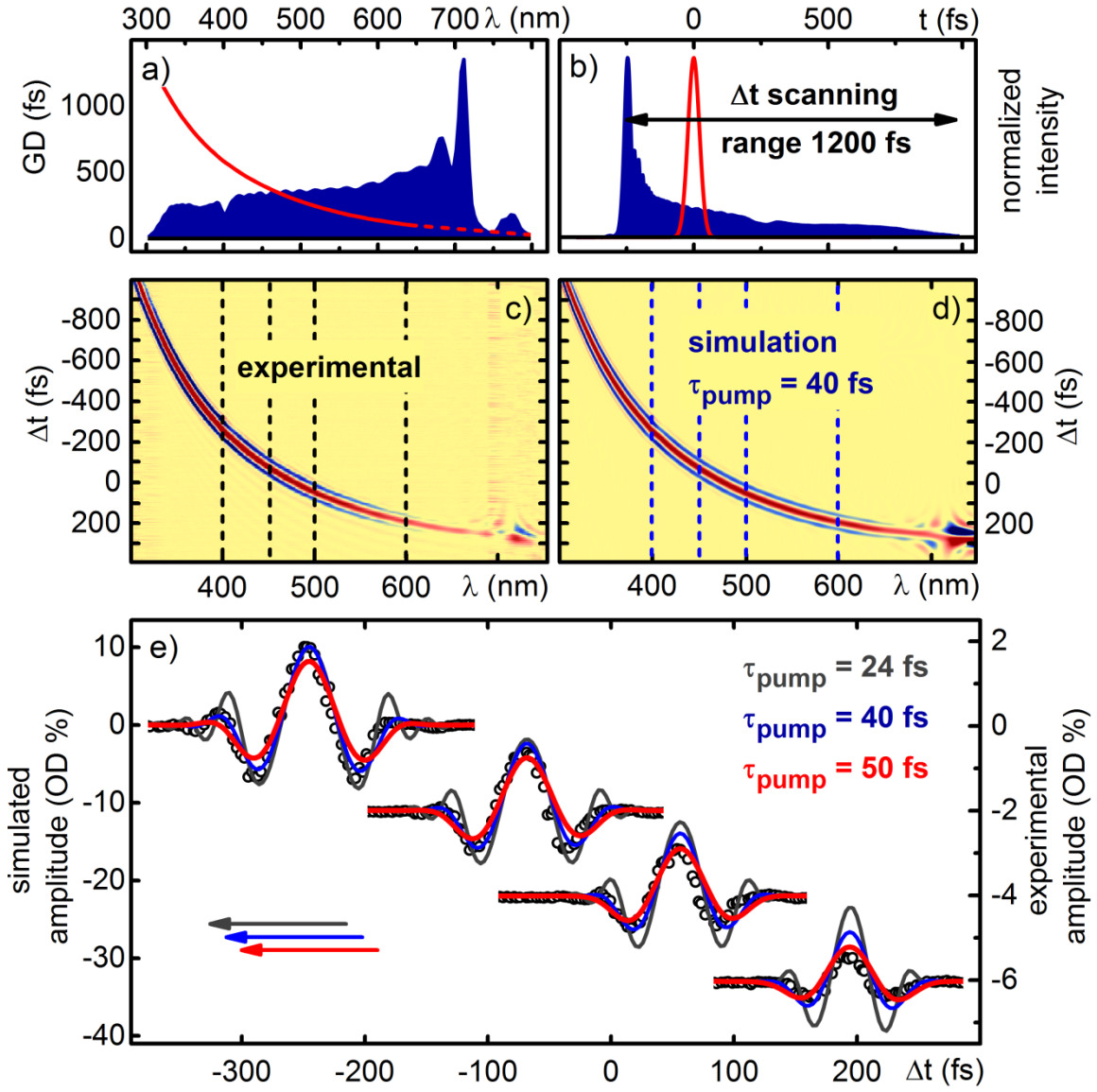

Fig. 2.11: Simulation using realistic probe spectrum and integrated phase from fitted group delay (GD) vs. experimental data. (a) Fitted GD (red, solid), extrapolated GD (red, dashed) and normalized experimental probe spectrum (blue). (b) Calculated pump (red) and probe (blue) time domain pulse shapes. (c) Experimentally obtained transient absorption (TA) signal. (d) Simulated TA signal. (e) Experimental (circles) and simulated time traces at spectral positions indicated in (d) for τ_{pump} = 24 fs (gray), 40 fs (blue) and 50 fs (red).

The amplitude factors in Φ_{XPM} are the pump pulse intensity as well as the length L and nonlinear refractive index n_2 of the medium (cf. Eq. 2.5). While the length and peak intensity are well known (183 µm, 300 GW/cm^2), the nonlinear refractive index is not. The value for Schott B270 taken from literature was measured at 800 nm in a 5 mm thick sample and could easily be considerably smaller for the visible [Mog10]. Another factor that needs to be considered is that the spatial profile of the pump pulse is a Gaussian, and the probe spot in the sample is smaller than the pump spot by about a factor of four. Hence, in practice the probe will not experience a uniform phase shift corresponding to the peak intensity.

Secondly, simulated signals tend to exhibit more fringes than the experimentally obtained ones. It was illustrated in Section 2.3.2 that the parameter responsible for the amount of fringes is the ratio between pump and probe pulse duration. The probe pulse duration of ca. 1200 fs obtained from the simulation already matches the scan interval in the experiment well and the evolution of the CA signal is well reproduced. Therefore the simulation was repeated assuming different pump pulse durations τ_{pump}. Figure 2.11e shows time traces extracted from the experimental data at wavelengths indicated in Fig. 2.11c and 2.11d, compared to their simulated counterparts. The left and right axes are scaled for best comparability of the simulated and experimental signal amplitudes. The simulation assuming a 24 fs pump pulse (gray) clearly overestimates the artifact fringes. Increasing the pulse duration to 40 fs (blue) reproduces the signal shapes a lot better, especially in the blue. However, the decreasing signal intensity towards the red is not well reproduced. This improves when the pump pulse duration is further increased to 50 fs (red), but the fringes in the strongly chirped blue part of the spectrum are now underestimated. Also, simulations using 40 fs and 50 fs increasingly overestimate the total width of the modulated probe interval. This deviation becomes more severe towards longer wavelengths: this can be quantified using the fitting algorithm presented in the next section. When comparing the fitted widths of the modulation, the simulation using τ_{pump} = 24 fs yields a value close to that of the experimental data, despite the more pronounced fringes. It follows that a good fit cannot be obtained by a simple increase in the pump pulse duration. Also, an error of this magnitude in the autocorrelation of the pump pulse seems very unlikely.

As the deviation is wavelength dependent, a likely reason lies in the propagation effects neglected in the simulation. Group velocity mismatch (GVM) would cause a wavelength dependent shift of the probe pulse w.r.t the pump while propagating through the sample, therefore modulating a broader spectral interval. By the same argument as presented in

Section 2.3.3 this would cause the interference fringes to wash out. The magnitude of the GVM w.r.t. a reference wavelength λ_{ref} can be estimated for B270 glass via

$$\mathrm{GVM}(\lambda) = \frac{1}{c}\left(n(\lambda) - \lambda \cdot \frac{\partial n}{\partial \lambda} \right) - \frac{1}{c}\left(n(\lambda_{ref}) - \lambda_{ref} \cdot \frac{\partial n}{\partial \lambda_{ref}} \right) \qquad (2.15)$$

where $n(\lambda)$ is approximated via the Sellmeier equation using coefficients for B270 glass obtained from Crystran Ltd, UK [Cry16]. Multiplying the GVM by the substrate's thickness of 183 µm, the total temporal shift of a given probe frequency can be calculated. At $\lambda_{probe} = 400\,\mathrm{nm}$ the total shift w.r.t. the 500 nm pump pulse amounts to approximately 24 fs. This is small enough not to cause significant broadening of the CA, but at the same time slightly larger than the temporal shift that caused suppression of interference fringes in Section 2.3.3. Hence, it is just enough to explain the observed discrepancies in the fringes as well as the spectral dependence of the amplitude.

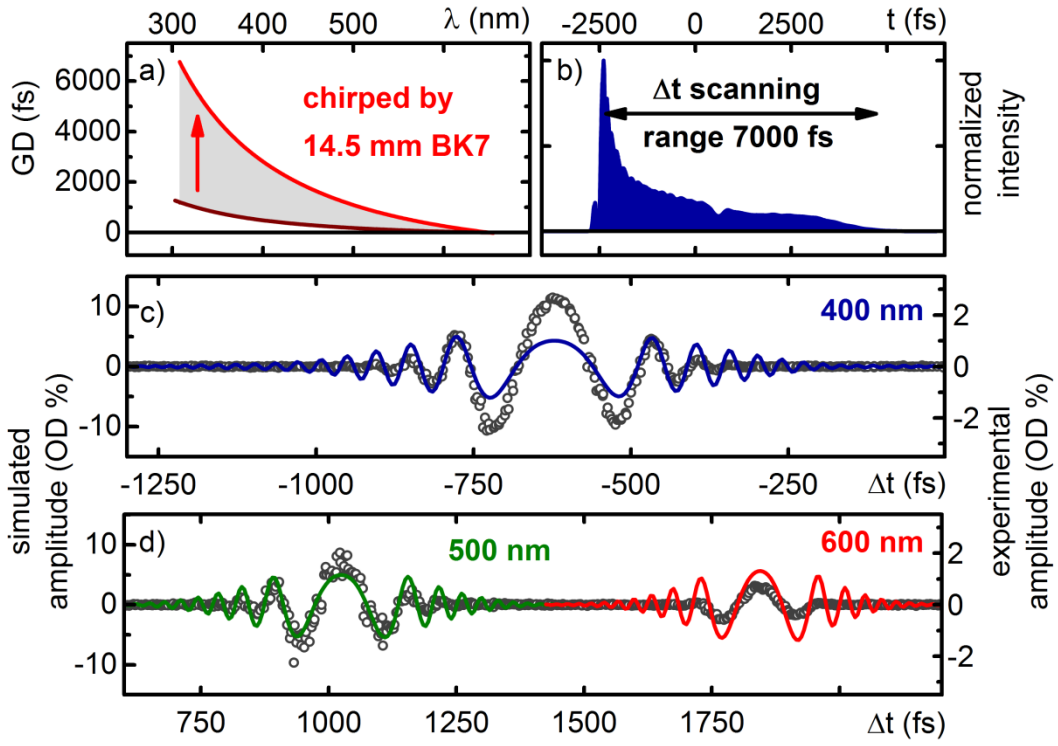

Fig. 2.12: Simulation using realistic probe spectrum and integrated phase from fitted GD vs. experimental data for highly chirped white light. (a) Fitted GD (red) compared to moderately chirped case (wine). (b) Calculated time domain pulse shape of the probe. (c) Simulated (blue) and experimentally obtained signal at 400 nm.(d) same as (c) for 500 nm and 600 nm.

Figure 2.12 shows the obtained TA signals at increased probe chirp (Dataset B), obtained in white light chirped by transmission through a 14.5 mm BK7 block and the corresponding simulation. The simulated scanning range has increased to 7000 fs, once more corresponding very well to the range scanned in the experiment. As before, the artifact fringes in the simulation are overpronounced. Nonetheless, the positions of maxima and minima are reproduced fairly accurately.

Qualitative agreement is also obtained in the extreme case of an unchirped probe (cf. Fig. 2.13). The simulated and experimental signals show similar features, i.e. two negative and two positive lobes with nodal planes at $\Delta t = 0$ fs and at the probe's central wavelength. In Fig. 2.13c the shift towards positive delay times at the blue edge of the experimentally obtained dataset indicates some residual chirp. In the simulation (Fig. 2.13d) zero chirp was assumed, i.e. no phase was added to the probe pulse. The Fourier-limited FWHM pulse duration corresponding to the experimentally obtained probe spectrum is 22 fs (cf. Fig. 2.13b). The probe pulse duration obtained by autocorrelation was 25 fs, so the pulse was not perfectly Fourier-limited. The experimental traces occupy about twice as large a temporal interval as the simulated ones. Again, this broadening is likely due to a large GVM between the 270 nm pump and the visible probe in the 100 μm thick α-BBO crystal. The temporal shift calculated via Eq. 2.15 is approximately 142 fs, comparable to the experimentally observed width of the signals.

While exact quantitative agreement has not been achieved, the above simulations do facilitate a qualitative understanding of the signals obtained under a wide range of conditions. It has further become clear that the coherent artifacts observed in the measurements presented herein are predominantly caused by XPM. In the following section fitting models for XPM induced coherent artifacts will be discussed.

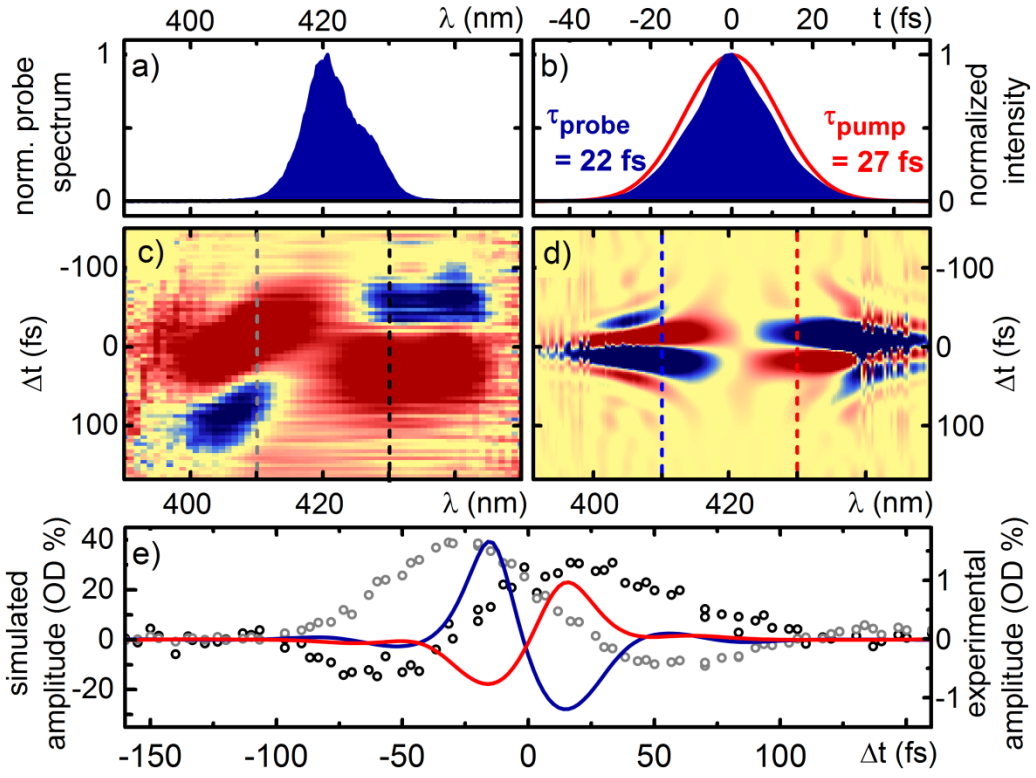

Fig. 2.13: Simulation using realistic probe spectrum vs. experimental data for an unchirped probe pulse. (a) Probe spectrum. (b) Calculated time domain pulse shape of pump and probe. (c) Experimentally obtained TA signal. (d) Simulated TA signal. (e) Simulated (circles) and experimentally obtained signals at wavelengths indicated by color coded cursors in (c) and (d).

2.4 Analytical Models & Parameterizations

A suitable model for the coherent artifact (CA) is absolutely essential for the accurate determination of the time origin. Ignoring features like asymmetry, artifact wings or fringes can yield fraudulent $\Delta t_0(\lambda)$ which lead to errors in the subsequent analysis of molecular dynamics. From a reference measurement in pure solvent or a solid substrate the probe chirp can be inferred by way of the CA. To obtain a 'clean' Gaussian artifact induced by two photon absorption (TPA) over a broad spectral range, one must carefully choose sample materials to avoid contributions due to other effects. This can prove challenging as negative wings often occur even close to the material's bandgap and at very low pump energies (cf. Fig. 2.2a). In most measurements presented in this thesis the dominating contribution to the artifact is cross phase modulation (XPM). While modeling TPA is certainly more straight-forward, being able to model artifacts partly or mainly induced by XPM with sufficient precision comes with two big advantages: chirp reference measurements can be performed at any pump wavelength without the need to provide a selected set of materials with appropriate bandgaps. The only requirement is for the material to be transparent throughout the spectral range of interest. Section 2.5 will show that precise measurements of $\Delta t_0(\lambda)$ throughout the entire visible range are possible in a single scan using e.g. Schott B270 glass. Secondly, current fitting models often do not reproduce CA fringes, leading to a residual contribution to the transient absorption (TA) data that can be mistaken for e.g. electronic wavepacket motion. As spectroscopists are moving to ever shorter pump pulses to resolve the fastest dynamics, an approach taking these fringes into account is needed. Approximate analytical models of pump induced XPM in a chirped broadband probe pulse exist. Many consider the white light probe pulse as a single chirped Gaussian [Kov99, Wan99, Ekv00, Lap11, Wah16]. Others consider the change in intensity detected by a given detector pixel, as only a small portion of the probe interacts with the pump at a given delay time [Lor02]. Models become increasingly complex when including propagation effects like broadening due to group velocity dispersion (GVD) in the medium. In this case one has to rely on numerical simulations [Ekv00]. While analytical models allow extraction of pulse parameters [Kov99, Wah16], most practitioners rely on simplified parameterizations in order to extract $\Delta t_0(\lambda)$. These are computationally less bulky and more robust in trace-by-trace fitting. In this section selected existing models are reviewed and a novel parameterization is introduced.

2.4.1 The Combined Gaussian & Derivative Model

The most common parameterization used to fit the coherent artifact in the delay time domain at a given wavelength λ is the sum of a Gaussian $G^{(0)}$ and its first and second derivatives $G^{(1)}$ and $G^{(2)}$ w.r.t. the delay time Δt [Kov99, Lor02, Meg09, Sla15].

$$FGauß(\Delta t) = \sum_{i=0}^{2} A_i(\lambda) \cdot G^{(i)}(\tau(\lambda), \Delta t_0(\lambda), \Delta t) \qquad (2.16)$$

Here the fit parameters are the time origin $\Delta t_0(\lambda)$, the amplitudes $A_i(\lambda)$, and the FWHM Gaussian width $\tau(\lambda)$. A_1 and A_2 carry the units s and s^2, respectively. In order to directly compare them to A_0 they must be scaled according to

$$A_1^* = \frac{2A_1}{\tau}\sqrt{\frac{\ln 4}{e}}, \qquad A_2^* = -\frac{A_2 \cdot 8\ln 2}{\tau^2} \quad . \qquad (2.17)$$

This is a practical approach that will fit contributions arising from TPA and XPM to a certain degree. The first derivative term facilitates the fit of asymmetric artifacts. Hence, especially when $A_0 >> A_1^*, A_2^*$, this practical model is sufficient in many cases. Yet, the determination of $\Delta t_0(\lambda)$ can become ambiguous when the first derivative term $A_1 \cdot G'$ becomes large.

Lorenc et al. offer a simplified but intuitive description motivating the second derivative term $A_2 \cdot G''$ [Lor02]. They describe a setup with slightly different parameters (τ_{pump} = 120 fs, grating spectrograph, fluid sample of up to 2 mm thickness in a flow cuvette), but the model is found to describe the data presented herein with the reasonable accuracy. Assuming a weak, linearly polarized probe pulse with a slowly varying envelope and a linear chirp, the time domain field can be decribed as

$$\tilde{E}_2(t) = \tilde{E}_2(0) \cdot \exp\left[-\frac{\sqrt{2\ln(2)} \cdot t^2}{{\tau_2}^2} + i \cdot (\omega_2 \cdot t + \tfrac{1}{2} \cdot \beta \cdot t^2) \right] \qquad (2.18)$$

where τ_2 is the FWHM duration of probe pulse and β the linear chirp rate. The instantaneous frequency is then (cf. Eq. 2.7)

$$\omega(t) = \omega_2 + \beta \cdot t + \Delta\omega(t) \qquad (2.19)$$

XPM will cause a modulation $\Delta\omega$ as given in Eq. 2.8 [Lor02]. Unless the frequency modulation due to XPM is so strong that the slope of $\omega(t)$ changes sign, Lorenc et al. argue that the transmitted intensity $T(\lambda, \Delta t)$ for a given detection wavelength λ and pump probe delay Δt is proportional to the square of the inverse slope of $\omega(t)$ [Lor02].

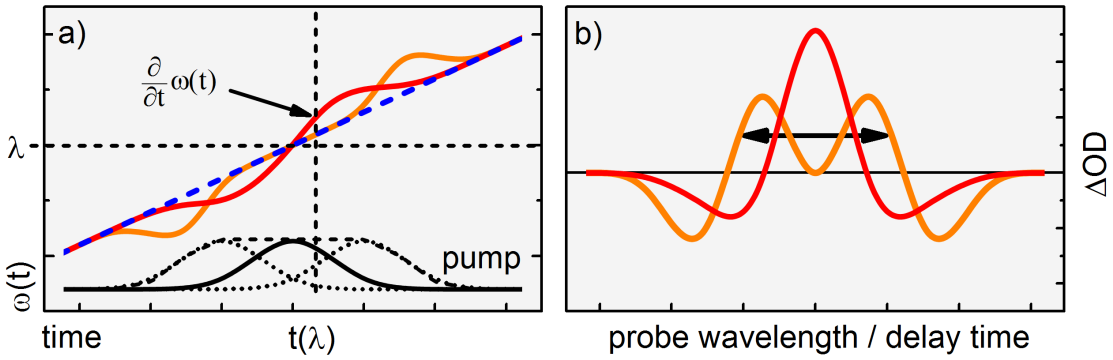

Fig. 2.14: Schematic illustration of (a) the XPM induced probe GD modulation and (b) the resulting transmission signals with (orange) and without (red) group velocity dispersion. Modulation of probe chirp in (a) exaggerated for clarity.

In other words, when the slope of $\omega(t)$ is small, a given CCD pixel will be irradiated for a longer amount of time and therefore acquire more counts during its integration time.

$$T(\lambda,\Delta t) \propto \left(\left(\frac{\partial}{\partial t}\omega(t,\Delta t)\Big|_{t(\lambda)} \right)^{-1} \right)^2 \tag{2.20}$$

Here the time derivative is evaluated at the time $t(\lambda)$ corresponding to the detection wavelength under consideration. This is illustrated in Fig. 2.14a. Since the probe is linearly chirped, each spectral component λ interacts with the pump at a different time $t(\lambda)$. For small frequency modulations $\Delta\omega$, $t(\lambda)$ can be obtained via

$$t(\lambda) = \frac{1}{\beta} \cdot \left[\frac{2\pi \cdot c}{\lambda} - \frac{2\pi \cdot c}{\lambda_2} \right], \tag{2.21}$$

where λ_2 is the central wavelength of the probe. Similar arguments are used in [Tok96, Kov99, Lor02, Nau03]. It follows from Eqs. 2.19 and 2.20 that without a modulation by a pump pulse the transmission $T_0(\lambda,\Delta t) \propto (1/\beta)^2$. Therefore, the TA signal $T(\lambda,\Delta t) / T_0(\lambda,\Delta t)$ can be written as

$$\frac{T(\lambda,\Delta t)}{T_0(\lambda,\Delta t)} = \left(\beta \cdot \left(\frac{\partial}{\partial t}\omega(t,\Delta t)\Big|_{t(\lambda)} \right)^{-1} \right)^2. \tag{2.22}$$

Finally combining Eq .2.8, 2.19 and 2.22, the signal $S(\lambda)$ in OD for a given pump probe delay can be written as

$$S(\lambda,\Delta t) = -\log\left[\frac{T(\lambda,\Delta t)}{T_0(\lambda,\Delta t)}\right] = 2\log\left(\frac{1}{\beta}\left(\frac{\partial}{\partial t}\omega(t,\Delta t)\Big|_{t(\lambda)}\right)\right) =$$
$$= 2\log\left[1 - \frac{4\pi\cdot n_2\cdot L}{\beta\cdot\lambda_2}\cdot\frac{\partial^2}{\partial t^2}I(t,\Delta t)\Big|_{t(\lambda)}\right] \qquad (2.23)$$

where λ_2 is the central wavelength of the probe. $S(\lambda,\Delta t)$ represents the signal in OD measured for a given pump probe delay Δt and probe wavelength λ. It should be noted that this model only holds for small modulations of the probe chirp. If the slope of $\omega(t)$ is reduced to zero at any spectral position, the transmission is not defined at that point (Eq. 2.22).

From Fig.2.14a and Eq. 2.21 one can infer that for a linearly chirped probe signal shapes in the frequency and delay time domains should be identical except for a stretching factor determined by the slope of the linear chirp β. Typical CA shapes are shown in Sections 2.2 and 2.3. When β increases, the delay time domain signal narrows because the modulation will affect a given probe wavelength only for a very limited delay time range while the frequency domain signal is stretched [Lor02]. Another crucial observation is that the artifact flips when β changes sign. These properties correctly reflect systematics observed in simulation as well as experiment, as will be presented in Chapter 3.

Asymmetry and fringes are not reproduced by the models discussed above. Figure 2.15 shows a coherent artifact generated in a 217µm Schott B270 glass by a 25 fs, 465 nm pump pulse in moderately and highly chirped white light (circles).

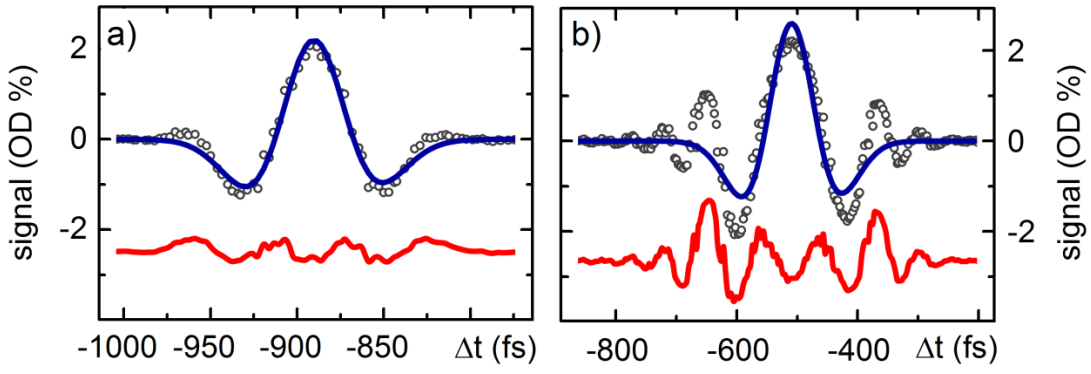

Fig. 2.15: (a) Coherent artifact in 183 µm Schott B270 (circles) and fits using FGauß (blue). τ_{pump} = 25 fs , λ_{pump} = 465 nm, λ_{probe} = 400 nm. Residual (red) offset for clarity. (b) Probe chirp increased by transmission through a 14.5 mm Schott BK7 glass block.

Blue lines indicate fits using FGauß (Eq. 2.16). The CA wings are not reproduced with high accuracy. In the residual (red) a periodic deviation is clearly visible. The obvious reason is that this model only describes the redistribution of spectral intensity into different frequencies. It does not take into account phase effects like interference.

In combination with CA asymmetries, periodic fluctuations can lead to unrealistic oscillations in the fitted $\Delta t_0(\lambda)$ which limit the measurement accuracy. It follows from the simulations in Section 2.3 that this model is only valid as long as the pump pulse is still long enough to not produce significant interference in the probe spectrum. On the path to resolve ever faster dynamics spectroscopists are moving to ever shorter pump pulses, so an approach taking into account this effect is needed. Recently, similar features were observed by Wahlstrand et al [Wah16].

2.4.2 The Kovalenko Model

A more rigorous analytical model has been proposed by Kovalenko et al [Kov99]. Neglecting GVD and assuming the pulses are long compared to the electronic dephasing, the delay time domain signal from a thin solid is derived for a given probe frequency. Starting from the third order polarization induced by the pump and probe electric fields, Kovalenko et al. argue that the probe can be described as a single nonlinearly chirped single pulse. They also discuss the special case of a linearly chirped probe with a slowly varying envelope and a linear chirp $E_2(\omega)$ (cf. Eqs. 2.9 and 2.10). Since the pump interacts with different spectral components of the probe at different delay times, a so-called time zero function $\Delta t_0(\Omega_2)$ can be defined via

$$\Delta t_0(\Omega_2) = \frac{\Omega_2 - \omega_2}{\beta}. \tag{2.24}$$

$\Delta t_0(\Omega_2)$ describes the delay time at which a certain spectral component Ω_2 interacts with the pump, provided that $\Delta t_0(\Omega_2)$ is set to zero when $\Omega_2 = \omega_2$ [Kov99].

Assuming Gaussian pump and probe pulses, the XPM induced differential transmission vs. delay time for an unchirped pump and a linearly chirped probe takes the following form [Kov99]:

$$\mathrm{FKov}(\Omega_2, \Delta t) = -D_0 \cdot$$

$$\mathrm{Im}\left\{ \exp\left[-\frac{8\ln(2)\cdot[\Delta t - \Delta t_0(\Omega_2)]^2}{\eta \cdot {\tau_1}^2} + \left(\frac{-8\ln(2)\cdot \Delta t_0(\Omega_2)}{\beta \cdot {\tau_2}^2} \right)^2 \cdot \frac{8\ln(2)}{\eta \cdot {\tau_1}^2} \right. \right. \quad (2.25a)$$

$$\left. \left. + i \cdot \frac{-2\cdot \Delta t_0(\Omega_2)}{\beta \cdot {\tau_2}^2} \frac{[\Delta t - \Delta t_0(\Omega_2)]\cdot (8\ln(2))^2}{\eta \cdot {\tau_1}^2} - \frac{i}{2} \cdot \arctan\left(\frac{\mathrm{Im}\,\eta}{\mathrm{Re}\,\eta} \right) \right] \right\}$$

with

$$\eta = 1 + 2 \cdot \frac{(\tau_2/\tau_1)^2}{1 - i \cdot \left(\beta \cdot {\tau_2}^2 / 16\ln(2) \right)}. \quad (2.25b)$$

Here $\tau_1 = \tau_{pump}$, τ_2 is the FWHM probe pulse duration and Ω_2 the probe frequency under consideration. In this convention $\beta \cdot {\tau_2}^2$ is a dimensionless measure of the probe bandwidth and should be kept constant if the spectral width is to remain unchanged. Kovalenko et al. use differential transmission as opposed to T/T_0, but for small signals these quantities are almost equivalent. The Gaussian envelope of Eq. 2.25a features a width dependent on the probe pulse's chirp and duration. In the case of a moderately chirped probe, the combined Gaussian & derivative model can be deduced by expanding Eq. 2.25a. The width of the envelope then becomes comparable to τ_{pump} [Kov99]. Delay time domain signals calculated via Eq. 2.25 are illustrated in Fig. 2.16.

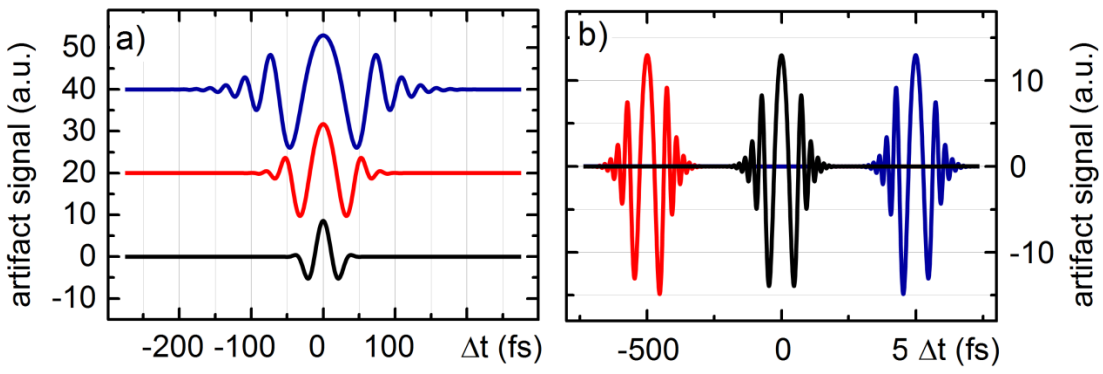

Fig. 2.16: Signals calculated via Eq. 2.25 with parameters $D_0 = 0.2$, $\tau_1 = 30$ fs. (a) For increasing chirp rates $\beta = 4000$ 1/fs^2 (blue), $\beta = 8000$ 1/fs^2 (red) and $\beta = 20000$ 1/fs^2 (black), but constant bandwidth $\beta \cdot {\tau_2}^2$ and $\Delta t_0(\lambda) = 0$ fs. Signals plottet offset for clarity. (b) Signals at $\Delta t_0(\lambda) = 0$ fs and ± 500 fs for $\tau_2 = 1000$ fs and $\beta = 4000$ 1/fs^2.

In Fig 2.16a the chirp rate β was increased while maintaining a constant bandwidth $\beta \cdot \tau_2{}^2$. The experimentally observed emergence of fringes with increasing chirp is nicely reproduced by FKov. This was not explicitly shown in [Kov99].

Yet, there is a drawback: equation 2.25 inherently carries a special asymmetry with respect to the assumed central frequency Ω_{2c} of the probe pulse, where $\Delta t_0(\Omega_{2c}) = 0$. The signal observed at a probe frequency $(\Omega_{2c} - \partial\Omega_2)$ equals the signal at $(\Omega_{2c} + \partial\Omega_2)$ when $\Delta t \rightarrow$ -Δt (cf. Fig. 2.16b). Artifact simulations confirm this for the Gaussian shaped probe pulse assumed in reference [Kov99], but not for a flat top pulse or a realistic probe spectrum, where the artifact is fairly symmetric over a broad spectral range (cf. Fig 2.6).

As a consequence, when Eq. 2.25 is to be employed as a fit function with parameters D_0, τ_1, τ_2, β and $\Delta t_0(\Omega_2)$ the axis origin $\Delta t_0(\Omega_2) = 0$ must be adjusted for each time trace to account for CA asymmetries in experimentally obtained datasets. The determination of the correct shift is not straightforward and introduces additional errors and ambiguities. Fitting transient data over a wide spectral range via FKov (Eq. 2.25) is computationally expensive and parameters (especially τ_2) tend to diverge. Fixing the pump and probe pulse durations τ_1 and τ_2 for the whole dataset is not an option either, since these parameters depend on Ω_2 due to material dispersion not included in the model.

For this reason, while fitting single time traces using FKov (Eq. 2.25) is possible and gives some insight into the characteristics of the pulses used, a more practical approach is required for a robust fit of entire transient datasets $S(\lambda, \Delta t)$ over a wide spectral range.

2.4.3 Combining Models for a Practical Parameterization

An oscillating fit function is needed in order to accurately fit artifacts without leaving a systematic contribution in the residual. Hence, the combined Gaussian and derivative model introduced in Section 2.4.1 is not ideal. The Kovalenko model [Kov99] allows reconstruction of actual pulse parameters in an idealized case, yet aforementioned challenges render it impractical for the fit of experimental broadband transient data (cf. Section 2.4.2). In practice the main interest usually lies in the accurate determination of $\Delta t_0(\lambda)$ over a large bandwidth as well as a minimal residual. Drawing from the experience gained from simulations and existing models [Lor02, Kov99, Wah16], the simplified parameterization Fcos can be introduced by using a Gaussian and its first derivative, modulated by a cosine with a quadratic argument.

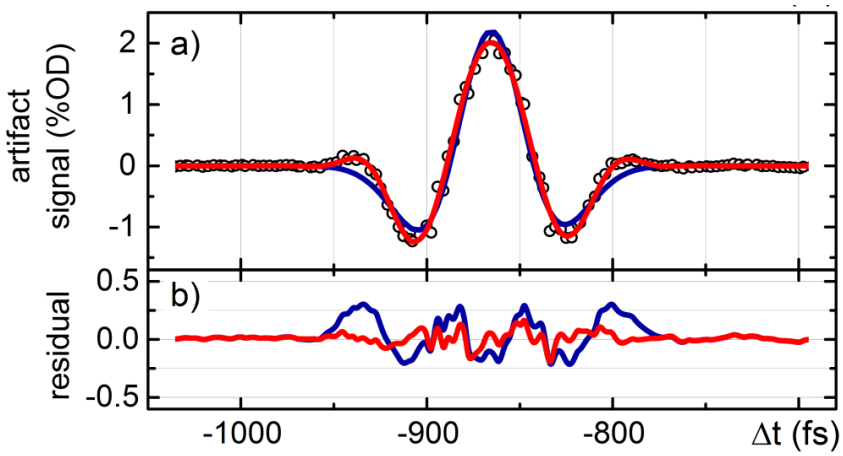

Fig. 2.17: (a) Coherent artifact from 183 µm Schott B270. τ_{pump} = 25 fs at λ_{pump}=465 nm and λ_{probe}=400 nm and fits using FGauss (blue) and Fcos (red). (b) Residuals.

$$\mathrm{Fcos}(\lambda,\Delta t) = \cos\left(B(\lambda)\cdot(\Delta t-\Delta t_0)^2+\Phi(\lambda)\right)\cdot\left\{A_0(\lambda)\cdot\exp\left[\frac{-4\ln 2\left(\Delta t-\Delta t_0(\lambda)\right)^2}{\tau(\lambda)^2}\right]\right. \\ \left. -A_1(\lambda)\cdot\frac{8\ln 2}{\tau(\lambda)^2}\left(\Delta t-\Delta t_0(\lambda)\right)\cdot\exp\left[\frac{-4\ln 2\left(\Delta t-\Delta t_0(\lambda)\right)^2}{\tau(\lambda)^2}\right]\right\} \quad (2.26)$$

The fit parameters are $A_0, A_1, \tau, \Delta t_0, B$ and Φ. This is only one additional parameter w.r.t. to the commonly used combined Gaussian and derivative model (cf. Section 2.4.1). The parameter B carries the unit $1/s^2$ and determines how quickly the fringe periodicity increases. When both TPA and XPM are contributing significantly, TPA will manifest as a phase shift of the modulation [Wan99], which can be adapted via the parameter Φ. The frequency factor B and phase Φ allow reproduction of artifact fringes independent of the signals envelope. The first derivative term facilitates the fit of asymmetric signals irrespective of their absolute position relative to the central wavelength. For highly asymmetric CAs, care must be taken to keep the appropriately scaled $A_1^* << A_0$ to avoid ambiguities (cf. Eq. 2.17).

In the following the performance of the new parameterization Fcos is compared to the models discussed above for typical signals from probe pulses with varying chirp. Selected experimentally obtained time traces are fitted in Mathcad Prime 3.1 using a Levenberg-Marquardt algorithm. Figure 2.17 clearly shows that Fcos reproduces the signal shape better than the second derivative in FGauss (Eq. 2.16), even for the most commonly observed artifact shape. The oscillating contribution in the residual is efficiently suppressed.

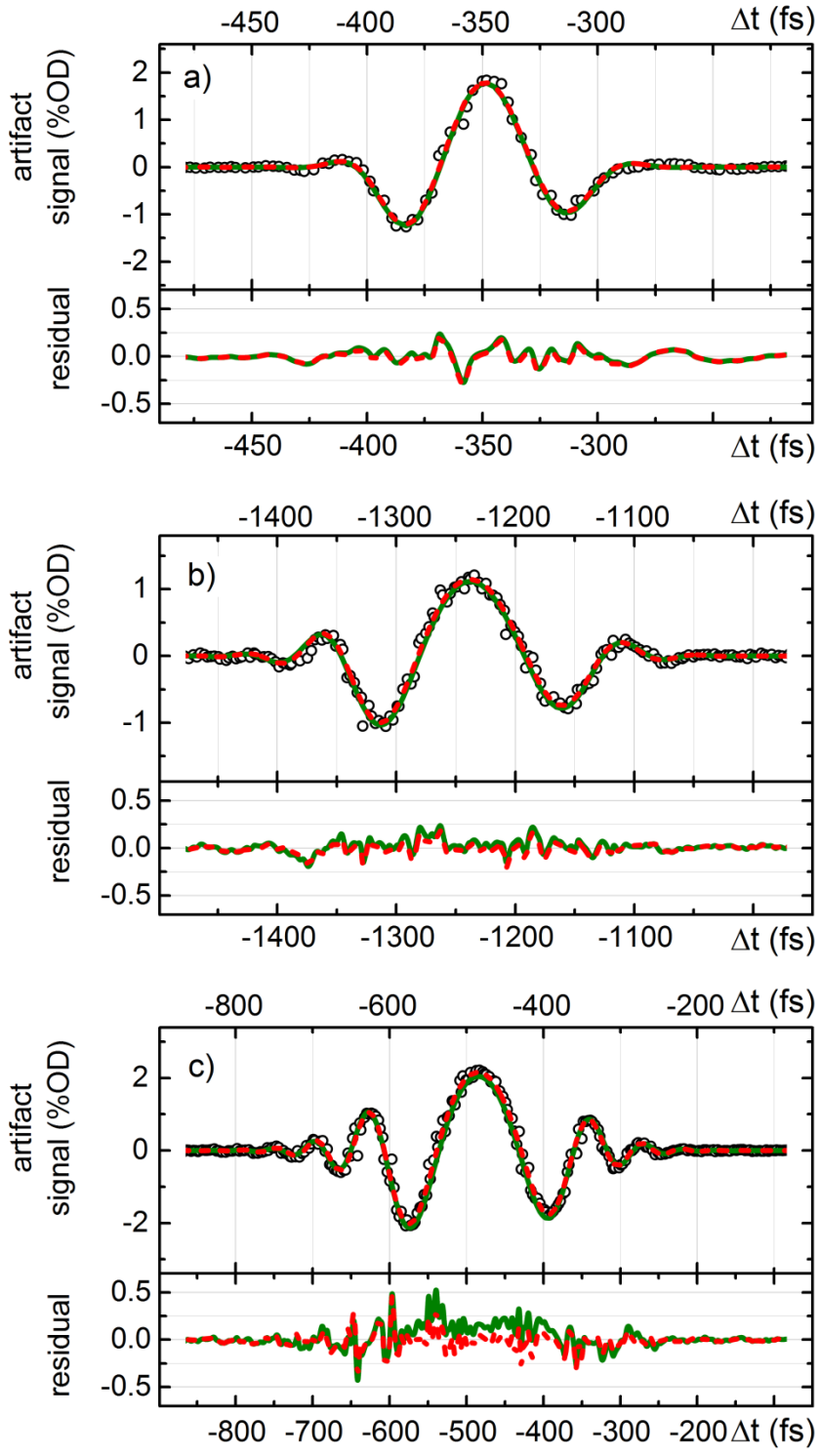

Fig. 2.18: Coherent artifact in 183 µm Schott B270 using 1000 nJ at λ_{pump} = 465 nm and fits using FKov (green) and Fcos (red dashes). (a) Signal at λ_{probe} = 600 nm. (b,c) Probe chirp increased utilizing a 14.5 mm Schott BK7 block, λ_{probe} = 420 nm and 500 nm, respectively. Bottom panels show residuals.

Compared to the analytical model FKov, Fcos yields an almost identical fit for a wide range of probe chirps (cf. Fig. 2.18). Parameters obtained by the fits in Fig. 2.18 are shown in Table 2.1. Note that the experimental probe spectrum is not Gaussian, so the obtained probe pulse duration is certainly misleading. The pump pulse duration is likely overestimated due to GVM not included in the model. Even though the trace in Fig. 2.18b already looks quite asymmetric, the fitted $\Delta t_0(\lambda)$ only shifts by 0.5 fs with respect to a fit where A_1^* was fixed at zero, so A_1^* represents only a small correction. Here $A_0 >> A_1^*$ was not enforced explicitly as a constraint. This is only necessary for larger asymmetries. While the obtained chirp β and probe pulse duration τ_2 from the trace in Fig. 2.18c are comparable to values obtained from that in Fig. 2.18b, the fitted pump pulse duration τ_1 is significantly shorter. This could be due to a smaller group velocity mismatch between the pump and the selected probe wavelength.

Due to its superior adaptability to changing artifact shapes in white lights carrying different chirps (or varying pump pulse durations in case of constant chirp), all transient datasets throughout the following chapters are fitted line-by-line using Fcos (Eq. 2.26). In the following the fit routine will be tested section on simulated and experimentally obtained data.

Table 2.1: Parameters for the artifacts shown in Fig. 2.18 from a fit using FKov. The time origin Δt_0 is compared to the value obtained via the parameterization Fcos.

Trace	τ_1 (fs)	τ_2 (fs)	β (10^{-3}fs^{-2})	Δt_0(FKov) (fs)	Δt_0(Fcos) (fs)	Diff.(fs)
2.18a	48	524	7.0	349.0	348.2	0.8
2.18b	78	1368	1.4	-1237.4	-1236.3	1.1
2.18c	69	1358	1.1	-484.2	-483.9	0.3

2.5 The Fit Routine and its Performance

For fits of complete TA datasets Mathcad Prime 3.1 was used. After postprocessing according to [Meg09] without chirp correction, the transient absorption datasets $S(\lambda, \Delta t)$ are fitted time trace by time trace for each wavelength. First each time trace is truncated such that the signal occupies ca. 1/3 of the remaining trace to speed up the calculation. A Levenberg-Marquardt algorithm is then employed to fit the truncated time traces using Fcos (Eq. 2.26) with fit parameters $A_0, A_1, \tau, \Delta t_0, B$ and Φ. To ensure stability, A_1 and B are reset to their respective starting values before fitting each trace, while for all other parameters the result of the previous trace is used as a new starting value. Figure 2.19 shows a small section of a $S(\lambda, \Delta t)$ dataset and the corresponding fit. Finally, the spectral evolution of each fit parameter is plotted and checked for unphysical discontinuities. As discussed above, the fitted time origin $\Delta t_0(\lambda)$ directly represents the white light's group delay (cf. Eq. 2.14).

For each trace the quality of the fit can be quantified via the residual's RMS deviation. Q1, the RMS inside the interval where the signal was fitted, can be compared to the noise RMS outside the fitted window Q2.

$$Q1 = \frac{\mathrm{RMS}(\mathrm{signal} - \mathrm{fit})}{\mathrm{RMS}(\mathrm{signal})} \tag{2.27}$$

$$Q2 = \frac{\mathrm{RMS}(\mathrm{noise})}{\mathrm{RMS}(\mathrm{signal})} \tag{2.28}$$

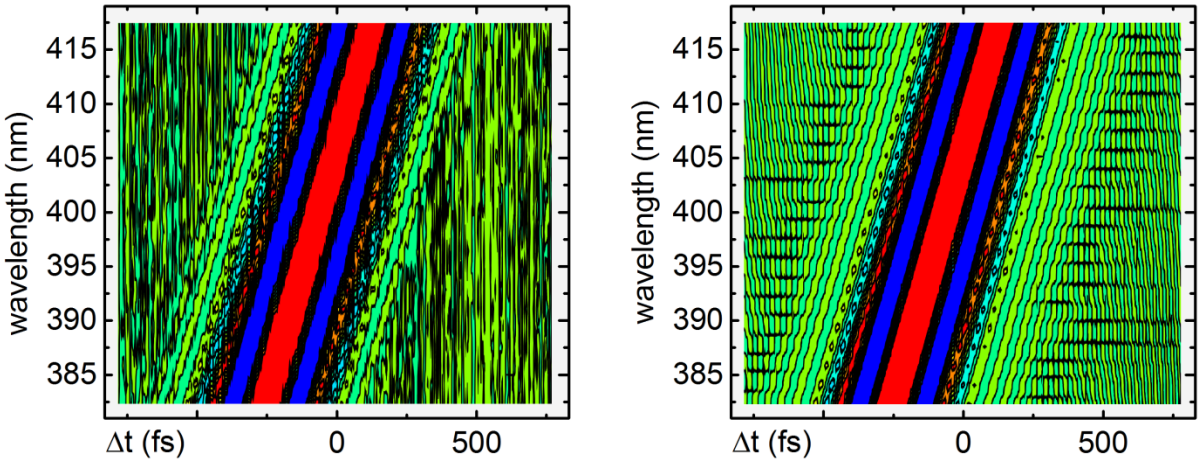

Fig. 2.19: Fit in Mathcad Prime 3.1: section of a dataset $S(\lambda, \Delta t)$ (left) and corresponding fit (right) in false color representation. Red indicates positive, blue negative signal. Data fitted time trace by time trace using the fit function Fcos (Eq. 2.26).

For experimentally obtained data, typically Q1 ~ 0.1 inside and Q2 ~ 0.01 outside the fitted window. These values signify that about 10 % of the integrated signal amplitude remain after the fit, while the signal to noise ratio is on the order of 100. Increased fluctuations on the time trace inside the fitted window likely originate from fluctuations in pump energy level and pump-probe overlap. Most importantly, systematic fluctuations in the residual are minimized.

2.5.1 Performance on Simulated Data

Different approaches come to mind when considering how to best find the true $\Delta t_0(\lambda)$ for increasingly asymmetric artifacts. As the GD can be defined without any uncertainty, CA simulations discussed in Section 2.3 represent a valuable tool to determine how well different fit functions are suited for fitting of the XPM induced CA. Test datasets are produced using the flat top spectrum shown in Fig. 2.5 centered at 530 nm with a width of 180 nm FWHM, a moderate chirp $\beta = 10^{-2}\, 1/\mathrm{fs}^2$ and a 25 fs pump pulse. The fit functions considered here are Fcos (Eq. 2.26), FGauß (Eq. 2.16) and a single Gaussian. Additionally, the position of the signal maximum and the signal's center of mass COM are determined numerically. The COM is computed via

$$\mathrm{COM}(\lambda) = \frac{\sum_{\Delta t} \left| S(\lambda, \Delta t) \right| \cdot \Delta t}{\sum_{\Delta t} \left| S(\lambda, \Delta t) \right|} \tag{2.29}$$

Figure 2.20a illustrates the true GD and fitted $\Delta t_0(\lambda)$ for the moderately chirped case. The fitted $\Delta t_0(\lambda)$ matches the true simulated GD well except for the red edge of the spectrum.

Figures 2.20b and 2.20c show the deviation from the true GD using different fit functions for moderate an high chirp. Except for the COM (green) and the position of the curve maximum (gray), all fit functions reproduce the true GD perfectly as long as the spectrum is flat. It is worth noting that with exception of $\Delta t_0(\lambda)$ all fit parameters are constant in this range. The COM and signal maximum position are limited by the sampling of the time trace and therefore oscillate as the signal moves across the delay time axis. Deviations are slightly worse at the red edge of the spectrum, since in the frequency domain the drop of the spectral intensity is significantly steeper in the red, leading to more pronounced asymmetries and distortions in the signal (cf. Fig 2.6). In the moderately chirped case (Fig. 2.20b) FGauss slightly outperforms Fcos in terms of the accuracy of the fitted $\Delta t_0(\lambda)$ at the edges of the spectrum. However, as was already shown in Fig. 2.17, Fcos reproduces the signal better.

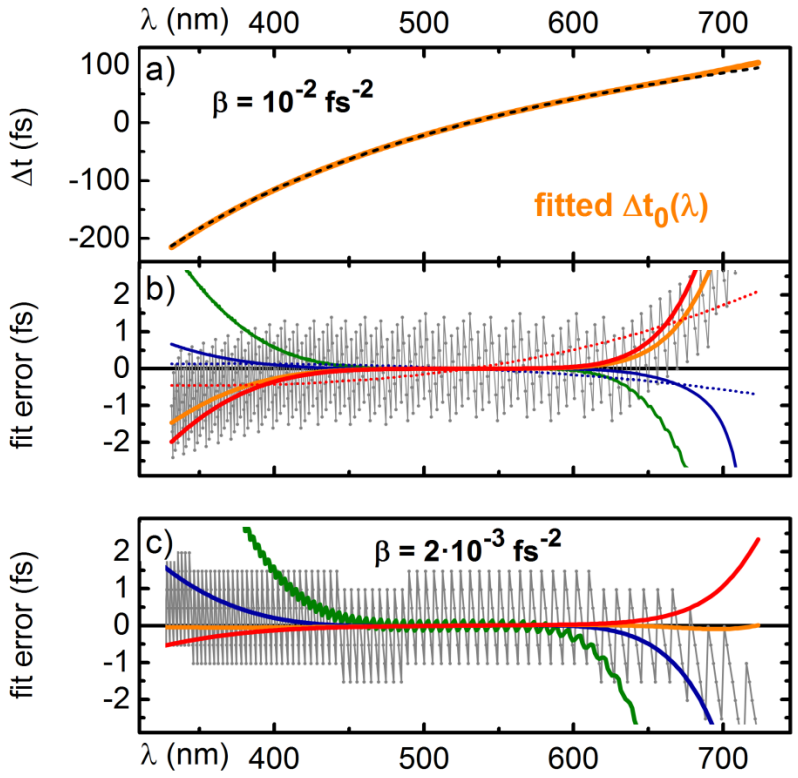

Fig. 2.20: Fit to simulated data. (a) GD (black) and fitted $\Delta t_0(\lambda)$ (orange) using Fcos. (b) deviation from true GD for moderate chirp for a flattop probe spectrum. Green: Center of mass COM. Orange: single Gaussian. Red: Fcos. Blue: FGauß. Dotted lines in (b) indicate the deviation in case of a Gaussian probe spectrum. (c) Same as (b) for high chirp.

Dotted lines in Fig 2.20b indicate the situation when the flattop is exchanged for a Gaussian probe. In this case, the error is zero only at the probe central wavelength, where the signal is perfectly symmetric.

In the strongly chirped case (Fig. 2.20c), Fcos is more accurate than FGauss. Surprisingly, the fit using a single Gaussian turns out to be the most robust against artifact asymmetries, but it is obviously inadequate when the artifact is to be subtracted due to the significant residual (cf. Fig. 2.17).

The conclusion here is that errors depend directly on the modulations of the probe spectrum. The first derivative of the Gaussian allows fitting to a certain accuracy, but strong asymmetries will lead to deviations no matter which fit function is used. Experimental white light spectra do exhibit modulations, so the error arising from these needs to be quantified. This will be addressed in the next section.

2.5.2 Performance on Experimental Data

In order to quantify the deviation of the fitted $\Delta t_0(\lambda)$ w.r.t the true time origin due to spectral modulations of the probe, simulated signals using an experimentally obtained probe spectrum and GD can be used as demonstrated in Section 2.3.4.

For moderate chirp, the error in the fitted $\Delta t_0(\lambda)$ is less than ±1 fs throughout most of the pedestal section of the probe spectrum both for Fcos (blue) and FGauß (red) (cf. Fig. 2.21a). The COM (green) also reproduces the time origin reasonably well, but is more sensitive to signal asymmetries due to modulations in the probe spectrum. Sample signals and fits are shown in the right panels.

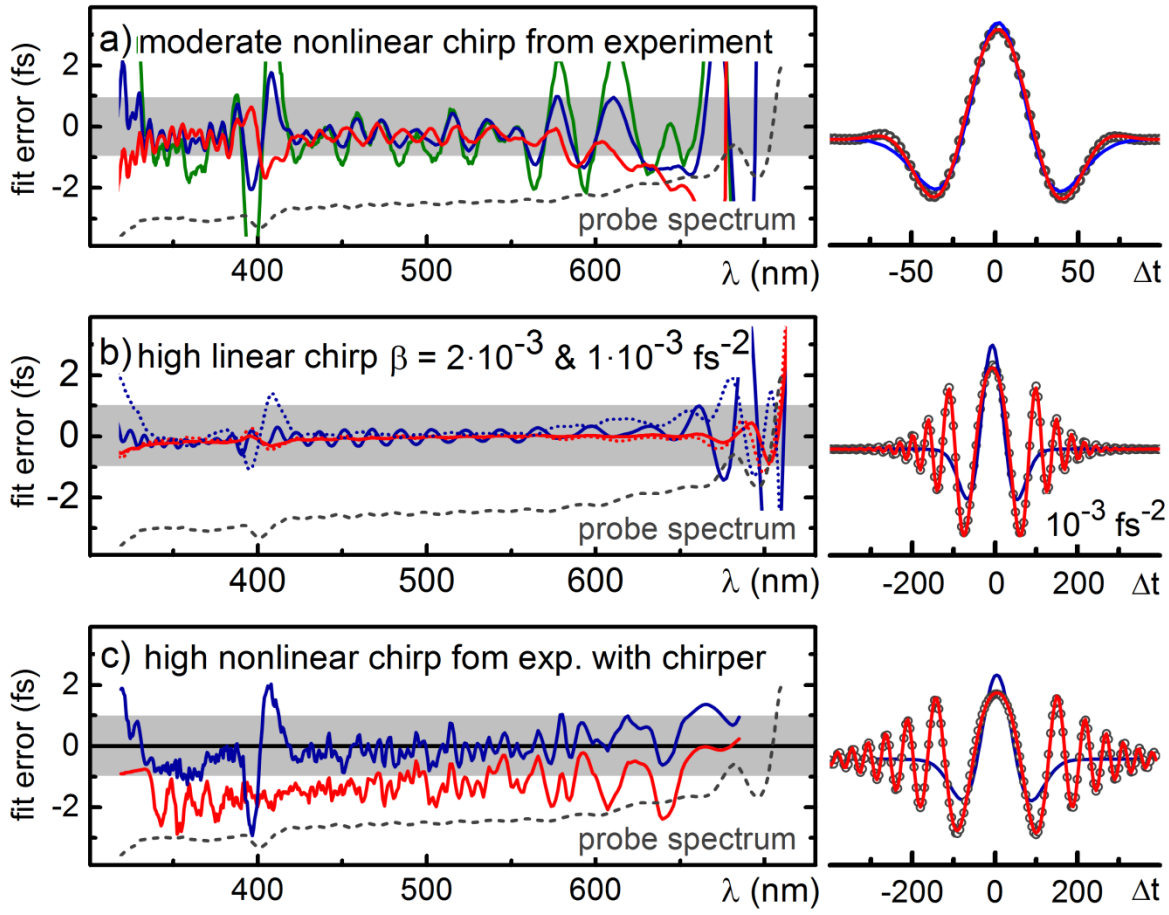

Fig. 2.21: Deviation of fits w.r.t. true $\Delta t_0(\lambda)$ for experimentally obtained probe spectra. (a) Moderate nonlinear chirp. Gray dash: probe spectrum. Green: COM. Red: Fcos. Blue: FGauß. (b) High linear chirps. Dotted lines refer to highest chirp.(c) High nonlinear chirp. Right: example signals & fits using Fcos (red) and FGauß (blue).

Figure 2.21b illustrates deviations as the chirp is increased. For $\beta = 2 \cdot 10^{-3}\,1/\mathrm{fs}^2$ (dotted lines) and $\beta = 1 \cdot 10^{-3}\,1/\mathrm{fs}^2$ (solid lines), the accuracy is even better than in the moderately chirped case. This graph also nicely illustrates how the modulations of the spectrum translate into the fitted $\Delta t_0(\lambda)$ when using FGauß (blue). As Fcos (red) models the oscillating signal well, it is less susceptible to this error.

There are limits to the fitted accuracy in the case of large nonlinear chirp, e.g. when the white light is chirped using a 14.5 mm BK7 glass block. In Fig. 2.21c, while the signal shape is still reproduced very accurately by Fcos, the fitted $\Delta t_0(\lambda)$ experiences a shift from the true value by about 1 fs (red).

A likely reason for this shift is the nonlinearity of the chirp. In the highly chirped case, artifact fringes contribute significantly over a wide spectral range. The signal in the delay time domain will then consist of data points stemming from spectra recorded over a wide range of Δt, i.e. with significantly different chirp values. This inevitably distorts the signal in the delay time domain. For the determination of the time origin, it is in this case more accurate to not take into account the entire signal. The deviation from the true value becomes more significant toward the blue, where the chirp is highest.

The accuracy of the fitted Δt_0 can also be estimated without the use of simulated data. In this case the real $\Delta t_0(\lambda)$ encoded in the data is unknown, but it is expected to be a reasonably smooth function without any high frequency fluctuations. Therefore, when a polynomial of high enough order is fitted to and subtracted from the experimentally obtained $\Delta t_0(\lambda)$ curve, ideally the residual should vanish.

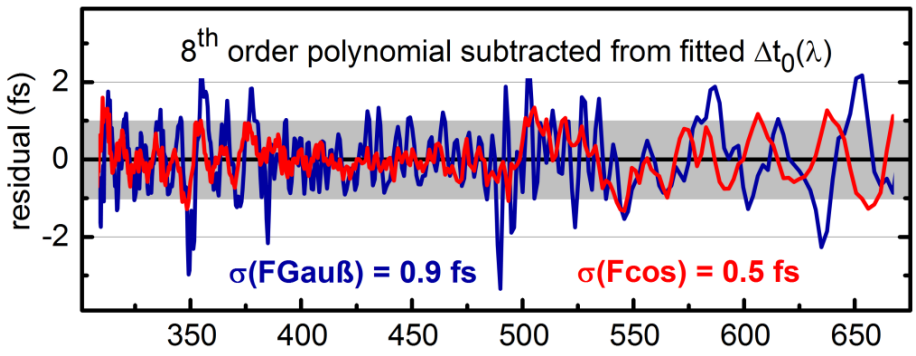

Fig. 2.22: Residual of a $\Delta t_0(\lambda)$ curve fitted to experimental data after subtraction of an 8th order polynomial. Blue: $\Delta t_0(\lambda)$ determined using FGauß. Standard deviation: 0.9 fs. Red: $\Delta t_0(\lambda)$ determined using Fcos. Standard deviation: 0.5 fs.

Figure 2.22 shows the residual from a subtraction of an 8th order polynomial from a $\Delta t_0(\lambda)$ curve fitted to a dataset obtained in 183 µm B270 glass at λ_{pump}=500 nm. Two kinds of high frequency fluctuations remain: The EKSMA "HR795-835 HT300-700" filter used to block the fundamental after white light generation not only modulates the spectrum, but also introduces some measurable group delay modulations. This slightly modulates the $\Delta t_0(\lambda)$, especially above ~600 nm. The group delay introduced by added dispersive optical elements will be the focus of the following chapter. Note that the group delay introduced by this filter will not contribute to the final results presented there, as it contributes to both reference and sample measurements.

The remaining high frequency fluctuations are caused by combination of artifact asymmetry and experimental noise. Their magnitude is comparable to the error seen in simulated time traces, but their frequency is much higher than that of the modulations in the probe spectrum. Using the new model Fcos, the precision of the fitted $\Delta t_0(\lambda)$ in this experimental time trace was increased from ± 0.9 fs to ± 0.5 fs compared to the combined Gaussian & derivative model (Eq. 2.16). This considerably increases the overall measurement accuracy for $\Delta t_0(\omega)$ from several fs to ~ 1 fs.

Fcos may not yield the highest accuracy in the fitted $\Delta t_0(\lambda)$ in all circumstances, but it does feature acceptable accuracy and at the same reproduces the varying signal shapes impressively well over a wide range of parameters. The final section will illustrate this advantage.

2.5.3 Subtracting the Fitted Artifact

While inclusion of the CA in the model used for data analysis is usually preferable, sometimes it can be instructive to subtract the CA contribution to the time traces, thereby revealing hidden spectral features. This becomes more relevant when artifacts occupy large time intervals. Current models either use FGauß, or separate the fast fluctuation via singular value decomposition [Sla15, Wil11]. The latter proves especially tricky when the sample exhibits fast dynamics on the timescale of the CA modulation. In fact, signals subtracted non perfectly in reference [Wil11] closely resemble simulated XPM signatures.

It has become quite clear throughout the previous chapters that Fcos yields a much better fit than FGauß whenever artifact fringes contribute significantly to the signal. For this reason, a quantitative inspection will be limited to the moderately chirped case (cf. Fig. 2.21a), where the improvement is least obvious.

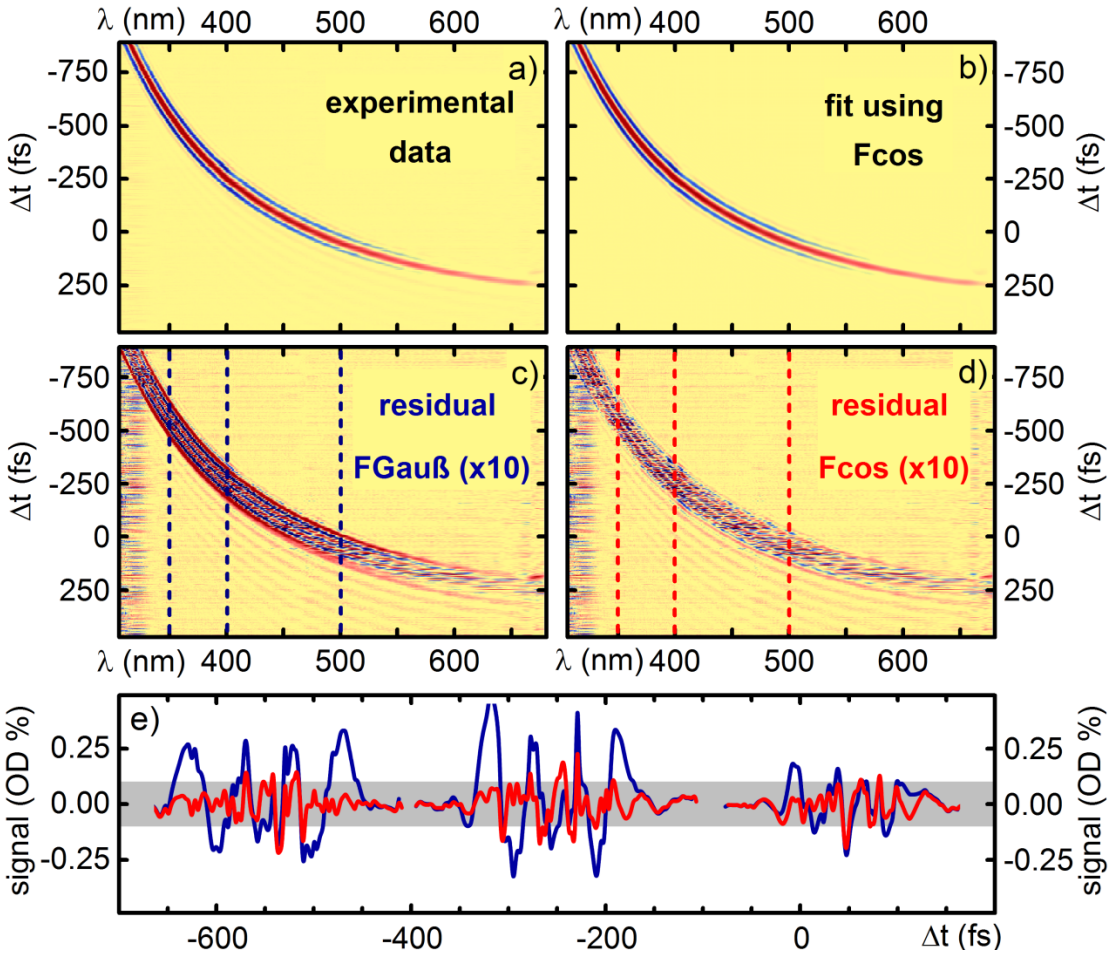

Fig. 2.23: Subtraction of the coherent artifact. (a) False color representation of experimental data in 183 µm B270 glass (λ_{pump}=500 nm). (b) fit using Fcos. (c,d) Residuals from Fit using FGauß and Fcos, multiplied by a factor of 10. (e) Residuals at selected spectral positions indicated by cursors for FGauß (blue) and Fcos (red). Gray area marks one standard deviation for the residuals obtained from Fcos-fit.

Figure 2.23 juxtaposes an experimentally obtained dataset to the fit using Fcos. Figures 2.23b and 2.23c show the fit residuals obtained when using FGauß and Fcos, enlarged by a factor of ten. When using FGauß, the amplitude of the residual is clearly wavelength dependent. This is due to the nonlinear chirp of the white light. In the blue the chirp is highest, causing the fringes not taken into account by the fit function to be more pronounced. A large wavelength dependent residual is unfavorable because after chirp correction it can be mistaken for a real transient contribution from the sample. Figure 2.23e directly compares the residual amplitudes at selected detection wavelengths. Even in the moderately chirped case, Fcos reduces the residual amplitude significantly. The residual is independent of the detection wavelength within measurement accuracy. A somewhat increased noise level within the

modulated interval is to be expected due to fluctuations in pump energy level and pump-probe overlap. Close inspection reveals a small oscillating contribution with a period of approximately 30 fs. Its amplitude is approximately 0.04 mOD, just above the noise limit of our referenced setup, which is about 0.02 mOD. This feature is likely due to impulsive stimulated Raman scattering in the sample [Sil85, Meg09].

Finally, as an example of a transient dataset with molecular contributions, the Pyrene data shown in Fig. 2.1 processed using Fcos (Eq. 2.26). Figure 2.24 shows the dataset after artifact subtraction and chirp correction. Subtraction of the coherent artifact reveals a ground state bleach signature just above 350 nm that was completely obscured by the CA (red arrow).

The data was fitted time trace by time trace using

$$f_i(\Delta t, \tau_i) = \mathrm{IRF}(t) \otimes \left\{ \Theta(t) * \left(\sum_i A_i \exp\left[-\Delta t / \tau_i \right] + \mathrm{const} \right) \right\} + \mathrm{CA}\,. \qquad (2.30)$$

Details on why a sum of exponential functions is a valid model will be provided in Chapter 4.

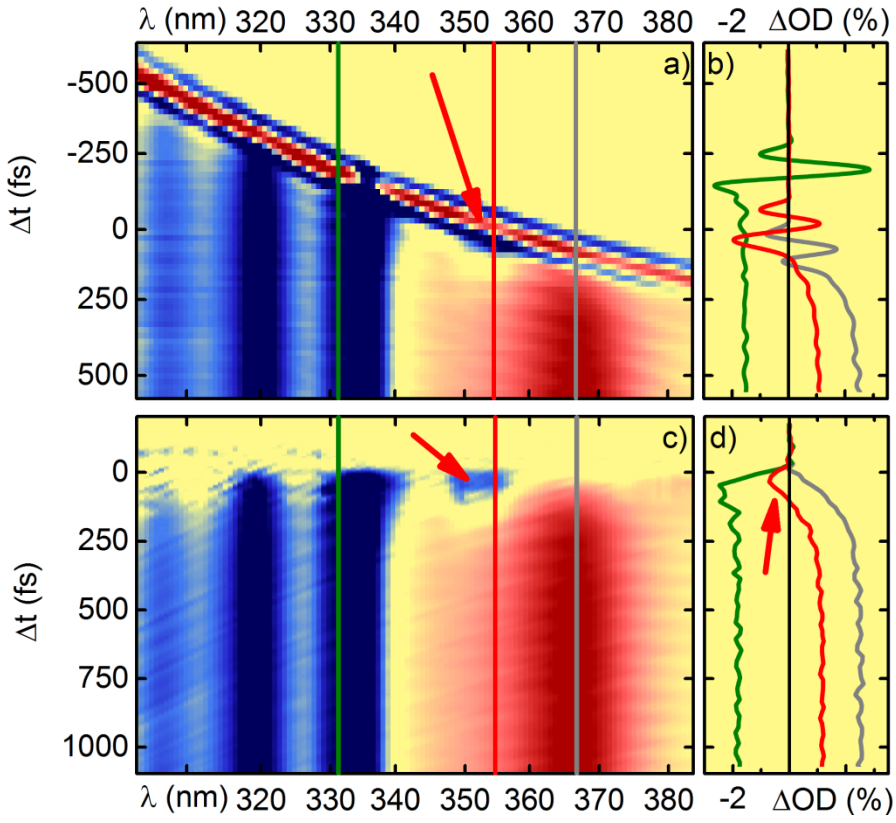

Fig. 2.24: Example dataset shown in Fig. 2.1 with corrected white light chirp and subtracted coherent artifact. (a,c) TA signal in false color representation, red (blue) indicates positive (negative) contributions. (b,d) Time traces at selected wavelengths.

The IRF is a Gaussian with the cross correlation width $FWHM_{CC}(\lambda)$. $FWHM_{CC}(\lambda)$ represents the wavelength dependent width of the cross correlation between the pump pulse and the portion of the probe observed on a given CCD pixel. The spectral resolution of the pump probe setup is ~ 3 THz in the VIS. Therefore, assuming a Fourier-limited Gaussian, every pixel detects a bandwidth equivalent to a ~150 fs pulse [Meg09]. Typically, fitted $FWHM_{CC}(\lambda)$ range between 40 fs and 80 fs. The fitted values are often used as a measure of the time resolution achieved in the experiment [Ras01, Meg09, Hom11]. In the moderately chirped case, the width of the artifact's envelope and the cross correlation width are very similar [Kov99]. Hence, when using the Gaussian & derivative model to fit the CA, the width of the Gaussians is commonly set to $FWHM_{CC}(\lambda)$. In analogy, the parameter $\tau(\lambda)$ in Fcos was set to equal $FWHM_{CC}(\lambda)$ in this example.

However, it should be noted that when artifact fringes become significant, the artifact envelope broadens significantly (cf. Fig. 2.8). According to the simulations, this will occur either when the probe chirp is increased or when a shorter pump pulse is used. While it would make sense for the cross correlation to broaden for a chirped probe pulse, a shorter pump pulse does not warrant a longer cross correlation. The best way to quantify the time resolution and its connection to the probe chirp and $FWHM_{CC}(\lambda)$ is not straightforward and still somewhat debated [Pol10]. From a purely Gaussian artifact the rime resolution can be obtained via $FWHM_{CC}(\lambda)$ [Pom98], but the simulations presented here suggest that the fitted width of the artifact is no longer an accurate measure when spectral interference contributes significantly.

2.6 Summary: Varying Artifact Shapes Require a New Parameterization

This chapter illustrated the importance of cross phase modulation in the modeling of the coherent artifact in the VIS/NIR. Depending on the probe chirp, artifacts can exhibit interference fringes, obscuring molecular dynamics over up to several hundreds of fs. Simulations suggest an optimum pump pulse duration for a given probe chirp, yielding an artifact with minimum width. For the parameters typical of the setup used herein this optimum is at ca. 27 fs, a pump pulse duration readily achieved with a NOPA and prism compressor.

The artifact asymmetry correlates with modulations in the probe spectrum. Analytical models for the cross phase modulation induced coherent artifact assuming idealized pump and probe pulses are therefore ill-suited as fit functions for experimentally obtained artifact signals. The novel parameterization presented in this chapter removes this constraint. It yields comparable or better accuracy in the determination of the time origin as the commonly used Gaussian & derivative model, while reproducing the signals much more accurately.

The new parameterization will likely improve future data analysis, especially due to its very accurate reproduction of the varying artifact shapes for a range of experimental parameters. In the following chapter, this new flexibility will be exploited for accurate analysis of probe pulses with strongly modulated group delay. The photophysics of pyrene will be investigated further in chapter 4.

3 Characterizing Broadband Dielectric Mirrors from UV to NIR Using the Coherent Artifact

In this chapter a novel method to characterize broadband dielectric mirrors in a transient absorption (TA) pump probe experiment is presented. Accurate fitting of coherent artifacts using the novel parameterization introduced in the previous chapter facilitates precise determination of the time origin $\Delta t_0(\lambda)$ for each spectral component of variably chirped probe pulses. This enables a direct measurement of the coating induced group delay (GD) using a source that is sensitive to pulse deformation and splitting. With recent advances in broadband coating technology, this will become increasingly interesting as GD data is often kept a secret by vendors for fear of plagiarism.

In the following, the GD characteristics of selected dielectric coatings are extracted from TA measurements on solid substrates. Examples from the ultraviolet to the near infrared spectral range will be presented to highlight advantages and as well as limits of this novel method.

3.1 Dielectric Mirrors Introduce Group Delay

Dielectric mirrors are composed of thin layers of dielectric materials. Their reflectivity is due to constructive interference of waves reflected by individual layers: High refractive index layers are interleaved with low index material such that the optical path length difference upon reflection matches the wavelength of the incident light. This condition can only be fulfilled for a limited wavelength range with a single stack. Broadband mirrors are usually realized by combining stacks for different wavelengths. To realize ultra broadband reflectors, more than 100 layer pairs are combined. Typically the outer layers of the coating are designed thinner than the ones closest to the substrate. This way the bluest components most prone to material dispersion do not penetrate deep into the coating. As a consequence, the red part of the spectrum is delayed with respect to the blue part.

The reflected field $\tilde{E}_{out}(\omega)$ is related to the incident field $\tilde{E}_{in}(\omega)$ via [Die96]:

$$\tilde{E}_{out}(\omega) = R(\omega) \cdot \exp\left[-i \cdot \Phi_S(\omega)\right] \cdot \tilde{E}_{in}(\omega) \tag{3.1}$$

Upon reflection spectral components of the incident light will not only experience an amplitude modulation according to the mirror's reflectivity $\left|R(\omega)\right|^2$ but also acquire different spectral phases $\Phi_S(\omega)$.

In the time domain, this translates to

$$\tilde{E}_{out}(t) = \frac{1}{2\pi}\int_{-\infty}^{+\infty} R(\omega)\cdot\tilde{E}_{in}(\omega)\cdot\exp\left[\,i(\omega t - \Phi_S(\omega))\,\right]d\omega \tag{3.2}$$

Taylor expanding the phase around a carrier frequency ω_c leads to

$$\begin{aligned}\tilde{E}_{out}(t) = \frac{1}{2\pi}\exp\left[\,i\left(\omega_c t - \Phi_{s0}(\omega_c)\right)\right]\cdot\int_{-\infty}^{+\infty} R(\omega)\cdot\tilde{E}_{in}(\omega) \\ \cdot\exp\left[-i\left(\omega-\omega_c\right)\cdot\left(t - \Phi_{s1}(\omega_c) - \tfrac{1}{2}\Phi_{s2}(\omega_c)(\omega-\omega_c) + \ldots\right)\right]d\omega\end{aligned} \tag{3.3}$$

where $\Phi_{s1}(\omega)$ and $\Phi_{s2}(\omega)$ represent the first and second derivatives of the spectral phase $\Phi_S(\omega)$ with respect to ω. While $\Phi_{s0}(\omega)$ will merely result in a shift of the carrier envelope phase without affecting the pulse shape and delay, $\Phi_{s1}(\omega)$ is a frequency dependent shift of the temporal pulse envelope, the group delay (GD), measured in fs. The second derivative represents the group delay dispersion (GDD), measured in fs^2. It is common amongst coating designers to only report GDD curves, since the GD is a relative quantity indicating the delay of a given spectral component with respect to another. The GD is however the more illustrative quantity - especially with respect to application in pump probe spectroscopy, where relative delays of spectral components in the chirped probe pulse have to be taken into account when evaluating the data. Coating induced phase modulations can cause significant pulse broadening, reshaping and even pulse splitting when the pulse length is comparable to the coating thickness [Die85, Wei85]. In addition the reflection from the outermost layer interferes with light reflected further within the coating and dispersion oscillations are observed. Hence, for use with ultrashort pulses the phase response has to be controlled as well as the reflectivity. Appropriate materials must be found and stack sequences carefully modeled in order to serve the respective application. Various concepts have been devised to overcome this problem and since the 1990s mirrors with controlled GD have become commercially available [Sci94, Mat99, Kaer01, Bau06, Hab16a, Raz17]. Applications include low GD broadband high reflectors and chirped mirrors for dispersion control in fs laser systems [Sci97, Kär01, Bau06].

Due to inherent and unavoidable uncertainties in the coating process, it is imperative to experimentally verify a given mirrors GD (or GDD) characteristics before use in a sensitive experiment [Tru13].

3.2 The Standard Technique: White Light Interferometry

Traditionally the response function of a mirror coating is measured using white light interferometry (WLI). Here a halogen lamp is used as a light source in a Michelson interferometer. After a reference measurement one or several mirrors are replaced by the dielectric mirrors under investigation. This method yields amplitude modulation and GDD via the Fourier transformation of spectrally resolved interference patterns [Die96, Gos05]. In addition the GD can be measured by careful evaluation of the shift of the interference pattern's maximum for each wavelength [Kno88, Nag90, Amo09, Hab16, Sch16]. GD accuracies reach from few fs [Kan15] down to ~0.1 fs [Kov95, Did96] in the VIS/NIR. Toward the ultraviolet spectral region measurements become more challenging due to a higher required scan interval for the interferometer [Nag90] and the limited availability of high quality optics such as UV beam splitters. A rare example for a WLI measurement in the UV is Razskazovskaya et al. [Raz16].

An alternative approach called Resonance Scanning Interferometry (RSI) has also been proposed by Trubetskov et al [Tru13]. Promising results are shown in the NIR, but towards the UV the measurement accuracy decreases just like in WLI.

Interferometric techniques enable coating characterization to high accuracy without the need of expensive pulsed light sources. The technique presented here is not meant to replace these established tools, but to enable groups with access to state of the art pump probe setups to evaluate the optics at their disposal using the very pulses that are being used in their pump probe experiments.

The pump probe method yields ±1 fs accuracy in the determination of the GD over a wide spectral range down to the UV and has the added capability of being sensitive to pulse deformation and splitting. Thereby it provides a simple test to determine the applicability of a mirror at hand for measurements on a given timescale. Measurements described in this work will concentrate on the UV/VIS spectral region, but it should be noted that this technique is in principle also applicable in the NIR, using white lights generated according to Riedle et al. [Rie13, Bra14a].

3.3 From Pump Probe Setup to Group Delay-Meter

Making use of the coherent artifact and the model described in Chapter 2, the transient absorption setup presented in [Meg09] and [Bra14] can easily be transformed into a group delay measurement device. All that is needed are four additional reflections in the probe beam path. A removable stage was developed that facilitates four added reflections under 45° without changing the downstream beam path (cf. Fig.3.1). Rear loaded mirror mounts are used to ascertain reflection in the same plane irrespective of the thickness of the mirror's substrate. Substrates are held in place by spring steel clips applying pressure from the back. This removes alignment uncertainties arising from screwing onto their often imperfect side surfaces.

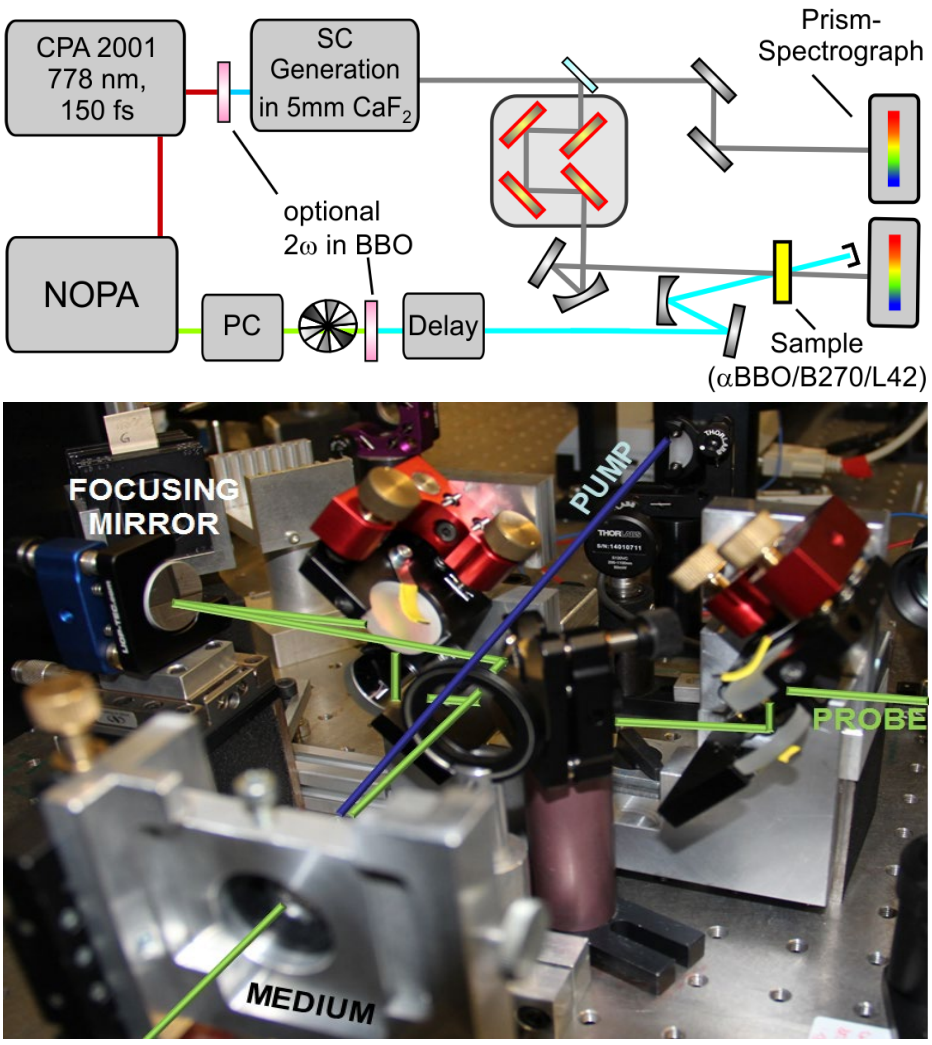

Fig. 3.1: Top: Transient absorption setup for mirror characterization measurements. PC: Prism Compressor. Bottom: Image of the removable reflection stage.

After traversing the reflection stage, the white light probe is focused and overlapped with a ~25 fs pump pulse featuring a peak intensity of 330 GW/cm^2 in a thin solid medium, where nonlinear effects lead to the delay time dependent signal called coherent artifact (cf. Chapter 2). For the experiments presented in this chapter, solid plane parallel HOYA L42 and Schott B270 glass substrates are used at the sample position. Substrates are approximately 200 µm thin and oriented perpendicular to the probe's propagation direction. A typical transient dataset $S(\lambda, \Delta t)$ is shown in Fig. 3.2a. Due to its generation in bulk CaF_2, the probe white light is chirped. This is why the pump pulse interacts with different spectral components of the probe at different delay times Δt. At negative delay the positively chirped probe precedes the pump. As the pump probe delay is scanned towards positive Δt the artifact moves from the blue to the red part of the recorded spectrum. The artifact shape changes with detection wavelength (right panel in Fig. 3.2a). Toward the visible spectral range cross phase modulation (XPM) replaces two photon absorption (TPA) as the dominating effect, causing the artifact's shape to deviate from a Gaussian. Changing shapes must be reproduced by the model in order to obtain a reliable fit for the time origin $\Delta t_0(\lambda)$, where a certain spectral component λ of the probe temporally overlaps the pump pulse. The model presented in Chapter 2 facilitates determination of $\Delta t_0(\lambda)$ with an error of less than 1 fs from purely Gaussian artifacts to oscillating signal shapes observed in strongly chirped white light.

After a reference measurement using four metallic Qioptiq RAL UV mirrors which are assumed to add negligible delay to the white light (Fig. 3.2a), one or more mirrors can be exchanged for the dielectrics under investigation (Fig. 3.2b). In this example four Qioptiq UVBB HR 240-400 are used, which feature high reflectivity over the entire range displayed, but are not GD optimized for use with fs pulses. Slight changes in alignment manifest as a subtle change in the wavelength calibration for the CCD camera pixels. This is managed by recalibration and interpolation of the sample to the reference wavelength axis after separate fitting of $\Delta t_0(\lambda)$. The reference $\Delta t_0(\lambda)$ is subtracted from the interpolated sample $\Delta t_0(\lambda)$. Thereby all GD modulations inherent to the system vanish, leaving only the contribution to the delay induced by the mirror coating (Fig. 3.2c). The modulation in this example is quite large, for some wavelengths the artifact is not only shifted but appears distorted and even inverted (cf. red line in Fig. 3.2b and c). How to understand and deal with such strong modulations will be discussed later in this chapter. For fs mirrors with controlled GD characteristics, modulations are usually much smaller. In the following, raw data will always be shown with the reference $\Delta t_0(\lambda)$ subtracted for better visibility (cf. Fig. 3.2c).

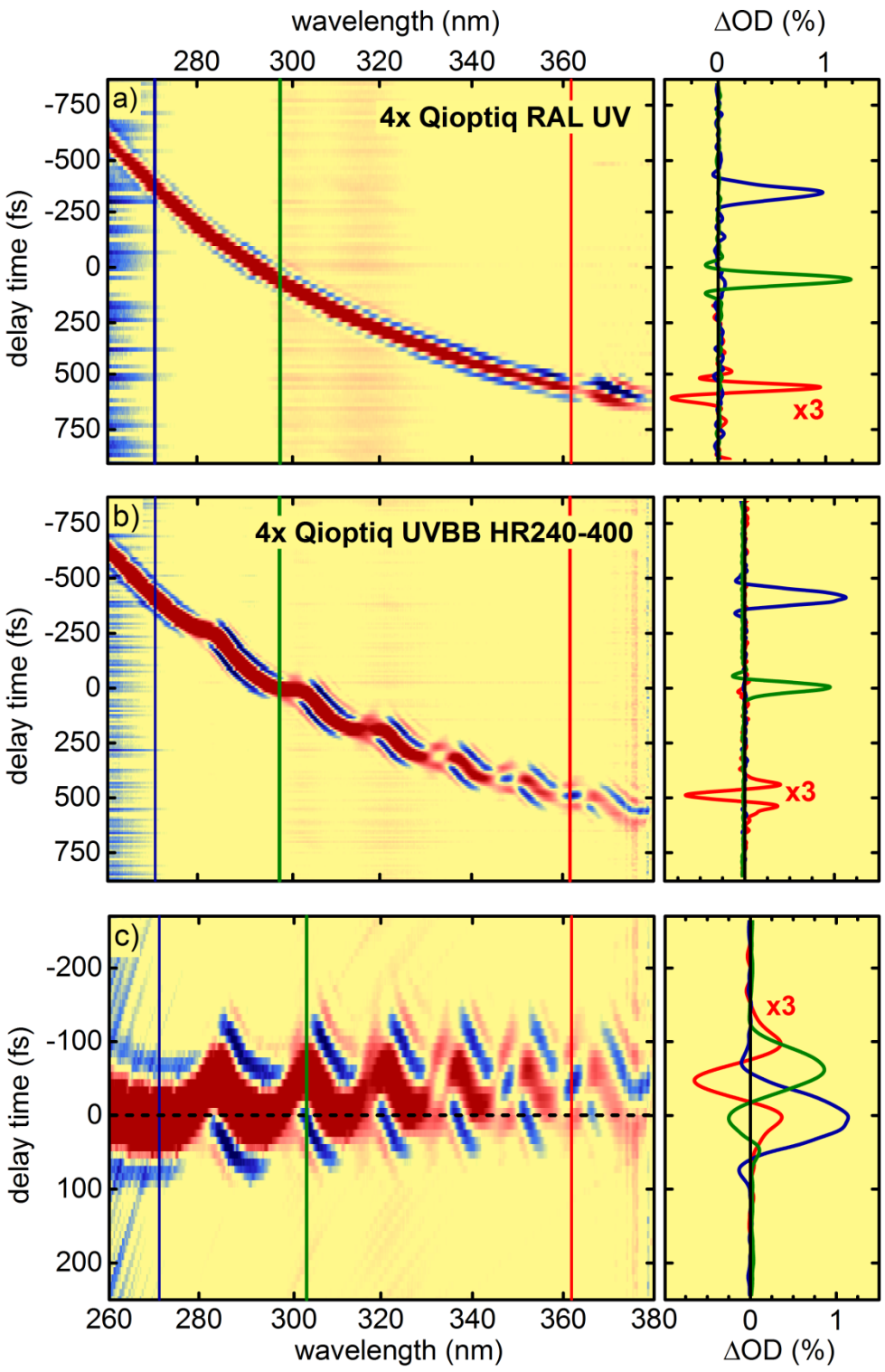

Fig. 3.2: Coherent artifact in 50 µm Sapphire using a pump pulse at 230 nm at 180 nJ and white light generated by the frequency doubled CPA at 389 nm in 5 mm CaF_2. Right panels: Lineouts taken at positions indicated by color coded vertical lines. (a) Reference measurement. (b) 4x Dielectric Qioptiq UVBB HR240-400 mirrors inserted. (c) Reference $\Delta t_0(\lambda)$ subtracted. Raw data provided by Elias Eckert.

3.4 Femtosecond Precision Despite Use of Much Longer Pulses

Several factors must be considered in order to determine the measurement accuracy. Uncertainties introduced by the fitting of $\Delta t_0(\lambda)$ were quantified in Chapter 2 to less than ±1 fs. Secondly, alignment uncertainties must be quantified. Fig. 3.3a shows the difference in $\Delta t_0(\lambda)$ after removal and reinsertion of all four metallic reference mirrors. The result is constant within 1 fs over the measured spectral range, the standard deviation is 0.70 fs. To remove the influence of noise at the relatively low 100 nJ pump energy used, the dataset was smoothed, resulting in a standard deviation of 0.57 fs. Since the GD is a relative quantity, the constant offset of 65 fs can be ignored. From this offset, one can infer a path difference of only 4.5 µm per mirror. Finally, overall alignment of the setup may change slightly on a daily basis due to temperature and humidity fluctuations. This can influence e.g. the pump pulse duration and the properties of the probe white light. The reproducibility of the measured GD is mostly below ±1 fs (cf. Fig. 3.3b), the standard deviation over the range displayed is 0.75 fs. Data in Fig. 3.3b was taken at 1000 nJ pump energy, resulting in an improved signal to noise at the expense of a small stray light contribution around 465 nm, probably due to an imperfect spot on the sample. The comparable standard deviations in Fig. 3.3a and b indicate that a tradeoff between signal to noise and manageable stray light must be found for the most accurate measurement. Averaging over many scans can introduce errors due to temperature fluctuations in the laboratory. It is therefore advisable to keep the measurement time below 30 min. The overall measurement accuracy of this method is estimated to be ±1 fs, which is comparable to common WLI setups.

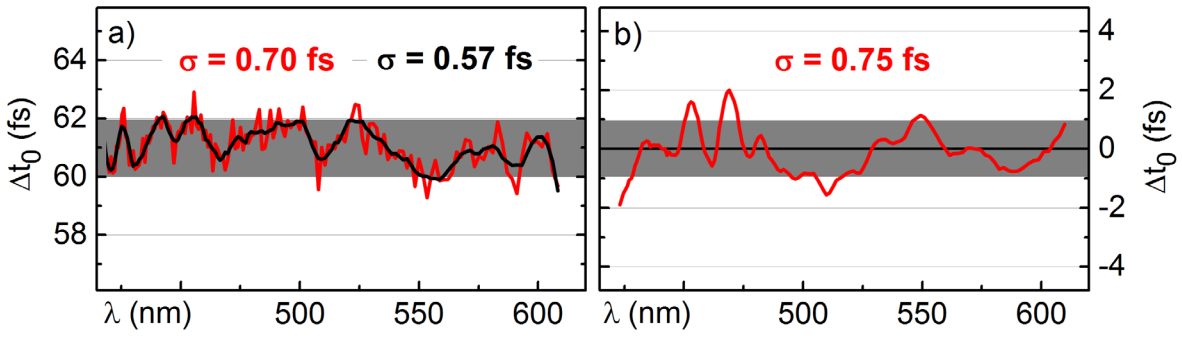

Fig 3.3: Measurements in 217 µm HOYA L42 glass at E_{pump} = 100 nJ. λ_{pump} = 465 nm. (a) $\Delta t_0(\lambda)$ after reinsertion of all four metallic mirrors. Black: Smoothed data. (b) Difference between resulting GD from measurements at E_{pump} = 1000 nJ on two consecutive days.

3.5 A Group Delay Optimized Broadband Mirror in the UV

A 2D-UV spectrometer under development requires mirrors supporting a bandwidth from 250 nm to 370 nm with controlled dispersion [Kre13]. This challenge was met by designing the "CMUV08" mirror coating, illustrated in Fig. 3.4a [Hab16b]. Figure 3.4b shows the coating put to the test in the pump-probe setup. Measurements using 385 nm and 775 nm pumped supercontinua were stitched together for this purpose [Rie13, Bra14a]. Measurements were performed using four CMUV08 to enhance precision. In contrast to the off-the-shelf solution presented in Fig. 3.2, between 250 nm and 370 nm the CMUV08 does not distort the pulse GD, but exhibits a controlled slope. Outside of the specified region one can observe large GD fluctuations as well as pulse distortions. The mirror features a reflectivity $R > 96$ % over the entire spectral range.

Figure 3.4c shows that the fitted GD (red) obtained using the pump probe technique is in approximate agreement with the coating design curve (black) and an interferometric measurement (blue). The pump probe measurement actually reproduces the calculated slope better than the corresponding WLI measurement, though the oscillating features appear somewhat smoothed. Results from measurements in 389 nm pumped and 778 nm pumped white light were stitched together to obtain the GD over the entire bandwidth. The coating exhibits moderate GD fluctuations of a few fs on top of a negative linear chirp. Negative chirp will help keep the pulse compressed in the sample plane of the 2D-UV experiment. Any residual linear chirp can be compensated using a prism compressor already incorporated in the setup. There are slight differences between WLI and pump probe data, but both measurements clearly indicate the CMUV08 is well suited for use in broadband UV applications.

Integrating the measured GD yields the spectral phase up to a constant. From the spectral phase the time domain pulse shape and phase after reflection on the mirror can be calculated for a Gaussian input pulse. Figure 3.4d shows a Fourier-limited 7.1 fs pulse (black dashes) at 325 nm central wavelength as well as its calculated pulse shape after six reflections on the CMUV08 (blue). This represents the number of reflections in the planned 2DUV setup [Kre13]. Since only the relative GD was measured, the information on the absolute time delay experienced is lost. The integration constant was chosen such that the reflected pulse experiences no significant delay w.r.t. the incident pulse. The FWHM pulse duration has increased to 16.1 fs. Simulating a prism compressor by fit and subtraction of the second order phase, this pulse can be recompressed to 9.4 fs.

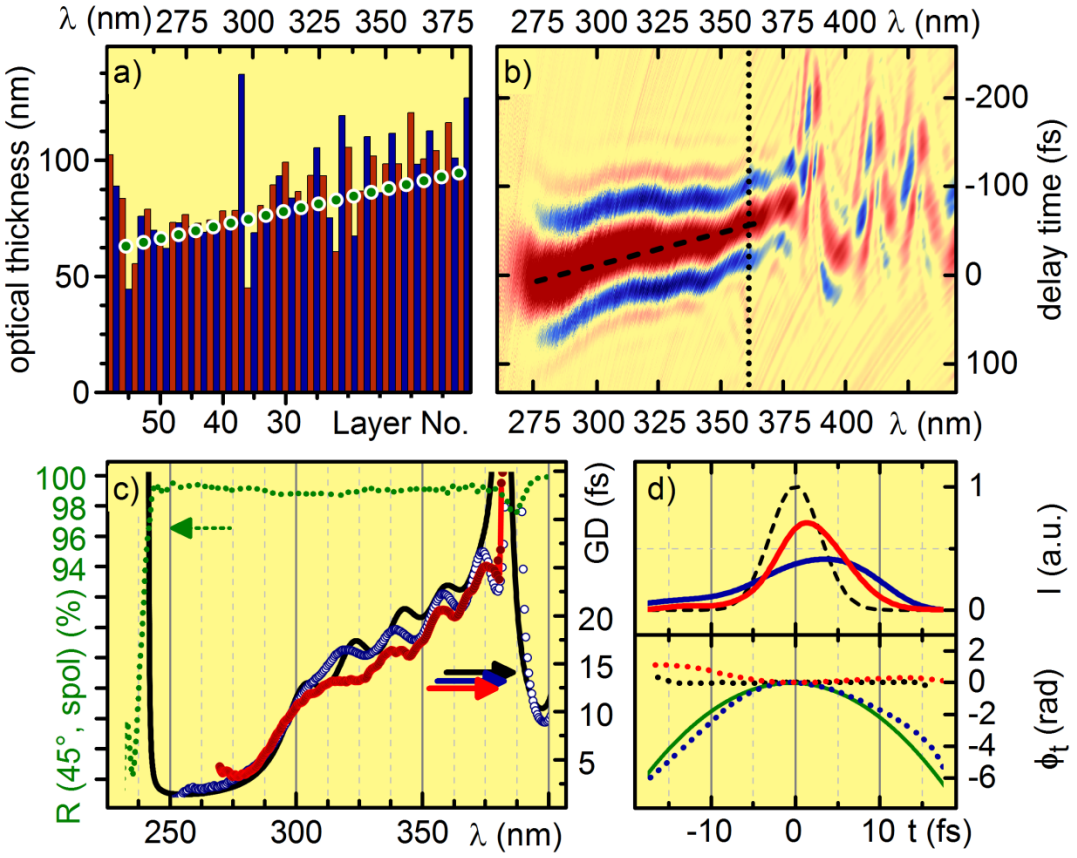

Fig. 3.4: (a) Coating design using SiO_2 (red) and HfO_2 (blue). Green dots indicate quarter wave thickness at wavelengths specified on top. (b) Pump probe GD measurement of four CMUV08 mirrors under 45° in s-pol using 385 nm and 778 nm pumped white light. Measurements stitched together at position indicated by dotted line. Excitation at 325 nm in 100 µm α-BBO using 100 nJ. (c) Fitted GD (red) of one CMUV08 compared to calculation (black) and interferometric data (blue). Green: coating reflectivity. Coating design and WLI data provided by F. Habel. (d) Calculated time domain pulse shape (top) and phase (bottom) of a Fourier-limited 7.1 fs pulse centered at 325 nm before (black) and after 6 reflections (blue) on a CMUV08 coating. Recompressed pulse (red) obtained by fit and subtraction of a parabola (green) to the phase of the reflected pulse. Amplitudes normalized to Fourier-limited amplitude.

3.6 Ultrabroadband Reflectors in the VIS/NIR

Recently, high reflectors covering the full visible and part of the UV and NIR spectral range have become commercially available. The Optics Balzers Diflex 1100 and 2000 coatings claim more than 99% reflectivity from 350 nm to 1100 nm and from 320 nm to 2000 nm, respectively. These coatings are not optimized for controlled GD, but nonetheless an interesting example to investigate.

Figure 3.5 shows reflectivity measurements taken in a Shimadzu UV-2600 spectrophotometer equipped with an Ulbricht sphere. Figure 3.5 indicates that the reflectivity of the Diflex 1100 (2000) decreases significantly below 325 nm (350 nm). A transmission scan shows the mirrors are not transparent in this region, therefore this is due to absorption in the coating material. Niobium- or zirconium oxide are examples of frequently used high index materials that absorb in this range [Fri03].

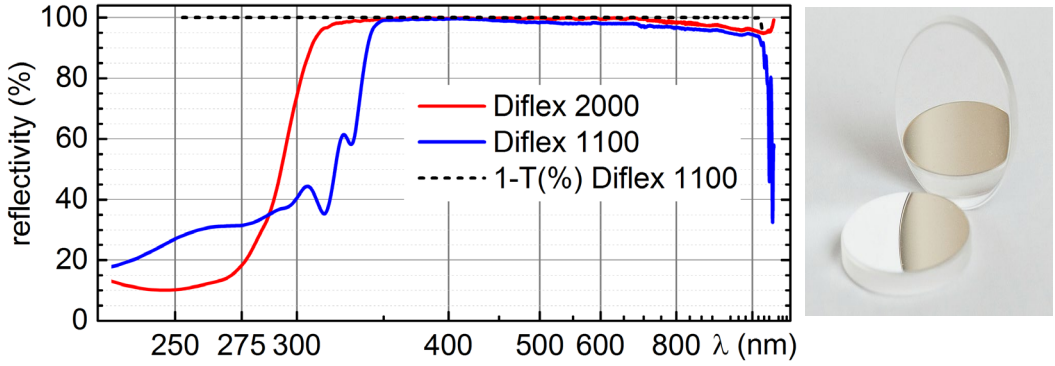

Fig. 3.5: Reflectivity and transmission of Diflex mirrors measured in a Shimadzu UV-2600 spectrophotometer with Ulbricht sphere. Below 325 nm the coating absorbs.

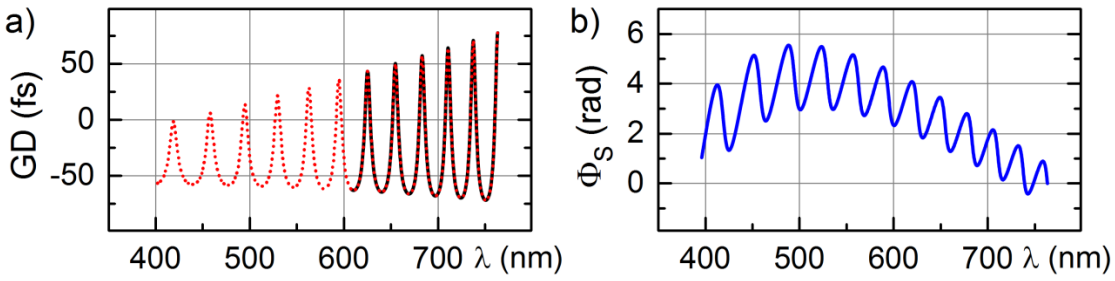

Fig. 3.6: (a) GD integrated (black line) and extrapolated (red dots) from calculation. (b) Spectral phase integrated from GD. Integration constant chosen such that delay of reflected pulse is zero w.r.t. the incident pulse.

3.6.1 Calculation of Time Domain Pulse Shapes

Optics Balzers generously provided a calculated GDD curve for the Diflex 1100 mirror, from which a theoretical GD could be obtained by integration. There is no information on the absolute time delay experienced by a pulse upon reflection. As before, the integration constant was chosen such that the reflected pulse experiences no additional delay with respect to the incident pulse. The GD shows large periodic poles of increasing amplitude. For the following simulations, the calculated data was extrapolated down to 400 nm (cf. Fig. 3.6a). From the calculated GD the spectral phase imprinted on an incident pulse can be obtained by integration (Fig. 3.6b).

In order to investigate the coating's effect on short pulses, time domain pulse shapes are calculated after one reflection on the Diflex 1100 using the spectral phase obtained. The central wavelength of the incident pulses was varied between 400 nm and 700 nm (Fig. 3.7a). Figures 3.7b and 3.7c show calculated pulse shapes before and after one reflection on a Diflex 1100 assuming Gaussian pulses with 10 nm FWHM. The GD modulations dramatically affect these short pulses. In the blue, pulses are broadened and oscillations in the GD induce a time shift. Increasing GD modulations above 450 nm already cause significant pulse splitting, reminiscent of the results presented in [Wei85]. Above 600 nm satellite pulses are formed (red), drifting apart for increasing central wavelengths. The next sections illustrate how such strongly modulated GDs can still be analyzed by this pump probe technique.

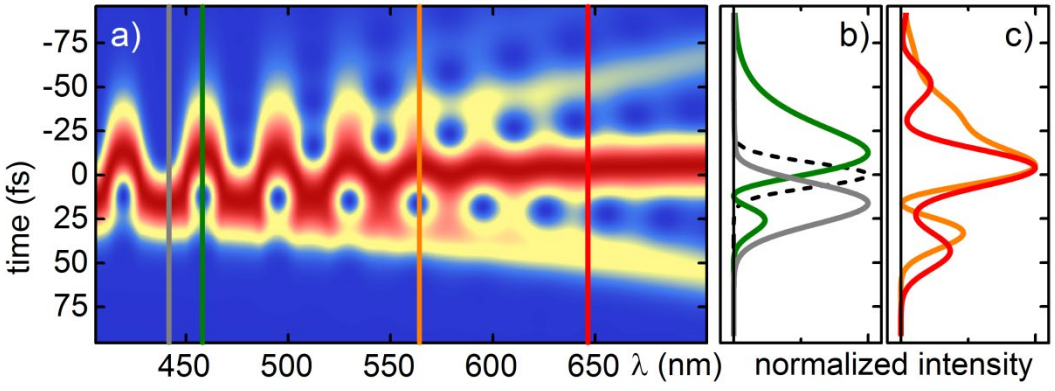

Fig. 3.7: (a) Normalized calculated time domain pulse shapes after one reflection of a 10 nm FWHM pulse on one Diflex 1100 mirror for different central wavelengths. (b,c) Incident pulse (black dashes) and pulse shapes after reflection for different central wavelengths (colored lines) as indicated by color coded cursors.

3.6.2 Pump Probe Group Delay Measurements on Diflex 1100 and 2000

Figure 3.8 shows the pump probe data obtained after reflection of the probe on one Diflex 1000 (a) as well as one Diflex 2000 mirror (d). A number of observations can be made straight from the raw data: Up to about 400 nm the coherent artifact slightly shifts in time, but the shape of the modulation does not change significantly (Fig. 3.8b and 3.8e). The mirror apparently introduces only moderate GD in this range, therefore extracting the GD trough a fit of $\Delta t_0(\lambda)$ is straightforward here.

Modeling & fitting the signal becomes more challenging in the spectral range above 400 nm. Two effects contribute here. Firstly, the modulated delay time interval broadens towards longer wavelengths. This is most obvious in Fig. 3.8d. This broadening looks very similar to the pulse splitting observed in the calculation above (Fig. 3.7). One way to explain the broadened and highly structured signal is to consider splitting of the white light probe. Satellites preceding and following the main pulse would interact with the pump at different delay times, causing modulations of their own, thereby widening the effective modulated interval. Secondly, the CA flips sign for certain wavelengths (cf. Figs 3.8c and f). In fact, time domain signals oscillate increasingly fast towards longer detection wavelengths.

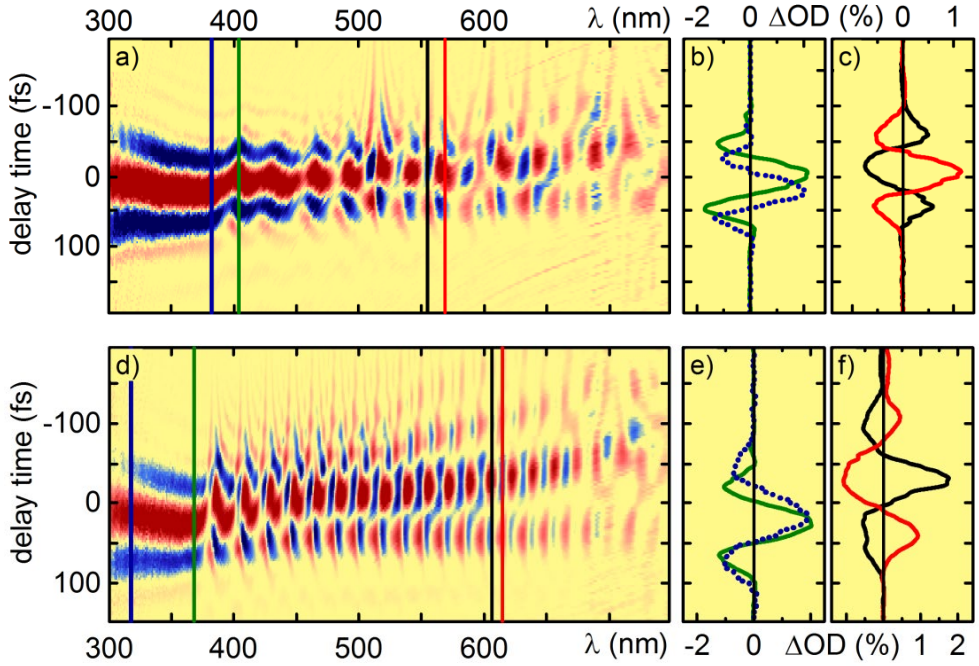

Fig. 3.8: (a,d) Coherent artifact after reflection on one Diflex 1100 (a) and 2000 (d). (b,c,e,f) Time domain artifact shapes for detection wavelengths specified by color coded cursors. Excitation at 465 nm in 183 µm Schott B270 glass using 1000 nJ.

To better understand these signals, a simulation was conducted using the experimentally obtained white light spectrum (cf. Section 2.3). Its spectral phase was characterized by integrating the $\Delta t_0(\lambda)$ obtained from the reference measurement using metallic mirrors. Calculated time domain pulse shapes before and after reflection are shown in Fig. 3.9a. As the white light chirp is small in the red, these spectral components concentrate in a spike at the front of the pulse, while green and blue components are increasingly stretched in time. Indeed, reflection causes the front half of the probe to become severely structured, resembling a pulse train rather than a single probe pulse. The rear half carrying the green and blue spectral components is not significantly altered upon reflection. Figure 3.9b shows the simulated signal obtained with this probe pulse due to XPM in a thin solid. Considering the coating phase was modeled using an extrapolated design curve, the simulation resembles the experiment very closely. Artifact flipping as well as broadening toward the red is reproduced. Artifact fringes in Fig. 3.9c are somewhat overestimated. This has already been discussed in Section 2.3. Inverting and splitting of the signals render quantitative extraction of the GD challenging. Fortunately there is a simple workaround which will be presented below.

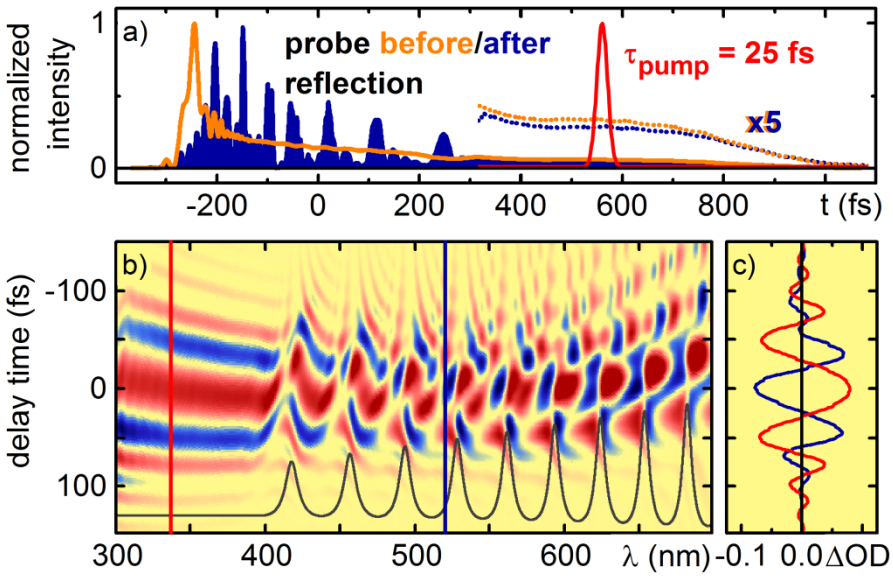

Fig. 3.9: (a) Time domain pulse shape of pump (red) and probe before (yellow) and after one reflection on a Diflex 1100 (blue), calculated using experimental probe spectrum and GD. Dotted lines: probe multiplied by a factor of 5. (b) XPM induced CA simulated using extrapolated GD (gray). (c) Delay time domain artifact shapes for detection wavelengths specified by color coded cursors.

3.6.3 Measurements in Highly Chirped White Light

For an intuitive understanding of the artifact flipping one can rely on the models presented in Chapter 2. Assuming a linearly chirped pulse with a chirp coefficient β, the signal is expected to change sign when β changes sign, as can be easily seen from equation 2.19. This effect is also predicted by the more general Kovalenko model, but the approximate picture by Lorenc et al. introduced in Section 2.41 is sufficient here [Kov99, Lor02].

A linearly chirped probe's instantaneous frequency vs. time can be represented as a straight line with a slope β (cf. Fig. 3.10, blue lines). When upon reflection the coating strongly modulates the probe's GD, the sign of the slope β may change sign for a finite wavelength interval (marked in yellow). If the slope was increased, at some point the same modulation would no longer be enough to reverse the sign of the slope, as is illustrated by solid lines in Fig. 3.10. It follows that increasing the white light chirp should remove the artifact flipping.

Clearly a strongly modulated probe pulse can no longer be considered linearly chirped as a whole. The Lorenc model explicitly covers only moderate modulations, where β does not change sign [Lor02]. However, one can view the probe chirp as locally linear for finite wavelength intervals (marked yellow in Fig. 3.10). At the edges, where $\beta = 0$, the signal is not defined in the Lorenc model. These are the points where experimentally obtained and simulated signals seem to exhibit singularities (cf. Figs. 3.8 & 3.9).

Testing the above hypothesis experimentally is straightforward. A 14.5 mm thick plane parallel BK7 chirper block is inserted into the white light before reflection by the Diflex 1100. The TA signal is then recorded in the same manner as before, except for a larger delay time scan interval due to an increased probe pulse duration (cf. Fig. 3.11).

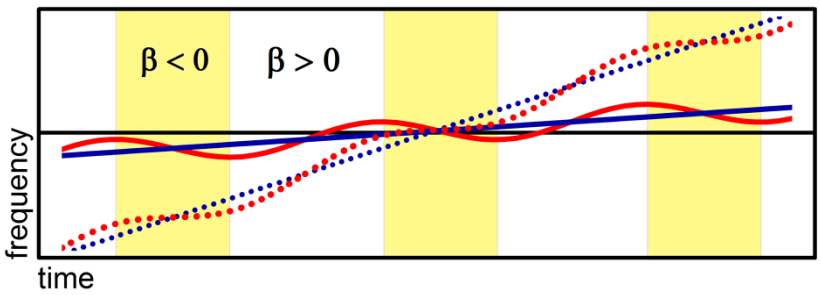

Fig. 3.10: Unmodulated (blue) linear probe chirp and modulation by a mirror coating (red). Dotted lines: effect of additional chirp. Yellow: intervals with flipped slope.

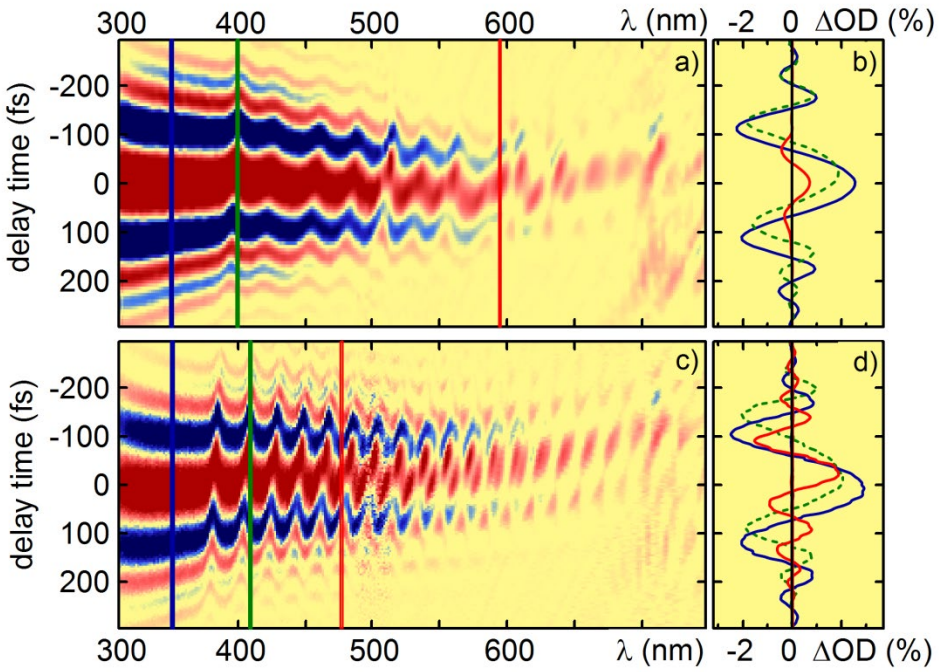

Fig. 3.11: (a,c) Coherent artifact after reflection on one Diflex 1100 (2000) mirror in white light chirped by a 14.5 mm BK7 block. Excitation at 500 nm in 183 µm Schott B270 glass using 1000 nJ. (b,d) Time domain signals for selected λ as indicated by color coded cursors.

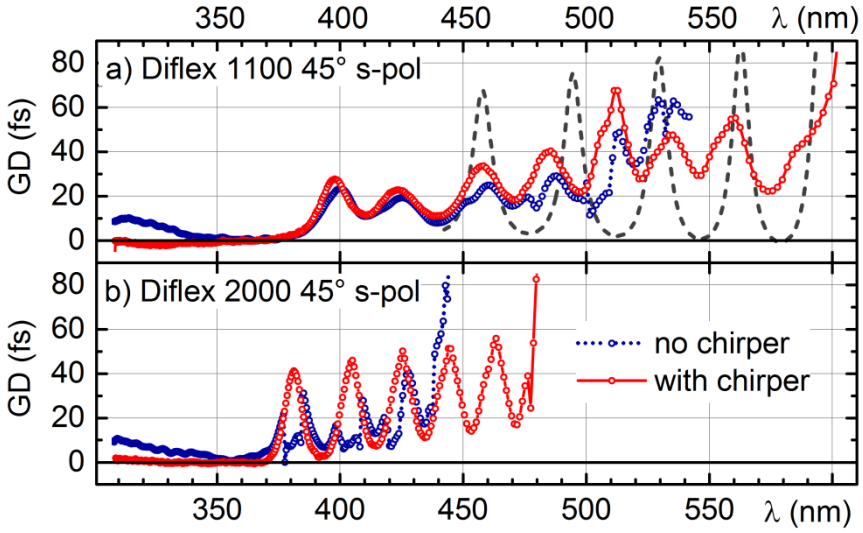

Fig. 3.12: Fitted GD of one Diflex 1100 (a) and 2000 (b) mirror compared to calculation (gray) measured in white light with (red) and without 14.5 mm BK7 chirper.

Indeed, flipping of the artifact can no longer be observed in Fig. 3.11. The width of the artifact has increased considerably and the shape has changed as described in Chapter 2. Thanks to the novel fitting model described therein, this drastically different shape does not represent a problem. In fact, the fit becomes more accurate due to the distinct modulation spanning many data points. Despite the large modulated interval of several 100 fs, the precision of the fitted $\Delta t_0(\lambda)$ is better than 1 fs (cf. Fig. 2.22b). Using the 14.5 mm BK7 chirper block, the Diflex GD can be evaluated up to 600 nm for one Diflex 1100 (cf. Fig. 3.12a). The modulations caused by the Diflex 2000 are even stronger than for the Diflex 1100 mirror. Pulse splitting inhibits reliable fitting of the signals above 480 nm.

Differences in the fitted GD between measurements with and without chirper block are observed below 350 nm and above 450 nm (380 nm for the Diflex 2000). In this range artifact shapes deviate increasingly from the model and reliable fits can only be obtained for several isolated time traces. At the blue edge of the spectrum, artifacts become increasingly asymmetric, causing the fitted $\Delta t_0(\lambda)$ to deviate from the true value (cf. Section 2.5). In chirped white light this effect is less severe. The GD fluctuations are only qualitatively comparable to the calculated GD. Neither the position nor the amplitude of the poles is reproduced exactly, but one has to keep in mind that the dashed gray line is extrapolated from a design calculation. The coatings real GD likely differs somewhat from the ideal design, especially considering the large number of stacks needed for this ultra broad bandwidth. Officially, only the reflectivity is specified by the vendor (cf. Fig. 3.5).

All measurements show a region in the blue with little GD fluctuations. This can be interpreted as light reflected from the outermost stack. This light does not penetrate deep into the coating and is therefore not significantly distorted (cf. Fig. 3.9a). Designing the coatings such that blue light is reflected first makes sense, since dispersion in the material will affect shorter wavelengths more strongly. It can be concluded that while a reflection on a Diflex mirror causes moderate GD in the blue, short pulses will be severely distorted when the incident spectrum exceeds 390 nm (370 nm for the Diflex 2000). Pulses will split and develop satellites on a timescale of approximately ±100 fs. The Diflex mirror can potentially still be used for measurements on longer timescales. The measurements in white light chirped using BK7 show that pulse splitting is less severe for longer pulses, as has been predicted by Weiner et al. [Wei85]. Furthermore, experiments using a BK7 chirper block illustrate that even strong GD modulations can be evaluated using this pump probe technique.

Results presented above demonstrate that chirping removes or at least reduces distortions inflicted on the probe by the mirror coating. Finally, a direct correlation between flipping of the signals observed without the chirper block (cf. Fig. 3.8) and the slope of the GD remains to be proven. In Fig. 3.13a the $\Delta t_0(\lambda)$ obtained from the reference measurement without additional chirp is plotted vs. wavelength (blue). This represents the white light's inherent GD due to the chirp gained from its generation in bulk CaF_2. When adding the measured Diflex 1100 GD to this reference, the modulation is indeed just strong enough to locally change the slope from positive to negative (red line). This is emphasized by the first derivative w.r.t. λ, plotted in black. A yellow background marks regions where the modulated slope has turned negative. Figure 3.13b shows lineouts taken from Fig. 3.8 in the spectral domain at delay times coinciding with the artifact's central peak (blue) and wing (red). Red areas mark intervals where flipped artifacts were observed in the experimental data. The remarkable correlation with the yellow areas proves that the observed flipping is indeed due to the GD modulation introduced by the Diflex 1100 mirror.

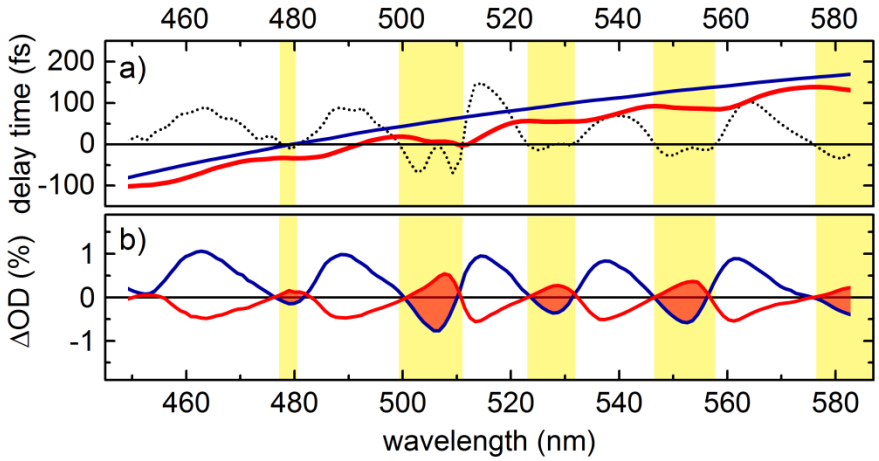

Fig. 3.13: Correlation of measured GD and artifact flipping. (a) $\Delta t_0(\lambda)$ measured in white light without chirper block unmodulated (blue) and modulated by measured GD of a Diflex 1100 (red). Black dots: first derivative w.r.t λ of the modulated curve (scaled). Intervals with negative slope are marked yellow. (b) Amplitude of the artifact's central peak (blue) and wing (red). Red areas mark wavelengths where flipped artifacts were observed.

3.7 A Group Delay Optimized Mirror in the VIS

Even though artifact flipping and pulse splitting can be circumvented as shown in the previous section, there is a limit to this method that is not dictated by the magnitude of a GD modulation, but its curvature. Since the true GD of the mirrors in the previous example is unknown, these measurements are not suited to quantitatively test the measurement accuracy in the VIS. This example will illustrate exactly how fast GD modulations can become, if they are to be accurately reproduced by a fit of $\Delta t_0(\lambda)$ using the fit function Fcos (c.f. Section 2.4.5). To this end, the Pervak PC5-L mirror was investigated, which exhibits a known & controlled GD in the VIS/NIR. The GD of the PC5-L looks very similar to the CMUV08 in the UV. A flat section is followed by a negative linear chirp as the wavelength increases. A matched pair of such chirped mirrors, one compensating the oscillating GD fluctuations of the other, can be used to compress NIR pulses [Mat99, Kär01, Kan15].

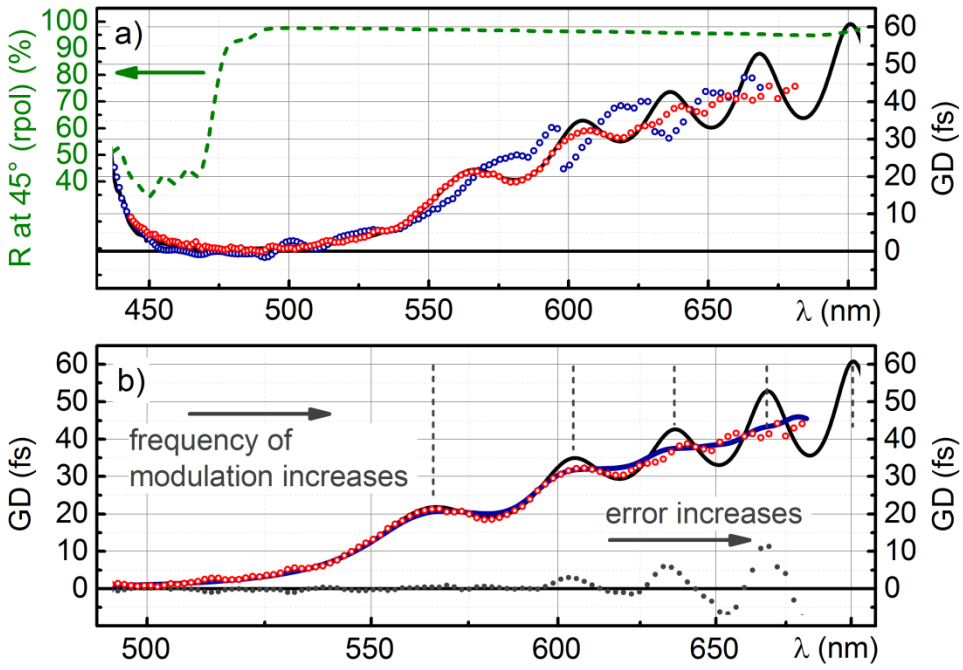

Fig. 3.14: (a) Fitted GD of one PC5-L in white light with (red) and without (blue) a 14.5 mm BK7 chirper block compared to calculated design (black, data supplied by F. Habel). PC5-L reflectivity shown in green. (b) Same as (a), plotted vs. a reciprocal abscissa. Blue line: $\Delta t_0(\lambda)$ fitted to simulated data obtained using the PC5-L design curve. Gray dots indicate difference between fitted $\Delta t_0(\lambda)$ and design curve.

While in a first experiment signal distortions rendered a reliable fit challenging above 550 nm, chirping the probe white light with a 14.5 mm BK7 block resulted in a 'well behaved' coherent artifact throughout the entire visible spectral range. The fitted $\Delta t_0(\lambda)$ reproduces the mirror's GD up to 600 nm within a measurement accuracy of ±1 fs (up to 550 nm without chirper, cf. Fig. 3.14a). In the interval close to the pump wavelength (500 nm), a small stray light contribution is observed in the data taken without chirper block.

In both measurements deviations from the true GD become increasingly severe towards longer wavelengths. Several factors may contribute to this increasing error. Firstly, the actual coating might deviate slightly from the design curve provided. Secondly, the signal to noise ratio decreases toward the NIR as the signal amplitude is roughly proportional to the probe frequency (cf. Eq. 2.19), while fluctuations in the probe light increase when detecting close to the white light's fundamental at 778 nm. However, with help of a simulation, these factors can be ruled out and a systematic deviation is revealed.

As in the previous section, the calculated mirror GD is input into the simulation using the experimental white light spectrum. The white light's inherent chirp before reflection is modeled by the $\Delta t_0(\lambda)$ obtained from the reference measurement. As there is no noise on the time traces, a fit to the simulated data should recover exactly the input GD. The curve obtained, shown in blue in Fig. 3.14b, does so up to about 600 nm and then exhibits almost exactly the same deviation as the experimentally obtained data (red). While the general slope of the GD is reproduced, the oscillating modulation appears smoothed out.

In an effort to replicate this effect, various GD modulations of different magnitude and shape were input into the simulation and subsequently fitted to retrieve the input GD. The absolute amplitude and sign of the GD could be ruled out as well as an increasing slope. Even for a GD proportional to λ^6 the fit accurately reproduces the input. Testing oscillating modulations yields two important observations. First, irrespective of the modulation amplitude, deviations occur when the frequency of the modulation increases beyond a certain limit. Second, when the modulation's periodicity is constant w.r.t. probe frequency, deviations are constant throughout the entire spectral range observed. When, however, the modulation is defined vs. wavelength, deviations become increasingly severe towards the red. Modulations induced by the PC5-L mirror exhibit an almost constant periodicity vs. wavelength (cf. Fig. 3.14a), but fluctuations become faster towards the red when the same GD is plotted on a reciprocal x-axis (Fig. 3.14b). This explains why the deviation becomes worse in the red, but what is its origin?

The deviation originates from the curvature of the GD modulation, or in other words, the high nonlinearity of the white light chirp induced by the coating. As has been discussed at length in Chapter 2, the coherent artifact significantly changes shape when the white light chirp increases. This is often not noticeable by eye when looking at the raw data, but simulation of an extreme case nicely illustrates the detrimental effect of a sudden change in chirp. Figure 3.15a shows a dataset simulated using two error step functions. Where the slope is large (i.e. the chirp is high), the CA exhibits significant fringes. Also, the central peak appears slightly broadened in the strongly chirped sections. Figure 3.15b shows the resulting $\Delta t_0(\lambda)$ when time traces (i.e. vertical slices) of the dataset are fitted using Fcos (red) and FGauß (blue) as defined in Section 2.4. The true GD assumed at the input of the simulation is shown in black. Irrespective of the fit function used, the fitted GD slightly washes out the abrupt change in the GD's slope, FGauß performing only slightly better than Fcos. The dotted line shows the fit error is slightly larger around 500 nm. This is because the step functions were deliberately defined vs. wavelength, making the right step slightly more abrupt in the frequency domain.

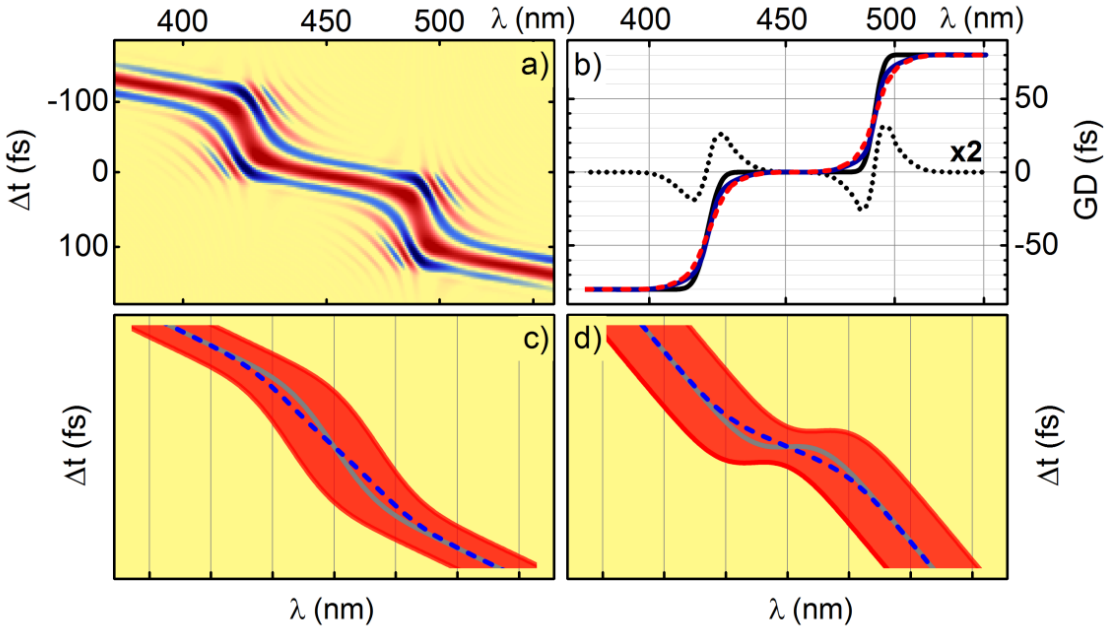

Fig. 3.15: (a) Simulated dataset using error step functions. (b) Assumed (black) and fitted GD using Fcos (red) and FGauß (blue). Black dots: fit error multiplied by two. (c,d) Effect of a broadening (thinning) signal. Red: signal. Gray: trace corresponding to true GD. Blue: center of red trace calculated by adding upper and lower edge and dividing by two.

Illustrations in Fig. 3.15c and 3.15d explain why the curvature is smoothed when the signal suddenly changes both slope and width. The broad red stripes represent a signal whose center is to be determined. While the gray line represents the 'true center' of the signal, the blue dashed line was calculated by considering vertical slices – as in the fitting algorithm. While it correctly reproduces the center at the edges of the depicted interval, the blue dashed line does not correctly reproduce abrupt changes in curvature.

Note that in practice this is not an obvious effect, as fits still reproduce the signals very well throughout the entire spectral range tested. For smooth GDs this error is usually negligible, but for fast oscillations this effect can leads to an averaging of the modulation. Most of the time, however, one is most interested in the part of the spectrum exhibiting no significant fluctuations. In case of the PC5-L, these fast fluctuations will be compensated by a matched counterpart downstream.

3.8 Summary: Making Good Use of an Undesired Effect

The method presented above utilizes the coherent artifact, a usually unwanted disturbance of TA data, to determine the GD characteristics of dielectric mirrors with an accuracy of ±1 fs. While the pump probe method yields comparable accuracy to the standard technique WLI, it has the added capability of being sensitive to pulse deformation and splitting, providing a simple and, if needed, quantitative tool to determine the applicability of a mirror at hand for a given task. Measurements described herein concentrate on the UV/VIS spectral region, but this technique is in principle applicable from 225 nm to at least 1600 nm using white lights generated according to [Rie13].

Instead of immediately dismissing a broadband high reflector for its unspecified GD, it can be worthwhile to take a closer look and quantify how bad the fluctuations really are in the spectral range needed for a specific application. For example in a TA setup Diflex 1100 mirrors could be applied to guide the probe light to the detectors after interaction with the sample, where the temporal structure is no longer an issue. Also, short pulse applications may in fact be possible in the range up to approximately 450 nm.

With recent advances in broadband coating technology as well as broadband spectroscopy, this will become increasingly interesting, since GD data is often kept a secret by vendors for fear of plagiarism.

4 Unraveling the Dynamics of the Pyrene Excimer and Covalently Linked Dimers

Pyrene and its derivatives have been extensively investigated as chromophores over the past decades due to their attractive photophysical properties such as solvent and concentration dependent fluorescence, high fluorescence quantum yield (QY), long fluorescence lifetimes and high photostability [Foe55, Bir63, Bir63a, Pos71, Zac85, And91, Fig11]. Bipyrenyls and oligopyrenyls have attracted attention because of their largely modifiable conformations and tunable optical properties [Pos76, Zac78, Kre94]. Recently there has been increasing interest in pyrene as a building block for functionalized materials in organic electronic devices such as organic light emitting diodes (OLEDs), organic photovoltaics, organic field-effect transistors (OFETs), as well as lasers [Fig11, Jia04, Zha07, Mog06, Wan06, Lee11].

Despite its many applications and extensive use as a textbook example [Bir70, Tur91, Dyk98, Kla09, Tur10], pyrene's excimer formation and decay dynamics are still debated to date [Zac85, Zac88, Dyk98, Win93, Fig11, Duh12, Han13, Yad15]. Probable reasons for lively debate were initially the absence of spectrally resolved detection techniques as well as the lack of pump pulses tailored to the compounds' respective absorption spectra [Han13]. Using spectrally integrating or single-line techniques, overlapping contributions originating from different excited states are hard to discern [And91, And92]. Moreover, probing the triplet state population is challenging using fluorescence detection. Hence, the role of triplet states in the excimer dynamics of pyrene and its derivatives is still unclear.

In this work a combination of comparable results from multiple broadband techniques and systematic variation of the molecular structure will remove long standing ambiguities concerning pyrene's excimer dynamics. In a first step, earlier conclusions on the evolution of the fluorescence are revalidated using time resolved single line as well as broadband fluorescence detection.

Secondly, a combination of broadband fluorescence and broadband transient absorption measurements provides direct insight into the triplet dynamics and oxygen quenching, both for pyrene as well as alkanediyl bridged pyrene dimers. A systematic approach to the functional linking of pyrene molecules provides insights on how pyrene porperties can be influenced and eventually tailored to better suit applications as a building block for functionalized materials in organic electronic devices as well as fluorescence microscopy.

4.1 Introduction to the Photophysics of Pyrene

4.1.1 Pyrene and its Derivatives

Pyrene falls into the class of polycyclic aromatic hydrocarbons (PAHs), its structure is shown in Fig. 4.1a. Pyrene features four six membered aromatic rings, where all C atoms are sp^2 hybridized. Therefore each carbon atom contributes 3 valence electrons to planar σ bonds, which enclose an angle of 120° and give the molecule its characteristic structure. The fourth valence electron contributes to a conjugated π-system extending across the entire molecule [Bir70]. Even though the charge density is not distributed evenly, positions 1, 3, 6 and 8 are equivalent due to pyrene's symmetry. The same is true for positions 4, 5, 9 and 10 as well as the pair 2 and 7.

In order to understand the effects introduced by dimerization, a systematic step-by-step approach is taken, moving from simple to ever more complex configurations: first a methyl group is attached at the 1-position, which is subsequently extended to a propyl chain. To investigate the effects of a heavy substituent, 1-bromopyrene is also included in this study (cf. Fig. 4.1a).

In a second step, a second pyrene unit is attached to the propyl chain (PY11-C3) and the chain length is doubled to address the influence of the linker length (PY11-C6, cf. Fig. 4.1b). In previous studies, a three membered chain was found to most effectively facilitate stacking, while shorter and longer linkers are less favorable ('Hirayama's Rule') [Hir65, Zac84, Zac91, Zac99].

Finally, directly linked pyrenes are investigated with the linker in the 1- (PY11) and 4- (PY44) positions as well as a "mixed" configuration (PY14), in order to address the dependence of the photophysics on the linker position (cf. Fig. 4.1c). Covalently linked pyrene dimers connected at the 1-position were synthesized before [Pos76, Rey90], but to our knowledge a link at the 4-position has only been reported once [Lor13]. The 1,3,6 and 8 positions have a larger atomic orbital coefficient compared to the so-called "K-region" (4,5,9 and 10), this should influence electronic interactions of the pyrene sub-units [Kre94, Lor13].

While pyrene and methylpyrene were purchased from Sigma-Aldrich (FLUKA TraceCERT®, 99.2 ± 0.2%), all other compounds were synthesized specifically for this study by Dr. Ashok Keerthi from the group of Prof. Dr. Klaus Müllen, at the Max Planck Institute of Polymer Research, Mainz, Germany.

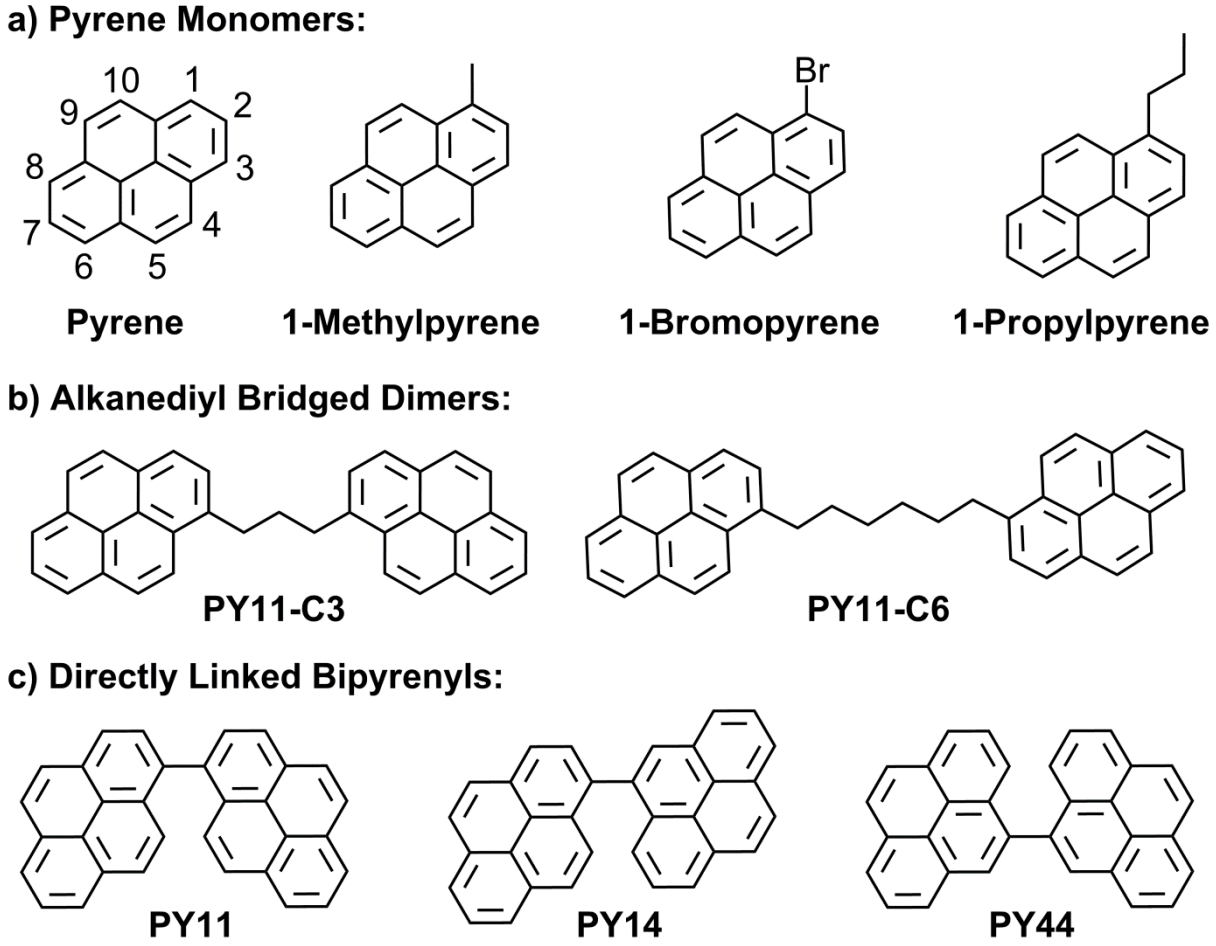

Fig. 4.1: Chemical structures of the pyrene derivatives studied.

4.1.2 Excimers

When two aromatic rings come into close proximity, their π-systems can interact. This can happen in a collision due to diffusion in a solvent or by conformational change of a molecule that carries multiple aromatic groups. A complex formed by one excited and one ground state (GS) molecule can be energetically favorable with respect to the separate molecules. Such a complex is called 'excimer' in case of two identical molecules or 'exciplex' if formed by two different species. Excimers are only stable in their excited state, in the GS the potential surface is entirely repulsive for the two monomer units.

It is widely agreed that the pyrene excimer is formed by offset-sandwich-stacking an excited and a GS pyrene unit after a diffusion-limited encounter, thereby maximally overlapping their π-orbitals ('π-stacking'). This is illustrated in figure 4.2. The interaction of π-orbitals gives rise to a concentration dependent fluorescence (cf. Section 4.1.3).

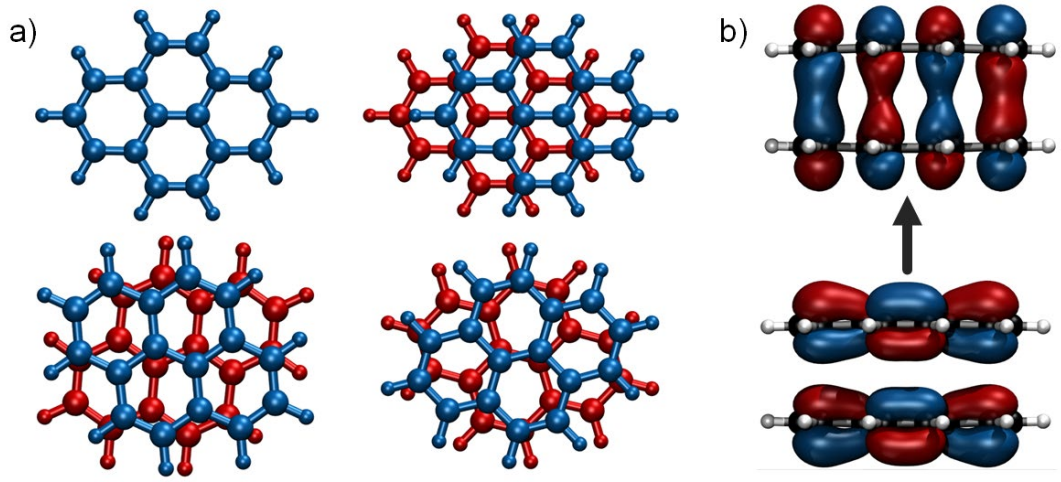

Fig. 4.2: (a) optimized geometries for the pyrene excimer obtained via time dependent density functional theory calculations and (b) example of stabilizing interaction of π-orbitals. Figures adapted from [Rei15].

Other conformers featuring partial overlap are also being considered [Rey90, Zac91, Win93, Yad15] in pyrene crystals and in compounds where the sandwich geometry is sterically unfavorable. In this thesis intermolecular excimers are considered to be formed by diffusional encounter of two separate pyrene units, while intramolecular excimers are formed via folding of a pyrene dimer or oligomer. Pyrene dimers and oligopyrenyls have attracted attention mainly because of their strong excimer formation [Duh12, Son88, Zac76, Kat97]. Dimers and oligomers do not have to rely on finding an excited partner via diffusional encounter, but can form intramolecular excimers by folding.

The following gives a brief explanation of why pyrene excimers are stable based on Chapter 2.2.3 of the book "Photochemistry of Organic Compounds" by Klán and Wirz [Kla09]. A trial wavefunction Ψ_{exc} for the excimer can be defined via

$$\Psi_{exc} = C_0 \cdot \left[\Psi_A \Psi_{B^*} \pm \Psi_{A^*} \Psi_B \right], \tag{4.1}$$

where C_0 is a constant, $\Psi_{A,B}$, Ψ_{A^*,B^*} are eigenfunctions of the separate molecules in the ground and the first excited singlet state, respectively. Then one can calculate the eigenenergies of the excimer using Rayleigh's variation theorem [Atk99, Kla09]. It states that the expectation value for the energy $\left\langle \overline{E}_1 \right\rangle$ given by an approximate wavefunction Ψ is always larger than its true energy E_1:

$$\frac{\left\langle \Psi \middle| \hat{H} \middle| \Psi \right\rangle}{\left\langle \Psi \middle| \Psi \right\rangle} = \left\langle \overline{E}_1 \right\rangle \geq E_1 \tag{4.2}$$

Here $\hat{H}$ is the Hamiltonian operator. To minimize $\langle \bar{E}_1 \rangle$ one must calculate $\partial \langle \bar{E}_1 \rangle / \partial C_0 = 0$. Nontrivial solutions only exist when the secular determinant equals zero,

$$\begin{Vmatrix} H_{11} - E & H_{12} \\ H_{21} & H_{22} - E \end{Vmatrix} = 0, \tag{4.3}$$

with elements $H_{ij} = \langle \Psi_i | H | \Psi_j \rangle$. In case of an excimer formed from two pyrene molecules $H_{11} = H_{22} = E(\text{pyrene}) + E(\text{pyrene}^*)$ and the interaction energy $H_{12} = H_{21}$. The determinant then reduces to

$$(H_{11} - E)^2 - H_{12}^2 = 0, \tag{4.4}$$

yielding two solutions for exciton energies which are shifted from the eigenenergies of separated pyrene molecules by the interaction energy $\pm H_{12}$. This is illustrated in the top panel of figure 4.3a. This splitting of energy levels leads to a net stabilization for one GS and one excited state molecule (cf. Fig. 4.3b, right), but not for two GS molecules (left).

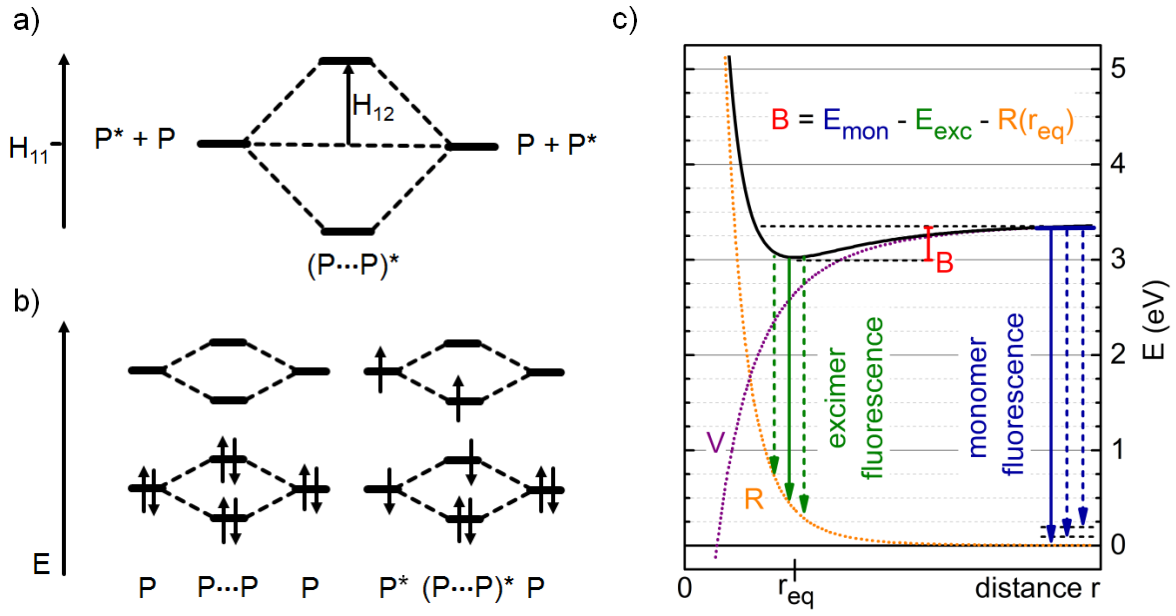

Fig. 4.3: (a) orbital diagram for bound and unbound molecules. (b) electron configurations with both molecules in the ground state vs. the situation with one excited molecule. Figures adapted from [Kla09]. (c) potential surface along reaction coordinate r representing the distance between molecules, modeled as the sum of an attractive (V, violet) and a repulsive potential R (yellow), contributing in the same way to the ground and excited state. Monomer (blue) and excimer fluorescence (green) are compared to the binding energy B of the excimer (red).

When the complex relaxes to the GS via fluorescence, the dissociative potential is causing individual molecules to separate again (cf. Fig. 4.3c). At room temperature most of the excimer fluorescence will originate from the potential minimum. Hence, the maximum of the excimer fluorescence spectrum corresponds to a photon energy E_{exc} (solid green arrow) [Bir70]. With the high energy cutoff of the monomer fluorescence E_{mon} (solid blue arrow),

$$E_{mon} - E_{exc} = B + R(r_{eq}) . \tag{4.5}$$

B can be determined by temperature dependent measurements, leading to ~0.4 eV [Bir65, Bir70]. Some calculations feature a shallow minimum in the GS, pointing to GS associated dimers [Hue08, Shi11]. Evidence of this has been found in crystals and in the gas phase [Win93]. To the author's knowledge, with one exception previously published results provide little evidence for GS dimers in solution at room temperature for pyrene and the derivatives considered herein [Rey90, And91, And92, Shi11].

The above treatment only considers excitonic interactions. Alone, these are too small to account for the considerable stabilization of more than 0.4 eV [Bir65, Rei15]. A crude approximation of the excitonic interaction energy H_{12} can be obtained via the transition dipole moment $M_{0\rightarrow1}$ of the transition between pyrene's GS and the S_1 excited state. After all, a GS and an S_1 excited state molecule are believed to form the pyrene excimer. Assuming a low molar extinction coefficient on the order of $\varepsilon = 10^3 \,\mathrm{L\,mol^{-1}\,cm^{-1}}$, a typical linewidth of $0.3 \cdot 10^4 \,\mathrm{cm^{-1}}$ and an average frequency of $8.45 \cdot 10^{14} \,\mathrm{s^{-1}}$ for the $S_1 \leftarrow S_0$ transition, $M_{0\rightarrow1}$ can be approximated to ~2.3 D via the formalism given in Chapter 2.1.4 of [Kla09] (see Appendix A1). The latest reported value for the equilibrium distance between pyrene units in the excimer is 3.38 Å [Rei15]. At this distance the reduction in potential energy resulting from the Coulomb interaction of two dipoles $M_{0\rightarrow1}$ amounts to a stabilization of -0.175 eV. It is widely acknowledged that other contributions like charge transfer and possible molecular orbital overlap also contribute to H_{12} [Kla09]. A net charge transfer is prohibited by symmetry arguments, but configuration interaction calculations confirm further stabilization due to 'charge resonance' [Azu64a, Azu64b, Mur64]. These did not yet accurately reproduce experimental fluorescence spectra, deviations were attributed to contributions from higher lying states [Bir68]. Recent calculations using time dependent density functional theory (TDDFT) attribute ca. 50% of the stabilization to non excitonic interactions [Shi11, Rei15]. An increased electrostatic contribution due to geometric effects, i.e. overlap of π-orb-itals and considerable electron delocalization between pyrene units has been discussed [Cor15]. Section 4.7.3 will add experimental insight to the charge transfer character of the excimer.

4.1.3 Steady State Absorption and Emission Properties

Pyrene's fluorescence spectrum depends on both solvent and concentration. The solvent dependence has led to the introduction of the pyrene scale for solvent polarity [Kal77, Don84]. The concentration dependent blue-green excimer fluorescence, was first observed by Förster and Kasper in 1955 [Foe55]. It finds important applications in studying the viscosity of micelles and also as a fluorescence marker for tracking transport of biomolecules in cells and biological membranes [Zac78, Alm82, Zac84, Con03, Con08]. Without question many insights can be gained by looking at the fluorescence spectra in depth. This work, however, focuses on the dynamics, so the discussion below concentrates on key features only.

Figure 4.4 shows absorption and emission spectra of pyrene and linked pyrene dimers in cyclohexane at $c \approx 10^{-5}\,\mathrm{mol}/\mathrm{l}$. All species show very similar vibronic features in the UV-visible absorption with strong maxima around 276 nm and 340 nm (Fig. 4.4a). These can be assigned to the $S_3 \leftarrow S_0$ and $S_2 \leftarrow S_0$ transitions in the pyrene monomer and the associated transitions in the linked dimers. The $S_1 \leftarrow S_0$ transition of pyrene is weak (black dots). While commonly this transition is considered symmetry-forbidden [Lap11, Sal83, Wan03, Han13, Kre13], a more recent study finds that this is not true in a strict sense. Instead, the weak S_1 absorption comprises two electronic excitations with antiparallel transition dipole moments, causing them to effectively cancel out [Rei15]. It is possible to partially overcome this 'destructive interference' when substituents are attached to pyrene units at the right positions (cf. Section 4.7.4). PY11 and PY14 are examples of such species (cf. Fig. 4.4b).

In linked dimers PY11-C3 and PY11-C6 the molar absorption coefficient ε approximately doubles, due to the additive contribution from two pyrene units. The spectra are otherwise comparable to monomer pyrene except for a bathochromic shift of ~10 nm. This shift can be understood by viewing the second pyrene unit as a heavy substituent. A similar shift is observed in the absorption spectrum of bromopyrene (not shown). The absorption of PY11-C6 (yellow) appears slightly less shifted than that of PY11-C3 (black), probably due to the mitigating effect of the longer linker. The absorption spectrum of the directly linked compound PY44 (blue) is very similar to PY11-C6, but the absorption of the $S_2 \leftarrow S_0$ transition has weakened with respect to the $S_3 \leftarrow S_0$ transition. In PY11 (red) the influence of effective conjugation and intramolecular interaction is clearly visible from the red-shifted absorption onset at 403 nm (Fig. 4.4b). PY14 (violet) represents an intermediate case. These findings indicate that the lowest excited states are influenced by the dimerization more strongly than higher excited states.

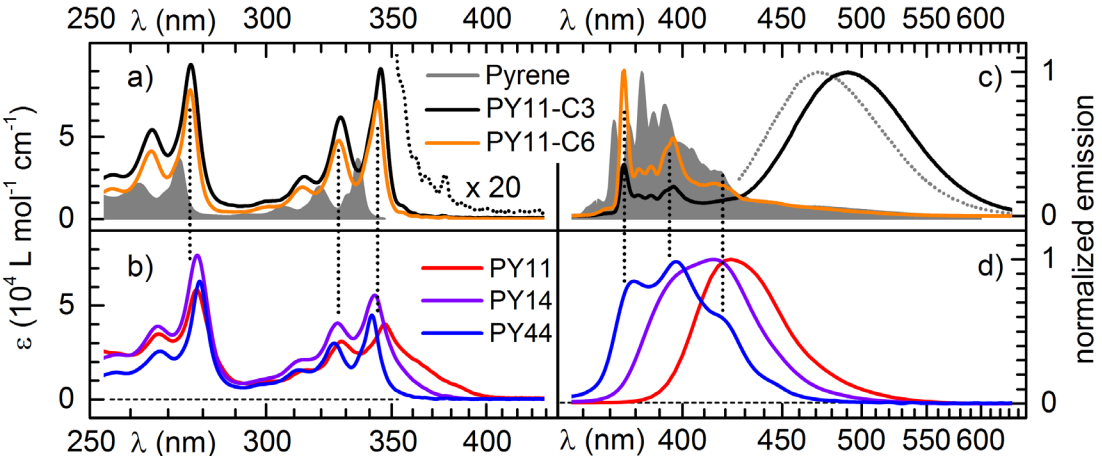

Fig. 4.4: Steady state absorption (a, b) and emission excited at 340 nm (c, d) of selected compounds in cyclohexane at room temperature, $c \approx 10^{-5}\,\mathrm{mol}/\mathrm{l}$. Gray: pyrene monomer. Gray dots: excimer fluorescence at 10 mM. Black dots: PY11-C3 absorption magnified x20 to illustrate the weak $S_1 \leftarrow S_0$ contribution.

Emission spectra were recorded at room temperature at 340 nm excitation (Fig. 4.4c,d). The known structured emission of the pyrene monomer is shown in gray. Relative heights of individual peaks depend on the solvent polarity [Don84]. The monomer fluorescence spectrum features a weak pedestal reaching far into the green. The pyrene excimer fluorescence gains appreciable intensity at $c > 0.5\,\mathrm{mM}$ showing as a broad unstructured band centered around 475 nm. Gray dots represent the excimer signal at $c = 10\,\mathrm{mM}$. The emission of PY11-C6 (yellow) is very similar to the monomer except for a different vibronic fine structure. PY11-C3 shows a comparable structured emission combined with an excimer band, slightly red shifted w.r.t. the excimer emission in pyrene (black). This excimer emission is observable irrespective of the concentration, because the pyrene units are linked. The stark difference between Py11-C3 and PY11-C6 is due to differing linker lengths. Chains with less than nine members generally prevent excimer formation with exception of the propyl chain, which sterically favours π-stacking [Hir65, Zac99]. For this reason PY11-C3 (a.k.a. 1,3-dipyrenylpropane) is an excellent example for the study of excimer dynamics and has received a lot of attention in the past [Zac78, Sna83 ,Zac84, Zac85, Zac85a, Sie87, Zac88, Sie89, Rey90, Zac91]. The fluorescence spectra of directly linked pyrenes show little to no vibronic fine structure. A direct link leaves less freedom to the molecular conformations and prevents π-stacking, yet close proximity of the pyrene units apparently strongly affects their properties. Results from a time resolved study that will be discussed in Section 4.7.4 illustrate just how dramatic these changes can be.

4.2 Combining State of the Art Time Resolved Methods

This section will provide an overview of the spectroscopic tools that were for the first time combined to yield a 'full picture' of the pyrene dynamics. The facilities at the chair for BioMolecular Optics (BMO) allow recording of time resolved broadband fluorescence and absorption data. Each individual technique has been described in detail elsewhere, the focus herein lies on measures taken to ensure the comparability of the results obtained.

4.2.1 Streak Camera for Broadband Emission Kinetics

For the spectrally resolved investigation of fluorescence dynamics on the ns timescale, a streak camera system (C5680-24 C; Hamamatsu GmbH) is employed. Essential parameters are given below. For detailed information on the streak camera setup refer to [Rys11].

Femtosecond UV pulses are focused by a 75 mm fused silica plano-convex lens onto a 2 mm flow cuvette (0.5 mm for some samples). The spot size in the sample is 20 µm. Compounds are dissolved in cyclohexane such that an OD of approximately 0.3 is reached. The target is illuminated from the back. The fluorescence is captured by an achromat (f = 80 mm, 20 mm diameter, Type OUV 4.20; Bernhard Halle Nachfl. GmbH) and transmitted through a wire grid polarizer (UBB01C, diameter 36 mm; Moxtek Inc.) set to magic angle. Subsequently a second achromatic lens (f = 75 mm NUV, 25 mm diameter; Edmund Optics) focuses the fluorescence onto the entrance slit of a spectrograph. The spectrograph (Princeton Instruments Acton SP2356) features a 50 lines/mm grating blazed at 600 nm and f = 300 mm.

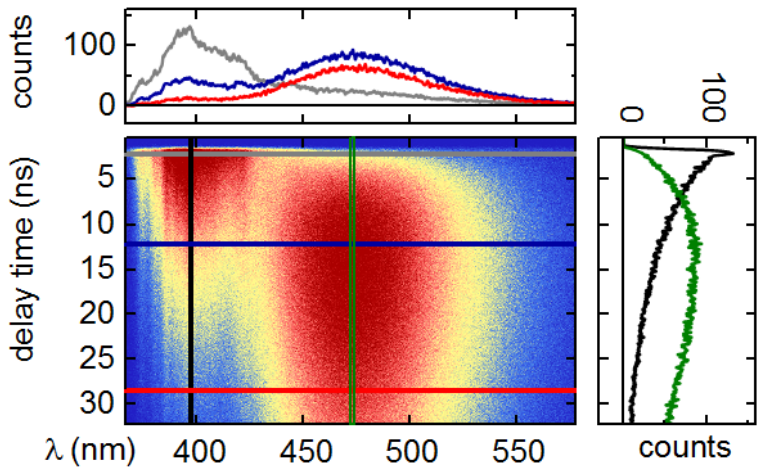

Fig. 4.5: Streak camera measurement of 10 mM pyrene in cyclohexane. Color coded vertical and horizontal lines mark positions of lineouts in the spectral and temporal domain shown in the top and right panels, respectively.

Finally, the focal plane of the spectrograph is imaged on to the photocathode of the streak camera. The pump energy is set to 130 nJ and slit widths are 5 µm (spectrograph entrance, spectral plane) and 10 µm (streak camera, temporal plane) unless otherwise indicated. This corresponds to 0.7 nm spectral and sub-350 ps temporal resolution. A typical dataset is shown in Figure 4.5. The maximum streaking window of this system is 32.3 ns. Dynamics on longer timescales were confirmed using a single line method described in Section 4.2.5.

Additional time resolved photon counting experiments on the µs timescale were carried out with a similar setup at the University of Regensburg. Here, a Ti:Sapphire amplifier laser system (Libra, Coherent) provides pulsed laser light at 800 nm that feeds into a collinear OPA (TOPAS-C, Coherent), generating the excitation pulses at the desired wavelength with a pulse duration of typically 80 fs. The fluorescence was collected front-face from a 10 mm cuvette at ca. 30° to the excitation path via a toric mirror (r_1 = 205 mm, r_2 = 191 mm; f = 99 mm; α = 15°; d = 75 mm) and detected with a streak camera (C7700, Hamamatsu) combined with a Bruker 200is spectrograph. Due to electronic jitter, the IRF is ca. 20 ps FWHM in the 10 ns and 8 ns In the 500 ns streaking window. The streak images were recorded on a CCD camera (ORCA-CR, Hamamatsu), the spectral resolution in this configuration is 2.5 nm. A 2 mm spot size and excitation energies between 200 nJ and 700 nJ were used. Here, samples were degassed via five freeze-pump-thaw cycles in a 10^{-5} mbar vacuum and sealed samples were stirred continuously via a magnetic stir bar.

4.2.2 Multiscale Transient Absorption Spectroscopy

The dynamics of pyrene and its derivatives range from femtoseconds way into the microsecond regime. The multiscale transient absorption (TA) setup utilized is based on a combination of two independent and fully synchronized 1 kHz pump beams (cf. Fig. 4.6). As broadband probe, a CaF_2 white light is used, generated from the Ti:Sapphire amplifier fundamental at 778 nm (CPA2001; Clark-MXR, Inc.) [Meg09]. Probing is possible from 225 up to 1700 nm [Rie13], in this work the 290 – 1100 nm range is used. Channels are spectrally calibrated using colored glass filters and dielectric mirrors with characteristic transmission oscillations. In the region around the CPA fundamental an appropriate blocking filter is employed, resulting in ~60% less counts on the CCD, leading to a smaller signal-to-noise ratio in the range between 700 nm and 830 nm. The probe chirp and therefore the time origin do exhibit a discontinuity at the CPA fundamental wavelength, but this is only relevant on the femtosecond timescale. The white light chirp is corrected in postprocessing according to [Meg09].

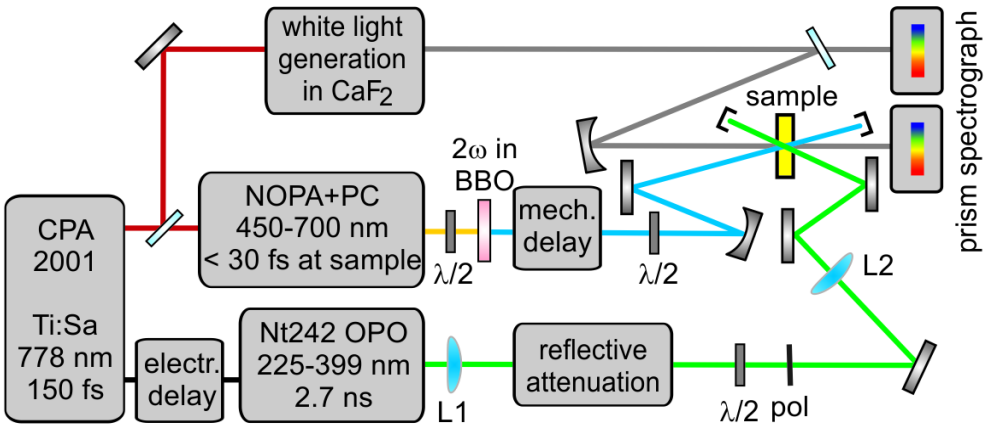

Fig. 4.6: Combined fs/ns transient absorption setup with synchronized Clark CPA 2001 and EKSPLA NT242 frequency doubled OPO. NOPA: two-stage noncollinearly phase-matched optical parametric amplifier. PC: prism compressor. PS: prism spectrograph. NOPA output frequency doubled in a 50 µm BBO. L1, L2: D-shaped focusing lens f = 1500 mm and f = 400 mm. pol: Thorlabs GL10 polarizer.

To record dynamics on the fs/ps timescale, sub-30 fs pump pulses are generated from a noncollinearly phase-matched optical parametric amplifier (NOPA) pumped by the second harmonic of the Ti:Sapphire amplifier. The tunable NOPA output is compressed in the sample plane via a fused silica prism compressor. The pump is frequency doubled in a 50 µm BBO, a λ/2 plate before the crystal facilitates attenuation of the pump energy. Finally the pump is mechanically delayed in 20 fs steps using a linear delay stage with sub 10 fs accuracy (M-531 PD; Physik Instrumente GmbH). The pump polarization can be set via a second λ/2 plate.

To access ns/µs dynamics, the tunable fs pump can be replaced by a ns pulse generated by an EKSPLA NT242 Optical Parametric Oscillator (OPO) [Rie13]. It is electronically synchronized to less than 200 ps w.r.t. the probe and delayed using a Stanford Research Inc. DG 645 electronic delay generator. The EKSPLA output is first attenuated reflectively. Fine adjustment of pump power and polarization is possible via a λ/2 plate and a polarizer.

Samples are diluted in 10 to 15 ml cyclohexane to yield an OD < 0.3 at 1 mm sample thickness. A pump circuit of our own design facilitates exchange of the probed sample volume between subsequent laser shots (cf. Section 4.2.5). The FWHM focal sizes of the pump spots are 100 µm and 200 µm for the fs/ps and ns/µs setups, respectively, and 30 µm for the white light probe. Pump energies were set to between 70 nJ and 200 nJ.

The TA signal is detected at 1 kHz using two prism spectrographs [Meg09, Bra14], dividing the sample's transmission with pump by the transmission without pump for each channel averaging over 500 shots. Transmission changes down to 0.02 mOD can be resolved using referenced detection [Bra14].

Fig. 4.7 shows sample data for the fs and ns timescales. Increased TA due to, e.g., excited state absorption (ESA) is plotted positive. The ground state bleach (GSB) as well as stimulated emission will manifest as a negative signal. Mimicking the inverted steady state absorption spectrum, the GSB reflects a decrease in the number of GS molecules, as a fraction of the molecules has been promoted to an excited state. Panels depicting spectral or temporal lineouts indicated by the color coded cursors in TA datasets are henceforth marked by a yellow background (cf. Fig. 4.7a,c,d,f).

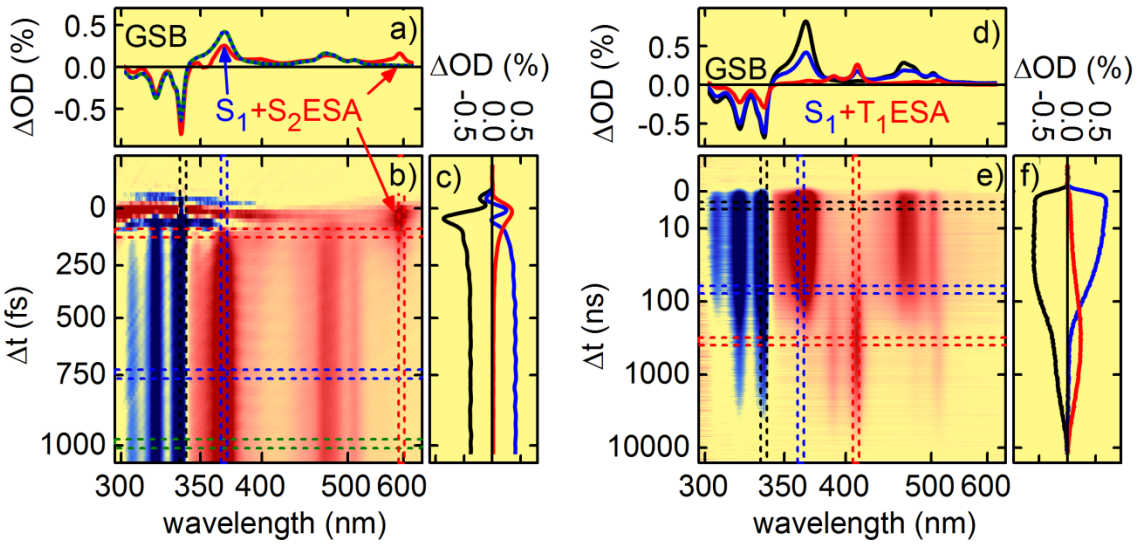

Fig. 4.7: Transient absorption data of 1mM pyrene in cyclohexane on the fs- (a-c) and ns timescale (d-f). Blue indicates negative, red positive contributions. Color coded cursors mark lineouts shown in the top and right panels, respectively. Top panel: transient spectra at different delay times. Right panel: time evolution of the GSB (black), the S_2 ESA (purple), the S_1 ESA (blue) and the triplet state (red).

4.2.3 Combining nanosecond and NIR Measurement Capabilities

In the current layout of the laboratories at the chair for biomolecular optics, NIR probe white light and the electronically delayed OPO for ns/µs timescale measurements are not available in the same room. Only in the NIR the transient absorption spectrum of the pyrene excimer can be observed without overlapping contributions of other states clouding the dynamics. To confirm results obtained in the VIS, the ns setup is combined with the NIR probe in an adjacent laboratory.

This is realized by coupling the output of the OPO into a 23.7 m long UV multimode fiber (Laser Components GmbH, FBP050070085) with 50 µm diameter. Two challenges had to be overcome, first the OPO output had to be attenuated by several orders of magnitude without causing thermal lensing in the attenuating optics. Second, the highly elliptical beam profile of the OPO has to be coupled into the circular fiber aperture. As most objectives and commercially available fiber couplers don't transmit in the UV, a customized solution is needed. The scheme shown in Fig. 4.8 proved most effective, relay imaging the focal plane of the OPO onto the fiber entrance via lenses L1 and L2. After reflective attenuation to avoid thermal lensing, the OPO fundamental is blocked using a 3 mm thick Schott UG5 filter. The power at the fiber entrance is fine-tuned by a variable metallic neutral density (ND) filter to ~1 µJ. The damage threshold of the UV fiber was not tested due to limited availability, fibers intended for the visible spectral range (Laser2000 GmbH, PLK-Patch-MM-FC-PC-25) showed no permanent damage up to 5 µJ pump power. At the fiber entrance, the resulting 50 µm spot is perfectly circular.

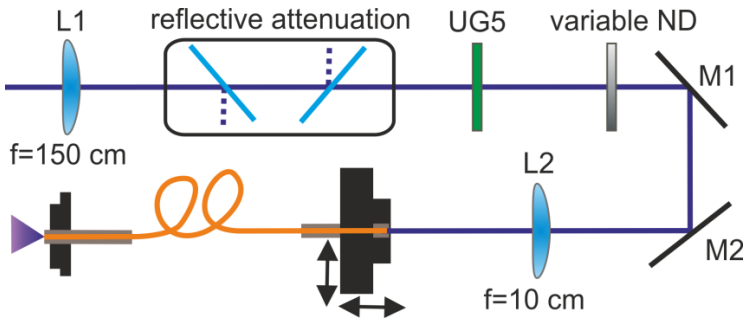

Fig. 4.8: Schematic of the fiber coupling assembly. M1, M2: coupling mirrors. L1, L2: Fused silica lenses. The fiber mount can be translated in x, y and z with µm precision. L1 and L2 are positioned 150 cm and 302 cm from the EKSPLA housing, respectively. 9.5 cm separate L2 and the fiber entrance.

This was confirmed for visible (460 nm) and ultraviolet (334 nm) light. A fiber transmission of up to 85% in the VIS and at least 20% using the 334 nm pulses needed for experiments on pyrene were reached. At 334 nm the UV fiber attenuates 100 dB/km, resulting in an attenuation of 58%. The ideal numerical aperture (NA) needed for the fiber used is about a factor of four larger as is easily determined by shining a fiber checker through the fiber and observing the NA at the output. In a single mode fiber a too large or too small NA would significantly reduce the coupling efficiency, but for a multimode fiber a smaller NA is acceptable. Also, the focal length and hence the spot size would decrease with higher NA, increasing the risk of damage to the fiber.

For use in the TA setup the divergent fiber output has to be imaged into the interaction plane of the TA setup. The required focal size is 200 µm FWHM. Combinations of specifically selected bestform lenses (Bernhard Halle Nachfl. GmbH) were tested for this purpose, however it could be shown that a single plano-convex 25 mm FS lens of 12.5 mm diameter is actually sufficient for this purpose, yielding a 208 µm FWHM in 145 mm distance from the lens (cf. Fig. 4.9a). Using a single lens is preferable, since this minimizes reflection losses. Speckle as well as diffraction on the fiber output significantly influence the beam profile. Measured beam profiles are reminiscent of Fresnel diffraction on a circular aperture (cf. Fig. 4.9b, [Mes05]). This causes the focus to appear closer to a flat top than a Gaussian (cf. Fig. 4.9c). This is advantageous because it facilitates a homogeneous pump distribution.

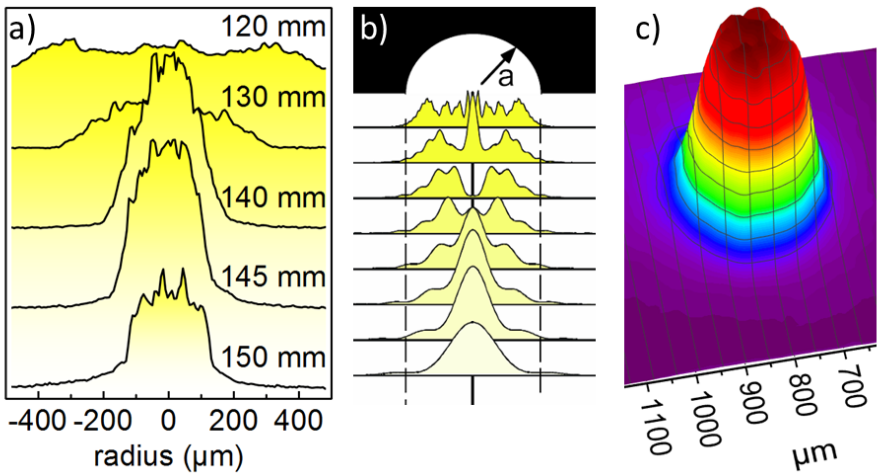

Fig. 4.9: Beam profile vs. distance from the lens (a) compared to Fresnel diffraction on a round aperture (b) taken from [Mes05] with permission of Springer Nature. (c) 3D profile in the focal plane.

4.2.4 Data Analysis: From Single Line to Global Fit and Maximum Entropy

Some assumptions have to be made in order to retrieve meaningful information from the time resolved data. It is assumed that the system can be modeled by a set of well-defined intermediate states with populations $N_m(t)$. Starting from initial conditions defined at $t = 0$, these states are populated (or depopulated) at rates k_{nm} (k_{mn}) parameterizing the transfer between individual states. The temporal change of each population is assumed to be proportional to its population at a given time, so that each state can be described by a set of first order ordinary differential equations.

$$\frac{dN_m(t)}{dt} = \sum_n \left(k_{nm} N_n - k_{mn} N_m \right) \tag{4.6}$$

For unimolecular processes the rates are independent of concentration and, hence, time. The solutions to these equations are then given by a linear combination of exponentials. The inverse of a rate corresponds to a $1/e$ decay time constant τ. Time dependent rates, e.g. due to diffusion controlled excimer formation, will give rise to non-exponential decays that are commonly modeled by stretched exponentials. Also, the above assumption only holds as long as a constant spectrum $A_i(\lambda)$ can be assigned to each intermediate state, i.e. there are no significant time dependent spectral changes like broadening or shifting of bands due to cooling or solvation processes. This is rarely an issue for processes on the timescale of ns/µs.

Under the assumption that all time traces can be reproduced by a linear combination of exponential decays, individual time traces can be fitted wavelength by wavelength. A single line fit function $f_{SL}(\lambda, A_i, \tau_i, \Delta t)$ can be defined as

$$f_{SL}(\lambda, A_i, \tau_i, \Delta t) = \sum_i f_i(A_i, \tau_i, \Delta t), \tag{4.7}$$

where $f_i(A_i, \tau_i, \Delta t)$ are single exponential decays with amplitudes A_i and decay times τ_i, convoluted with the instrumental response function (IRF) of the setup

$$f_i(\lambda, A_i, \tau_i, \Delta t) = \mathrm{IRF}(\Delta t) \otimes \left\{ \Theta(\Delta t) * \left(\sum_i A_i(\lambda) \exp\left[-\Delta t / \tau_i \right] \right) \right\} + \mathrm{const} + \mathrm{CA} \tag{4.8}$$

Here, $\Theta(\Delta t)$ is the Heaviside step function and CA is the coherent artifact described at length in chapter 3 of this thesis. The IRF is a Gaussian function

$$\mathrm{IRF}(\Delta t) = \frac{2\sqrt{\ln 2}}{\sqrt{\pi} \cdot \tau_{CC}} \exp\left[-\left(\frac{2\sqrt{\ln 2}}{\tau_{CC}} \cdot \left(\Delta t - \Delta t_0 \right) \right)^2 \right], \tag{4.9}$$

with an FWHM width τ_{CC}. The statistical error in the fitted parameters is

$$\sigma(P_i) = \sigma \cdot \sqrt{\left(J^T J \right)^{-1}}, \tag{4.10}$$

with the Jacobi matrix J and the standard deviation

$$\sigma = \sqrt{\sum_n \left(Y_n - f_n \right)^2 / (N - q)}, \tag{4.11}$$

where Y_n are individual data points, f_n the respective fitted values, N the total number of samples and q the total number of fitted parameters.

Basing the analysis on a select few individual time traces can lead to ambiguities when spectral contributions of different states overlap significantly. Harnessing the power of broadband techniques to disentangle overlapping signal contributions requires consideration of the entire spectrally resolved dataset. A global fit (GF) routine can be applied to matrix data sets $S(\lambda, \Delta t)$ from TA or streak camera experiments based on the formalism detailed in [Sto04, Fit06, Meg11, Kut13]. The algorithm fits the time traces at all wavelengths with one common set of decay time constants τ_i. Under the assumption that all time traces can be reproduced by a linear combination of exponential decays, the fit function is defined as

$$f_{GF}(A_i(\lambda), \tau_i, \Delta t) = \sum_i A_i(\lambda) \cdot \tilde{f}_i(\tau_i, \Delta t), \tag{4.12}$$

with a predefined number of exponential decays. Applying a Levenberg-Marquard algorithm to minimize the least squares error for all spectral channels simultaneously, the routine finds an optimal set for the τ_i as well as the decay associated difference spectra $A_i(\lambda)$ (DADS) corresponding to these decays. In DADS positive contributions indicate decaying features whereas negative signal corresponds to features growing in. Assuming a specific rate model, the species associated spectra (SAS) can be retrieved as linear combinations of the DADS and the GS absorption spectrum. The linear coefficients depend on the model assumed.

Both methods described above yield optimized decay time constants τ_i, but rely on the user's judgement to pick the correct number of distinct exponential decays needed to model the data. This can become ambiguous when different states exhibit similar decay times. A method to determine the smallest set of decays needed to fully describe a transient dataset is a maximum entropy analysis [Lor07, Kut13]. Under the assumption that all time traces can be reproduced by a linear combination of exponential decays, the maximum entropy routine fits matrix data sets $S(\lambda, \Delta t)$ starting from a distribution of decay rates

$$f_{ME}(p, \tau, \Delta t) = \int_0^\infty p(\tau) \cdot f(\tau, \Delta t) \tag{4.13}$$

Two constraints must be fulfilled: First, the fit has to reproduce the data to a given accuracy. Second, the entropy of the distribution $p(\tau)$ is maximized, i.e. $p(\tau)$ should not contain more information than required to fit the data. Without a priori assuming a model, a maximum entropy analysis results in a distribution function that describes the probability of a given rate. Fig. 4.10a shows an example distribution obtained from 1 mM pyrene in cyclohexane (corresponding TA data shown in Fig. 4.7e). Peak widths in the τ domain are a measure for the uncertainty in these lifetimes (Fig. 4.10b). The blue curve in Fig. 4.10b shows the distribution around 360 nm where decay of the S_1 excited state absorption (ESA) dominates with a decay time of approximately 100 ns. A subtle contribution of the excimer rise is also observed at $\tau = 30$ ns, contributing a negative dip to the blue curve. At $c = 1$ mM the excimer's ESA is weak compared to the other signals and is only revealed in the global analysis. Around 410 nm (red), the triplet state decay resides at ~3100 ns. The negative contribution at just below 100 ns is also due to the rise of the triplet ESA. When no excimer is present this feature coincides with the singlet decay time. Here it appears slightly shifted towards faster times since the triplet is fed by both the S_1 state and the excimer. Spectra integrated over selected decay time intervals resemble the GF DADS associated with these decays (cf. Fig. 4.10c), except for the weak excimer contribution (green).

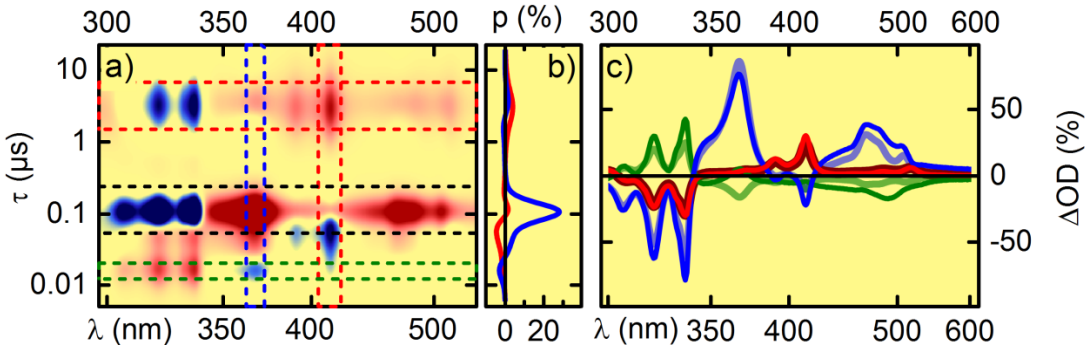

Fig. 4.10: (a) Maximum Entropy analysis of the nanosecond measurement in 1 mM pyrene shown in Fig. 4.7. Decays correspond to positive features (red), negative features (blue) indicate exponential growth. (b) Lifetime density distribution at selected wavelengths. (c) Integrated lifetime density according to color coded cursors. Thin lines represent DADS obtained from a global fit with three decay time constants. The fit yields $\tau_1 = 37$ ns (green), $\tau_2 = 99$ ns (blue) and $\tau_2 = 3135$ ns (red), corresponding to the decay times of the S_1, excimer and triplet states.

4.2.5 Degassing Control Using a Single Line Time Resolved Fluorescence Setup

The oxygen concentration in the pyrene solutions probed dramatically affects the lifetime of observed singlet and triplet states [Gre94, Wil99, Bie14]. Under ambient conditions the pyrene triplet state has a decay time of approximately 1.8 µs [Sli70], while under properly degassed conditions up to millisecond decay times have been observed in a sealed container [Par62]. This also affects fluorescence intensity and decay times [Bir70]. Successful degassing is verified by repetitive measurement of fluorescence decays in a single line time resolved fluorescence setup (cf. Fig: 4.11). This setup also offers a relatively simple approach to determine fluorescence lifetimes of samples with known fluorescence spectrum, especially for lifetimes exceeding the streak camera's detection window.

The sample is illuminated "front face" by an appropriately attenuated laser source. Care must be taken to block the fundamental light of the oscillator or other generating light wavelengths, so that only photons of the desired energy reach the target. Some of the fluorescence emission is collected by a 1" diameter f = 50 mm FS lens. The fluorescence light is filtered by selected bandpass filters (FWHM ~ 10 nm) and is finally imaged via a f = 100 mm lens onto a photomultiplier tube (PMT – H5783-03; Hamamatsu GmbH). The PMT has a spectral sensitivity from 185 nm to 650 nm and an active area of 8 mm diameter.

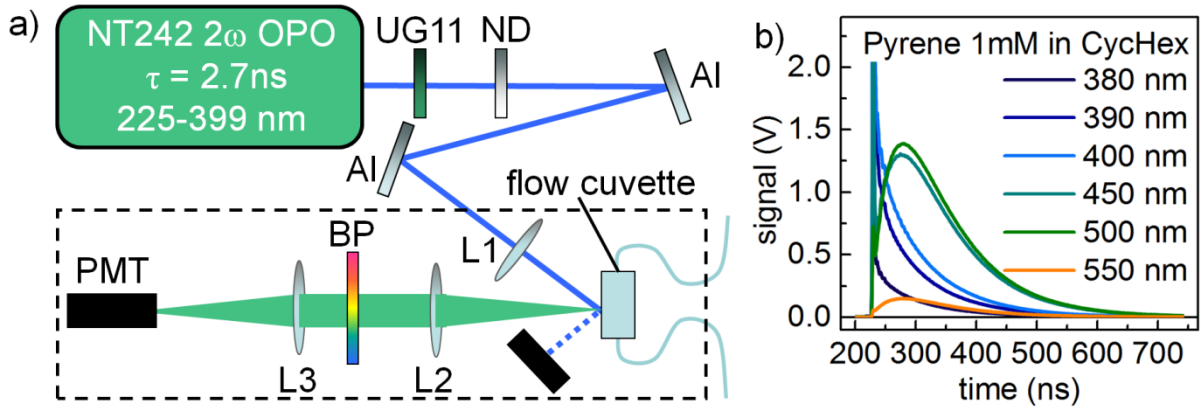

Fig.4.11: (a) Single line time resolved fluorescence setup using EKSPLA NT242 frequency doubled OPO: UG11: Schott UG11 filter to block the OPO fundamental. ND: metallic neutral density attenuator. Al: aluminum mirror. L1, L3: f = 100 mm FS lens, L2: f = 50 mm FS lens. BP: set of different bandpass filters with 10 nm FWHM. PMT: photomultiplier tube. (b) Oscilloscope traces obtained in Pyrene with different BP filters using 65 nJ at 372 nm excitation at room temperature.

The signal from the PMT is read out by an oscilloscope (YOKOGAWA DL9040, 5GS/s, 500MHz). Care is taken to stay in the linear response regime of the PMT by avoiding signals > 3 V. The signal from 2048 consecutive laser shots is averaged and the electronic background signal, originating from the Pockels cell of the EKSPLA OPO's Nd:YAG pump laser, is subtracted. Exponential decays can then be fitted to the traces, yielding fluorescence decay times. For measurements on short time scales the instrumental response function (IRF) must be taken into account. The IRF consists of an asymmetric peak with a width of 2-4 ns for the EKSPLA OPO and a weak, nearly exponential tail decaying with approximately 20 ns.

The target can be a flow cuvette, but samples can also be analyzed directly in the sealed sample container, provided the container is transparent in the respective wavelength range (Fig. 4.12a). Measurements in sealed containers prove useful in cases where the need of reliable degassing outweighs uncertainties due to possible photoproducts. This is especially convenient for quick verification of the degassing process [Bie14]. Measured decay times will increase and saturate when the sample is fully degassed. From the measured pyrene fluorescence lifetime τ an estimate for the oxygen concentration in solution can be calculated using a version of the Stern-Vollmer equation

$$c[O_2] = \frac{1}{k_Q} \cdot \left(\frac{1}{\tau} - \frac{1}{\tau_0} \right). \tag{4.14}$$

τ_0 is the 'intrinsic' fluorescence lifetime of the pyrene monomer and k_Q the quenching rate.

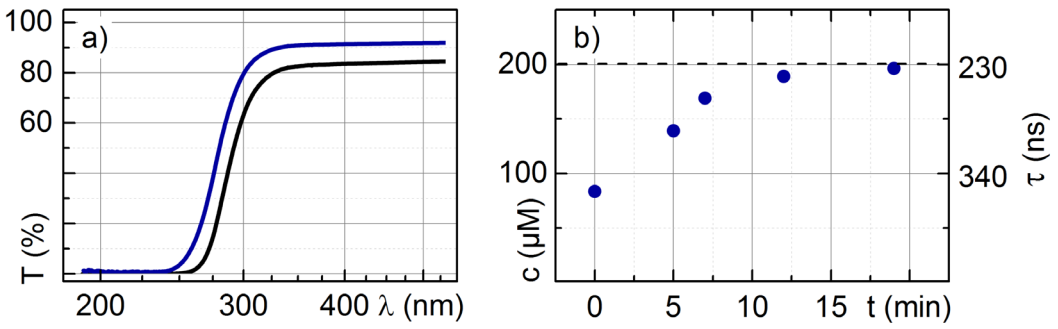

Fig. 4.12: (a) transmission of a 20ml CS Chromatographie Service Boerdelflask (black) and calculated transmission of one side (blue). (b) Regassing: Oxygen concentration in a flow cell with a running circuit vs. time. Right axis: Measured fluorescence lifetime of the pyrene monomer at c = 0.1 mM in cyclohexane.

When the oxygen concentration in the non-degassed solvent is known, oxygen quenching rates can be calculated from equation 4.14 using decay times measured under ambient and fully degassed conditions. Patterson et al. calculate a quenching rate $k_{QS} = 2.5 \cdot 10^{10}\,M^{-1}s^{-1}$ for singlet quenching of pyrene in cyclohexane [Pat70, Mon06]. In pyrene k_Q is one order of magnitude larger than the triplet quenching rate k_{QT} [Pat70, Mon06, Tur10]. Patterson et al. used an oxygen concentration of 2 mM, and values of $\tau = 20\,ns$ and $\tau_0 = 450\,ns$.

However, according to newer data in [Mon06], the oxygen concentration in cyclohexane is 2.4 mM under ambient conditions. Also, longer intrinsic lifetimes of the pyrene monomer have meanwhile been reported, the maximum value found in cyclohexane is $\tau_0 = 650\,ns$ [Del79]. Using these updated values and a lifetime $\tau = 28\,ns$, measured in the setup described above under ambient conditions, Biewald et al. determine a smaller quenching rate of $k_{QS} = (1.4 \pm 0.5) \cdot 10^{10}\,M^{-1}s^{-1}$. In streak camera measurements a lifetime as short as $\tau = 19\,ns$ was obtained without degassing. This leads to a slightly larger oxygen quenching rate of $k_{QS} = 2.0 \cdot 10^{10}\,M^{-1}s^{-1}$. This value is accurately reproduced by a comparison of non-degassed and degassed streak camera measurements presented in Section 4.7.2 (cf. Table 4.11). A probable reason for the slight discrepancy is that for short decay times the setup used in [Bie14] is less reliable than the streak camera. As a consequence, the oxygen concentrations given in [Bie14] are exaggerated and must be multiplied by 0.67. The minimal oxygen concentration reached by bubbling with nitrogen in a sealed container is therefore not 16 µM [Bie14], but 11 µM.

To avoid accumulation of photoproducts [Shi07], transient experiments were carried out using a flow circuit. While a perfectly air-tight flow circuit is hard to realize with reasonable experimental effort, triplet decay times can be reliably and reproducibly increased to up to ca. 6 µs using the following approach. The circuit features double-walled air tight tubing (PTFE-NO-OX; Knauer GmbH) as well as an inline degasser (V7620; Knauer GmbH). To reduce the amount of residual oxygen the pump circuit is flushed with degassed solvent before inserting the sample. The sample is degassed in a sealed container (CS Chromatographie Service, 20ml Boerdelflask 300040) by bubbling with nitrogen for 5 min. After insertion into the flow circuit the sample regasses slightly, but after ~10 min a stable equilibrium is reached at an O_2 concentration of less than 200 µM, less than 10% of the ambient value (cf. Fig. 4.12b). Hence, before every experiment 15 min are allowed for the system to stabilize.

4.3 Pyrene Dynamics Within the First Nanosecond

The following gives an overview over effects that can be observed in pyrene within the first ns. Although pyrene does feature intriguing ultrafast dynamics, the focus of this work lies elsewhere, so sub-ns effects are covered only briefly in order to assess their possible contribution to the excimer dynamics.

The S_1 state of pyrene is only very weakly absorbing (cf. Fig. 4.4a). Therefore in most studies pyrene is excited into the stronger $S_2 \leftarrow S_0$ transition with its maximum absorption at 334 nm [Foe55, Bir63]. After excitation into the S_2 state, pyrene undergoes very effective internal conversion (IC) into the S_1 state within the first 150 ± 50 fs [Fog95, Neu99]. More recent publications report a sub-100 fs IC [Kre13]. IC as fast as 85 fs can be observed in femtosecond TA experiments (cf. Fig. 4.6 a-c, [Kre13a]).

The fast relaxation to the S_1 state is shown in Fig. 4.13. To exemplify that exciting into higher lying states only affects the fast dynamics within the first ps, a sample was excited into the S_3 maximum at 273 nm (Fig. 4.13). The coherent artifact was subtracted as described in chapter 2.5.3. Comparing figures 4.7b and 4.13a, a subtle change of the signal around 600 nm at very early times is observed, likely due to a contribution of the S_3 ESA. Figures 4.13c and d compare transient spectra at pump probe delays of 250 fs (red), 1 ps (violet), and 2 ps (blue) from S_3 and S_2 excitation, as well as a TA spectrum taken from a ns-TA experiment at 5 ns pump probe delay (dashed).

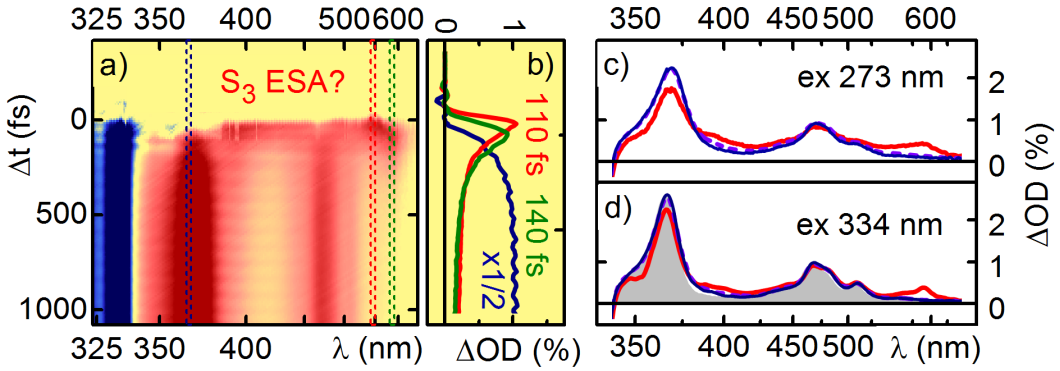

Fig. 4.13: (a) fs-TA data from 1 mM pyrene in cyclohexane, $\lambda_{ex} = 273$ nm. Red (blue) indicates positive (negative) contributions. (b) Selected time traces marked by color coded cursors. Blue trace divided by 2 for comparability. (c) TA Spectra at $\Delta t = 0.25$, 1 and 2 ps (red, violet, blue). (d) same as (c) for $\lambda_{ex} = 334$ nm. Gray: scaled spectrum at $\Delta t = 5$ ns from ns-TA.

The observed spectra at Δt = 1 ps, 2 ps and 5 ns are indeed identical within measurement accuracy, representing the S_1 ESA as previously reported in [Kre13]. An exception is the preparation of 'hot' excited states, i.e. excitation in between absorption maxima. Here, within the first 100 ps band shifts of up to 3 nm are observed. Figure 4.14a illustrates the shift after excitation at 285 nm, the minimum between the S_2 and S_3 absorption bands. Green lines in Fig. 4.14b illustrate that the observed shift becomes less severe when the excitation is moved to 305 nm, closer to the S_2 origin. Note that the latter dataset was taken in methanol, leading to a slightly blue shifted final position. The time dependence of the peak positions can be evaluated by parameterizing the transient spectra using Gaussian functions and performing a fit for each delay. The resulting peak position vs. time is shown in Fig. 4.14c. The 'shifting time' τ_{shift} is determined via an exponential fit to the peak position.

While the unambiguous determination of the origin of the observed shifts would benefit from a more systematic investigation, the excess energy dependence of this blue shift is a strong indication for vibrational cooling. Also, a cooling tim e close to 20 ps has been reported previously in cyclohexane [Hir91]. The relevant conclusion for this work is that irrespective of the excitation wavelength in ns pump probe experiments we expect to see either S_1 signatures or signatures of states the relaxation proceeds to from the S_1 state. The tunable excitation can therefore be utilized to ensure a suitable OD of ~ 0.3 at a given concentration or sample thickness.

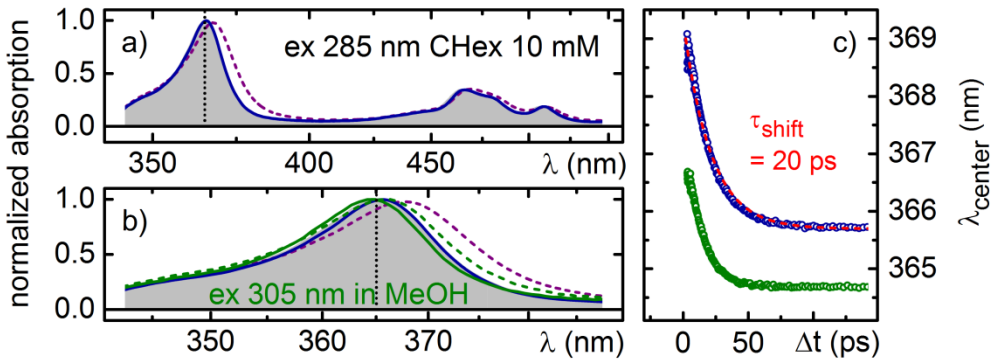

Fig. 4.14: (a) TA Spectra at Δt = 10 and 100 ps (violet, blue) obtained from 10 mM pyrene in cyclohexane at λ_{ex} = 285 nm. Gray: spectrum at Δt = 5 ns from ns-TA. (b) Same as (a), green curves obtained at λ_{ex} = 305 nm in MeOH at c = 1 mM. (c) Fitted peak postitions at λ_{ex} = 285 nm (blue) and λ_{ex} = 305 nm (green) vs. delay time .

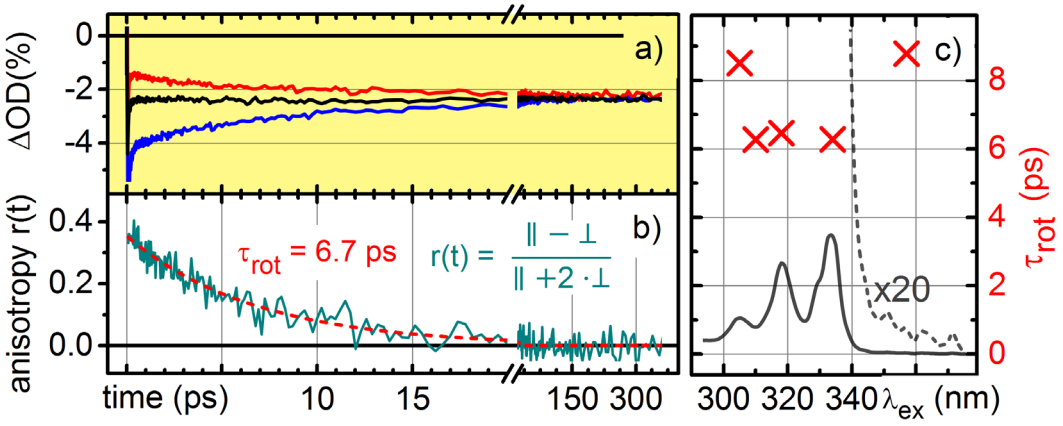

Fig. 4.15: (a) Evolution of the largest GSB band at 334 nm in 1mM pyrene in cyclohexane for parallel (blue), perpendicular (red) and magic angle (black) detection. (b) anisotropy r(t) and exponential fit. (c) Excitation wavelength dependence of τ_{rot} for pyrene in MeOH. Gray lines show pyrene absorption spectrum for orientation.

One last effect worth mentioning here is pyrene's surprisingly fast anisotropy decay. When linearly polarized light is used to excite a molecule in solution, the interaction probability depends on the angle between the molecule's transition moment and the polarization of the pump and probe pulses [Fle76]. Rotational diffusion of the molecules between excitation and interaction with the probe leads to a delay time dependent change of the measured absorption. This is illustrated in Fig. 4.15a. From signals recorded with parallel (∥) and perpendicular (⊥) polarizations of the probe w.r.t the pump, the anisotropy r(t) can be evaluated [Fle76, Kla09]. Generally, for an isotropic sample of initially randomly oriented chromophores, r(t) can take values between 0.4 and -0.2, as $r(t) = 0.2 \cdot \left\langle 3\cos^2(\theta) - 1 \right\rangle \cdot \exp\left[-t/\tau_{rot}\right]$, where $\langle\ \rangle$ denotes an average over all possible orientations of chromophores. θ is the angle between the relevant transition dipole moments for excitation and whatever process is employed for detection [Kla09]. The transition dipole moment for absorption of pump and probe is the same for those probe photons also absorbed by GS molecules. Hence, for the GSB θ = 0 and the expected amplitude of r(t) is 0.4 (cf. Fig. 4.15b). Typical decay times for rotational diffusion range between 9 ps for perylene in methanol up to several hundreds of ps [Kle79]. An overview can be found in [Fle76]. For pyrene, values significantly below 9 ps are obtained both in methanol and cyclohexane (cf. Fig. 4.15c). This indicates that pyrene does not interact significantly with the solvents used, i.e. does not reside in a large solvent shell. This could also be connected to its high solubility in polar and unpolar solvents. When excited state populations are investigated, this effect is usually suppressed by choosing a 'magic angle' of 54.7° between pump and probe polarizations (black line in Fig. 4.15a) [Les76].

4.4 Introduction to the Pyrene's Debated Nanosecond Dynamics

In the 1960s, fluorescence dynamics were most often probed using flash photolysis, where a flash lamp excites the sample and a photomultiplier is used to detect the emitted light vs. time. A combination of bandpass filters was employed to select a portion of the spectrum for detection. Gaining a clear picture of the pyrene dynamics using this technique is difficult for two reasons. First, as Hanlon and Milosavljevic recently pointed out, an appropriate choice of excitation wavelength is crucial since too high an absorbance results in inhomogeneous excitation of the sample volume, which can lead to fraudulent dynamics [Han13]. Many studies either used a broad excitation bandwidth [Foe55, Zac84] or an excitation wavelength well above the S_2 origin. In this work particular attention was paid to excite very close to the origin in all measurements to avoid excess vibrational energy. Second, the streak camera measurements presented below confirm findings by Andriessen et al., indicating a significant overlap of monomer and excimer fluorescence bands down to below 380 nm [And91, And92]. This is a likely cause for double exponential fluorescence decay times observed for the monomer, depending on the detection wavelength [Bir63, Roy11].

In studies on pyrene dimers linked at the 1- or 2- position, complex fitting models using up to four exponential decays attributed to different conformers have been discussed [Zac76, Zac78, Zac84, Zac85, Zac85a, Sie87, Zac88, Sie89, Rey90, Zac91, Win93, Tsu95]. The systematic approach to the functional linking of pyrene units presented here will help categorize linked dimers according to their dynamics and identify compounds with desirable or interesting properties.

Figure 4.16 is adapted from a model shown in [Bir70], illustrating the most commonly assumed relaxation pathways for pyrene. In addition to monomer and excimer fluorescence, several interconnected relaxation pathways are postulated (cf. Table 4.1). Unambiguous assignment of rate constants is therefore not possible from the fluorescence alone, as only net decay rates k_M, k_D and k_T (right column) can be directly accessed. Assumptions about e.g. the role of the triplet state are usually made to obtain a complete picture.

In the following sections, ambiguities in the models are removed by combining spectrally resolved broadband TA and fluorescence decay measurements, directly probing the monomer, excimer and triplet states. The redundancy of information on the decays of the S_1- and excimer states as well as similarities between linked and unlinked compounds aid in the analysis of the debated dynamics.

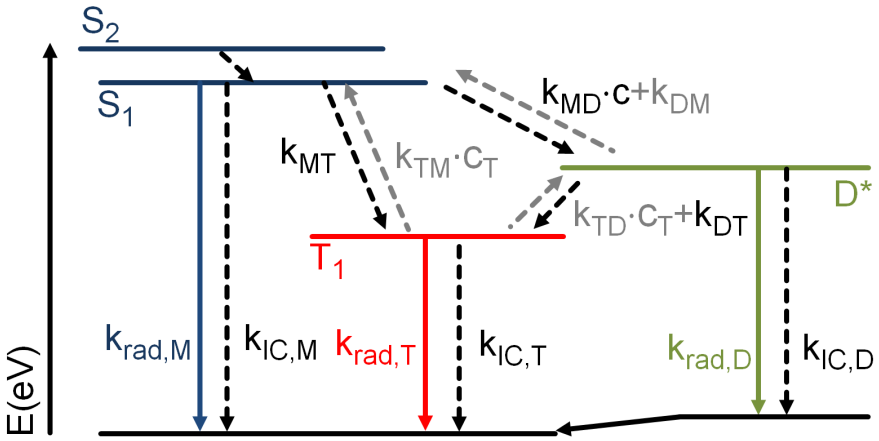

Fig. 4.16: Jablonski diagram adapted from Birks et al., showing possible relaxation pathways in pyrene [Bir70]. Solid arrows indicate radiative transitions, drawn to scale according to TDDFT calculations [Rei15]. S_1, S_2: singlet excited states of the monomer. T_1: triplet excited state of the monomer. D*: excimer.

Table 4.1: Definition of rate constants depicted in Fig. 4.16 and abbreviations used below.

rate	description	net decay rates
$\mathbf{k_{rad,M}}$	monomer fluorescence	
$\mathbf{k_{IC,M}}$	internal conversion of the monomer	} $\mathbf{k_M}$
$\mathbf{k_{MT}}$	intersystem crossing (ISC) of monomer	
$\mathbf{k_{MD}\cdot c}$	excimer formation from monomer	
$\mathbf{k_{rad,D}}$	excimer fluorescence	
$\mathbf{k_{IC,D}}$	internal conversion of the excimer	} $\mathbf{k_D}$
$\mathbf{k_{DT}}$	triplet formation from excimer	
$\mathbf{k_{DM}}$	dissociation of excimer	
$\mathbf{k_{TM}\cdot c_T}$	triplet triplet annihilation (TTA)	
$\mathbf{k_{TD}\cdot c_T}$	excimer formation from triplet	
$\mathbf{k_{rad,T}}$	phosphorescence	
$\mathbf{k_{IC,T}}$	internal conversion of the triplet	} $\mathbf{k_T}$

4.4.1 Approximate Energy Levels

Table 4.2 shows estimates for the energy levels of the states displayed in Fig. 4.16. Even though some values carry considerable errors, it is clear that at room temperature the excimer, stabilized w.r.t. the S_1 state by more than 0.4 eV, is highly unlikely to dissociate. Excimers have been claimed to dissociate back into a singlet excited and a GS pyrene via k_{DM}. Even at room temperature a value of $k_{DM} = 0.65 \cdot 10^7\ s^{-1}$ has been reported [Bir63], comparable to the fluorescence decay rates observed in millimolar solutions. This reversibility has been disputed in more recent publications [Bir70, Del79, Mar87, Mar88, Duh12, Han13]. As all of the following experiments are carried out at room temperature, k_{DM} is assumed to be negligible for the work presented here, unless strong evidence to the contrary presents itself.

Table 4.2: Rough estimates of pyrene energy levels (w.r.t. the monomer S_0 state) according to [Bir70], TDDFT calculations [Rei15] and observations of absorption and fluorescence band positions.

Source:	**Bir70 (pp. 303,357)**		**TDDFT calculation[a]**		**absorption**	
State	**E (eV)**	**λ (nm)**	**E (eV)**	**λ (nm)**	**E (eV)**	**λ (nm)**
S_2	3.65	341	3.91	317	3.72	334
S_1	3.33	372	3.64	341	3.37	368
D*	2.92	425	2.58	481	2.64[c]	470
T_1	2.08	594	2.03	612	2.08[b]	594

[a] courtesy Matthias Roos and Sebastian Reiter [Rei15]. [b] [Zan78]. [c] from fluorescence.

4.4.2 Diffusion Controlled Processes

Some of the rates in Fig. 4.16 are concentration dependent second order rate constants. The formation of the excimer D* relies on diffusional encounter of an excited and a GS pyrene, described by k_{MD}. k_{TM} and k_{DT} represent the recovery of one singlet excited molecule or an excimer by triplet triplet annihilation (TTA). This depends on the concentration of excited triplets c_T. TTA gives rise to pyrene's delayed fluorescence, dubbed 'p-type' delayed fluorescence [Bir70, Bir75, Kla09]. Second order rate constants, given in $L\ s^{-1}mol^{-1}$, need to be multiplied by a concentration to obtain a rate parameter in s^{-1}, as indicated in Fig. 4.16.

A common way of modeling diffusion is combining Fick's law of diffusion with the Einstein-Smoluchowski relation. The diffusion coefficient is defined as

$$D = \frac{k_B \cdot T}{6\pi \cdot \eta \cdot r}, \tag{4.15}$$

where k_B denotes Boltzmann's constant, T the temperature in K, η the dynamic viscosity of the solvent and r the particle's Stokes radius. The theory is based on the assumptions that a spherically symmetric concentration gradient around an excited (spherical) particle is set up, and that the rate of flow of particles in this concentration gradient is governed by Fick's law of diffusion [Smo17, Col49]. The theory is constantly being improved, useful reviews can be found in [Ric85, Bur04]. Most commonly the approximate relation for the diffusional quenching rate

$$k_{diff}(t) = 4\pi \cdot R \cdot p \cdot D' \cdot \left(1 + \frac{p \cdot R}{\sqrt{\pi D' t}}\right) \tag{4.16}$$

is used, with R the sum of the stokes radii of the interacting partners, and D' the sum of their diffusion coefficients. p is a factor for the interaction probability upon encounter. While Birks et al. report an efficiency p = 1 for the pyrene excimer formation [Bir63, Bir70], a more recent publications claims p = 0.4 [Han13]. This will be reviewed in Section 4.6. Equation 4.16 can be understood as a limiting rate $k_{diff,lim}$ plus a time dependent variation proportional to $\sqrt{t}$. The approximated rate therefore features a pole at $t = 0$ and asymptotically approaches $k_{diff,lim}$ for large t. A second time dependence of the rate ensues when the quencher is not present in excess and hence its concentration is significantly altered by the reaction. Whenever the rate parameter for a process is not constant, the differential equations describing the system can no longer be solved by simple exponential decays. The solutions of such systems are often approximated by stretched exponentials, however exact solutions are best obtained numerically [Mar87].

For the excimer formation in pyrene, pyrene itself is the quencher and in experiments where the number of excited molecules is at the per cent level, the concentration of the quencher can be regarded as constant. Birks et al. repeatedly claim that the time dependent term in 4.16, also called the 'transient contribution', is 'normally on the order of unity' [Bir 63, Bir70, Han13].

When all time dependencies can be neglected, the situation is commonly referred to as 'pseudo first order conditions'. The dynamics then follow classical rate equations and can be accurately described by a sum of exponential decays. The rate constants describing the diffusive process increase linearly with the concentration (cf. Section 4.6).

The following example will examine this for the case relevant to pyrene. For pyrene in cyclohexane at T = 295 K, assuming r = 8.9 Å (average of long and short axis) and a dynamic viscosity of $\eta = 0.941 \cdot 10^{-3}\,\mathrm{kg \cdot m^{-1}s^{-1}}$ (Dortmund Databank, ddbst.com), the diffusion coefficient is D = 25.8 Å²/ns and $k_{diff,lim} = 6.95 \cdot 10^{9}\,\mathrm{M^{-1}s^{-1}}$. Note that this is one order of magnitude slower than the singlet quenching constant of solvated oxygen, explaining the considerable enhancement of the excimer fluorescence upon O_2 removal (cf. Section 4.2.5).

Fig. 4.17 shows quenching rates k(t) calculated via equation 4.16 including the transient term for selected concentrations next to simulated fluorescence decay curves. The rate model used to obtain the fluorescence decays will be discussed in detail later in this chapter. Fig. 4.17b indicates that at early times the decay of the monomer as well as the excimer growth are significantly accelerated when the transient contribution is included. For all concentrations it takes 195 ns for $k_{diff}(t)$ to stabilize to within 10% of $k_{diff,lim}$. Thus, it is questionable whether the time evolution of the rate of diffusion can be ignored.

The rate constant for TTA can be estimated via the above formalism. In contrast to the excimer that forms upon collision with any GS pyrene, a triplet excited molecule must collide with a triplet excited partner for TTA to occur. Assuming a typical 1% of molecules to be excited and a triplet quantum yield of 60% at c = 10mM, the rate of interaction is $k_{TM} = k_{diff,lim} \cdot 10\mathrm{mM} \cdot 0.01 \cdot 0.6 = 4.17 \cdot 10^{5}\,\mathrm{s^{-1}}$, which corresponds to rise times of several µs. Even in streak camera experiments on the µs timescale, no significant fluorescence is detected at room temperature. Therefore TTA processes are not relevant on the ns timescale and both k_{TM} and k_{TD} can be neglected here.

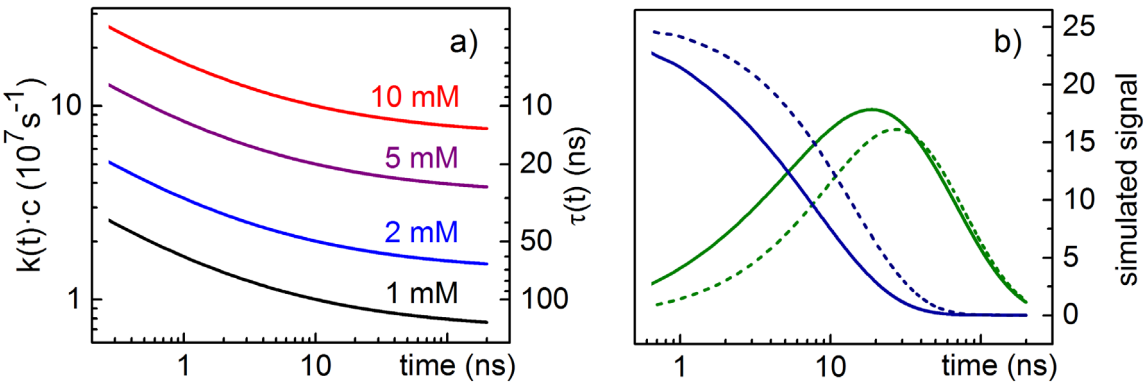

Fig. 4.17: (a) Calculated diffusional quenching rate for pyrene in cyclohexane: r = 8.9 Å, $\eta = 0.941 \cdot 10^{-3}\,\mathrm{kg \cdot m^{-1}s^{-1}}$, D = 25.8 Å²/ns, $k_{diff,lim} = 6.951 \cdot 10^{9}\,\mathrm{M^{-1}s^{-1}}$ (b) Simulated monomer (blue) and excimer (green) fluorescence signals with (solid) and without (dashed) transient term for c = 10mM.

4.5 Single Line Fluorescence Decay Analysis Facing Overlapping Bands and Photoproducts

The single line time resolved fluorescence setup described in Section 4.2.5 not only allows monitoring the degassing process, but can also serve to elucidate challenges faced by single wavelength fluorescence experiments, which are still an important source of information today [Han13]. Using the EKSPLA ns-OPO as a light source, the excitation wavelength can easily be tuned. 10 nm FWHM bandpass filters are used: '500 nm' and '550 nm' probe the excimer fluorescence, '380 nm' and '390 nm' are employed in an effort to single out the 'monomer region'. Fluorescence decays recorded by the photomultiplier are fitted using a sum of two exponentials (cf. Fig. 4.18).

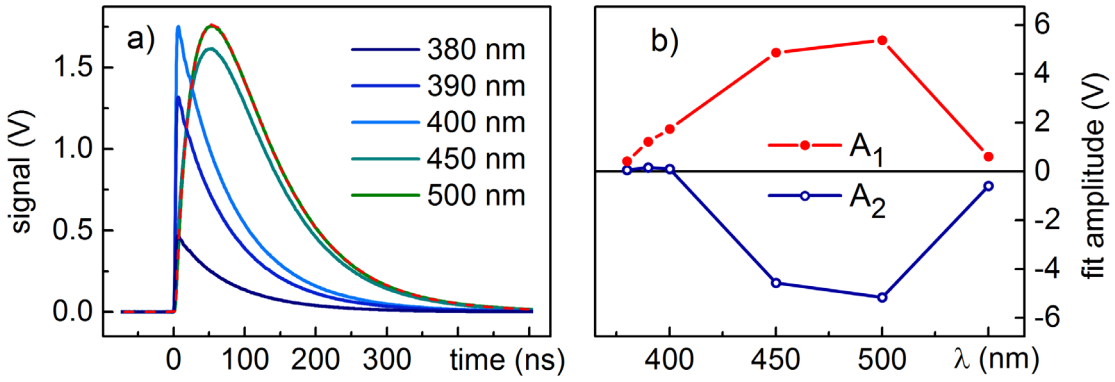

Fig.4.18: (a) Fluorescence traces from 1 mM pyrene in cyclohexane using λ_{ex} = 334 nm and E_{pump} = 230 nJ with double exponential fit (red dashes). (b) Fit amplitudes.

Table 4.3: Single line fluorescence decay analysis of 1 mM pyrene in cyclohexane.

	λ_{ex} = 334 nm 230 nJ					**λ_{ex} = 372 nm 1245 nJ**				
λ_{det} (nm)	**τ_1 (ns)**	**τ_2 (ns)**	**A_1 (mV)**	**A_2 (mV)**	**A_1/A_2**	**τ_1 (ns)**	**τ_2 (ns)**	**A_1 (mV)**	**A_2 (mV)**	**A_1/A_2**
380	35	82	62	427	0.14	10	81	245	331	0.74
390	33	83	161	1224	0.13	9	79	975	965	0.99
400	35	82	95	1745	0.05	6	79	1376	1182	-0.86
450	34	85	-4561	4868	-0.94	36	85	-3347	3827	-0.88
500	34	85	-5156	5367	-0.96	36	84	-4140	4403	-0.94
550	34	84	-596	609	-0.98	36	83	-444	473	-0.94

The fitted decay times and their corresponding amplitudes are summarized in Table 4.3. For excitation into the S_2 maximum at 334 nm, the resulting decay times show the excimer fluorescence rising with 34 ns and subsequently decaying with 85 ns. A_1/A_2 ratios close to unity in the excimer region indicate that there is no sudden step in the excimer's fluorescence. Instead it grows from and decays back to zero. Preassociated dimers would cause a step-like increase [Rey90, And91, And92], this is not evident from the data. Both decay times are also found in the monomer fluorescence. Note that even at the bluest detection wavelength the 35 ns decay contributes more than 10% to the fitted amplitude, (cf. Table 4.3).

With feedback processes via k_{DM}, k_{TM} and k_{TD} ruled out, according to the model in Fig. 4.16 the monomer is expected to decay monoexponentially with a sum of rates

$$k_M(c) = \frac{1}{\tau_2(c)} = k_{rad,M} + k_{IC,M} + k_{MT} + k_{MD} \cdot c \,. \tag{4.17}$$

Birks et al. were first to offer a model for the excimer formation dynamics [Bir63, Bir70]. They include a reversibility of the excimer formation $k_{DM} \neq 0$, leading to double exponentials with concentration dependent decay times and amplitudes. Many following reports on pyrene and pyrene derivatives base their analysis on variations of this model [Zac84, Zac85, Zac85a, Mar87, Win93, Han13]. However, at room temperature a reversibility is unlikely due to the large stabilization of the excimer (cf. Section 4.4.1). When $k_{DM} = 0$, Birks' model predicts single exponential monomer decays for all concentrations [Bir63].

Other possible reasons for deviations from a monoexponential decay are inhomogeneous excitation of the sample volume or transient effects caused by diffusion neglected by Birks et al. [Mar87, Han13]. When pyrene units are linked, attached to larger molecules or in pyrene crystals, different conformers of the excimer were suggested to cause multiexponential fluorescence decays [Zac84, Zac85, Zac85a, Sie87, Zac88, Sie89, Zac91, Win93]. Simpler explanations, that seem to have been overlooked, are a nonzero overlap between monomer and excimer fluorescence bands as well as chemical impurities. These will be explored below.

4.5.1 Overlapping Fluorescence Bands

It has been pointed out before that there is in fact some overlap between monomer and excimer fluorescence to below 380 nm [And91, And92], but it appears the consequences of this overlap have not been seriously considered. A simulation was conducted to investigate the effects of overlapping excimer contributions on a single exponential 'monomer' trace.

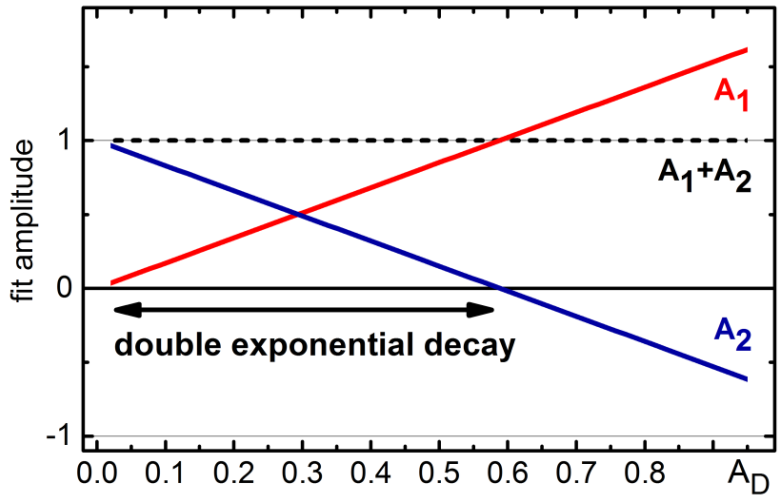

Fig. 4.19: Amplitudes obtained by double exponential fit to calculated fluorescence traces $F(t)$ for increasing excimer amplitude A_D and $A_M = 1$. Dashed line: A_1+A_2.

At a given concentration the excimer population at $[D^*](t)$ obeys the relation

$$[D^*](t) = [S_1^*](t=0) \cdot \frac{k_M(c)}{k_M(c) - k_D} \left(\exp[-k_D \cdot t] - \exp[-k_M(c) \cdot t] \right). \qquad (4.18)$$

Here $[S_1](t = 0)$ is the initial excited state concentration of the monomer and $k_D = k_{DG} + k_{FD} + k_{DT}$ is the sum of all decay channels for the excimer. Equation 4.18 holds for any intermediate in a sequential reaction $X \rightarrow Y \rightarrow Z$ and represents an analytical solution to Birks' model in the case $k_{DM} = 0$ [Kla09, Bir63]. The observed growth of the signal always follows the faster rate. For $k_M(c) > k_D$ the behavior is intuitive. When the excimer formation is slower than it's decay ($k_M(c) < k_D$) the denominator changes sign. This sign change is compensated by an exchange of the two exponentials in the brackets, leading to an all positive signal that grows with the excimers' decay rate. This is the reason why for low concentrations the excimer signal grows faster than the S_1-state decays.

The fluorescence signal at a given detection wavelength can be modeled as a superposition of such a trace $[D^*](t)$ and a monoexponential excimer decay

$$F(t) = A_1 \cdot [S_1](t=0) \exp[-k_M(c) \cdot t] + A_2 \cdot [D^*](t), \qquad (4.19)$$

with scaling factors A_M and A_D. Setting $[S_1](t = 0) = 1$ and rearranging yields

$$F(t) = \left(A_M - A_D \frac{k_M(c)}{k_M(c) - k_{MD}} \right) \exp[-k_M(c) \cdot t] + A_D \frac{k_M(c)}{k_M(c) - k_{MD}} \exp[-k_D \cdot t], \qquad (4.20)$$

a double exponential with a net amplitude A_M. Figure 4.19 illustrates amplitudes of double exponential fits to $F(t)$ for increasing excimer amplitude A_D and $A_M = 1$.

Rates $k_M = 1/85\,ns$, and $k_{MD} = 1/35\,ns$ were chosen to resemble the measured values. While the rates obtained from the fit reproduce the input values exactly, amplitudes A_1 and A_2 are significantly affected by the growing excimer contribution. For $A_2 > 0.6$, a rise and a decay are observed as is intuitively expected for the sum of a monomer and an excimer trace (cf. Fig. 4.19). However, when the excimer contribution becomes small, the fit results in two positive amplitudes (red arrow), just as observed in the experiment for 390 nm and 380 nm detection. A similar observation was made in [And91]. The simulation also accurately predicts the growth of A_2 towards smaller fractions (i.e. wavelengths). A truly monoexponential decay is only observed at $A_2 = 0$ and $A_2 = 0.6$.

It follows that even minute contributions from the excimer band may well be responsible for the double exponential decays observed. One must either select the detection wavelength very carefully, which requires the appropriate optical filters, or detect at several wavelengths and analyze the evolution of these fit parameters. The best choice is, of course, broadband detection, as presented in the Section 4.6.

4.5.2 Impurities Due to Photodegradation

Shifting the excitation into the S_1 region (372 nm) reveals an anomaly. While the green excimer fluorescence shows the same dynamics as before, in the monomer region a sub 10 ns decay time (red) is found to contribute more than 70% of the fitted amplitude (cf. Table 4.3, right). An excitation scan reveals discrepancies between the samples absorption (black dashes) and excitation spectrum, pointing to an impurity in the sample (cf. Fig. 4.20a). The fitted decay times remain constant across the entire range evaluated and the amplitude A_2 (blue crosses), corresponding to the ~84 ns decay, reproduces pyrene's S_1 absorption spectrum (dashed line) quite nicely. However, A_1 (blue circles), shows significant differences, especially around 370 nm.

It follows that even though the purest available pyrene sample was used (Sigma-Aldrich FLUKA TraceCERT®, 99.2 ± 0.2%), fluorescence reveals a short lived impurity, likely due to a photoproduct caused by prolonged exposure to the excitation source or ambient light in the laboratory. This is despite the fact that sample containers were wrapped in aluminum foil and kept in the dark when not in use, in order to minimize exposure. Even after purification by collaborators in the chemistry department, the purity was found to quickly deteriorate again, as can be seen in Fig. 4.20b [Lan13]. Such short decay times were also found in [Zac84, Zac85, Zac88].

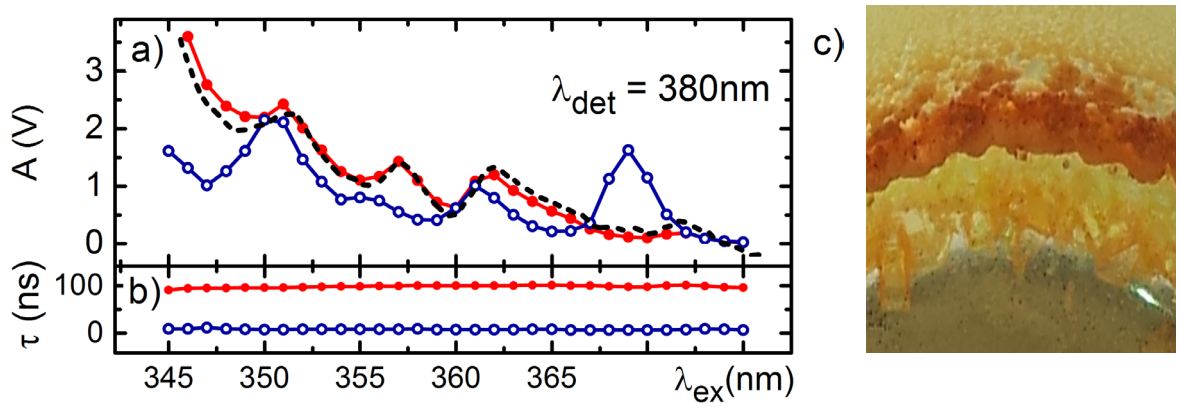

Fig. 4.20: Excitation scan at c = 1 mM and λ_{det} = 380 nm. (a) fitted A_1 (red) and A_2 (blue). Dashed line: scaled pyrene absorption spectrum. (b) τ_1 (red) and τ_2 (blue). (c) Condensed pyrene (bottom) & impurity (top) in a glass beaker, analyzed 24 h after purification.

As it proves very hard to keep pyrene samples pure, the best approach is to quantify how strongly measurement results are affected by the photoproducts. A photoreaction causes a time dependent change in solute concentration $[Py](t_h)$, the index h signifies that these reactions typically proceed on a timescale of minutes or hours. Typical streak camera or TA measurements take up to 1 hour.

$$\frac{d}{dt}[Py](t_h) = -[Py]_0 \cdot \frac{N_{Ph}}{N} \cdot \nu_{Laser} \cdot A_{Py}(t_h) \cdot \Phi_q, \tag{4.21}$$

with

$$A_{Py}(t_h) = 1 - 10^{-\varepsilon(\lambda_{ex}) \cdot [Py](t_h) \cdot d}. \tag{4.22}$$

Here, $N_{Ph} = E_{Pump} \cdot \lambda_{ex} / h \cdot c$ the number of photons per exciting pulse, $\nu_{laser} = 1\,kHz$ is the pump repetition rate. $N = V \cdot N_A \cdot [Py]_0$ is the total number of molecules in the illuminated sample volume V. It is assumed that the entire sample volume is illuminated uniformly - the sample is exchanged effectively between laser shots by stirring or pumping. The conversion efficiency is given by the sample's steady state absorption A_{Py} and the quantum yield of the photoreaction Φ_q. This assumes that there is only one photoproduct, which does not absorb significantly at λ_{ex}. Further assuming that the OD at the pump wavelength is not significantly lowered by the photoreaction ($A_{Py}(t_h) \approx$ const.), a linear approximation is sufficient to describe $[Py](t_h)$.

In an experiment with well-defined illumination the only unknown is the reaction quantum yield Φ_q. It can be obtained from a fit to the measured change in sample absorption.

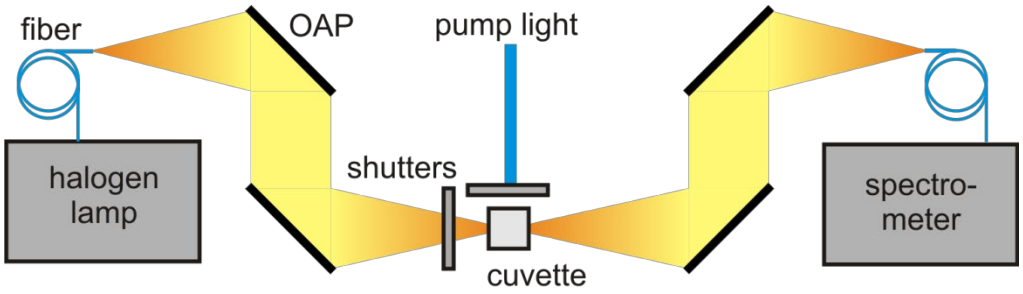

Fig. 4.21: Illumination setup [Ric14]. OAP: aluminum coated off-axis parabolic mirror.

Table 4.4: Irradiation of Pyrene in DCM: selected concentrations and excitation parameters.

c_0 (mM)	0.01			1.38
V (mL)	3.6			1.8
λ_{ex} (nm)	337			355
E_{Pump} (µJ)	14			88
duration (h)	1			1.3
fitted λ (nm)	273	313	337	337
fitted Φ_q ($\cdot 10^{-3}$)	1.43	1.31	1.47	1.6
Φ_q (averaged)	$(1.5 \pm 0.2) * 10^{-3}$			

An ideally suited experimental setup is shown in Fig 4.21 [Ric14]. The output of a fiber coupled broadband halogen lamp (DH-2000 BAL, Ocean Optics GmbH, 215 nm– 2000 nm) is imaged into the 10 mm sample cuvette via two off-axis parabolas (OAP). Two further OAPs couple the transmitted light into the fiber of a micro spectrometer (USB2000, Ocean Optics GmbH, 200 nm– 850 nm), which is read out at selected time intervals. The sample is illuminated by, e.g., a tunable ns OPO (EKSPLA NT 242).The sample is constantly stirred via a magnetic rotor. Two automated shutters are used to block the probe during illumination and the pump while the transmission is recorded.

Figure 4.22 illustrates that pyrene as well as 1-methylpyrene do exhibit photodegradation when exposed over extended time periods. Parameters used in this illumination study are shown in Table 4.4. Φ_q is determined via a linear fit at selected wavelengths for two vastly different concentrations and pump powers, yielding comparable results. Averaging the results, in methanol and dichloromethane (DCM) $\Phi_q = (3.2 \pm 0.6) \cdot 10^{-4}$ and $\Phi_q = (1.5 \pm 0.2) \cdot 10^{-3}$ are obtained, respectively. $\Phi_q = 1.8 \cdot 10^{-3}$ is reported for pyrene in DCM [Kub00, Shi07].

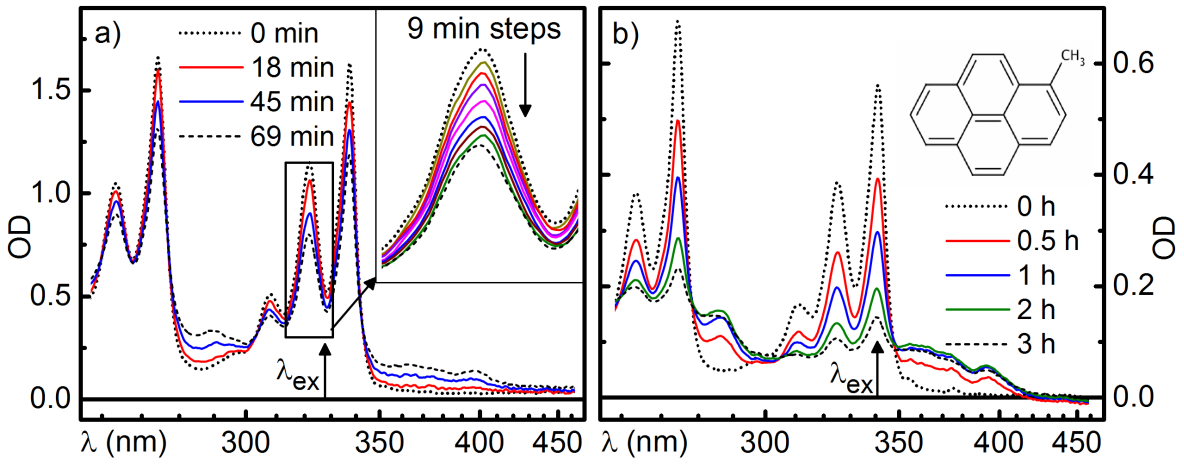

Fig. 4.22: (a) Illumination of pyrene in DCM at c = 0.04 mM, V = 3.6 mL, $\lambda_{ex} = 328\,\text{nm}$. $E_{pump} = 14.3\,\mu\text{J}$, t = 1.1 h. (b) 1-Methylpyrene in MeOH. c = 0.013 mM, V = 3.2 mL, $\lambda_{ex} = 341\,\text{nm}$, $E_{pump} = 11\,\mu\text{J}$, t_h = 3 h [Ric14].

Table 4.5: Calculated fraction of photodegraded sample after $t_h = 2\,\text{h}$, $V = 3.5\text{ml}$, d = 1 mm, $\Phi = 2 \cdot 10^{-3}$, $\varepsilon = 38000\,\text{L mol}^{-1}\,\text{cm}^{-1}$, $\lambda_{ex} = 334\,\text{nm}$, $E_{pump} = 1.5\,\mu\text{J}$.

c_0 (mM)	0.1	1	2	5	10
conversion (%)	10.0	1.7	0.9	0.3	0.2

Pyrene derivatives exhibit similar yields. Resulting values for methyl- and bromopyrene in methanol are $\Phi_q = (4.1 \pm 0.5) \cdot 10^{-4}$ and $\Phi_q = (2.5 \pm 0.3) \cdot 10^{-4}$.

Upper limts for the conversion in a typical transient measurement can now be predicted by pessimistically assuming a quantum yield of $\Phi = 2 \cdot 10^{-3}$, a measurement duration of two hours and excitation into the pyrene S_2 maximum with $\varepsilon = 38000\,\text{L mol}^{-1}\,\text{cm}^{-1}$, using a high pump energy of 1.5µJ at $\lambda = 334$ nm. Table 4.5 shows computed conversion ratios $[\text{Py}](2\text{h})/[\text{Py}]_0$ for a typical sample thickness of d = 1 mm.

The conclusion is that while for millimolar concentrations the obtained values are at or below the per cent level, photodegradation becomes quite significant at low concentrations. Photoproducts are even more likely for the high photon fluxes used in flash photolysis studies. Also, in fluorescence even tiny concentrations of a highly fluorescent product can contribute significantly to the measured dynamics. This can be circumvented by, e.g. significantly increasing the sample volume or, decreasing the pump power used.

4.6 Broadband Fluorescence Analysis: A More Complete Picture

Broadband fluorescence decay measurements allow separation of overlapping fluorescence signatures. Streak camera measurements were performed with streaking windows from 5 ns to 2 µs. For this measurement series 0.01 mM to 10 mM solutions of pyrene in cyclohexane were prepared in a sealed 1 cm cuvette containing a magnetic stir bar and degassed by 5 cycles of freeze pump thaw using a 10^{-5} mbar vacuum. A typical streak dataset at c = 10 mM is illustrated in Fig. 4.23.

Initially, a direct analysis of selected band integrals is performed. A typical streak dataset at c =10 mM is displayed Figure 4.23b. To avoid the region of possible spectral overlap, a spectral interval from 350 nm to 400 nm (60 pixels) is averaged to analyze the monomer dynamics (bright blue cursor). The range from 450 nm to 540 nm (100 pixels) is chosen for the excimer (bright green cursor). Figure 4.23c shows band integrals for selected concentrations, probed in the 500 ns streaking window. The IRF is obtained from scattered pump light detected by the streak camera (black). In the 500 ns streaking window, the IRF has a 8 ns FWHM width.

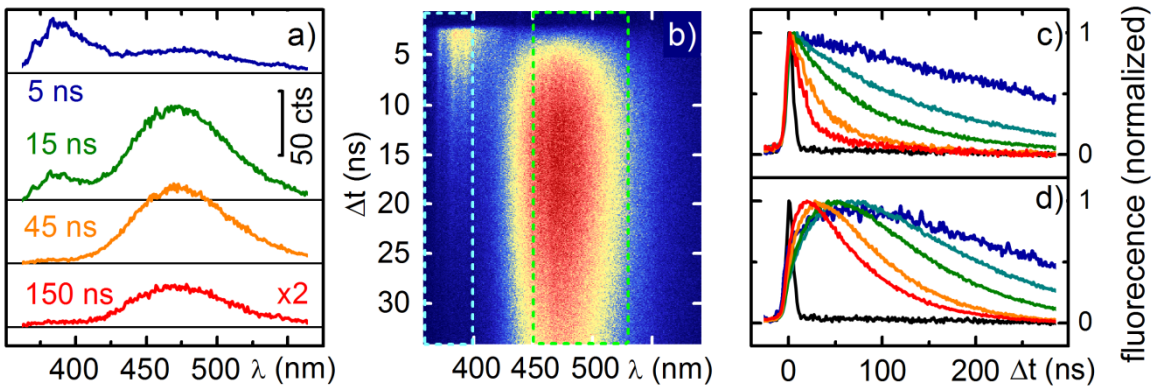

Fig. 4.23: Streak data from pyrene in cyclohexane at c = 10 mM: (a) fluorescence spectra at selected delays averaged over 20 samples. (b) typical dataset in false color representation. Cursors indicate selected monomer (blue) and excimer (green) band integrals. (c) IRF (black) and normalized monomer band integrals, at c = 0.01 mM (blue), 0.1 mM (dark cyan), 1 mM (green), 2 mM (yellow) and 10 mM (red). (d) same as (c) for excimer band integral.

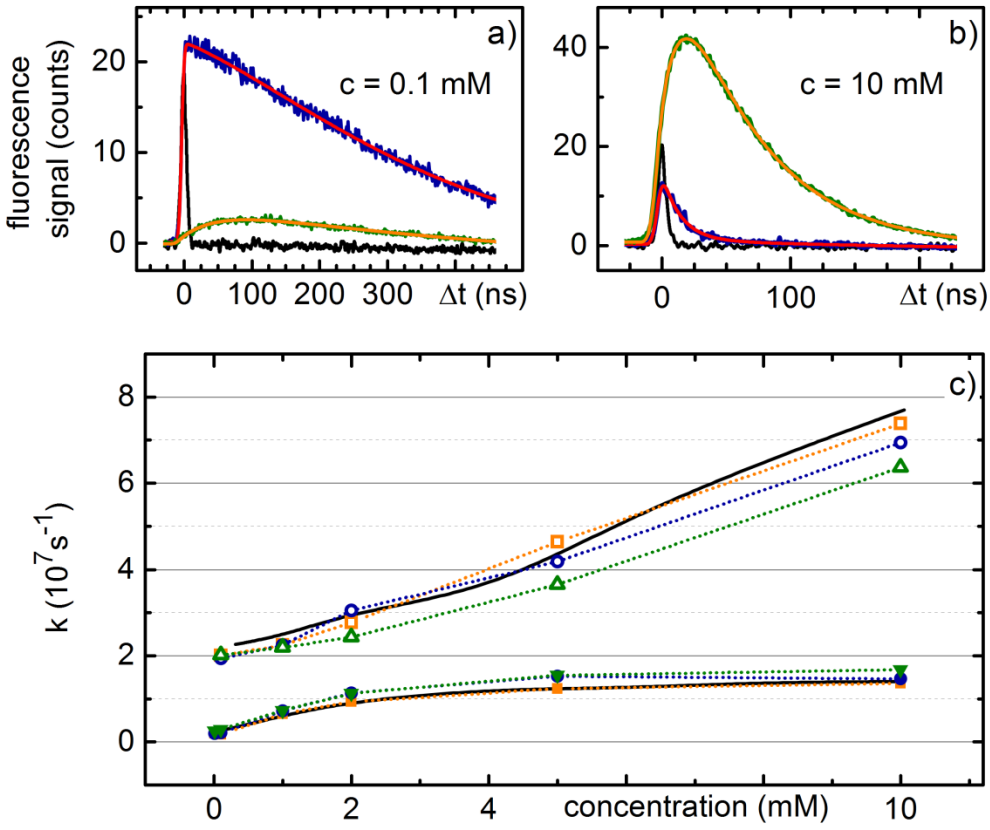

Fig. 4.24: (a,b) biexponential fits to monomer (blue) and excimer (green) fluorescence band integrals. (c) Results from monomer band (circles), excimer (triangles) and global analysis (squares), compared to results from Birks et. al. at 293 K (black lines).

In Fig. 4.24a and 4.24b fits of the selected band integrals are displayed. First, excimer traces are fitted using the difference of two exponentials, then the obtained decay times are used as starting values to fit the monomer trace.

Figure 4.24c shows rate constants resulting from the monomer (circles) and excimer (triangles) band integrals vs. concentration. Similar rates are obtained from a global analysis (GA) of the entire streak dataset using two exponential decays (squares). For reference, results reported by Birks et al. are shown as black lines [Bir63]. Irrespective of the analysis scheme, the results are similar to those reported in [Bir63]. Double exponential decays are found at all concentrations except for the monomer band integral at 0.01 mM.

From a rate model without feedback from the excimer ($k_{DM} = 0$ in Fig. 4.16), one concentration independent excimer decay rate $k_D = k_{rad,D} + k_{IC,D} + k_{DT}$ and one monomer decay rate linear in c $k_M(c) = k_{rad,M} + k_{IC,M} + k_{MT} + k_{MD} \cdot c$ are expected [Bir63]. While none of these properties are evident in Fig. 4.24, the following will present evidence that this is the consequence of band overlap and a transient contribution due to diffusion.

4.6.1 Decomposition of Overlapping Contributions via Spectral Analysis

Global analysis allows the reconstruction of species associated emission spectra. At c = 10 mM, where the excimer fluorescence is most distinct, the obtained spectra clearly indicate a significant overlap of the fluorescence bands down to below 375 nm (cf. Fig. 4.25), even further than reported in [And91, And92]. At 380 nm the excimer contribution still amounts to up to 25% of the monomer's amplitude.

The fact that the excimer fluorescence reaches far into the blue does not necessarily imply that the excimers excited state potential minimum is close in energy to the excited monomer's (cf. Section 4.1.2). Instead, the weak blue fluorescence tail can be interpreted as fluorescence from 'hot' excimers, where pyrene units were not able to fully optimize the overlap of their π-systems before the fluorescence occurred. Theory predicts several possible more or less stable configurations, so when pyrene units collide there may well be contributions from less stabilized collision complexes (cf. Section 4.1.2., Fig. 4.3c). While this fluorescence tail disturbs the observed time evolution, it amounts to less than 10% of the excimer's total fluorescence amplitude (cf. Fig. 4.25a). Assuming hot excimers have a fluorescence quantum yield $\Phi_D = 0.75$ comparable to regular excimers [Bir63], the fraction of 'hot excimers' is small and no significant recovery of singlet excited monomers is to be expected at room temperature. The confirmed band overlap indicates that double exponential decays observed in past studies have likely been caused by a small but significant fluorescence band overlap (cf. Section 4.5.1) [Bir63, Bir70, Han13].

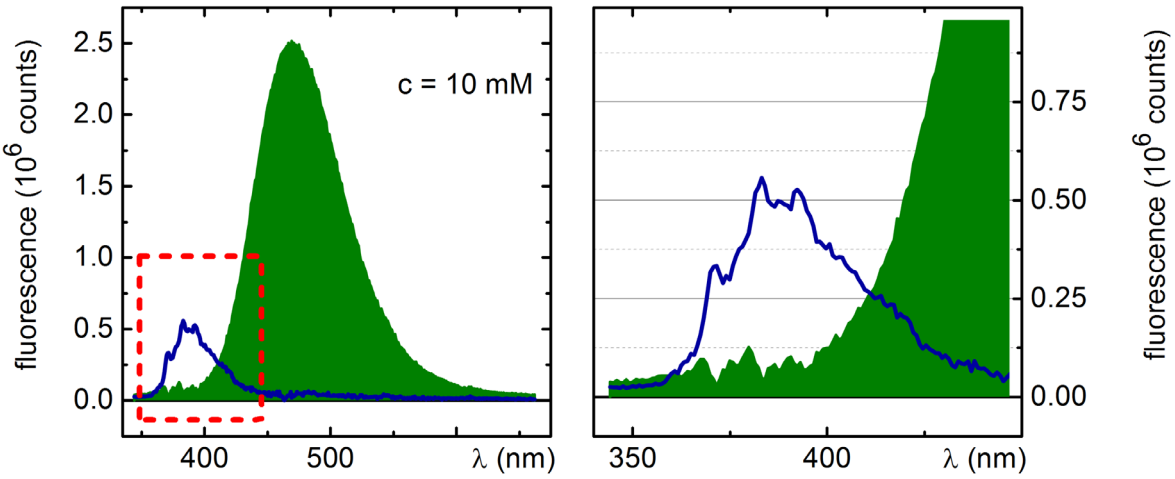

Fig. 4.25: Species associated spectra for pyrene monomer (blue) and excimer (green) from global analysis using two exponentials.

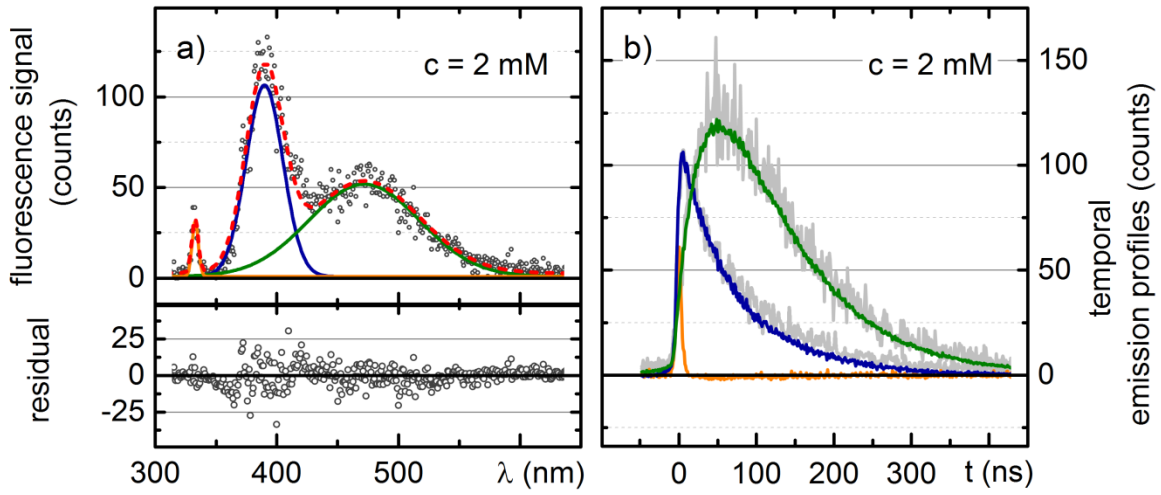

Fig. 4.26: (a) fit of the transient spectrum (grey circles) at $\Delta t = 50$ ns using three Gaussians and residual (bottom). (b) resulting time traces of individual contributions compared to raw signals at $\lambda = 390$ nm and 470 nm (gray).

To disentangle dynamics of overlapping fluorescence bands, the broadband nature of the datasets is exploited. Instead of fitting single lines or averaging over wavelength intervals, a fit is performed in the spectral domain. parameterizing the spectra using a sum of Gaussians functions. While many global analysis techniques assume first order kinetics, no assumption regarding the dynamics must be made a priori. This parameterization can also handle shifting and reshaping bands, known to cause artifacts in common global analysis algorithms.

Fig. 4.26a shows an example of a spectral decomposition for c = 2 mM using three Gaussians. One Gaussian is used to model the excitation stray light (orange), the other two parameterize the monomer and excimer fluorescence bands. Initially, band positions and widths are assigned to best fit a selected transient spectrum, where all contributions are well pronounced. The assigned central wavelengths of monomer and excimer bands are 390 nm and 472 nm with respective widths of 33 nm and 90 nm FWHM. Assuming that on the ns timescale processes resulting in significant band shifts and reshaping are irrelevant, these parameters are then kept fixed as the transient fluorescence spectra for each delay time are fitted by varying the amplitudes of the three Gaussians independently. Figure 4.26b shows resulting time traces for the monomer (blue) and excimer fluorescence bands (green). The spectrally decomposed temporal profiles differ slightly from raw fluorescence traces at $\lambda = 390$ nm and 470 nm shown in gray.

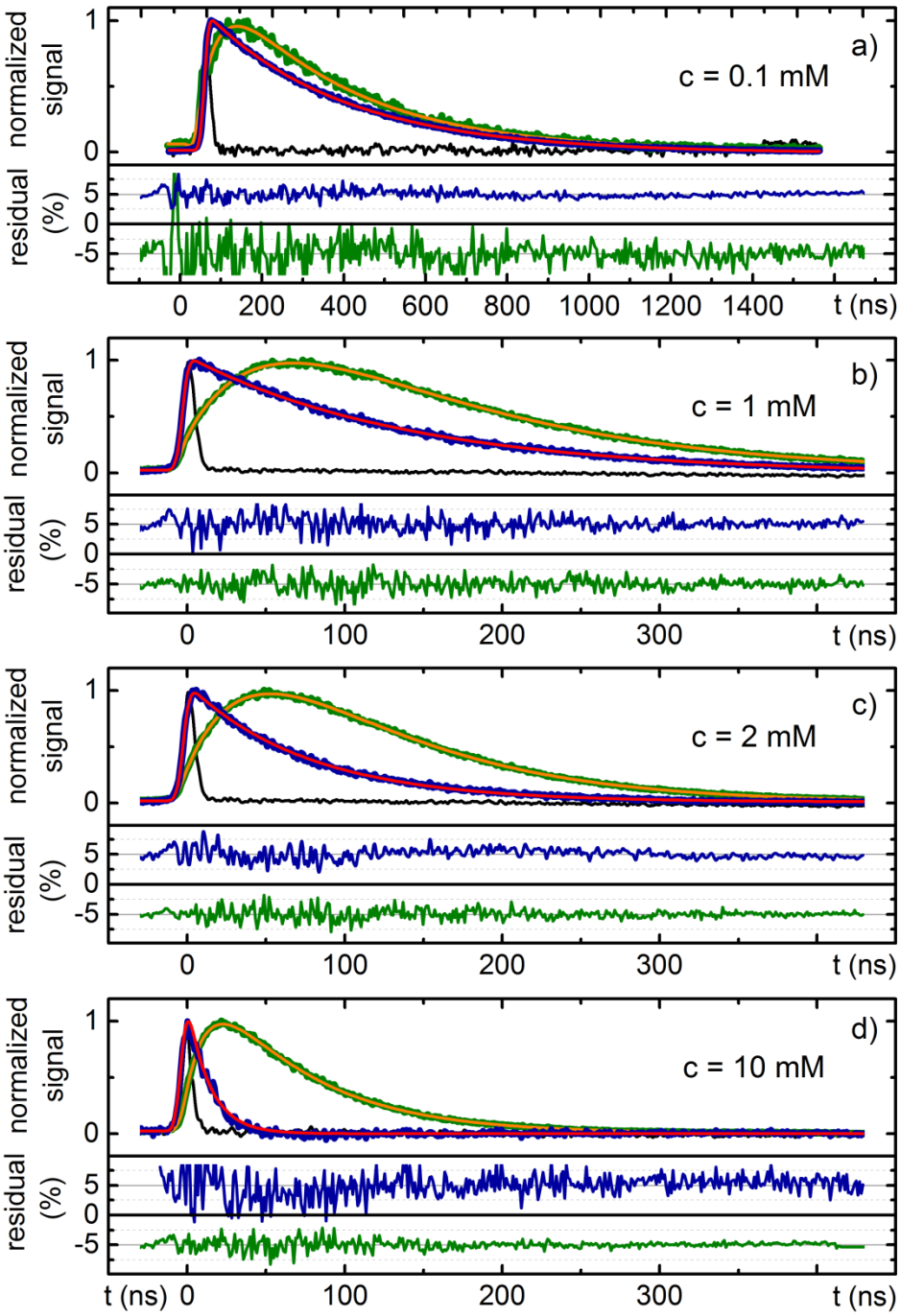

Fig. 4.27: Retrieved monomer (blue) and excimer (green) flourescence decays (normalized) under well degassed conditions with monoexponential (red) and biexponential fits (orange). Bottom panels show residuals, for monomer (blue) and excimer (green) plotted as a fraction of the respective signal maximum for better comparability.

Table 4.6: Fit results obtained after spectral decomposition. The assigned central wavelengths of monomer and excimer bands are 390 nm and 472 nm with respective widths of 33 nm and 90 nm FWHM.

concentration (mM)	**τ_M (ns)**	**A_M (counts)**	**τ_1 (ns)**	**A_1 (counts)**	**τ_2 (ns)**	**A_2 (counts)**	**$-A_1/A_2$**	**τ_{lim} (ns)**
0.01	522	136.6	61	-3.8	478	8.3	0.46	14400
0.1	413	232.4	60	-42.0	366	42.0	1.00	1440
1	132	163.2	53	-316.4	119	330.7	0.96	144
2	72	114.6	46	-484.1	84	506.7	0.96	71.9
5	26	36.5	28	-180.7	65	182.7	0.99	28.8
10	13	34.8	14	-115.2	63	116.2	0.99	14.4

After spectral decomposition the monomer traces can (to a first approximation) be fitted well using a single exponential decay (cf. Fig. 4.27). Fitting the excimer traces independently, three rates and amplitudes for each concentration are obtained. All values are listed in (Table 4.6). A decay time well above 500 ns at 0.01 mM indicates that oxygen has been removed quite effectively and excimer amplitude ratios close to unity indicate the absence of sigificant preassociation.

The concentration dependence of the obtained rates is illustrated in in Fig. 4.28. The fitted excimer rise (green upward triangles) and decay (green downward triangles) rates exibit a similar concentration dependence as all pairs of rates in Fig. 4.24. The fitted monomer decay rate $k_M(c)$, however, shows a distinct evolution. For $c < 2$ mM it follows the excimer decay rate, while for $c > 2$ mM the monomer decays with the same rate as the excimer growth. This clarifies why the system is usually described using only two exponentials: the monomer decay rate is always similar to either the growth or the decay of the excimer signal.

This is a direct consequence of the exchange of rise and decay in equation 4.18: the rise of the observed excimer signal is always characterized by the faster rate (k_D or $k_M(c)$), so at low concentrations the signal rises with the excimer's decay rate and decays with its growth rate, matching $k_M(c)$. As a consequence, for $c \leq 5$ mM the excimer's growth rate is faster than the monomer decay.

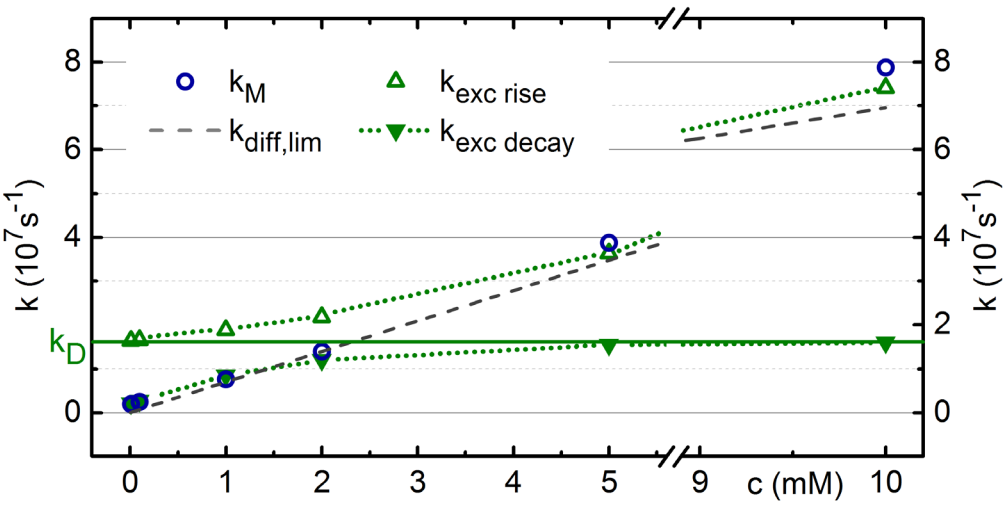

Fig. 4.28: Fitted monomer decay rate $k_M(c)$ (blue circles) and excimer rise (green upward triangles) and decay rates (green downward triangles) vs. concentration. Green line: excimer decay rate k_D. Black dashes: rate of diffusion $k_{diff,lim}$ according to Section 4.4.2.

As the concentration increases, the excimer decay asymptotically approaches $k_D = 1.64 \cdot 10^7 s^{-1}$ (green solid line), corresponding to $\tau_D = 61$ ns. k_D can be interpreted as the intrinsic decay rate of the excimer, i.e. the sum of all radiative and nonradiative decay rates $k_D = k_{rad,D} + k_{IC,D} + k_{DT}$. The excimer decay can never exceed this rate. The excimer growth rate (green upward triangles) approaches this value for low concentrations, but is always slightly faster than k_D.

Note that the asymptote k_D is approached to within measurement accuracy at both ends of the concentration range. According to the modeling applied by Birks et al. a back transfer from the excimer to the monomer would manifest as a deviation from this asymptote [Bir63, Bir70]. The absence of this effect is another indication that back transfer from the excimer can indeed be excluded at room temperature.

An intuitive explanation of this behaivour is that for high concentrations the excimer formation is quite efficient, therefore the monomer decay and excimer buildup share the same rate. In the low concentration limit excimer formation is slow, yet as long as there are excited monomers present in the sample, some excimers will be formed, which leads to a slow decay of the excimer population with the monomer's decay rate. Fitted excimer decays exceeding the monomer decay rate (c = 0.01-1 mM) must be regarded as a measurement error. Small drifts in the streaking field impact the results when evaluating very long decays.

4.6.2 Impact of the Transient Contribution of Diffusional Quenching

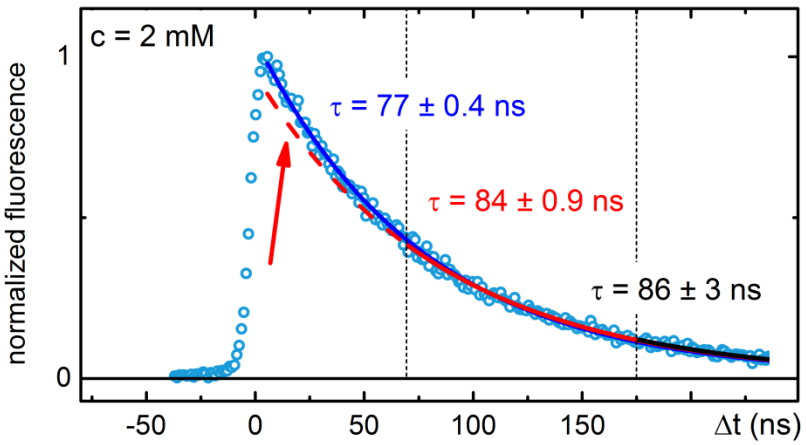

Fig. 4.29: Monomer decay trace from spectral decomposition of well degassed pyrene in cyclohexane at c = 2 mM (blue circles) and monoexponential fits to selected delay time ranges. Red dashes indicate extrapolation.

While the spectral decomposition in Section 4.6.1 provides a good intuitive picture, some discrepancies remain. In pseudo first order conditions diffusion controlled processes are expected to follow exponential kinetics with rates proportional to the concentration of the quencher - in this case pyrene itself (cf. Section 4.4.2). Yet, fits to the decomposed time evolutions at c = 2 mM and 10 mM in Fig. 4.27c&d exhibit small but systematic residuals on the order of 1%. Close inspection reveals that the time evolution of the monomer fluorescence at $c = 2$ mM is not perfectly exponential. Figure 4.29 shows fits to selected delay time intervals. The fitted decay time increases by almost 10% when the initial part of the trace is not included in the fit (red). The effect is noticeable up to about 150 ns (black). As discussed in Section 4.4.2 the first 150 ns are the time range in which the transient contribution to the rate of diffusion is significant.

Secondly, for $c \geq 2$mM, the monomer's single exponential decay rate increases (to a first approximation) linearly with the concentration, with a slope $k_{MD} = 7.75 \cdot 10^9 M^{-1}s^{-1}$. Yet, this exceeds the upper limit given by $k_{diff,lim} = 6.95 \cdot 10^9 M^{-1}s^{-1}$ for cyclohexane at room temperature (cf. Section 4.4.2) by more than. 10%. Excimers should not be formed at a rate faster than the rate of diffusional collision. At lower concentrations, monomer decay rates deviate significantly from this linearity, as shown in Fig. 4.30a. Here a fit to $k_M(c)$ taking into account only the range $c < 2$mM (blue dots) is plotted next to a fit to the entire concentration range (red dashes).

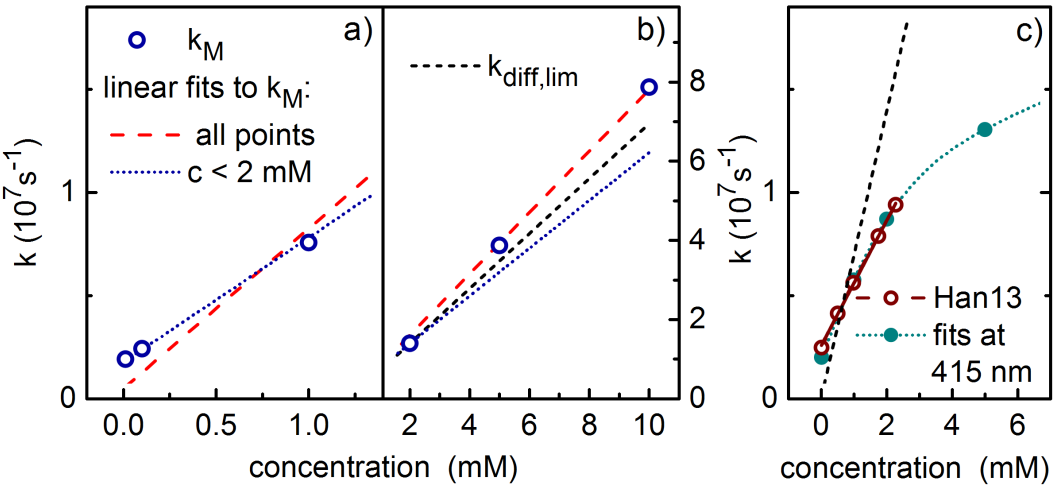

Fig. 4.30: (a) Monomer decay rates $k_M(c)$ (blue circles) and linear fits taking into account only c < 1,5 mM (dots) and all datapoints (red dashes). (b) same as (a) for c > 2 mM compared to rate of diffusion $k_{diff,lim}$ (black dashes), according to the Smoluchovski theory. (c) rates reported in [Han13] (red circles) and linear fit (solid red line) compared to values obtained by averaging over a 10 nm interval around 415 nm detection (turquoise). $k_{diff,lim}$ for p = 1 shown in black.

For $c < 2$ mM the fitted slope is only $k_{MD} = 5.71 \cdot 10^9 M^{-1}s^{-1}$. Figure 4.30b compares these fits to $k_{diff,lim}$ (black).

The smaller value obtained here for c < 2 mM corresponds to an excimer formation efficiency of $p = k_{MD}/k_{diff,lim} = 0.82$. This is well within the range of values obtained for other compounds [Bir70]. The significant difference in the two values obtained for k_{MD} in different concentration ranges points to an underlying concentration dependent effect.

A close match between k_{MD} and $k_{diff,lim}$ was obtained by Birks et al., who concluded that the excimer formation is a diffusion-limited process with an efficiency of p = 1 [Bir63, Bir70]. A much smaller value for $k_{MD} = 3.11 \cdot 10^9 M^{-1}s^{-1}$, corresponding to p = 0.4, was recently reported [Han13]. Hanlon et al. evaluated exclusively below c = 2.3 mM at a single detection wavelength of 415 nm. The small k_{MD} can be explained by their choice of detection wavelength for the 'monomer' fluorescence. The rates obtained in [Han13] (dark red circles in Fig. 4.30c) can be accurately reproduced by analyzing an averaging over a 10 nm spectral interval centered around 415 nm in the streak camera data (turquoise dots). The overlapping excimer fluorescence spectrum significantly impacts this wavelength (cf. Fig. 4.25). The conclusion is that not only the appropriate excitation as stated by Hanlon et al. [Han13], but also the choice of detection wavelength is crucial in the evaluation of $k_M(c)$.

Further evidence pointing to an efficiency p = 0.82 is gained by considering the decay rate of the pyrene monomer in absence of excimer formation $k_M(c = 0)$, the intercept yielded by the linear fit to $k_M(c)$. Reported values of $k_M(c = 0)$ vary slightly as they do depend on the concentration of other quenchers like oxygen. Birks et al. find $k_M(c = 0) = 2.25 \cdot 10^6 s^{-1}$ and, assuming a fluorescence quantum yield of $\Phi_{FM} = 0.65$, calculate the radiative rate of the pyrene monomer to be $k_{FM} = k_M \cdot \Phi_{FM} = 1.46 \cdot 10^6 s^{-1} = 1/680\,ns$ [Bir63]. This is in the vicinity of the, to our knowledge, highest reported fluorescence lifetime of 650 ns for pyrene in cyclohexane, obtained via degassing by freeze-pump-thaw [Del79]. Assuming the same Φ_{FM}, this corresponds to $k_{FM} = 1.00 \cdot 10^6 s^{-1}$.

Our result in the range below $c = 2$ mM is $k_M(c = 0) = 1.77 \cdot 10^6 s^{-1} = 1/565\,ns$ and assuming $\Phi_{FM} = 0.65$ this corresponds to $k_{FM} = 1.15 \cdot 10^6 s^{-1} = 1/870\,ns$, which is closer to the rate reported in [Del79] than that reported in [Bir63], probably due to the modern degassing technique used. A fit to $k_M(c)$ up to 10 mM, however, yields $k_M(c = 0) = 0.49 \cdot 10^6 s^{-1}$, less than half of the smallest value reported [Del79]. It is unlikely that both Birks and Delouis et al. erred by more than a factor of 2, therefore the range above $c \geq 2$mM requires closer investigation. The following section will offer an explanation for the abovementioned discrepancies by exploring the effect of the commonly neglected transient contribution to the rate of diffusion $k_{diff}(t)$ in a simulation.

4.6.3 Simulating Diffusion Including the Transient Contribution

As was pointed out in the previous section, the monomer fluorescence decay rate $k_M(c) = k_{rad,M} + k_{IC,M} + k_{MT} + k_{MD} \cdot c$ for $c < 2$mM suggests an efficiency p = 0.82 for the excimer formation. The significantly larger slope observed for higher concentrations may be due to an apparent acceleration of the observed decays due to the transient contribution of diffusion (cf. Section 4.4.2). To investigate this, a simulation was set up in Mathcad Prime 3.1, where rate equations with a time dependent rate of excimer formation $k_{MD} = k_{diff}(t)$ are solved numerically.

Following considerations in Section 4.4, a reversibility of the excimer formation and excimer formation by encounter of two triplet molecules are neglected. When there is no feedback from the triplet into the S_1 and D* states, the evolution of the triplet state has no impact on the excimer dynamics. Hence, the triplet state is not explicitly represented in the rate model used in the simulation. Radiative and nonradiative decays of the monomer and excimer are accumulated in k_{MG} and k_{DG}. This simplifies the Jablonski diagram as indicated in Fig. 4.31.

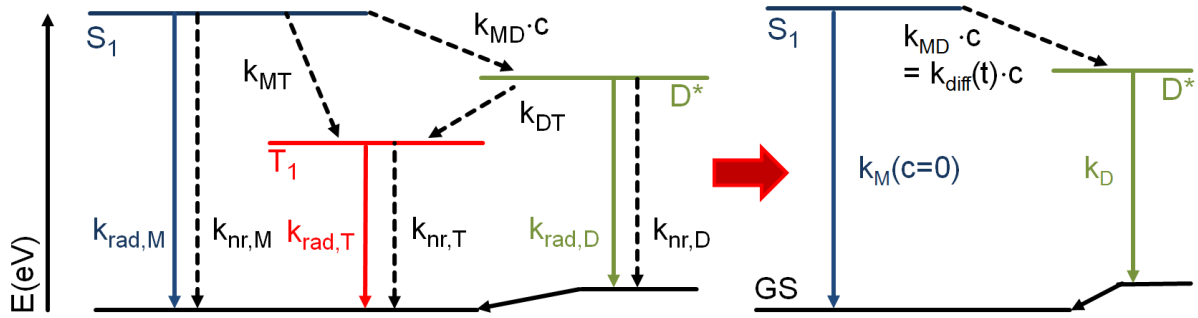

Fig. 4.31: Simplification of the Jablonski diagram previously shown in Fig.4.16. S_1: singlet excited state of the monomer. T_1: triplet excited state of the monomer. D*: excimer. Rates accumulated into deactivation of the monomer $k_M(c = 0)$ and excimer k_D. $k_{diff}(t)$: time dependent diffusion rate according to Eq. 4.16.

Table 4.7: Parameters for the simulation of the pyrene fluorescence dynamics.

pyrene Stokes radius	**r**	8.9 Å	**monomer decay rate**	$\mathbf{k_M(c=0)}$	$1/565$ ns
diffusion constant	**D**	25.8 Å²/ns	**excimer decay rate**	$\mathbf{k_D}$	$1/61$ ns
efficiency of excimer formation	**p**	0.82	**initial concentrations**	$\mathbf{c_0}$	0.01 mM – 10 mM

Diffusion parameters were chosen analogous to the calculation in Section 4.4.2. The monomer and excimer decay rates as well at the efficiency of excimer formation p were chosen to resemble the experimentally determined values from Sections 4.6.1 and 4.6.2. All input parameters are listed in Table 4.7.

The simplified rate model is defined using $k_{diff}(t)$ according to equation 4.16.

$$\frac{d}{dt}\begin{pmatrix}[S_1](t)\\ [D^*](t)\end{pmatrix}=\begin{pmatrix}-k_{diff}(t)\cdot c-k_M(c=0) & 0\\ k_{diff}(t)\cdot c & -k_D\end{pmatrix}\begin{pmatrix}[S_1](t)\\ [D^*](t)\end{pmatrix} \qquad (4.23)$$

First, we assume instantaneous excitation of 1% of a ground state concentration c_0 into an excited state S_1 of the monomer $[S_1](t=0)=0.01\cdot c_0$. The population $[S_1](t)$ subsequently decays with a constant first order rate $k_M(c = 0)$ into the ground state and forms excimers via $k_{MD}(t)=k_{diff}(t)\cdot c$ $1/565$ ns, where $c=0.99\cdot c_0$. The minute change in ground state concentration due to the formation of excimers is neglected here. The population of the excimer [D*] decays into the ground state with a first order rate k_D.

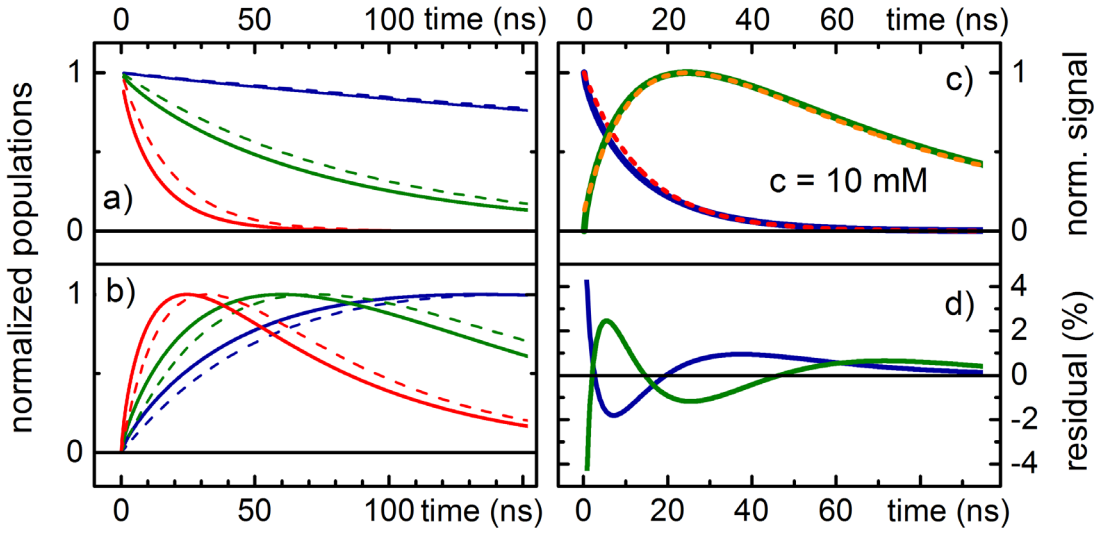

Fig. 4.32: (a) calculated monomer populations $[S_1](t)$ with (solid) and without (dashed) the transient contribution for c = 0.1 mM (blue), 2 mM (green) and 10 mM (red). (b) same as (a) for the excimer population $[D^*](t)$. (c) Single exponential fit (red) to the computed monomer population $[S_1](t)$ (blue) and double exponential fit (yellow) to the computed excimer population (green) $[D^*](t)$. (d) Residuals of fits shown in (c), as percentage of the maximum of the respective signal.

The transient term in $k_{diff}(t)$ is proportional to $\sqrt{t}$ (cf. equation 4.16). Hence, it exhibits a pole a $t = 0$. To circumvent this, the simulation starts at $t = 0.1$ ns. This does introduce an error, yet equation 4.16 is also an approximation. In reality $k_{diff}(t = 0)$ cannot be infinite. It has been pointed out that to realistically treat the very early times, one must consider that for an excitation by a pulse of finite width, the time origin is not the same for all molecules. Therefore one always finds a mixture of excited state species of different 'ages' [Mar87]. For this simulation targeting a timescale of tens and hundreds of ns, such considerations are disregarded.

Fig. 4.32 shows solutions of the rate model 4.23 for selected concentrations with (solid lines) and without the transient term in $k_{diff}(t)$. As expected, the transient contribution manifests as an accelerated decay of the S_1 population as well as an accelerated growth of the excimer population (cf. Fig. 4.32a and 4.32b). When the transient contribution is neglected, the solutions to the rate model 4.23 are exponential functions and exponential fits reproduce the simulated signals perfectly. To judge the error introduced by an exponential fit of a trace severely affected by the transient term in $k_{diff}(t)$, Figs. 4.32c and 4.32d illustrate the situation at $c = 10$ mM. Here exponential fits deviate from the simulated traces, leaving residuals of a few percent of the observed signal amplitudes. Deviations due to the transient

contribution decrease with time, after 100 ns they account for less than 0.5% of the observed signal maximum. This is roughly the time in which $k_{diff}(t)$ stabilizes to within 10% of its limiting value $k_{diff,lim}$. These findings are compatible with the residuals obtained in Fig. 4.27.

Table 4.8: Results of exponential fit to simulated data neglecting the transient contribution.

concentration (mM)	τ_M (ns)	A_M (mM)	τ_1 (ns)	A_1 (mM)	τ_2 (ns)	A_2 (mM)
0.01	548	0.0001	61	-3.88E-7	5485	3.88E-7
0.1	428	0.001	61	-4.03E-5	428	4.03E-5
1	135	0.01	61	-0.0062	136	0.0062
2	77	0.02	61	-0.068	76	0.068
2.5	63	0.025	62	-1.84	62	1.84
3	53	0.03	54	-0.22	61	0.22
4	41	0.04	41	-0.11	61	0.11
5	33	0.05	33	-0.10	61	0.10
10	17	0.01	17	-0.13	61	0.13

Table 4.9: Results of exponential fit to simulated data including the transient contribution.

concentration (mM)	τ_M (ns)	A_M (mM)	τ_1 (ns)	A_1 (mM)	τ_2 (ns)	A_2 (mM)
0.01	546	0.0001	49	-3.91E-7	564	4.08E-7
0.1	417	0.001	48	-4.01E-5	436	4.18E-5
1	122	0.010	45	-0.0049	140	0.0051
2	66	0.019	40	-0.0215	89	0.0221
2.5	54	0.023	37	-0.0312	79	0.0320
3	45	0.028	33	-0.0397	74	0.0410
4	33	0.037	27	-0.0526	68	0.0547
5	26	0.046	22	-0.0626	66	0.0657
10	12	0.091	11	-0.1058	63	0.1142

Table 4.8 and 4.9 detail monomer and excimer decay times and amplitudes obtained from the exponential fits to simulated fluorescence decays. The concentration dependence of $k_M(c)$ is illustrated in Fig. 4.33. Neglecting the transient contribution results in a perfectly linear

increase of the monomer decay rate $k_M(c)$ (blue circles). As expected, the fitted slope $k_{MD} = 5.68 \cdot 10^9 M^{-1}s^{-1}$ (blue dashed line) equals $k_{diff,lim} = 6.95 \cdot 10^9 M^{-1}s^{-1}$ multiplied by the assumed efficiency p = 0.82 (cf. Fig. 4.33b). For reference, experimentally obtained rates from spectral decomposition of the data in Section 4.6.1 are shown as gray dots. The difference between the calculated $k_M(c)$ and experimentally obtained values increases significantly with the concentration. When taking the transient contribution into account, this deviation vanishes (red area in Fig. 4.33b). The fitted slope $k_{MD} = 7.89 \cdot 10^9 M^{-1}s^{-1}$ now closely matches the experimental value of $k_{MD} = 7.75 \cdot 10^9 M^{-1}s^{-1}$ and exceeds the theoretical $k_{diff,lim}$ (dashed black line). Note that just as in the experiment the rates obtained including the transient term slightly deviate from linearity due to the increasing effect of the transient contribution towards higher concentrations.

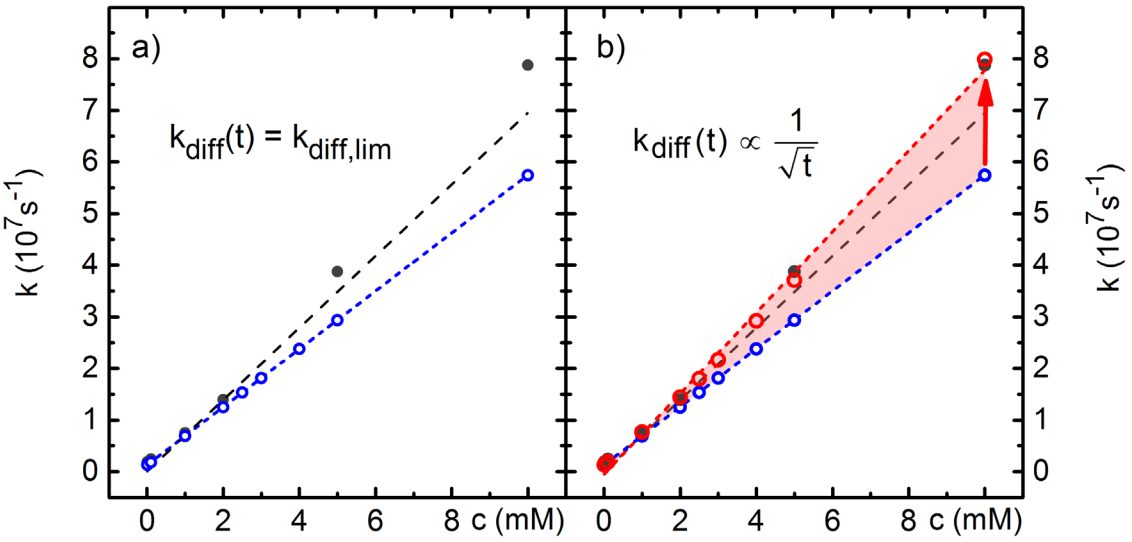

Fig. 4.33: Simulations neglecting and including the transient contribution. Rates obtained from experiment shown in gray for reference. (a) $k_M(c)$ (blue circles) obtained from monoexponential fits of caclulated time evolutions $[S_1](t)$ and linear fit (blue dashes) without transient term. Black dashed line indicates $k_{diff,lim}$ for p =1 according to Smoluchowski theory. (b) same as (a), compared to $k_M(c)$ and linear fit including the transient contribution (red).

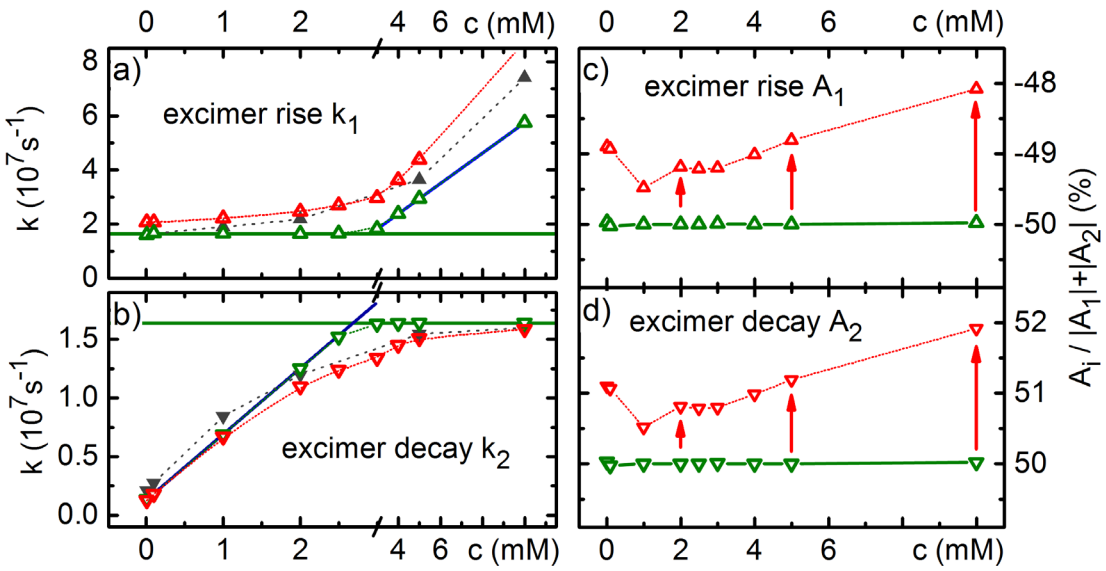

Fig. 4.34: Simulations neglecting and including the transient contribution. Rates obtained from experiment shown in gray for reference. (a,b) upward and downward triangles signify rise and decay rates from double exponential fits of [D*](t) neglecting (green) and including (red) the transient contribution. Blue line indicates $k_M(c)$, green line indicates k_D. (c,d) fitted amplitudes as a fraction of the total amplitude without (green) and with (red) the transient contribution.

The experimentally observed behavior of the excimer rise and decay rates is also reproduced well by exponential fits to [D*](t) (cf. Fig. 4.34), exhibiting an asymptotic behavior toward k_D (green line) and $k_M(c)$ (blue line) as discussed in Section 4.6.1. At the intersection between $k_M(c)$ and k_D the difference between calculations with (red) and without (green) the transient term is most pronounced. While theory predicts an abrupt change in the slope as reflected by the behavior of the green triangles, the rates calculated including the transient contribution (red) display a smooth convergence toward k_D, just as observed in the experiment (cf. Fig. 4.28) and in [Bir63].

With the transient contribution included, the fitted growth rate is slightly overestimated (Fig. 4.34a, red triangles). This is understandable, since deviations from the exponential fits are most severe for the increasingly accelerated growth of [D*](t) at early times (cf. Fig. 4.32).

Figures 4.34c and 4.34d show the fraction of the fitted rise and decay amplitudes of [D*](t) w.r.t. the total fitted amplitude. When $k_{diff}(t) = k_{diff,lim}$, the rise and decay amplitudes are always exactly equal (green lines, cf. Table 4.8). With the transient contribution included a slight decrease in the amplitude of the fitted rise is compensated by a matching increase the

decay amplitude. This effect can be observed in the experimental data presented in Sections 4.5 and 4.6.1 and is in accordance with observations made in [Mar87].

The above observations clearly indicate that the transient contribution to the rate of diffusion is a likely cause for the different k_{MD} observed at $c \leq 2$ mM versus high concentrations. The transient contribution also explains the smooth convergence of the excimer rise and decay rates towards k_D. It follows that the excimer formation is a diffusion limited process with an efficiency $p \approx 0.82$, yet at high concentrations exponential fits yield exaggerated rates. An efficiency less than unity can be explained by alignment constraints: molecules colliding at an angle unfavorable for π-orbital overlap may drift apart again without forming an excimer [Han13]. An equality of excimer fluorescence rise and decay amplitudes is a good indicator for the absence of preassociated dimers. Studies in which such were postulated solely on the basis of unequal rise and decay amplitudes should be double checked for transient contributions, indicated, e.g., by a smoothing around the intersection between $k_M(c)$ and k_D. This splitting and smoothing effect was observed by Birks et al. [Bir63], who wrongfully concluded a reversibility of the excimer formation and an excessive efficiency of $p = 1$.

Exponential functions no longer represent solutions to dynamics significantly influenced by time dependent rates, i.e. at high concentrations. However, while the resulting rates are considerably increased, even at $c = 10$ mM time evolutions are still reproduced fairly accurately (cf. Figs. 4.27 and 4.32). Commonly, time dependent rates are parameterized by stretched exponentials, but for the dataset presented in the above study, the use of stretched exponentials does not significantly improve the fits. In fact a 'stretch parameter' of $\beta = 1$ is often found, which corresponds to a classical exponential. Fitting segments of time evolutions separately can help identify whether transient effects come into play (cf. Fig. 4.29).

While the spectral decomposition presented in Section 4.6.1 has an advantage in being model-free w.r.t. the dynamics, pseudo first order conditions allow the use of classical global fit (GF) algorithms that facilitate retrieval of the species spectra of the intermediates involved. To this end, being aware of the impact of the transient contribution studied above, exponential decays will be used to describe the TA data in the following sections, leading to 'pseudo first order' rate constants.

4.7 The Full Picture: Augmenting Broadband Fluorescence with Transient Absorption

Broadband transient absorption (TA) measurements allow direct access to the S_1, excimer and triplet dynamics and extraction of excited state spectra. The role of the triplet state in the excimer dynamics has been a matter of speculation in previous discussions [Bir63, Bir70, Par62, Med66, Mis80, Mar89, Boh90]. Overlapping signatures in the VIS often complicate data analysis [Pos71, Pos76, Tsu95, Fog95, Kat97]. This spectral congestion is disentangled in this, to our knowledge, first combined streak and TA study of pyrene and derivatives.

Similar decay times are found in fluorescence as well as TA when a comparable O_2 concentration is maintained. Specifically, the decay time of the absorption band around 360 nm is similar to the monomer fluorescence decay (cf. Table 4.10). This feature can be attributed to the S_1 state's excited state absorption (ESA) [Kre13]. With exception of PY11, all investigated compounds form triplet states with lifetimes of several µs. A TA dataset of PY11-C6 is shown in Fig. 4.35 as an example. The triplet ESA exhibits vibrationally structured features around 400 nm and 500 nm [Del79, Fog95], the latter overlapping the S_1 ESA. Below 350 nm the 'inverted' absorption spectrum is imprinted as ground state bleach (GSB).

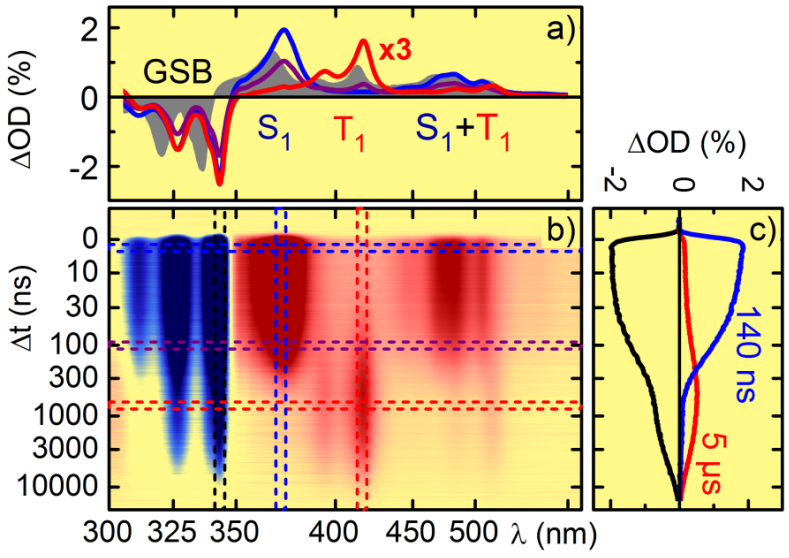

Fig. 4.35: 0.1 mM PY11-C6 in cyclohexane: (a) TA spectra at selected delay times marked by cursors in (b). Red spectrum multiplied by 3. Gray: TA spectrum of pyrene at Δt = 100 ns. (b) False color representation of TA data. Blue implies negative, red positive signal. (c) time evolution of GSB (black), S_1 ESA (blue), T_1 ESA (red).

Table 4.10: Results obtained in a combined time resolved fluorescence and TA study.

compound (c = ~ 0.1 mM in cyclohexane)	excitation wavelength (nm)	fluorescence decay time [a] (ns)	S_1 ESA decay time [b] (ns)	triplet QY [b] (%)	fluo. QY [c] (%)
Pyrene	334	[d] 133	187	62	62
1-Methylpyrene	343	130	130	44	62
1-Propylpyrene	343	[d] 132	140	44	
1-Bromopyrene	345	2	2	98	9
PY11-C6	343	101	140	33	30
PY44	341	70	90	64	40
Pyrene (10 mM)	357	9	12	no GSB	
PY11-C3	344	7	7	23	68
PY14	342	[d] 17	11	20	
PY11	334	2	2	no triplet	93

[a] from streak fluorescence data. [b] estimated from GSB amplitudes. [c] from sealed degassed cuvette in spectrometer using an Ulbricht sphere. [d] from single line time resolved fluorescence at λ_{det} = 400 nm.

The comparability of results is limited by the oxygen concentration in the samples, due to oxygen quenching of both singlet and triplet excited pyrene [Gre94, Wil99, Bie14]. A flow circuit employed to avoid photoproducts sets a lower limit to the residual oxygen concentration, even though it features air tight tubing and an inline degasser (cf. Section 4.2.5). As a consequence, S_1 lifetimes of only 130 ns to 190 ns are observed here and oxygen quenching must be included in the modeling. In perfectly degassed conditions the lifetime of the pyrene S_1 state reaches several hundreds of ns, depending on the concentration and the solvent. Fluorescence studies report values between 357 ns at c = 0.1 mM and 420 ns at 0.05 mM in cyclohexane. 445 ns were reported at 0.01 mM in decane [Bir63, Han13]. In the streak camera study presented in Section 4.6, where the freeze pump thaw method was used for degassing in a sealed cuvette, an even longer decay time 522 ns was achieved in cyclohexane at c = 0.01 mM. Streak camera measurements at the BMO do not allow delays exceeding 32.3 ns, so fitting of long decay times carries increased uncertainty. However, in most cases the resulting decay times are comparable to those obtained from the S_1 ESA in TA, retrospectively validating the times obtained from the fluorescence. Triplet lifetimes of several milliseconds have been reported for pyrene in polar solvents in fully degassed

solutions [Med66, Par68], while in cyclohexane the longest reported life time is 180 µs [Sli70]. Herein a lifetime much larger than the singlet lifetime indicates a triplet state.

Table 4.10 also lists triplet quantum yields (QY) and reference values for the fluorescence QY of all compounds. The sum of triplet and fluorescence QY in Table 4.10 differs from 100% for many compounds. This is a consequence of oxygen quenching of the S_1 state in the TA, leading to increased triplet yields [Gre94, Wil99, Bie14]. The fluorescence QY were determined in well degassed conditions in a sealed cuvette by means of a spectrometer featuring an Ulbricht sphere (Hamamatsu C9920-02G). The OD was kept below 0.15 at the respective excitation wavelength to avoid reabsorption. No reliable result was obtained for pyrene at c = 10 mM due to the large OD. The triplet QY in Table 4.10 are obtained from the TA datasets in two ways: values in brackets are obtained from the observed GSB. Its amplitude carries information about the number of excited particles at a given delay time. Directly comparing the GSB amplitudes at times where only the initial (S_1) or triplet (T_1) excited state is populated yields an estimate for the triplet quantum yield (QY). In pyrene the S_1 ESA overlaps the GSB region. To take this into account the steady state absorption spectrum is added to the TA spectrum at the selected times and scaled such that the GSB vanishes and a smooth, all positive ESA spectrum with no perceivable GS features remains (cf. Fig. 4.36). The scaling factors are then compared to yield the triplet QY. This is achieved without assuming any specific model and with no need of triplet sensitizers or quenchers. A concrete model for the pyrene dynamics is suggested in the following section.

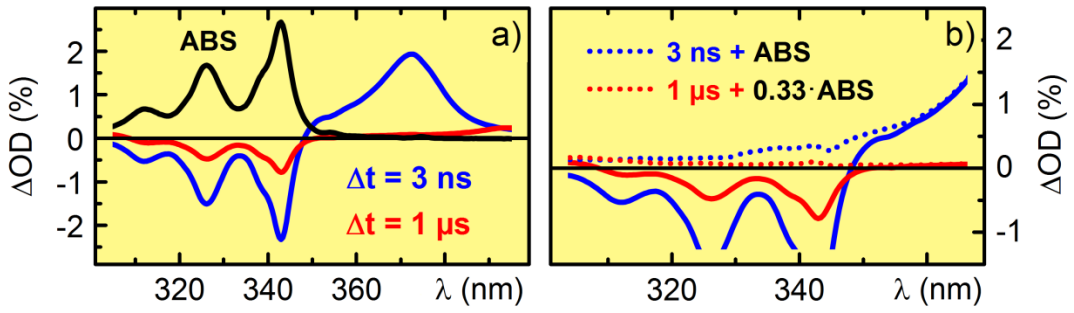

Fig. 4.36: (a) TA spectra of 0.1 mM PY11-C6 in cyclohexane at Δt = 3 ns (blue) and Δt = 1 µs (red) and steady state absorption spectrum (black), scaled by a factor 0.093. (b) Same as (a), with dotted lines showing the sum of the scaled absorption spectrum and the transient spectra.

Comparing the TA data the set of compounds can be subdivided into three categories: 'monomer-like', 'excimer-like' and 'novel photophysics' (horizontal lines in Table 4.10). Each category will be investigated separately in the following sections. A typical monomer-like TA dataset was shown above (Fig. 4.35). The TA spectrum of pyrene at 100 ns delay is shown as a gray area in Fig. 4.35a for comparison. It exhibits the same features as PY11-C6 blue shifted by about 5 nm, which is in accordance with the shift observed in the steady-state absorption spectra. A complete pyrene dataset can be found in Fig. 4.7d-f. In the monomer-like case the only decay channels are fluorescence, internal conversion and intersystem crossing into the triplet state. The excimer decay channel opens up when the concentration is increased or pyrene units are linked in a favorable configuration. An example of an excimer-like dataset is shown in Fig. 4.37a. Here pyrene in cyclohexane at c = 10 mM was excited into the weaker S_1 band in order to avoid inhomogeneous illumination [Han13]. Due to the high concentration no probe light was transmitted in the ground state absorption range below 350 nm. Compared to the monomer-like case the decay time of the S_1 ESA has shortened significantly and a 'blurring' of the ESA around 500 nm as well as an additional band in the NIR emerge.

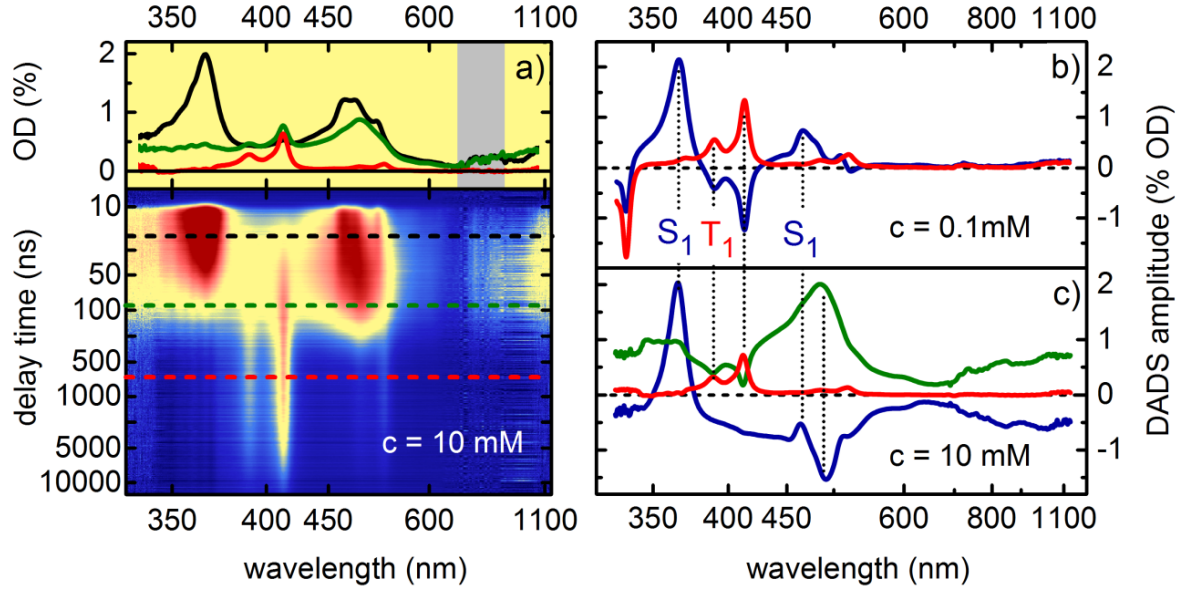

Fig. 4.37: (a) TA dataset of pyrene in cyclohexane at c = 10mM. Between 700 nm and 830 nm amplitudes should be interpreted cautiously as only a small amount of probe light was transmitted by the fundamental blocking filter. (b,c) Global fit DADS for pyrene at c = 0.1 mM (b) and at c = 10 mM (c).

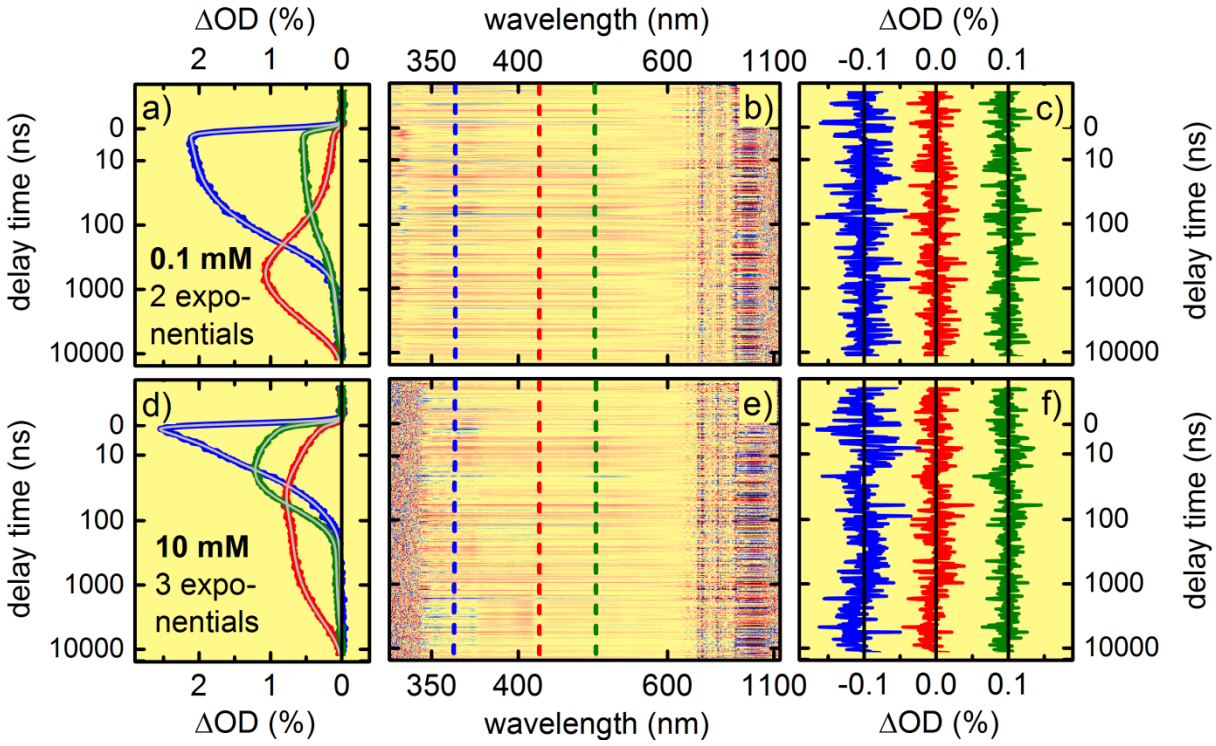

Fig. 4.38: Global fit of 0.1 mM and 10 mM pyrene in cyclohexane. (a,d) selected time traces at positions indicated by color coded cursors and global fits (gray). (b,e) false color representation of global fit residuals, z-scale set from OD = -0.001 to OD = 0.001. (c,f) residuals corresponding to (a,d), plotted offset by ±0.1%.

Being aware of transient effects (cf. Section 4.6.2), a global fit (GF) algorithm using exponentials is employed in the analysis of the TA datasets in order to retrieve species spectra for the pyrene S_1, excimer and triplet states. While the TA of monomer-like compounds can be accurately reproduced using only two exponential decays, a third exponential is needed to fully describe excimer-like dynamics. A maximum entropy analysis confirms this observation (cf. Fig. 4.10). Global fits are illustrated in Fig. 4.38. They reproduce the data fairly accurately even though diffusion controlled rate parameters play a role in both excimer formation and oxygen quenching. Figures 4.38b&c compare decay associated difference spectra (DADS) for a monomer-like dataset of pyrene at c = 0.1 mM (b) and an excimer-like dataset of pyrene at 10 mM (c). In (b) the perfect match of the negative contribution in the DADS associated with the S_1 decay (blue) and the known triplet signature (red) reflects that the triplet feature grows with the S_1 decay time of 187 ns. In (c) the DADS representing the accelerated 12 ns decay of the S_1 state is negative over almost the entire spectral range, with a peak at 470 nm and a characteristic increase towards the NIR. This signifies the rise of a broad ESA signature with the S_1 decay time. Interestingly, the DADS no longer features a

significant contribution from the triplet state. The new broad DADS (green) is a mirror image of the S_1 DADS in the NIR and features a 52 ns decay – matching the excimer fluorescence decay in the corresponding streak measurement. Hence, the additional broad signature can be attributed to the pyrene excimer. Up to this point no specific rate model has been assumed. The following sections will feature model-specific considerations.

4.7.1 One Model to Describe Them All

Assuming a specific kinetic model, species associated spectra (SAS) can be reconstructed and QYs can be computed using the DADS displayed in Fig. 4.37. A Jablonski diagram illustrating the simplified kinetic model is shown in Fig. 4.39. Fluorescence and internal conversion (IC) to the ground state (GS) are aggregated into rates k_{MG}, k_{DG} and k_{TG}. Due to the large stabilization w.r.t the S_1 state (cf. Section 4.4.1), a hypothetical reversibility of the excimer formation is disregarded. Triplet triplet annihilation can also be ignored on the ns timescale (cf. Section 4.4.2). This leads to a system of first order differential equations for the concentrations $[S_1](t)$, $[D^*](t)$ and $[T](t)$ of the intermediate species:

$$\frac{d}{dt}\begin{pmatrix}[S_1](t)\\ [D^*](t)\\ [T](t)\end{pmatrix}=\begin{pmatrix}-k_M & 0 & 0\\ k_{MD}\cdot[GS] & -k_D & 0\\ k_{MT} & k_{DT} & -k_T\end{pmatrix}\begin{pmatrix}[S_1](t)\\ [D^*](t)\\ [T](t)\end{pmatrix} \tag{4.24}$$

$$k_M = k_{MD}\cdot[GS](t) + k_{MG} + k_{MT} \tag{4.25}$$

$$k_D = k_{DT} + k_{DG} \tag{4.26}$$

$$k_T = k_{TG} + k_{QT}[O2] \tag{4.27}$$

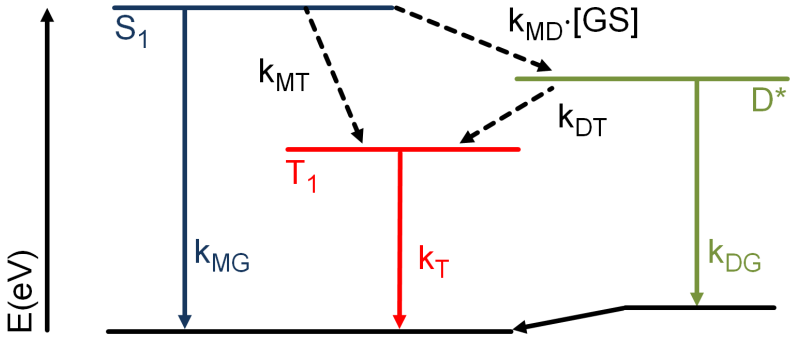

Fig. 4.39: Simplified Jablonski diagram for the pyrene dynamics, drawn to scale according to TDDFT calculations. S_1, S_2: singlet excited states of the monomer. T_1: triplet excited state of the monomer. D*: excimer.

As in the previous chapters k_M, k_D and k_T represent the net decay rates of the S_1, D* and T_1 populations, which constitute the eigenvalues of this system of differential equations. These net decay rates correspond to the rates found in the global fit. Species associated spectra (SAS) can be reconstructed from the DADS using these three rates. k_T includes a triplet oxygen quenching contribution $k_{QT}[O_2]$.

The most likely processes for oxygen quenching of a singlet pyrene result in a triplet pyrene [Gre94, Wil99, Bie14]. Hence, $k_{MT} = k_{ISC} + k_{QS}[O_2]$ and $k_{DT} = k_{ISC,D} + k_{QD}[O_2]$, represent triplet growth rates due to both inter system crossing (ISC) and oxygen quenching of the singlet populations of monomer and excimer via $k_{QS}[O_2]$ and $k_{QD}[O_2]$.

The model 4.24 results in the following relationship between SAS and DADS

$$S_{S_1} = \frac{1}{dc^*}(\mathrm{DADS}_1 + \mathrm{DADS}_2 + \mathrm{DADS}_3) + \mathrm{GS} \tag{4.28}$$

$$S_{D^*} = \frac{1}{2dc^*}\left(\frac{(\kappa_M - \kappa_T)}{k_{MD}[GS]}\mathrm{DADS}_2 + \frac{(\kappa_D - \kappa_M)k_{DT}}{k_{MT}(\kappa_D - \kappa_T) - k_{MD}[GS]\cdot k_{DT}}\mathrm{DADS}_1\right) + \mathrm{GS} \tag{4.29}$$

$$S_{T_1} = \frac{1}{dc^*}\left(\frac{(\kappa_M - \kappa_D)(\kappa_D - \kappa_T)}{k_{MT}(\kappa_D - \kappa_T) - k_{MD}\cdot[GS]\cdot k_{DT}}\mathrm{DADS}_3\right) + \mathrm{GS} \tag{4.30}$$

Here, d represents the sample thickness and c* the excited state concentration. In the monomer-like case, where no significant excimer formation occurs, k_{MD} approaches zero and the rate model has only two eigenvalues corresponding to two DADS. Equations 4.28 and 4.30 then simplify to

$$S_{S_1} = \frac{1}{dc^*}(\mathrm{DADS}_1 + \mathrm{DADS}_2) + \mathrm{GS} \tag{4.31}$$

$$S_{T_1} = \frac{1}{dc^*}\frac{(\kappa_M - \kappa_T)}{k_{MT}}\mathrm{DADS}_2 + \mathrm{GS} \tag{4.32}$$

The DADS are difference spectra w.r.t the ground state absorption. An additional constraint is that all SAS must be strictly positive. The remaining unknowns can be therefore determined ‘by eye’ as shown in the following sections.

4.7.2. Dynamics of the Monomer and Monomer-like Compounds

The pyrene derivatives 1-methylpyrene and 1-propylpyrene exhibit dynamics very similar to the pyrene monomer both in emission and TA. 1-bromopyrene undergoes a faster ISC due to the heavy atom effect [Bir70], but it exhibits similar S_1- and triplet signatures. The latter also applies to the linked compounds PY11-C6 and PY44, likely because the stacking of pyrene units is sterically inhibited [Hir65, Zac84, Zac91, Zac99]. Note that in emission PY11-C6 and PY44 do exhibit an additional signature with a few ns decay time. This was first attributed to an impurity, yet recent measurements on pyrene oligomers suggest it could also be the contribution of a less stable excimer, resulting from imperfect stacking (cf. Section 4.9). A closer look at the TA reveals a slight broadening of the S_1 ESA around 500 nm, where an excimer absorption is typically observed, yet no additional time constant was found in the TA.

Figure 4.40 exemplifies how the S_1- and triplet SAS are determined from the pyrene DADS using equations 4.31 and 4.32. In equation 4.31, dc^* is determined by adding the sum of the DADS (violet dots in Fig. 4.40a) to a scaled GS absorption spectrum. The scaling factor is chosen such that the ground state bleach (GSB) vanishes and a smooth, all positive S_1 ESA spectrum with no significant GS features is obtained (cf. Fig. 4.40b, blue). The remaining feature at $\lambda = 334$ nm can be attributed to pump stray light. The resulting excited state concentration of $c^* = 8.5 \cdot 10^{-8}$ M, is then used in Eq. 4.32, where the only remaining free parameter is k_{MT}. To obtain an all positive triplet spectrum (red line in Fig. 4.40b), k_{MT} must be fixed at $k_{MT}^{TA/0.1mM} = 3.42 \cdot 10^6\ s^{-1}$, corresponding to a total triplet yield $\Phi_{MT} = k_{MT}/k_M$ of ca. 64% in 0.1 mM pyrene.

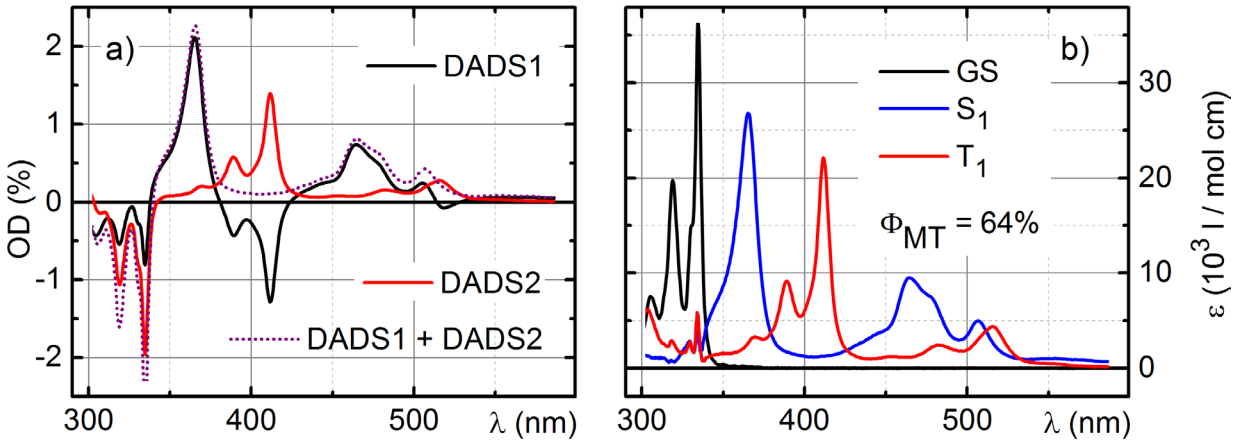

Fig. 4.40: (a) Decay associated difference spectra from biexponential global fit to 0.1 mM pyrene in cyclohexane. (b) Species associated spectra using Eqs. 4.31 and 4.32.

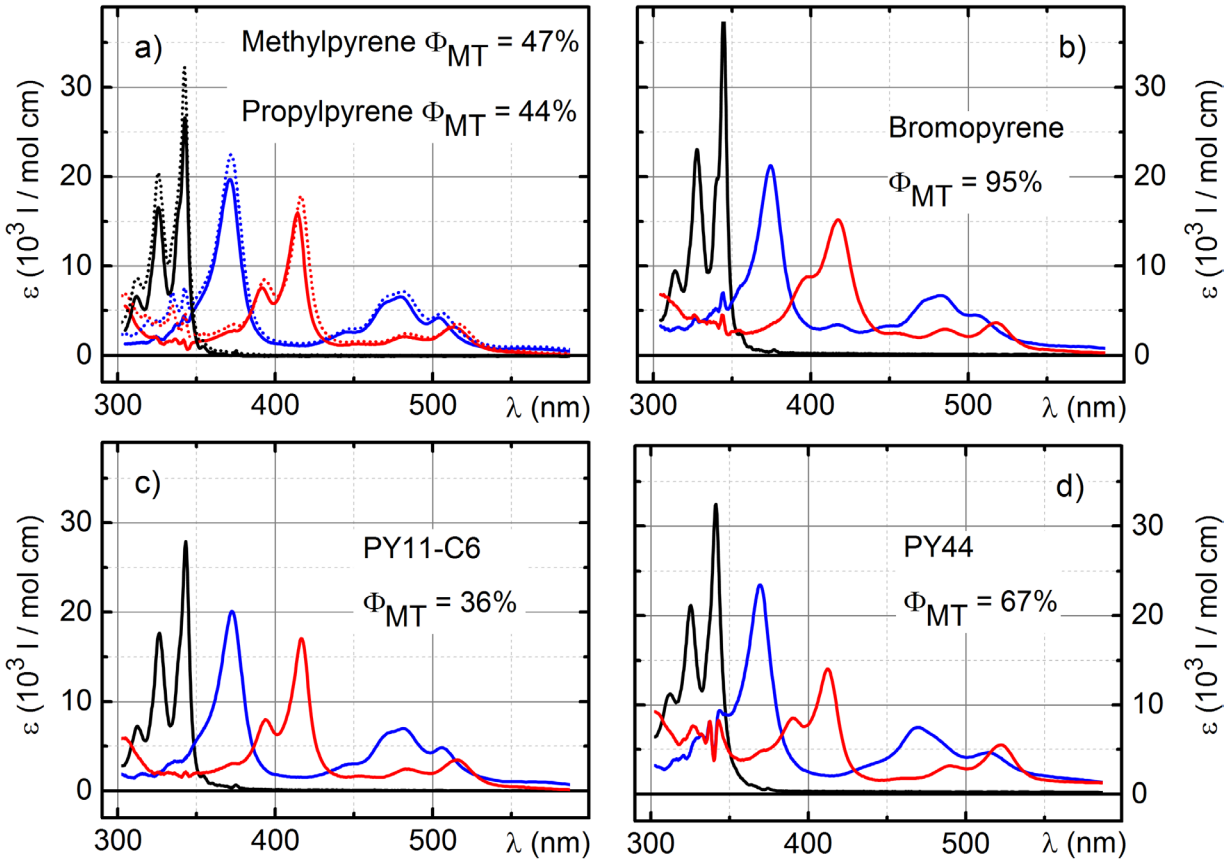

Fig. 4.41: Species associated spectra of the ground state (black), S_1- (blue) and T_1-states (red) with respective quantum yields. (a) Methylpyrene (solid lines) and propylpyrene (dotted lines), (b) Bromopyrene, (c) PY11-C6 and (d) PY44.

SAS and corresponding values of Φ_{MT} for the remaining monomer-like compounds are presented in Fig. 4.41. The obtained Φ_{MT} are very similar to the triplet quantum yields obtained by direct evaluation of the GSB amplitudes (cf. Table 4.10). This indicates that the model is consistent with directly observed quantities. For the linked dimers the molar absorption coefficient ε of the transient ground state SAS is only half of the steady-state value (cf. Fig. 4.4). This signifies that only one pyrene moiety was excited in each molecule due to the moderate excitation energies used. In addition to the transient spectra, rough estimates for the impact of oxygen quenching on the respective QYs can be obtained by referencing the decay rates obtained from the global analysis to the well degassed streak camera study presented in Section 4.6. These computations are lengthy and therefore shown in Appendix A2.

In brief, the fluorescence study shows that there is a slight excimer formation already at c = 0.1mM with a quantum yield of $\Phi_{MD} \leq 10\%$, which does not contribute significantly to

the TA. Secondly, the increased singlet decay rate seen in the TA can be used to estimate a quenching rate $k_{QS}^{TA/0.1mM}[O_2] = 2.93 \cdot 10^6\ s^{-1}$ and, hence, an oxygen concentration ca. 0.15 mM for the pyrene TA measurement. This is a realistic value in the pump circuit used (cf. Section 4.2.5). Knowledge of $k_{QS}^{TA/0.1mM}[O_2]$ facilitates subdivision of Φ_{MT} into singlet quenching and inter system crossing yields Φ_{QS} and $\Phi_{ISC,M}$, and also determines Φ_{MG}. These yields correspond to ISC and combined fluorescence/IC rates of $k_{ISC,M} = 0.48 \cdot 10^6\ s^{-1}$ and $k_{MG} = 1.45 \cdot 10^6\ s^{-1}$ for pyrene.

No fully degassed datasets exist for the pyrene derivatives, but comparison of the respective triplet decay rates yields an estimate for the oxygen concentration in each measurement. Results including oxygen quenching are listed in Table 4.11.

Table 4.11: Estimated quantum yields of pyrene and derivatives including oxygen quenching.

compound	Φ_{MT} (%) from SAS	Φ_{QS} (%)	Φ_{MD} (%)	$\Phi_{ISC,M}$ (%)	Φ_{MG} (%)
Pyrene	64	55	10	9	26
1-Methylpyrene	47	36	7	11	46
1-Propylpyrene	44	30	7	15	49
1-Bromopyrene	95	0	0	95	5
PY11-C6	36	28	7	8	57
PY44	67	19	5	48	29

Table 4.12: Predicted individual quantum yields of pyrene derivatives without oxygen quenching.

compound	$\Phi_{ISC,M}$ (%)	Φ_{MG} (%)
Pyrene	26	74
1-Methylpyrene	20	80
1-Propylpyrene	23	77
1-Bromopyrene	95	5
PY11-C6	12	88
PY44	62	38

Using the monomer's ISC rate QYs expected in a perfectly degassed environment can be estimated. 'Oxygen corrected' QYs are listed in Table 4.12. Here Φ_{MG} represents an upper limit to the fluorescence quantum yield due to the inclusion in internal conversion processes into k_{MG}. Accordingly, the oxygen corrected Φ_{MG} are either larger or similar to the reference values for the fluorescence QY shown in Table 4.10. The inter system crossing yield $\Phi_{ISC,M}$ obtained for pyrene is slightly smaller than previously reported values of 0.33 [Med66], 0.30 [Del79, Tur10], and 0.35 [Val01]. The differences can likely be attributed to the increased uncertainty of the rate constants due to the transient contribution to the rate of diffusion, which also affects the singlet quenching process. While the methyl and propyl substituents do not significantly affect the triplet yield, in bromopyrene nearly all excited molecules undergo ISC due to the heavy atom effect. Directly linked PY44 also features an elevated triplet QY, while for PY11-C6 the yield is surprisingly low.

4.7.3 Excimer Dynamics and the Role of the Triplet State

Excimer-like TA data and corresponding DADS obtained from pyrene at 10 mM are displayed above (Figs. 4.37a and 4.37c). As shown by the emission study in Section 4.6, at c = 10 mM the decay rate of the S_1 state is limited by diffusion. It's decaytime of 9 ns matches the growth of the broad green excimer fluorescence band, which subsequently decays with 52 ns, corresponding to $k_D = 1.9 \cdot 10^7\ s^{-1}$.

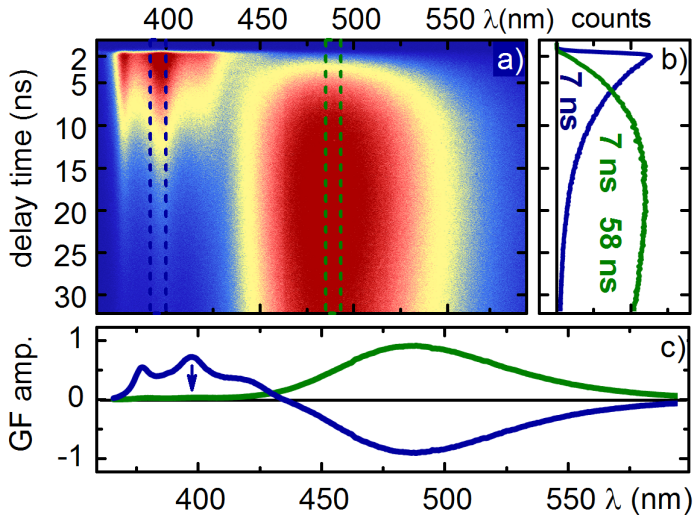

Fig. 4.42: (a) Streak camera measurement of 0.05 mM PY11-C3 excited at 345 nm. (b) averaged temporal evolution from intervals indicated by color coded cursors. (c) global fit DADS corresponding to a 7 ns (blue) and 58 ns (green) time constants.

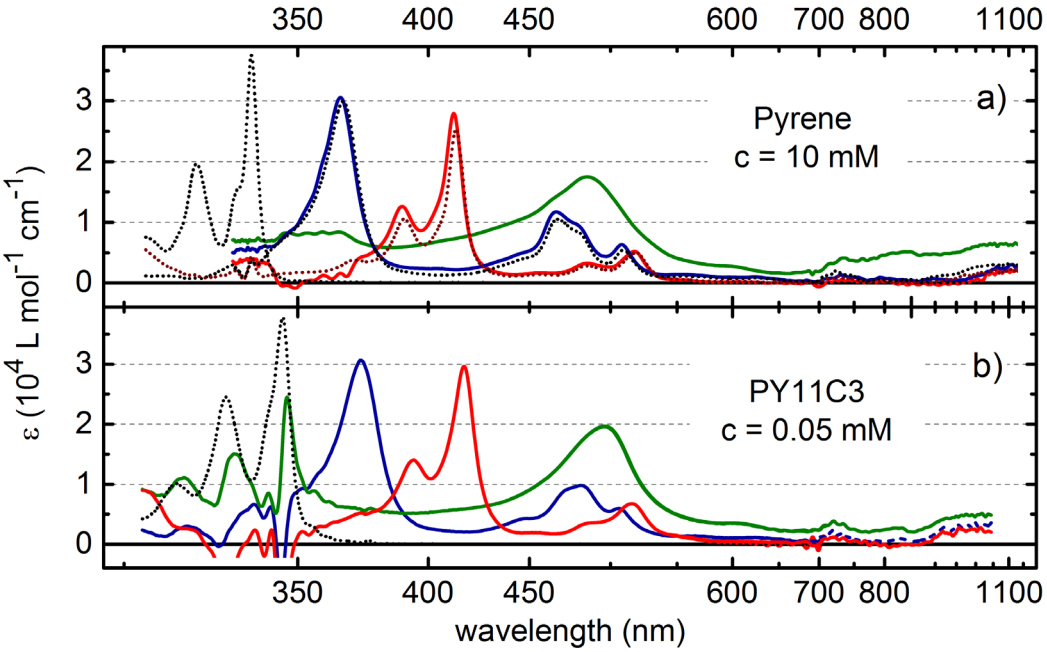

Fig. 4.43: (a) Species associated spectra (SAS) for pyrene at c = 10 mM in cyclohexane. Dotted lines indicate SAS determined from the diluted (monomer) measurement. (b) SAS for PY11-C3 at c = 0.05 mM. Black dots show GS contribution. Above 700 nm only a small amount of probe light was transmitted by the white light fundamental blocking filter. Amplitudes in this range carry increased uncertainty.

At such a high concentration the entire probe light is absorbed in the range below 350 nm, so the GSB cannot be used to directly evaluate the triplet quantum yield from the raw data. Fortunately, the linked PY11-C3 closely mimics the dynamics of pyrene at 10 mM, forming excimers very efficiently already at c = 0.05 mM. As proof, Fig. 4.42 shows the corresponding streak camera measurement, resembling the data obtained from 10 mM pyrene very closely (cf. Figs. 4.5 and 4.23). The bottom panel shows the corresponding DADS from a global analysis, indicating overlap of the fluorescence bands as discussed in Section 4.6.

To obtain the SAS, it is assumed that $k_{MT}^{TA/0.1mM} = 3.42 \cdot 10^6\,s^{-1}$ as in the low concentration limit (cf. Section 4.7.2) and that the excimer formation rate at c = 10 mM is $k_{MD} \cdot 10\,mM = 7.68 \cdot 10^7\,s^{-1}$, as obtained from the fluorescence study presented in Section 4.6. The remaining free parameters in Equations 4.28 to 4.30 are then dc^* and k_{DT}. SAS obtained from pyrene at c = 10mM for $k_{DT}^{TA/10mM} = 3.85 \cdot 10^6 s^{-1}$ are shown in Fig. 4.43a. The S_1- (blue) and triplet (red) signatures agree closely with those obtained in the monomer-case at low concentration (dotted lines). The GSB cannot be evaluated here because the sample absorbed the entire probe light in this region.

A TA measurement of 0.05 mM PY11-C3 allows evaluation of the GSB during excimer formation. The corresponding SAS in Fig. 4.43b show very similar features and amplitudes w.r.t. pyrene. The redshift of about 7 nm is similar to that observed in the steady state absorption spectra. Due to the moderate excitation energies used, only one pyrene moiety will be initially excited, thereby effectively halving the extinction coefficient of the linked dimer compared to the steady state absorption. This consistent with the similar signal amplitudes observed in TA for the pyrene monomer and the linked dimers. However, the correction of the GS absorption is not perfect. No value of k_{DT} could be found that would remove the dips originating from the triplet state in the excimer DADS and at the same time yield smooth spectra below 350 nm. Hence, k_{DT} was optimized for a smooth spectrum above 350 nm, while signatures reminiscent of the GS absorption remain.

A likely reason for this is that the interaction between linked pyrenes changes when one of the moieties is excited, slightly altering the absorption spectrum of the remaining GS moiety. This altered absorption spectra will exhibit the same dynamics as the corresponding excited states and must therefore be viewed as a negative transient contribution that cannot be corrected by adding a scaled steady state absorption spectrum. Hence, the structures in the GSB region are not representative of the respective ESA. Given the good overall comparability of the obtained SAS, it seems quite likely that the pure S_1- and triplet SAS behave similar to SAS obtained in the low concentration limit in the GSB region.

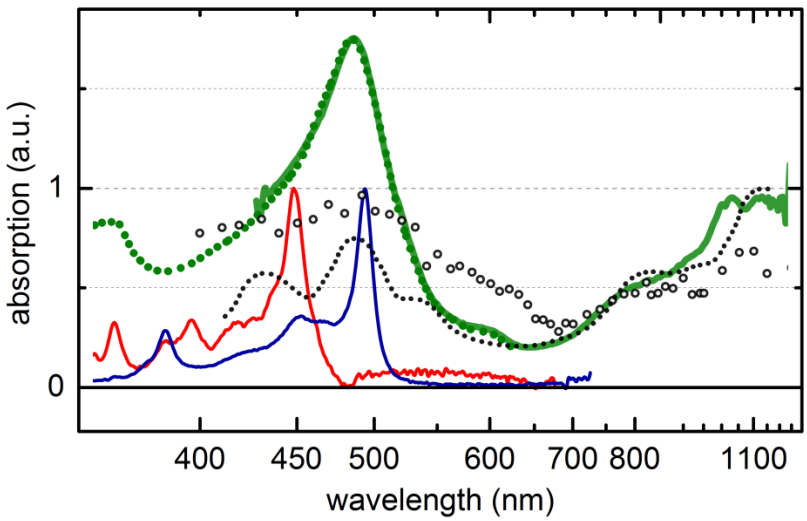

Fig. 4.44: Excimer SAS obtained using VIS (green dots) and NIR (green line) probe compared to scaled excimer spectra from [Pos76] (dots) and [Kat97] (circles). Pyrene radical anion (blue) and cation (red) spectra from [Rei14].

So far the transient spectrum of the pyrene excimer has not been reported in the VIS with high accuracy due to the many overlapping contributions [Fog95], but the literature agrees that it exhibits a characteristic rise toward the NIR, where neither the S_1 nor the triplet state contribute to the signal [Pos71, Pos76, Kat97]. Figure 4.44 shows stitched excimer spectra (green) from TA measurements using visible 778 nm pumped as well as 1200 nm pumped NIR probe supercontinua (cf. Section 4.2.3).

The excimer spectrum obtained is in good agreement with the spectrum reported by Post et al. in the NIR and reveals the excimer's exact signature in the VIS [Pos76].

This can be used to shed some light on the charge transfer character of the excimer. Normalized pyrene cation (red) and anion (blue) spectra from [Rei14] illustrate that, while their main signatures occupy the same spectral range, the excimer's ESA is not just a superposition of the cation an anion signatures. More likely than a complete charge transfer between the two identical pyrene units is a stabilization due to charge resonance and electron delocalization between pyrene units [Rei15, Cor15]. The ion spectra were obtained via quenching experiments in acetonitrile (ACN) and methanole (MeOH), which will be detailed in the following section.

The additional information obtained from TA also offers new insight into the role of the triplet state. Since at room temperature there is no back transfer from the triplet on the ns timescale, a distinct excimer triplet species as considered in [Med66] and [Bir70] would not change our model for the dynamics of the excimer formation. It would merely constitute a third decay channel for the excimer, which might exhibit a distinct spectral signature or decay time. At $c = 0.1$ mM the overwhelming triplet population is due to oxygen quenching of the excited singlet state. At $c = 10$ mM the monomer contributes only 26% of the observed triplets (including oxygen quenching), while 74% are generated from the excimer.

Despite this difference, the triplet decay times obtained at $c = 0.1$ mM and $c = 10$ mM are equal ($\tau = 3.6$ µs) and the triplet ESA signatures are very similar both in magnitude and spectral position. Fig. 4.45a shows the obtained triplet SAS. The difference in extinction coefficients is less than 10%, and a spectral shift of ca. 1 nm is observed. This is just within the margin of error of the wavelength calibration in this spectral range [Meg09].

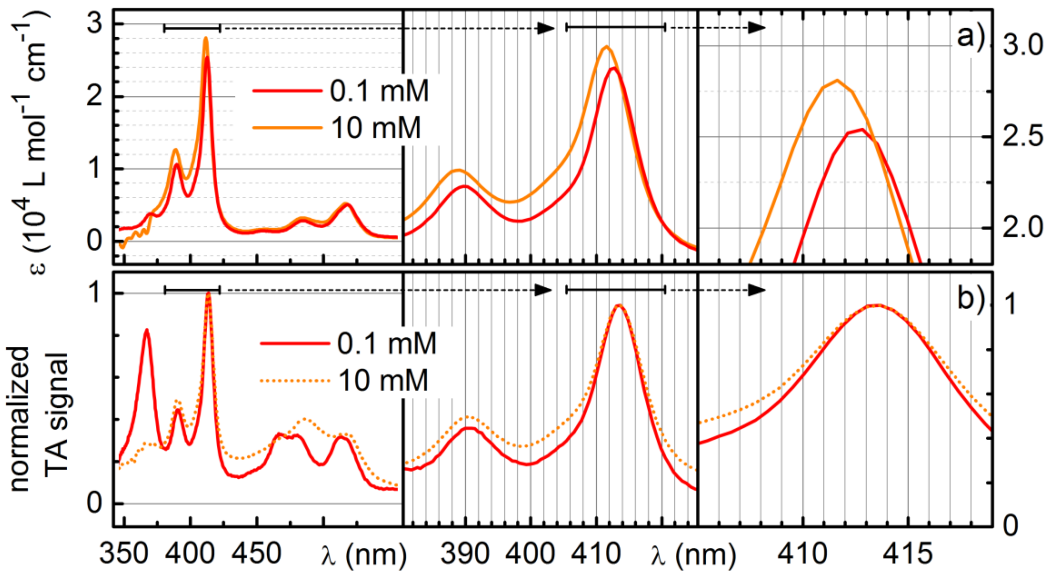

Fig. 4.45: Comparison of triplet signatures from (a) global fit SAS and (b) averaging raw TA data over suitable delay time intervals.

While the SAS do not suffer from overlapping contributions of other states, the SAS amplitude is dependent on the decay rates obtained from the GF, which are susceptible to slight changes in the oxygen concentration and the yields determined 'by eye' via the SAS. To rule out any discrepancies caused by the fitting procedure and modeling, normalized signatures directly obtained from the raw data averaged over suitable delay time intervals are shown in Fig. 4.45b. These spectra are affected by overlapping contributions from the excimer and S_1 ESA, yet the peak positions fit perfectly. Normalization of the signals reveals slight differences in band shape and relative peak heights.

In conclusion, a distinct triplet state of the excimer cannot be excluded completely, yet the evidence is far from compelling. Within measurement accuracy the triplets formed from the excimer have almost identical spectral features in the VIS and show no difference in their dynamics. A reason for slight discrepancies could be a difference in the direct environment of the excited molecule after ISC. While c = 10 mM is not enough to significantly affect the overall solvent polarity, it is certainly true that just after ISC from the tightly bound excimer, the second pyrene unit is still in very close proximity to the new triplet molecule. It is therefore more likely that ISC from the excimer results in one triplet monomer and one GS molecule, which subsequently drift apart.

Table 4.13: Estimated quantum yields of pyrene at c = 10 mM and PY11-C3 including oxygen quenching (top) and predicted values without oxygen quenching (bottom).

compound	Φ_{QS} (%)	Φ_{MD} (%)	Φ_{MG} (%)	$\Phi_{ISC,M}$ (%)	Φ_{QD} (%)	$\Phi_{ISC,D}$ (%)	Φ_{DG} (%)
Pyrene	6	92	1.50	0.50	17.5	2.5	80
PY11-C3	2	97	0.75	0.25	17.5	2.5	80
Pyrene	0	98	1.60	0.53	0	3	97
PY11-C3	0	99	0.75	0.25	0	3	97

Table 4.13 summarizes quantum yields obtained the model 4.39. The calculations can be found in Appendix A3. For the pyrene excimer an inter system crossing rate of $k_{ISC,D} = 0.40 \cdot 10^6 s^{-1}$ is found - quite similar to the ISC rate of the monomer. The combined fluorescence/internal conversion rate from the excimer to the ground state was determined to $k_{DG} = 1.55 \cdot 10^7 s^{-1}$, one order of magnitude larger than that of the monomer.

As in the monomer case, the total triplet and fluorescence yields can be compared to the reference values in Table 4.10. For the pyrene measurement a total triplet yield from monomer and excimer of $\Phi_{T1} = 0.25$ and a total fluorescence yield of $\Phi_{rad} \leq 0.75$ are found. For PY11-C3, $\Phi_{T1} = 0.22$ and $\Phi_{rad} \leq 0.78$. The directly measured total fluorescence yields are slightly smaller than the limits obtained. No reference value exists for the triplet yield in the pyrene measurement at c = 10 mM, since the GSB was not observed. Yet, for PY11-C3, the triplet yield closely matches the 23% obtained by direct evaluation of the GSB. As in the monomer case, the modeling is consistent with direct observations.

4.7.4 Unprecedented Behavior in Pyrene 1-1

Compared to the directly linked PY44, which can be counted among monomer-like species, the dynamics exhibited by PY11 are faster by almost two orders of magnitude – an impressive example of the linker position greatly influencing the dynamics. PY11 completely relaxes back to the GS within a few picoseconds and no triplet state with a microsecond life time is observed. PY14 represents an intermediate case with already significantly decreased decay times and triplet quantum yield (cf. Table 4.10). A TA measurement on the picosecond timescale is shown in Fig. 4.46a-c. Immediately after optical excitation at magic angle we

observe the GSB between 300 nm and 350 nm along with a sharp band around 375 nm, which decays with a 4 ps decay time. A previously unobserved broad ESA with a 1.73 ns lifetime is found above 500 nm, overlapped by a negative contribution that can be identified as stimulated emission via comparison with the fluorescence spectrum (gray dashes in Fig. 4.46a). The fluorescence also disappears within a few ns and its unstructured spectrum is blue-shifted w.r.t. the known excimer fluorescence. The measured fluorescence QY of 93% is unusually large compared to other pyrene dimers. Global analysis reveals two decay times, 3.95 ps as well as 1731 ps. Since the sample was excited slightly above what would usually be called the S_2 maximum at 334 nm, the most straightforward interpretation is to assign the shorter time to the S_2 population transitioning into the S_1 state, followed by a – for pyrene - super fast fluorescence to the GS. Figure 4.46d shows SAS corresponding to this model.

A possible explanation can be given via computed spin densities for the PY11 and PY44 radical cations calculated via TDDFT (cf. Fig. 4.47). Pyrene carries twice as much spin density on its 1-position, than on the 4-position [Lor13]. One consequence is that significantly more effort is required to establish 4-4 links between the pyrene units [Fig11]. Secondly, pyrene units will arrange differently, dihedral angles obtained in the crystal phase are $\theta = 70.4°$ for PY44, $\theta = 68.2°$ for PY14 and $\theta = 64.1°$ for PY11. [Kee15]. According to the calculated spin densities in Fig. 4.47, a nodal plane can be drawn between the pyrene units in PY44, so there is no strong interaction of orbitals from separate units. The opposite is the case in PY11, where the pyrene units are oriented such that orbitals partially overlap, though no perfect π–stacking can be achieved for steric reasons. This interaction may disturb the system enough to cause an increased transition dipole moment for the $S_1 \leftarrow S_0$ transition. An increased transition probability would explain the reduction of the S_1 state's lifetime from hundreds of ns to 1.7 ns and is consistent with the observed change in the steady state absorption spectrum, where absorption in the S_1 region is much more pronounced than in pyrene (cf. Fig. 4.4). The increase in the S_2 state's lifetime from ca. 0.1 ps to 4 ps could be a consequence of the detachment of a conical intersection between S_2 and S_1 state, slowing down the sub-100 fs internal conversion observed in pyrene [Fog95, Neu99, Kre13, Kre13a]. Recent theoretical calculations indeed predict an increased oscillator strength of 0.71 for the $S_1 \leftarrow S_0$ transition while that of the $S_2 \leftarrow S_0$ transition is reduced to 0.01, while the respective values for pyrene are approximately 0.02 and 0.3 [Küb15].

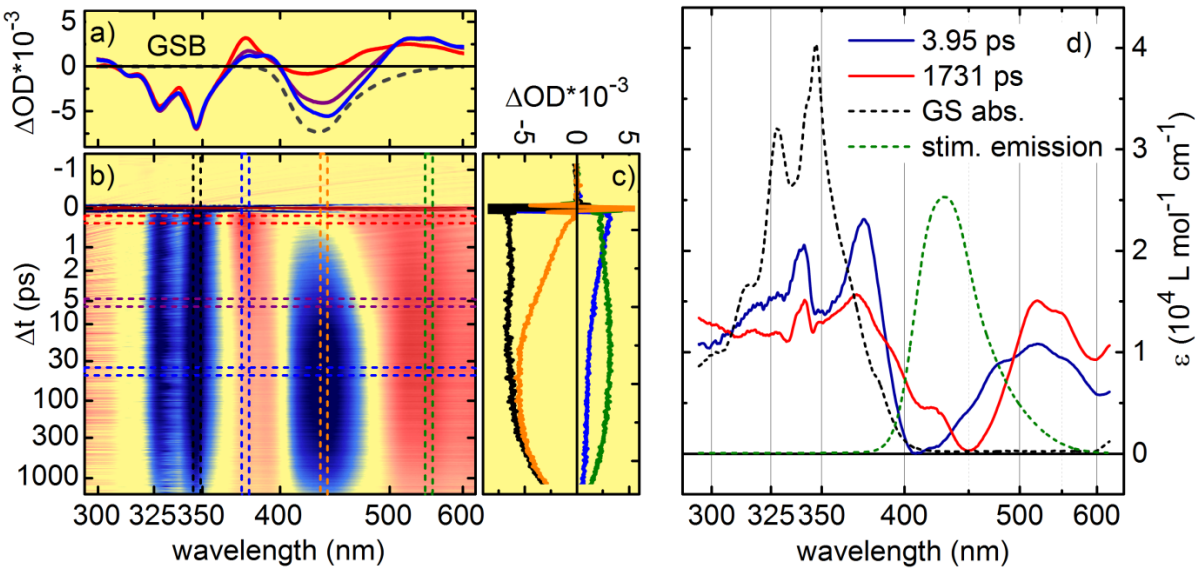

Fig. 4.46: TA dataset of PY11 in cyclohexane in the picosecond regime, excited with 200 nJ pulse energy at λ = 334 nm. Blue indicates negative, red positive contributions. (a) transient spectra at selected delay times and inverted fluorescence spectrum scaled by λ^4 (gray dashes). (c) time evolution of GSB (black), short-lived ESA (blue), stimulated emission (orange) and long-lived ESA band (green). (d) Species associated spectra for short- (blue) and long-lived (red) component from global fit assuming a sequential reaction scheme $S_2 \rightarrow S_1 \rightarrow$ GS. Dashed lines show GS (black) and stimulated emission (green).

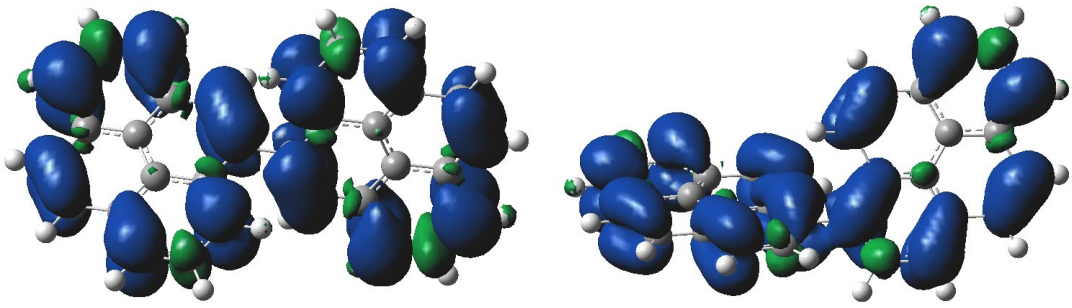

Fig. 4.47: Spin density distributions of PY44 (left) and PY11 (right) radical cations calculated via TDDFT. Figure courtesy Matthias Roos.

4.8 Summary: Broadband Analysis Reveals 'Full Picture'

This chapter has revealed new information on the pyrene excimer dynamics, partially contradicting and augmenting the early models. These models are fundamental not only to publications from the 1960's, but with pyrene's many modern applications also to recent studies and textbooks [Bir63, Bir75, Win93, Tur10, Duh12, Han13].

Overlapping bands detrimentally impact the analysis of fluorescence decays. In combination with a disregard for the effects of the transient contribution to the rate of diffusion this lead to unnecessarily complex models for the excimer formation of pyrene. Combining broadband measurements of time resolved fluorescence and transient absorption facilitates the decomposition of spectrally overlapping signatures, which results in a much more complete picture of the dynamics. Simulations of fluorescence decays including the commonly neglected transient contribution to the rate of diffusion resolve inconsistencies in prior publications.

The rate model used to describe the pyrene dynamics was significantly simplified compared to earlier studies. It accurately describes the dynamics of all investigated compounds at room temperature except PY11. There is no need to include a back transfer from the excimer or contributions due to different conformers in linked dimers to model the dynamics observed herein. Contributions from TTA can also be neglected on the ns timescale. Using the model, the TA spectrum of the excimer in the VIS/NIR was retrieved with high accuracy and additional information was obtained regarding the charge transfer character of the excimer and the role of the triplet state in excimer formation [Bir63, Mar89, Med66].

Even though pyrene in cyclohexane does not strictly exhibit pseudo first order behavior, its dynamics can be described by a sum of exponentials to reasonable accuracy. When modeling with exponentials, the transient contribution to the rate of diffusion increasingly shortens the fitted decay times towards higher concentrations. Taking this into account, the monoexponential decay of the monomer fluorescence indicates an efficiency of the excimer formation for pyrene in cyclohexane of ca. $p = 0.82$, corresponding to an excimer formation rate $k_{MD} = 5.71 \cdot 10^9 M^{-1}s^{-1}$ in cyclohexane at room temperature. The rise and decay rates of the excimer fluorescence are also affected. When the transient contribution is negligible the corresponding amplitudes have the same magnitude. Slight deviations from this equality may be indicative of preassociated dimers, but can also stem from the transient contribution to the rate of diffusion.

The evolution of the pyrene triplet state was studied in transient absorption experiments. A flow circuit was used to avoid photoproducts, limiting the residual oxygen concentration to ca. 0.15 mM. Despite the use of an inline degasser and oxygen tight tubing, residual oxygen severely impacts both the singlet and triplet dynamics. The overwhelming fraction of the observed triplets is generated by oxygen quenching of the singlet state. Despite this, triplet and fluorescence quantum yields for all compounds could be estimated by including oxygen quenching in the model. The resulting decay rates for the S_1-state and the excimer are $k_{MG} = 1.45 \cdot 10^6\,s^{-1}$ and $k_{DG} = 1.55 \cdot 10^7 s^{-1}$. The ISC rates are $k_{ISC,M} = 0.48 \cdot 10^6\,s^{-1}$ and $k_{ISC,D} = 0.40 \cdot 10^6 s^{-1}$ for monomer and excimer, respectively. At $c = 10$ mM the monomer has been replaced by the excimer as the main source of triplet molecules.

PY11-C3 is a good model system for excimer formation and shows no sign of multiexponential decays due to different conformers in cyclohexane. Most of the other linked dimers tested follow dynamics very similar to the pyrene monomer, most notably the directly linked compound PY44, despite the close proximity of the pyrene units. While the linker length can favor or inhibit excimer formation, the position of the linker affects the dynamics drastically for directly linked compounds. PY11 exhibits fast dynamics on the few ns timescale previously undocumented for pyrene.

A logical next step would be the development of a fit algorithm which takes into account the transient contribution to the excimer formation rate. A temperature dependent study could determine at what point a back transfer from the excimer to the excited singlet state becomes relevant. Early measurements reported by Birks et al. [Bir63], indicate interesting effects starting already at temperatures around 310 K, which have to be reevaluated in light of the new information obtained. The original interpretation of a significant backtransfer from the excimer still does not seem likely at this temperature.

Secondly, with their tunable properties the pyrene dimers investigated here offer ample opportunity for future studies. More detailed calculations should be performed on PY11 and a chain length-dependent study could help clarify the nature and size of the disturbance causing the dynamics to change so drastically. PY44 maintains most of its properties despite the direct link, making it an interesting candidate for polymerization towards functionalized materials such as organic light emitting diodes (OLEDs), organic photovoltaics, organic field-effect transistors (OFETs), as well as lasers [Fig11, Jia04, Zha07, Mog06, Wan06, Lee11]. The outlook below provides a first glimpse at the properties of such 4-bridged oligomers.

4.9 Outlook: PY44 as a Candidate for Novel Materials

Recently there has been increasing interest in pyrene as a building block for functionalized materials in organic electronic devices. However, when many pyrene units are connected, often the traits of the monomer are not preserved. In order to investigate how the properties of directly linked PY44 change when polymerized, the novel compounds shown in Fig. 4.48 were synthesized by Dr. Ashok Keerthi from the group of Prof. Dr. Klaus Müllen, at the Max Planck Institute of Polymer Research, Mainz, Germany. Results below are preliminary.

The absorption spectra of the oligomers feature similar redshifts as observed in the linked dimers. Changes to the features of higher lying states are less pronounced. At a first glance, all compounds feature monomer-like dynamics in transient absorption (TA) with S_1 ESA features slightly shifted but similar to those observed in pyrene as well as long-lived triplet states. The obtained triplet life times are comparable to those of the monomer and the dimers. The known excimer TA signature is not observed for any of the compounds.

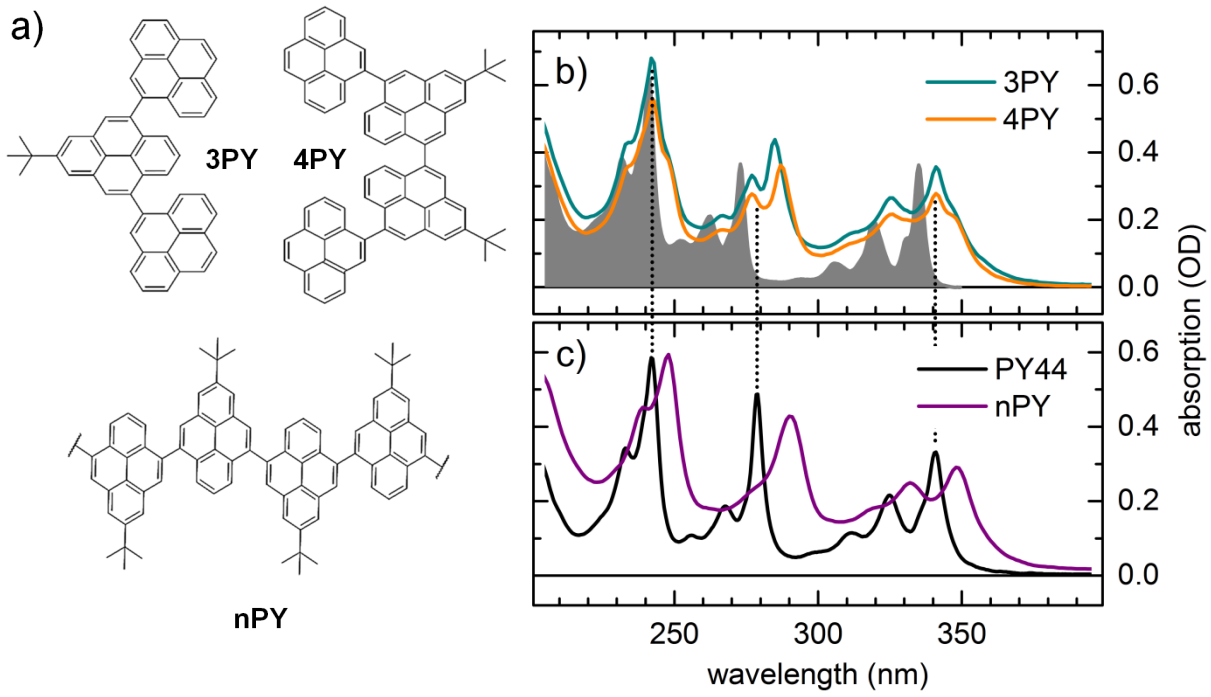

Fig. 4.48: (a) structures of pyrene oligomers linked at the 4-position and their steady state absorption spectra compared to PY44 (b,c). nPY is a polymer with an average length of more than 30 units. Pyrene absorption shown in gray for comparison.

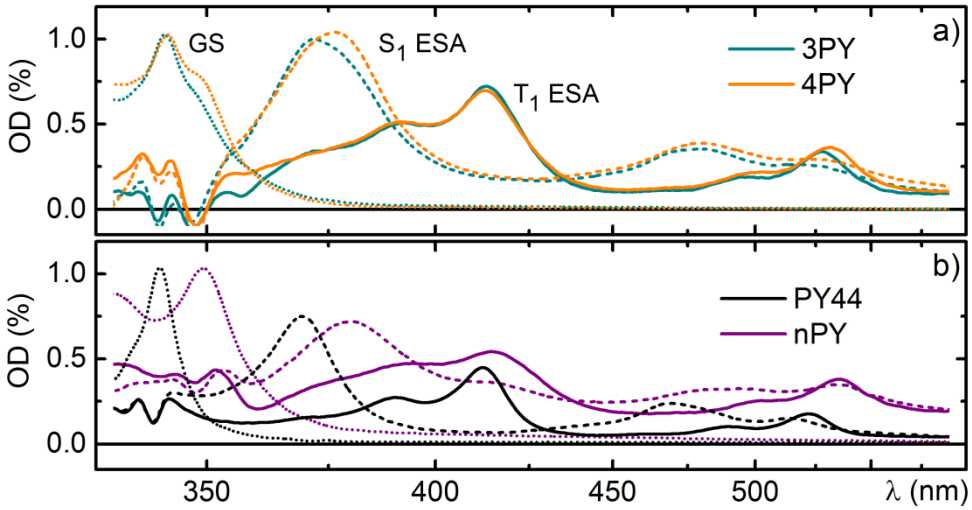

Fig. 4.49: GS (dots) as well as species associated spectra of the S_1 ESA (dashed) and the triplet ESA (solid) obtained from double exponential global fits using the model detailed in Section 4.7.1. Spectra normalized to their respective GS maximum for comparability.

Table 4.14: S_1 ESA decay rate of pyrene oligomers connected at the 4-position excited into their respective S_2-origin with a pulse energy of 200 nJ, degassed, in flow circuit.

compound (in cyclohexane)	**PY44**	**3PY**	**4PY**	**nPY**
S_1 ESA (ns)	90	74	67	37
triplet QY (%)	65	65	70	74

Double exponential global fits reveal a decrease in the lifetimes of the excited singlet state with increasing chain length in favor of a faster and slightly more efficient ISC. Table 4.14 lists the obtained times as well as triplet QY values obtained by applying the 'monomer-like' model presented in Section 4.7.1. Species associated spectra are plotted in Fig. 4.49, revealing that all observed ESA features broaden with increasing number of pyrene units.

All compounds feature a blue fluorescence band reminiscent of the pyrene monomer, though with less fine structure (cf. Fig. 4.50a). Fitted decay times are similar to those obtained from TA listed in Table 4.14. In addition to the monomer-like fluorescence (blue line), nPY features a broad unstructured fluorescence with a short lifetime of only 2.7 ns (violet line).

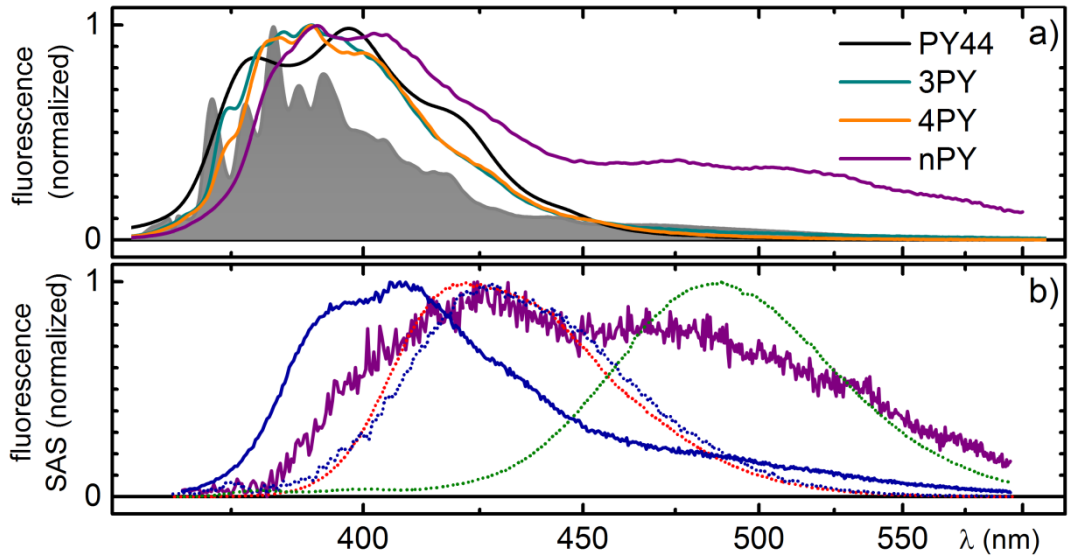

Fig. 4.50 (a) Normalized time integrated fluorescence spectra compared to pyrene (gray) and (b) SAS obtained from global analysis of a streak camera measurement: 2.7 ns (violet) and 21 ns (blue). For comparison the species associated spectra of short lived components obtained from PY11 (1.7 ns, red dots) and PY11-C6 (1.7 ns, blue dots) are plotted, as well as the excimer signature obtained from PY11-C3 (58 ns, green dots).

This new band appears blue shifted compared to the known pyrene excimer fluorescence (green line). A short lived unstructured fluorescence blue shifted from the classical excimer signature is also observed in the directly linked compounds PY11 and PY44. Furthermore, a similar feature with a few ns life time appeared in PY11-C6 (blue dots) where it was initially attributed to an impurity. Both for PY11-C6 and nPY no clear signatures with corresponding decay times can be found in TA. When an additional few ns decay is fitted to the nPY TA, it does not greatly improve the fit and the associated spectrum is not distinct, but reproduces the S_1 ESA spectrum almost exactly.

Fig. 4.50b compares all of the abovementioned fluorescence signatures. It seems as if a combination of the known green excimer fluorescence and the fluorescence signal obtained from PY11 could reproduce the observed nPY spectrum. An interpretation of this previously unobserved feature can be attempted by pointing out that pyrene units sterically inhibited from attaining the perfect sandwich geometry can still interact with one another. While the system will not be able to reach a stabilization as pronounced as the classical excimer (cf. Section 4.1.2), some excitonic splitting of the energies of the involved orbitals is conceivable. This would explain why the new signal appears closer to the monomer fluorescence. The lack

of structure indicates that there is no corresponding ground state minimum for this configuration. As discussed for PY11, the presence of the second pyrene unit will change the symmetry of the entire system, making the fluorescence more efficient and reducing its decay time. Polymers comprised solely of pyrene units linked at the 4-position are still uncommon, yet for other compounds helical structures have been reported [Fig11, Kee15].

The conclusion would be that when the chain becomes long enough, directly linked polypyrenes and dimers with a long spacer (like PY11-C6) can find configurations where their π-systems can somewhat interact, albeit at a larger distance and probably not in a perfectly parallel orientation, leading to 'short-lived excimer'. Linking pyrene units at the 4-position facilitates minimal interaction between neighboring units and preserves most of the features of the monomer, like the long-lived triplet state and a blue fluorescence with a life time of at least several tens of nanoseconds. While the S_1 state lifetime drops by ca. 60% when polymerized, the triplet yield is only slightly increased w.r.t. the monomer. These features make pyrenes linked at the 4-position an interesting candidate for functionalized materials.

5 Conclusions and Future Perspectives

This chapter summarizes the conclusions reached in Chapters #2 to #4 and outlines possible future directions for the respective projects.

Researchers in transient absorption spectroscopy employ ever shorter pump pulses in order to resolve the fastest dynamics. The so-called 'coherent artifact' often obscures the early time dynamics. For chirped broadband probe pulses, such as bulk generated white light, simulations indicate that this unwanted distortion does not narrow infinitely with decreasing pump pulse duration. Instead, there is an optimum pump pulse duration beyond which the interval modulated by the artifact broadens due to spectral interference. For parameters typical of the setup used herein, this optimum is a pump pulse duration of ca. 27 fs, which can be readily achieved with a NOPA and prism compressor. Accurate modeling of the coherent artifact is crucial in order to extract meaningful information at early pump probe delay times. Chapter #2 illustrated the importance of cross phase modulation in the modeling of the coherent artifact in the VIS/NIR. Depending on the probe chirp, artifacts can exhibit interference fringes obscuring molecular dynamics up to several hundreds of fs. Analytical models for the cross phase modulation induced coherent artifact assume idealized pump and probe pulses. Yet, the artifact asymmetry is found to correlate with modulations in the probe spectrum. Hence, while they allow inference of meaningful pulse parameters, analytical models are ill-suited as fit functions for broadband TA signals. The novel parameterization Fcos presented in Chapter #2 removes this constraint.

$$\begin{aligned} \mathrm{F\cos}(\lambda,\Delta t) = \cos\left(B(\lambda)\cdot(\Delta t-\Delta t_0)^2+\Phi(\lambda)\right)\cdot\left\{A_0(\lambda)\cdot\exp\left[\frac{-4\ln 2\left(\Delta t-\Delta t_0(\lambda)\right)^2}{\tau(\lambda)^2}\right]\right. \\ \left. -A_1(\lambda)\cdot\frac{8\ln 2}{\tau(\lambda)^2}\left(\Delta t-\Delta t_0(\lambda)\right)\cdot\exp\left[\frac{-4\ln 2\left(\Delta t-\Delta t_0(\lambda)\right)^2}{\tau(\lambda)^2}\right]\right\} \end{aligned} \tag{5.1}$$

Here, the fit parameters are A_0, A_1, τ, Φ, B and the time origin Δt_0. This is only one additional parameter w.r.t. to the commonly used combined Gaussian and derivative model. The frequency factor B and phase Φ allow reproduction of artifact fringes independent of the signals envelope. For coherent artifacts generated by two photon absorption and cross phase modulation Fcos yields a better accuracy in the determination of Δt_0 than the commonly used Gaussian & derivative model, while reproducing the signals much more accurately.

The new parameterization will likely improve future data analysis, especially due to its very accurate reproduction of the varying artifact shapes for a wide range of experimental parameters. An obvious next step is the parameterization of propagation effects like group delay dispersion.

While in the most common moderately chirped case the width of the artifact's envelope and the cross correlation width are very similar, the simulations presented here suggest that the fitted width of the artifact is no longer an accurate measure when spectral interference contributes significantly. The new information obtained from the analysis herein provides an interesting perspective for future work: the best way to quantify the time resolution and its connection to the probe chirp and cross correlation width is not straightforward and remains a focus of current research [Pol10].

In Chapter #3 this new flexibility was exploited for accurate analysis of probe pulses with strongly modulated group delay. The method presented utilizes the coherent artifact to determine the group delay characteristics of dielectric mirrors with an accuracy better than ±1 fs from the UV/VIS to the NIR. While this pump probe method yields comparable accuracy to the standard technique white light interferometry, it has the added capability of being sensitive to pulse deformation and splitting, providing a simple and quantitative tool to determine the applicability of a mirror at hand for a given task. Measurements described herein concentrate on the UV/VIS spectral region, but this technique is in principle applicable from 225 nm to at least 1600 nm using white lights generated according to [Rie13, Bra14a].

Custom broadband high reflectors with controlled group delay were cross-examined using both interferometric and pump probe techniques and recent, commercially available ultrabroadband high reflectors were evaluated. Instead of immediately dismissing an off the shelf broadband mirror for its unspecified group delay, it can be worthwhile to quantify how bad its group delay fluctuations really are in the spectral range needed for a specific application. For example, Balzers DIFLEX 1100 mirrors could be applied in a TA setup to guide the probe light to the detectors after interaction with the sample, where the temporal structure is no longer an issue. Also, short pulse applications may in fact be possible in the range up to approximately 450 nm. With recent advances in broadband coating technology as well as broadband spectroscopy, mirror characterization will play an increasingly important role, since GD data is often kept a secret by vendors for fear of plagiarism.

Chapter #4 revealed new information on the pyrene excimer dynamics, partially contradicting and augmenting previous models. These models are fundamental not only to publications from the 1960's, but with pyrene's many modern applications also to recent studies and textbooks [Bir63, Bir75, Win93, Tur10, Duh12, Han13].

Overlapping bands detrimentally impact the analysis of fluorescence decays. In combination with a disregard for transient effects of diffusion this has lead to unnecessarily complex models for the excimer formation of pyrene. Simulations of fluorescence decays including the commonly neglected transient contribution to the rate of diffusion resolve inconsistencies in prior publications [Bir63, Del79, Han13]. Combining broadband measurements of time resolved fluorescence and transient absorption allows the decomposition of spectrally overlapping signatures, which results in a clearer and more complete picture of the dynamics.

A new, simplified rate model describes the room temperature nanosecond dynamics of all compounds investigated herein except PY11. There is no need to include a back transfer from the excimer or contributions due to different conformers in linked dimers. Contributions from TTA can also be neglected on the nanosecond timescale. Using this model, the TA spectra of the S_1-, excimer- and triplet states was retrieved in the VIS/NIR with high accuracy. New information was uncovered regarding the charge transfer character of the excimer and the role of the triplet state in excimer formation [Bir63, Mar89, Med66].

Even though pyrene in cyclohexane does not strictly exhibit pseudo first order behavior, its dynamics can be described by a sum of exponentials to reasonable accuracy. When modeling with exponentials, the transient contribution to the rate of diffusion causes increasingly exaggerated rates towards higher concentrations. Taking this into account, the monoexponential decay of the monomer fluorescence indicates an efficiency of the excimer formation for pyrene in cyclohexane of ca. $p = 0.82$, corresponding to an excimer formation rate $k_{MD} = 5.71 \cdot 10^9 M^{-1}s^{-1}$ in cyclohexane at room temperature. An efficiency less than unity can be explained by an alignment constraint: molecules colliding an angle unfavorable for π-orbital overlap can drift apart again without forming an excimer [Han13]. Transient effects also affect the growth and decay rates of the excimer fluorescence. The corresponding rise and decay amplitudes have the same magnitude as long as the transient contribution is negligible. Slight deviations from this equality may be indicative of preassociated dimers, but can also stem from the transient contribution to the rate of diffusion.

The evolution of the pyrene triplet state was studied in transient absorption experiments. A flow circuit was used to avoid photoproducts, limiting the residual oxygen concentration in cyclohexane to ca. 0.15 mM - a significant reduction compared to 2.4 mM under ambient conditions. Yet, despite the use of an inline degasser and oxygen tight tubing, residual oxygen is found to severely impact both the singlet and triplet dynamics. The overwhelming fraction of the observed triplets is generated by oxygen quenching of the singlet state. Despite this, estimates for triplet and fluorescence quantum yields for all compounds could be extracted by including oxygen quenching in the model. The resulting decay rates for the S_1-state and the excimer are $k_{MG} = 1.45 \cdot 10^6\,s^{-1}$ and $k_{DG} = 1.55 \cdot 10^7 s^{-1}$. The ISC rates are $k_{ISC,M} = 0.48 \cdot 10^6\,s^{-1}$ and $k_{ISC,D} = 0.40 \cdot 10^6 s^{-1}$ for monomer and excimer, respectively. At c = 10 mM the monomer has been replaced by the excimer as the main source of triplet molecules.

PY11-C3 is a good model system for excimer formation and shows no sign of multiexponential decays due to different conformers in cyclohexane. Most of the other linked dimers tested follow dynamics very similar to the pyrene monomer, most notably the directly linked compound PY44, despite the close proximity of the pyrene units. While the linker length can favor or inhibit excimer formation, the position of the linker affects the dynamics drastically for directly linked compounds. PY11 exhibits fast dynamics on the few ns timescale previously undocumented for pyrene.

A logical next step would be the development of a fit algorithm which takes into account the transient contribution to the excimer formation rate. A temperature dependent study could determine at what point a back transfer from the excimer to the excited singlet state becomes relevant. Early measurements reported by Birks et al. [Bir63], indicate interesting effects starting already at temperatures around 310 K, which have to be reevaluated in light of the new information obtained. The original interpretation of a significant backtransfer from the excimer still does not seem likely at this temperature.

Finally, with their tunable properties the pyrene dimers investigated here offer ample opportunity for future studies. When the chain becomes long enough, directly linked polypyrenes and dimers with a long spacer (like PY11-C6) can find configurations where their π-systems can somewhat interact, albeit at a larger distance and probably not in a perfectly parallel orientation. This leads to a less stabilized ‘short lived excimer’. While the properties of pyrenes linked at the 4-position do change when polymerized, they exhibit minimal interaction between neighboring units and preserve at least some of the features of

the monomer, like the long-lived triplet state and a blue fluorescence with a life time of at least several tens of ns. These features make them an interesting candidate for polymerization towards functionalized materials such as organic light emitting diodes (OLEDs), organic photovoltaics, organic field-effect transistors (OFETs), as well as lasers [Fig11, Jia04, Zha07, Mog06, Wan06, Lee11]. More detailed calculations should be performed on PY11 and a chain length-dependent study could help clarify the nature and size of the disturbance causing the dynamics to change so drastically.

6 References

[Aal59] W. Ij. Aalbersberg, G. J. Hoijtink, E. L. Mackor, W. P. Weijland, J. Chem. Soc. **0**, 3049-3054 (1959)

[Agr89] G.P. Agrawal, P.L. Baldeck, R.R. Alfano, Physical Review A **40**, 5063-5072 (1989)

[Alf86] R.R. Alfano, Q.X. Li, T. Jimbo, J.T. Manassah, P.P. Ho, Optics Letters **11**, 626-628 (1986)

[Alf89] R.R. Alfano, *The Supercontinuum Laser Source*, Springer Berlin Heidelberg (1989)

[Alm82] L. M. Almeida, W. L. C. Vaz, K. A. Zachariasse, V. M. C. Madeira, Biochemistry **21**, 5972. (1982)

[Amo09] T. V. Amotchkina, A. V. Tikhonravov, M. K. Trubetskov, D. Grupe, A. Apolonski, V. Pervak, Applied Optics **48**, 949-956 (2009)

[And91] R. Andriessen, N. Boens, M. Ameloot, F. C. De Schryver, Journal of Physical Chemistry **95**, 2047-2058 (1991)

[And92] R. Andriessen, M. Ameloot, N. Boens, F. C. De Schryver, Journal of Physical Chemistry **96**, 314-326 (1992)

[Atk99] P.W. Atkins, R.S. Friedman, *Molecular Quantum Mechanics, 3rd edn*, Oxford Universiy Press, New York (1999)

[Azu64a] T. Azumi, S. P. McGlynn, J. Chem. Phys. **41**, 3131-3138 (1964)

[Azu64b] T. Azumi, A. T. Armstrong, S. P. McGlynn, J. Chem. Phys. **41**, 3839-3852 (1964)

[Bau06] P. Baum, M. Breuer, E. Riedle, G. Steinmeyer, Optics Letters **31**, 2220 - 2222 (2006)

[Bie14] A. Biewald, *Oxygen- and Water free Conditions in Organic Solvents*, Bachelor Thesis, LMU München (2014)

[Bir63] J. B. Birks, D. J. Dyson, I. H. Munro, Proc. Roy. Soc. A **275**, 575-588 (1963)

[Bir63a] J. B. Birks, L. G. Christophorou, Nature **197**, 1064-1065 (1963)

[Bir63b] J. B. Birks, L. G. Christophorou, Spectrochimica Acta **19**, 401-410 (1963)

[Bir65] J.B. Birks, C. L. Braga, M. D. Lumb, Proc. Roy. Soc. A **283**, 83-99 (1965)

[Bir68] J. B. Birks and A. A. Kazzaz, Proc. Roy. Soc. A. **304**, 291-301 (1968)

[Bir70] J. B. Birks, *Photophysics of Aromatic Molecules*, Wiley Interscience, London, (1970)

[Bir75] J. B. Birks, Rep. Prog. Phys. **38**, 903-947 (1975)

[Boh90] C. Bohne, E. B. Abuin, J. C. Scaiano, J. Am. Chem. Soc. **112**, 4226-4231 (1990)

[Bou09] J. Bouwman, D. M. Paardekooper, H. m. Cuppen, H. Linnartz, L. J. Allamandola, The Astrophysical Journal 700, 56-62 (2009)

[Bra14] M. Bradler and E. Riedle, JOSA B **31**, 1465-1475 (2014)

[Bra14a] M. Bradler, *Bulk continuum generation: The ultimate tool for laser applications and spectroscopy. From new insights to ultrafast amplifiers and spectrometers*, Dissertation, LMU München (2014)

[Bur04] A. I. Burshtein in Advances in Chemical Physics, Vol. **129**, S. A. Rice (ed.), Wiley & Sons, New York (2004)

[Col49] F. C. Collins and G. E. Kimball, J. Colloid. Sci. **4**, 425 (1949)

[Con03] P. B. Conibear, C. R. Bagshaw, P. G. Fajer, M. Kovacs, A. Malnasi-Csizmadia, Nature Structural Biology **10**, 831-835 (2003)

[Con08] P. Conlon, C. J. Yang, Y. Wu, Y. Chen, K. Martinez, Y. Kim, N. Stevens, A. A. Marti, S. Jockusch, N. J. Turro, W. Tan, J. Am. Chem. Soc **130**, 13058 (2008)

[Cor15] J. Jara-Cortés, T- Rocha-Rinza, J. Hernández-Trujillo, Comp. Theor. Chem. **1053**, 220-228 (2015)

[Cry16] https://www.crystran.co.uk/optical-materials/optical-glass-n-bk7-and-others

[Das83] P. K. Das, J. Chem. Soc., Faraday Trans. I **79**, 1135-1145 (1983)

[Del79] J. F. Delouis, J. A. Delaire, N. Ivanoff, Chem. Phys. Lett. **61**, 343-346 (1979)

[Des02] G. R. Desiraju, Accounts of Chemical Research **35**, 565-573 (2002)

[Des99] G. R. Desiraju, T. Steiner, *The Weak Hydrogen Bond in Structural Chemistry and Biology*, Oxford University Press (1999)

[Did96] S. Diddams, J.-C. Diels, JOSA B **13**, 1120-1129 (1996)

[Die07] B. Dietzek, T. Pascher, V. Sundström, A. Yartsev, Laser Physics Letters **4**, 38-43 (2007)

[Die96] J.C. Diehls, W. Rudolph, *Ultrashort Laser Pulse Phenomena*, Academic Press, San Diego (1996)

[Don84] D.C. Dong and M. A. Winnik, Canadian Journal of Chemistry **62**, 2560-2565 (1984)

[Duh12] Duhamel, J. Langmuir **28**, 6527-6538 (2012)

[Dyk98] D. A. v. Dyke, B. A Pryor, G. Smith, M. R. Topp, J. Chem. Ed. **75**, 615-620 (1998)

[Far73] J. A. Farrington, M. Ebert, E. J. Land, K. Fletcher, Biochim. et Biophys. Acta **314**, 372-381 (1973)

[Fig11] T. M. Figueira-Duarte, K. Müllen, Chemical Reviews **111**, 7260-7314 (2011)

[Fit06] P. Fita, E. Luzina, T. Dziembowska, C. Radzewicz, A. Grabowska, J. Chem.Phys. **125**, 184508 (2006)

[Fle76] G.R. Fleming, J. M. Morris, G. W. Robinson, Chem.Phys. **17**, 91-100 (1976)

[Foe55] T. Foerster, K. Kasper, Zeitschirft für Elektrochemie **59**, 976-980 (1955)

[Fog95] P. Foggi, L. Pettini, I. Sànta, R. Righini, S. Califano, J. Phys. Chem. **99**, 7439-7445 (1995)

[Fri03] M. Friz and F. Waibel, *Coating materials*, pp. 105–130, in N. Kaiser and H. K. Pulker (eds.), Optical Interference Coatings, Springer-Verlag (2003)

[Göp31] M. Göppert-Mayer, Annals of Physics. **9**, 273–295 (1931)

[Gos05] A. Gosteva, M. Haiml, R. Paschotta, U. Keller, JOSA B **22**, 1868-1874 (2005)

[Gou59] R. G. Gould in P. A. Franken, R. H. Sands (Eds.), *The Ann Arbor Conference on Optical Pumping, the University of Michigan*, OCLC 02460155 (1959)

[Gre94] C. Grewer, H.-D. Bauer, J. Phys. Chem **98**, 4230-4235 (1994)

[Hab16] F. Habel, M. Trubetskov, V. Pervak, Optics Express **24**, 16705-16710 (2016)

[Hab16b] F. Habel, Dissertation, Ludwig Maximilians Universität, München (2016)

[Ham95] P. Hamm, Chemical Physics **200**, 415-429 (1995)

[Han13] A. D. Hanlon, B. H. Milosavljevic, Photochem. Photobiol. Sci. **12**, 787-797 (2013)

[Hir65] F. Hirayama, J. Chem. Phys. **42**, 3163-3171 (1965)

[Hir82] H. Hirano, T. Azumi, Chemical Physics Letters **86**, 109-112 (1982)

[Hir91] Y. Hirata and T. Okada Chemical Physics Letters **187**, 203-207 (1991)

[Hom11] C.Homann, N.Krebs, E.Riedle, Applied Physics B **104**, 783-791 (2011)

[Hue08] R. Huenerbein, S. Grimme, Chem. Phys. **343**, 362-371 (2008)

[Jia04] W.-L. Jia, T. Mc Cormick, Q.-D. Liu, H. Fukutani, M. Motala, R.-Y. Wang; Y. Tao, S. Wang, Journal of Materials Chemistry **14**, 3344-3350 (2004)

[Kal77] K. Kalyanasundaram, J. K. Thomas, J. Am. Chem. Soc. **99**, 2039-2044 (1977)

[Kan15] K. Kaneshima, M. Sugiura, K. Tamura, N. Ishii, Allpied Physics B **119**, 347-353 (2015)

[Kär01] F. X. Kärtner, U. Morgner, R. Ell, T. Schibli, J. G. Fujimoto, E. P. Ippen, V. Scheuer, G. Angelow, and T. Tschudi, JOSA B **18**, 882-885 (2001)

[Kat97] R. Katoh, E. Katoh, N. Nakashima, M. Yuuki, M. Kotani, Journal of Physical Chemistry A **101**, 7725-7728 (1997)

[Kee15] Conversation with Dr. Ashok Keerthi, Max Planck Institute of Polymer Research, Mainz, Germany (19.08.2015)

[Kla09] P. Klán and J. Wirz, *Photochemistry of Organic Compounds*, Wiley&Sons Ltd., Chichester, (2009)

[Kle79] U. K. A. Klein & H.-P. Harr, Chem. Phys. Lett. **63**, 40 (1979)

[Kno88] W. H. Knox, N. M. Pearson, K. D. Li, C. A. Hirlimann, Optics Letters **13**, 574-576 (1988)

[Kov95] A. P. Kovács, K. Osvay, Zs. Bor, Optics Letters **20**, 788-790 (1995)

[Kov99] S.A. Kovalenko, A.L. Dobryakov, J. Ruthmann, N.P. Ernsting, Physical

Review A **59**, 2369-2384 (1999)

[Kre13] N. Krebs, I. Pugliesi, J. Hauer, E. Riedle, New Journal of Physics **15**, 085016 (2013)

[Kre13a] N. Krebs, *New insights for femtosecond spectroscopy*, Dissertation, LMU München (2013)

[Kre94] M. Kreyenschmidt, M. Baumgarten, N. Tyutyulkov, K. Müllen, Angewandte Chemie Intl. Ed. in English **33**, 1957-1959 (1994)

[Kry05] V. N. Krylov, V. G. Bespalov, D. I. Stasel'ko, S. A. Lobanov, E. V. Milogkyadov and G. Seyfang, Optics and Spectroscopy **99**, 798-802 (2005)

[Kub00] P. Kubát, S. Civis, A. Muck, J. Barek, J. Zima, J. Photochem. Photobiol. A **132**, 33-36 (2000)

[Küb15] T. Küblböck, *Eine quantenchemische Untersuchung der elektronischen Anregungen im Pyren und 1,1'-Bipyren*, Bachelor thesis, LMU München (2015)

[Kut13] R.-J. Kutta, T. Langenbacher, U. Kensy, B. Dick, Applied Physics B **111**, 203-216 (2013)

[Lan13] Personal conversation with Prof. H. Langhals, Department for Organic and Molecular Chemistry, LMU München (2013)

[Lap11] A. Lapini, S. M. Vázquez, P. Tourón, M. Lima, Journal of Molecular Structure **993**, 470-473, (2011)

[Lee11] O. P. Lee, A. T. Yiu, P. M. Beaujuge, C. H. Woo, T. W. Holcombe, J. E. Millstone, J. D: Douglas, M. S. Chen, J. M. J. Fréchet, Advanced Materials **23**, 5359-5363 (2011)

[Lee70] R. M. Lees, J. Molec. Sprectrocsc. **33**, 124.136 (1970)

[Les76] H.E. Lessing and A. v. Jena, Chem. Phys. Lett. **42**, 213-217 (1976)

[Lor02] M. Lorenc, M. Ziólek, R. Naskrecki, J. Karolczak, J. Kubicki, A. Maciejewski, Applied Physics B **74**, 19–27 (2002)

[Lor07] V. A. Lórenz-Fonfriá, H. Kandori, Applied Spectroscopy **61**, 428-442 (2007)

[Lor13] D. Lorbach, M. Wagner, M. Baumgarten, K. Müllen, Chem. Comm. **49**,

10578-10580 (2013)

[Mac00] A. Maciejewski, R. Naskrecki; M. Lorenc, Journal of Molecular Structure **555** 1-13 (2000)

[Mai60] T. H. Maiman, Nature **187**, 493–494 (1960)

[Mar87] J. M. G. Martinho and M. A. Winnik, J. Phys. Chem. **91**, 3640-3644 (1987)

[Mar88] J. M. G Martinho, K. Sienicki, D. Blue, M. A. Winnik, J. Am. Chem. Soc. **110**, 7773-7777 (1988)

[Mas74] S. F. Mason, R. H. Seal, D. R. Roberts, Tetrahedron **30**, 1671-1682 (1974)

[Mat99] N. Matuschek, F.X. Kärtner, U. Keller, IEEE J. Quantum Elecrton. **35**, 192-137 (1999)

[Med66] T. Medinger, F. Wilkinson, Trans. Faraday Soc. **62**, 1785-1792 (1966)

[Meg09] U. Megerle, I. Pugliesi, C. Schriever, C. F. Sailer; E. Riedle, Applied Physics B **96**, 215–231 (2009)

[Meg11] U. Megerle, M. Wenninger, R.-J. Kutta, R. Lechner, B. König, B. Dick, E. Riedle, Phys. Chem. Chem. Phys. **13**, 8869-8880 (2011)

[Meg11a] U. Megerle, *Photoinduced molecular dynamics in increasingly complex systems: From ultrafast transient absorption spectroscopy to nanoscopic models*, Doktorarbeit, Ludwig-Maximilians-Universität München (2011)

[Mes05] D. Meschede, *Optik, Licht, Laser*, pp. 35-82, Springer, Berlin (2005), with permission of Springer Nature.

[Mis80] K. Mistelberger, H. Port, Mol. Cryst. Liq. Cryst **57**, 203-226 (1980)

[Mog06] F. Moggia, C. Videlot-Ackermann, J. Ackermann, P. Raynal, H. Brisset, F. Fages, Journal of Materials Chemistry **16**, 2380-2386 (2006)

[Mog10] A. Moghaddam saray, K. Jamishidi-Ghaleh, Journal of Theoretical and Applied Physics **4**, 21-25 (2010)

[Mon06] M. Montali, A. Credi, L. Prodi, M. T. Gandolfi, *Handbook of Photochemistry*, 3rd. Ed., CRC Taylor & Francis, Boca Raton, (2006)

[Mur64] J. N. Murrell and J. Tanaka, Molecular Physics **7**, 363-380 (1964)

[Nag90] K. Naganuma, K. Mogi, H. Yamada, Optics Letters **15**, 393-395 (1990)

[Nak99] K. Nakashima, T. Miyamoto, S. Mashimoto, Chem. Commun., 213-214 (1999)

[Nau03] A.N. Naumov, A.M. Zheltikov, Applied Physics B **77**, 369–376 (2003)

[Neu99] F.V.R. Neuwahl, P. Foggi, Laser Chem. **19**, 375 (1999)

[Nue09] P. Nuernberger, K.F. Lea, A. Bonvalet, T. Polack, M. H. Vos, A. Alexandrou, M. Joffre, Optics Letters **34**, 3226-3228 (2009)

[Pab12] S. Pabst, A. Sytcheva, A. Moulet, A. Wirth, E. Goulielmakis, R. Santram Phys. Rev. A **86**, 063411 (2012)

[Par62] C. A. Parker , C. G. Hatchard, Trans. Faraday Soc. **59**, 284-295 (1962)

[Par68] C.A. Parker, *Photoluminescence of Solutions. With Applications to Photochemistey and Analytical Chemistry*, Elsevier, Amsterdam (1968)

[Pat70] L. K. Patterson, G. Porter, M. R. Topp, Chem- Phys. Lett. **7**, 612-614 (1970)

[Pat77] L. K. Patterson, R. D. Small Jr., J. C. Scaiano, Radiation Research **72**, 218-225 (1977)

[Pol07] D. Polli, M.R. Antognazza, D. Brida, G. Lanzani, G. Cerullo, S. De Silvestri, Chemical Physics **350**, 42-55 (2008)

[Pol10] D. Polli, D. Brida, S. Mukhamel, G. Lanzani, G. Cerullo, Phys. Rev. A **82**, 053809 (2010)

[Pom98] S. Pommeret, R. Naskrecki, P. v.d. Meulen, M. Ménard, G. Vigneron, T. Gustavsson, Chem. Phys. Lett. **288**, 833-840 (1998)

[Pos71] M. F. M. Post, J. Langelaar, J. D. W. van Voorst, Chem. Phys. Lett. **10**, 468-472 (1971)

[Pos76] M. F. M. Post, J. Langelaar, J. D. W. van Voorst. Chem. Phys. Lett. **42**, 133-136 (1976)

[Ras01] M. Rasmusson, A. N. Tarnovsky, E. Åkesson, V. Sundström, Chem. Phys. Lett. **335**, 201-208 (2001)

[Raz16] O. Razskazovskaya, M. Th. Hassan, T.T. Luu, E. Goulielmakis, V. Pervak, Optics Express **24**, 13628-13633 (2016)

[Rei14] R. Reiel, *Investigation of vibrational cooling and ionic spectra with time resolved spectroscopy*, Master Thesis, LMU München (2014)

[Rei15] S. Reiter, *Electronic excitation processes in pyrene dimers and excimers*, Bachelor thesis, LMU München (2015)

[Rey90] P. Reynders, W. Kuehnle, K. A. Zachariasse, Journal of Physical Chemistry **94**, 4073-4082 (1990)

[Ric14] A. Richter, *Testing the photostability of spectroscopically relevant specimen – A measurement of the reaction-quantum-yield via online-monitoring of the spectral behaviour*, Bachelor Thesis, LMU München (2014)

[Ric85] A. Rice in Comprehensive Chemical Kinetics, Vol. 25, *Diffusion-Limited Reactions*, C. H. Bamford, C. F. H. Tripper and R. G. Kompton, (eds.), Elsiever, Amsterdam (1985)

[Rie13] E. Riedle, M. Bradler, M. Wenninger, C. F. Sailer, I. Pugliesi, Faraday Discussions **163**, 139-158 (2013)

[Roy11] P. Roy, A. K. Jana, S. Das, D. N. Nath, Chem. Phys. Lett. **516**, 182-185 (2011)

[Rys11] G. Ryseck, T. Schmierer, K. Haiser, W. Schreier, W. Zinth, P. Gilch, Chem. Phys. Chem. **12**, 1880-1888 (2011)

[Sal83] P.R. Salvi, O. Foggi, E. Catellucci, Chem. Phys. Lett. **98**, 206-210, (1983)

[Sch16] S. Schlichting, T Willemsen, H. Ehlers, U. Morgner, D. Ristau, Optics Express **24**, 22516-22527 (2016)

[Sch73] H. Schomburg, H. Staerk, A. Weller, Chem. Phys. Lett. **22**, 1-4 (1973)

[Shi07] J. Shirdel, A. Penzkofer, R. Procházka, Z. Shen, J. Strauss, J. Daub, Chemical Physics **331**, 427-437 (2007)

[Shi11] S. Shirai, S. Iwata, T. Tani, S. Iganaki, J. Phys. Chem. A **115**, 7687-7699 (2011)

[Shi66] T. Shida, W. H. Hamill, J. Chem. Phys. **44**, 4372-4377 (1966)

[Sie87] A. Siemiarczuk, W. R. Ware, Chem. Phys. Lett. **140**, 277-280, (1987)

[Sie89] A. Siemiarczuk, W. R. Ware, Chem. Phys. Chem. **93**, 7609-7618 (1989)

[Sil85] S. De Silvestri, J.G. Fujimoto, E.P. Ippen, Chem. Phys. Lett. **116**, 146-152 (1985)

[Sla15] C. Slavov, H. Hartmann, J. Wachtveitl, Analytical Chemistry **87**, 2328-2336 (2015)

[Sli70] M. A. Slifkin, R. H. Walmsley, Journal of Physics E **3**, 160-162 (1970)

[Smo17] M. V. Smoluchowski, Z. Phys. Chem. **92**, 129 (1917)

[Sna83] M. J. Snare, P. J. Thistlethwaite, K. P. Ghiggino, J. Am. Chem. Soc. **105**, 3328-3332 (1983)

[Son88] M. F. Sonnenschein, R. G. J. Weiss, Physical Chemisrty **92**, 6828-6835 (1988)

[Sto04] I. H. M. v. Stokkum, D. S. Larsen,R. v. Grondelle, Biochimica et Biophysica Acta **165**7, 82-104 (2004)

[Szi94] R. Szipöcs, K. Ferencz, C. Spielmann, F. Krausz, Optics Letters **19**, 201-203 (1994)

[Szi97] R. Szipöcs and A. Köházi-Kis, Applied Physics B **65**,115–135 (1997)

[Tok96] E.Tokunaga, A Terasaki, T. Kobayashi, JOSA B **13**, 496-513 (1996)

[Tow58] A. L. Schawlow and C. H. Townes, Phys. Rev. **112**, 1940-1949 (1958)

[Tru13] M.K.Trubetskov, M. von Pechmann, I. B. Angelov, K. L. Vodopyanov, F. Krausz, V. Pervak, Optics Express **21**, 6658-6669 (2013)

[Tsu95] A. Tsuchida, T. Ikawa, T. Tomie, M. Yamamoto, J. Phys. Chem. **99**, 8196-8199, (1995)

[Tur91] N. J. Turro, V. Ramamurthy, J. C. Scaiano, *Modern Molecular Photochemistry of Organic Molecules*, University Science Books, Sausalito, CA (1991)

[Tur10] N. J. Turro, *Modern Molecular Photochemistry*, University Science Books, Sausalito, CA (2010)

[Wah16] J. K. Wahlstrand, S. Zahedpour, H.M. Milchberg, JOSA B. **33**, 1476 (2016)

[Wan03] B. C. Wang, J.-C. Chang, H.-C. Tso, H.-F. Hsu, C.-Y. Cheng, J. Mol. Struct. (THEOCHEM) **629**, 11-20 (2003)

[Wan06] Y. Wang, H. Wang, Y. Liu, C.-a. Di, Y. Sun, W. Wu, G. Yu, D. Zhang, D. Zhu, J. Am. Chem. Soc. **128**, 13058-13059 (2006)

[Wan99] J.K. Wang, T.-L. Chiu, C.H. Chi, C.-K. Sun, JOSA B **33**, 651-661 (1999)

[Wat82] T. Watanabe, K. Honda, J. Phys. Chem. **88**, 2617-2619 (1982)

[Wei85] A.M. Weiner, J.G. Fujimoto, E.P. Ippen, Optics Letters **10**, 71-73 (1958)

[Wil11] M. W. B. Wilson, A. Rao, J. Clark, R. S. S. Kumar, D. Brida, G. Cerullo, R. H. Friend, J. Am. Chem. Soc. **133**, 11830-11833 (2011)

[Wil99] F. Wilkinson, A. A. Abdel-Shafi, J. Phys. Chem. A **103**, 5425-5435 (1999)

[Win93] F. M. Winnik, Chem. Rev. **93**, 587-614 (1993)

[Wir11] A. Wirth, M. Th. Hassan, I. Grguraš, J. Gagnon, A. Moulet, T. T. Luu, S. Pabst, R. Santra, Z. A. Alahmed, A. M. Azzeer, V. S. Yakovlev, V. Pervak, F. Krausz, E. Goulielmakis, Science **334**, 195-200, 2011

[Wit15] E. Wittmann, M. Bradler, and E. Riedle, K. Yamanouchi et al. (eds.), Ultrafast Phenomena XIX, Springer Proceedings in Physics **162**, 725-728 (2015)

[Yad15] A. Yadav, N. D. Kurur, S. Pandey, Journal of Physical Chemistry B **119**, 13367-13378 (2015)

[Yan11] S. Yan, M. T. Seidel, H-S. Tan, Chem. Phys. Lett. **517**, 63-40 (2011)

[Zac76] K. Zachariasse, W. Kühnle, Zeitschrift für Physikalische Chemie **101**, 267-276 (1976)

[Zac78] K. A. Zachariasse, Chemical Physics Letters **57**, 429-432 (1978)

[Zac84] K. A. Zachariasse, G. Duveneck, R. J. Busse, J. Am. Chem. Soc. **106**, 1045-1051 (1984)

[Zac85] K. A. Zachariasse, R. J. Busse, G. Duveneck, W. Kühnle, Chemical Physics Letters **113**, 337-343 (1985)

[Zac85a] K. A. Zachariasse, R. J. Busse, G. Duveneck, W. Kühnle, Journal of Photochemistry **28**, 237-253 (1985)

[Zac88] K. A. Zachariasse, G. Striker, Chemical Physics Letters **145**, 251-254 (1988)

[Zac91] K. Zachariasse, W. Kühnle, U. Leinhos, P. Reynders, G. Striker, Journal of Physical Chemistry **95**, 5476-5488 (1991)

[Zac99] K. A. Zachariasse, A. L. Macanita, W. Kühnle, Journal of Physical Chemistry B **105**, 9356-9365 (1999)

[Zan78] M. Zander, Zeitschrift für Naturforschung **33**, 998-1000 (1978)

[Zha07] Z. Zhao, X. Xu, Z. Jiang, P Lu, G. Yu, Y. Liu, The Journal of Organic Chemistry **72**, 8345 (2007)

[Zio01] M. Ziólek, M. Lorenc, R. Naskrecki, Appl. Phys. B **72**, 843–847 (2001)

Appendix

A Mathematical Derivations and Supplemental Information

A1 Excimer Stabilization Estimate

A1 Estimate Stabilization of Pyrene Excimer via Dipole-Dipole Interaction [Kla09]
Baudisch, 20.08.2017

$m_e := 9.10938 \cdot 10^{-31}\ kg$ $e := 1.602 \cdot 10^{-19}\ C$ $eV := e \cdot \frac{J}{C}$

molar absorption coefficient

$\varepsilon := 1 \cdot 10^{3}\ L \cdot mol^{-1} \cdot cm^{-1}$

average frequency (& wavenumber) of S1 transition

$f_{avg} := \frac{c}{355\ nm} = (8.445 \cdot 10^{14})\ \frac{1}{s}$ $v_{avg} := \frac{1}{355\ nm} = 2.817\ \frac{1}{\mu m}$

Transition dipole moment M proportional to oscillator strength [Kla09]: $f_{01} := \frac{8\ \pi \cdot m_e \cdot f_{avg}}{3 \cdot h \cdot e^2} \cdot |M_{01}|^2$

Obtain "Experimental" f_{01} : $f_{01}(\varepsilon) := 4.3 \cdot 10^{5} \cdot \int \frac{\varepsilon(v)}{L \cdot mol^{-1} \cdot cm^{-1}}\, dv$ with wavenumber v

Typical width of a transition is 0.3/µm [Kla09] $v := 0.1\ \frac{1}{\mu m}, 0.2\ \frac{1}{\mu m} .. 10\ \frac{1}{\mu m} = \begin{bmatrix} 0.1 \\ \vdots \end{bmatrix} \frac{1}{\mu m}$

$\varepsilon(v) := \varepsilon \cdot \exp\left(-\left(\frac{(v - v_{avg})}{0.3\ \mu m}\right)^2\right)$

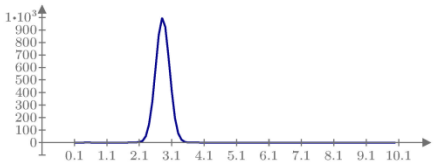

$\varepsilon(v)\ \left(\frac{L}{mol \cdot cm}\right)$

$v\ \left(\frac{1}{\mu m}\right)$

$v_{lo} := 1.1\ \mu m^{-1}$ $v_{hi} := 4.1\ \mu m^{-1}$ $f_{01} := 4.3 \cdot 10^{-5} \cdot \int_{v_{lo}}^{v_{hi}} \frac{\varepsilon(v)}{L \cdot mol^{-1} \cdot cm^{-1}}\, dv \cdot \mu m = 0.023$

Hence:

$M_{01} := \left| \frac{3 \cdot h \cdot e^2}{8\ \pi \cdot m_e \cdot f_{avg}} \cdot f_{01} \right|^{0.5} = (7.767 \cdot 10^{-30})\ C \cdot m$

In Debye: $D := 3.336 \cdot 10^{-30}\ C \cdot m$

$M_{01} = 2.328\ D$

Distance d between pyrene units according to literature is 2.4 to 3.9 Angstrom, therefore pot. E (factor 2 for perfect sandwich geometry): $V(d) := -\frac{2 \cdot M_{01} \cdot M_{01}}{4\ \pi \cdot \varepsilon_0 \cdot d^3}$

$V(3.9\ Angstrom) = -0.114\ eV$ $V(2.4\ Angstrom) = -0.49\ eV$

Total stabilisation of Excimer w.r.t. S1 is > 0.3 eV. So about half of the stabilization can be attributed to non excitonic interactions like charge resonance and orbital overlap / delocalization between rings [Shi11, Cor15, Rei15].

A2 Estimation of Quantum Yields for Monomer-like Compounds

To assess the relative contributions of oxygen quenching and ISC to the total triplet yield, one can recall the results of the well degassed fluorescence study presented in Section 4.6. Therein, a monomer decay rate of $k_M^{lim} = (522\,ns)^{-1} = 1.92 \cdot 10^6\,s^{-1}$ is reached at c = 0.01 mM. We assume this to be the limiting value where no excimer formation or oxygen quenching 'disturb' the S_1 state's dynamics. Under the same conditions, the rate increases to $k_M^{0.1mM} = (413\,ns)^{-1} = 2.42 \cdot 10^6\,s^{-1}$ at $c = 0.1$ mM. This is likely due to a subtle excimer formation, with a rate

$$k_{MD} \cdot 0.1\,mM = k_M^{0.1mM} - k_M^{lim} = 0.50 \cdot 10^6\,s^{-1}. \qquad (A1)$$

All other parameters being equal, the difference between $k_M^{0.1mM}$ and the rate measured in TA $k_M^{TA/0.1mM} = (187\,ns)^{-1} = 5.35 \cdot 10^6\,s^{-1}$ must be due to oxygen quenching. Hence, the oxygen quenching rate $k_{QS}^{TA/0.1mM}[O_2]$ in this experiment was

$$k_{QS}^{TA/0.1mM}[O_2] = k_M^{TA/0.1mM} - k_M^{0.1mM} = 2.93 \cdot 10^6\,s^{-1}. \qquad (A2)$$

According to equation 4.14 this corresponds to a residual oxygen concentration of ca. 0.15 mM, which is a realistic value in the pump circuit used (cf. Section 4.2.5).

The rates determined above lead to oxygen quenching and excimer formation yields of

$$\Phi_{QS}^{TA/0.1mM} = 0.55 \text{ and } \Phi_{MD}^{TA/0.1mM} = 0.09, \qquad (A3)$$

leaving only ca. 36% to the monomer decay, $\Phi_{MG}^{0.1mM} + \Phi_{ISC,M}^{0.1mM} = 0.36$. The excimers do not contribute significantly to the TA because they decay much faster ($k_D = 1.9 \cdot 10^7\,s^{-1}$, cf. Section 4.7.3) than they are formed under these conditions.

According to Table 4.10 the fluorescence QY for 'undisturbed' pyrene $\Phi_{rad}^{lim} = 0.62$. The prompt fluorescence yield of the monomer at c = 0.1 mM in the presence of oxygen is then

$$\Phi_{rad}^{TA/0.1mM} = \Phi_{rad}^{lim} \cdot 0.36 = 0.22, \qquad (A4)$$

which limits the triplet yield from the excited monomer $\Phi_{ISC,M}^{TA/0.1mM}$ to ≤ 14% - about a fourth of the number of triplets generated by oxygen quenching. The maximum achievable total triplet yield is then limited to

$$\Phi_{MT}^{TA/0.1mM} = \Phi_{QS}^{TA/0.1mM} + \Phi_{ISC,M}^{TA/0.1mM} \le 0.69. \qquad (A5)$$

Φ_{rad}^{lim} is the time integrated fluorescence yield, including possible contributions from TTA on longer timescales. In TTA two triplets result in one excited S_1 and one GS pyrene. $\Phi_{rad}^{lim} = 0.62$ therefore constitutes an upper limit to the prompt fluorescence yield. If all fluorescence stemmed from TTA, $\Phi_{ISC,M}^{TA/0.1mM}$ would increase to 0.36, yet this would require the prompt fluorescence to vanish. A strong prompt emission is observed, so the lower limit is the most likely.

The total triplet yield obtained from the modeling is $\Phi_{MT}^{TA/0.1mM} = 0.64$. Assuming that the few excimers do not contribute significantly, the monomer's ISC yield in this experiment was

$$\Phi_{ISC,M}^{0.1mM} = \Phi_{MT}^{TA/0.1mM} - \Phi_{QS}^{TA/0.1mM} = 0.09 \qquad (A6)$$

and the aggregate of fluorescence and internal conversion amounted to

$$\Phi_{MG}^{0.1mM} = 1 - \Phi_{QS}^{TA/0.1mM} - \Phi_{MD}^{TA/0.1mM} - \Phi_{ISC,M}^{TA/0.1mM} = 0.27, \qquad (A7)$$

corresponding to the rates $k_{ISC,M} = 0.48 \cdot 10^6\,s^{-1}$ and $k_{MG} = 1.45 \cdot 10^6\,s^{-1}$.

Without oxygen quenching and excimer formation the ISC yield would have amounted to $\Phi_{ISC,M} = k_{ISC,M} / k_M^{lim} = 0.26$, which would imply $\Phi_{MG} = k_{MG} / k_M^{lim} = 0.74$.

No fully degassed datasets are available for the pyrene derivatives. Yet, since conditions were comparable in TA and streak camera experiments, comparison of singlet decay rates obtained from TA with streak camera measurements under ambient conditions also allow a rough estimate of the oxygen quenching rates. The oxygen concentration in cyclohexane under ambient conditions is 2.4 mM [Mon06], while in the degassed pump circuit the concentration slightly varied across measurements. The O_2 concentration for each TA measurement is estimated via the respective triplet decay time observed, assuming that all triplets are quenched with the same triplet quenching rate k_{QT}. As a reference the pyrene data discussed above is used, where an oxygen concentration of 0.15 mM was determined and the triplet decay time is 3.52 µs. The literature claims an intrinsic triplet lifetime of 180 µs [Sli70], therefore the triplet quenching rate is ca.

$$k_{QT}[O2] = \frac{(3.52\,\mu s)^{-1} - (180\,\mu s)^{-1}}{0.14\,mM} = 1.95 \cdot 10^9\,s^{-1}, \qquad (A8)$$

which is quite close to values reported in the literature [Pat70, Med06, Tur10]. Rearranging A8, the oxygen concentrations for all measurements can be computed via

$$[O_2] = \frac{\left(\tau_{triplet}\right)^{-1} - \left(180\,\mu s\right)^{-1}}{k_{QT}}. \qquad \text{(A8b)}$$

Respective decay times and corresponding oxygen concentrations are listed in Table 4.11. Finally, the obtained oxygen concentrations are used in conjunction with the respective S_1 decay rates k_M to obtain the singlet oxygen quenching rate for each measurement via

$$k_{QS}^{TA} = \frac{k_M^{Fluo/ambient} - k_M^{TA}}{2.4\,mM - [O_2]}, \qquad \text{(A9)}$$

with $k_M^{Fluo/ambient} = 1/19ns$. The quenching rates are listed in Table 4.11. The rates for pyrene and PY11-C6 closely match the quenching rate calculated in Section 4.2.5, the slight variation in the remaining values might be due to slightly altered energy levels of the substituted compounds, leading to slightly slower or faster interaction with triplet oxygen. Non-degassed data is not available for propylpyrene, so it is assumed that the same k_{QS} as for methylpyrene applies. In analogy to the formalism described above (Equations A1 to A7) total as well as intrinsic quantum yields can be computed. Since at 0.1 mM a nonzero excimer formation rate was found (cf. Eq. A1), the same rate is assumed for all compounds. Its quantum yield is, however, less than 10%. As above, any triplet yield from this excimer contribution is neglected. The results with and without the oxygen contribution are summarized in Tables 4.12 and 4.13. Results from measurements with smaller oxygen concentrations are less affected by the assumptions made about the quenching process in the analysis above, which makes them more reliable than the others.

Table A1: Parameters for the estimation of individual singlet quenching rates k_{QS} of pyrene derivatives. The oxygen concentration in cyclohexane under ambient conditions is ca. 2.4 mM (cf. Section 4.2.5).

compound (c = ~ 0.1 mM in cyclohexane)	**ambient fluo. decay (ns)**	**S_1 ESA decay time (ns)**	**T_1 ESA decay time (µs)**	**$c(O_2)$ (mM)**	**k_{QS} ($10^{10} M^{-1} s^{-1}$)**
Pyrene	19	187	3.5	0.15	2.10
1-Methylpyrene	25	130	2.8	0.18	1.46
1-Propylpyrene	--	140	3.7	--	--
1-Bromopyrene	2	2	6.5	0.08	0
PY11-C6	19	140	5.1	0.10	1.97
PY44	15	90	6.0	0.08	2.40

A3 Estimation of Quantum Yields for Excimer-like Compounds

In the analysis of the excimer-like TA measurements, oxygen quenching is taken into account using the same arguments as in the monomer-case (Section A5). For pyrene in well degassed conditions (cf. Section 4.6) the S_1 lifetime reduced from $\tau_M^{lim} = 522\,ns$ to $\tau_M^{10mM} = 12.7\,ns$ at c =10 mM.

It is therefore assumed that the excimer formation rate undisturbed by oxygen quenching is

$$k_{MD} \cdot 10\,mM = k_M^{10mM} - k_M^{lim} = 7.68 \cdot 10^7\,s^{-1}. \qquad (A10)$$

The S_1 decay rate obtained in the partially degassed TA measurement is $k_M^{TA/10mM} = (12\,ns)^{-1} = 8.33 \cdot 10^7 s^{-1}$ and in analogy with Eq. A2 the oxygen quenching rate of the monomer is

$$k_{QS}^{TA/10\,mM}[O_2] = k_M^{TA/10\,mM} - k_M^{10mM} = 4.59 \cdot 10^6\,s^{-1}, \qquad (A11)$$

corresponding to an oxygen concentration on 0.22 mM. The resulting quantum yields for oxygen quenching and excimer formation are

$$\Phi_{QS}^{TA/10mM} = 0.06 \text{ and } \Phi_{MD}^{TA/10mM} = 0.92, \qquad (A12)$$

leaving a maximum of $\Phi_M^{0.1mM} = 0.02$ for the monomer branch. Without the oxygen, the excimer formation would only compete with $k_M^{lim} = 1.92 \cdot 10^6\,s^{-1}$, leading to 98% excimer yield.

Using k_{MT} from the low consideration limit the only free parameters in the model detailed in Section 4.7.1, are dc and k_{DT}. These can be determined by combining the DADS according to equations 4.28 to 4.30, while making sure that the obtained spectra are smooth, all positive and feature no signatures from other states. The resulting SAS are plotted in Fig. 4.41a. The analysis leads to optimized values of $\Phi_{DT}^{TA/10mM} = 0.2$ and $k_{DT}^{TA/10mM} = 3.85 \cdot 10^6 s^{-1}$.

This yield includes a contribution from oxygen quenching of the excimer

$$\Phi_{DT}^{TA/10mM} = \Phi_{ISC,D}^{TA/10mM} + \Phi_{QD}, \qquad (A13)$$

where Φ_{QD} denotes the triplet yield of the excimer due to oxygen quenching. In analogy to Equation A11, the rate for oxygen quenching of the excimer can be estimated by comparing the excimer's decay times from degassed fluorescence and TA. The resulting excimer

quenching rate $k_{QD}^{TA/10\,mM}[O_2] = 3.36 \cdot 10^6 s^{-1}$ is slightly smaller than $k_{QS}^{TA/10\,mM}[O_2]$. It follows that $\Phi_{QD} = 0.175$ and $\Phi_{ISC,D}^{TA/10mM} = 0.025$. The remainder of the excimer population relaxes via $k_{DG} = 1.55 \cdot 10^7 s^{-1}$ and $k_{ISC,D} = 4.03 \cdot 10^5 s^{-1}$. This corresponds to $\Phi_{DG}^{TA/10mM} = 0.8$ in the presence of oxygen, which is slightly larger than the excimer fluorescence yield of 75% reported in [Bir63]. When the oxygen is completely removed, $\Phi_{DG}^{TA/10mM}$ increases to 97.5%. As internal conversion was neglected, these values represent upper limits for the intermolecular excimer's fluorescence QY.

For linked PY11-C3, the monomer decay accelerates to 7 ns, matching the excimer rise. Well degassed measurements are not available here, yet, since most of its properties resemble pyrene very closely, we can assume the intrinsic decay rate k_{Sl}^{lim} obtained for pyrene is still valid here. It is further assumed that the oxygen quenching rates are similar. For an oxygen quenching rate on the order of $k_{QS}[O_2] = 3 \cdot 10^6\, s^{-1}$, the rate of excimer formation is

$$k_{MD} \cdot 0.05\,mM = (7\,ns)^{-1} - k_M^{lim} - k_{QS}[O_2] = 1.38 \cdot 10^8\, s^{-1}, \qquad (A14)$$

almost twice as fast as for pyrene at c = 10 mM. The corresponding oxygen quenching and excimer quantum yields are

$$\Phi_{QS}^{PY11-C3} = 0.02 \text{ and } \Phi_{MD}^{PY11-C3} = 0.97, \qquad (A15)$$

leaving only 1% for the monomer branch. Using the model to reconstruct the SAS from the global fit DADS in analogy to the above treatment, $\Phi_{DT}^{PY11-C3} = 0.2$ is found, the exact same value as for the intermolecular excimer. The resulting SAS for PY11-C3 are shown in Fig. 4.41b. Table A1 summarizes the resulting yields for the monomer and excimer branch of the Jablonski diagram 4.39. Values for oxygen-free conditions were calculated under the assumption that oxygen quenching rates are the same for Pyrene and PY11-C3.

Finally the total triplet quantum yields are computed. The total triplet and fluorescence quantum yields rare given by

$$\Phi_{T1} = \Phi_{QS} + \Phi_{ISC,M} + \Phi_{QD} + \Phi_{MD} \cdot \Phi_{ISC,D} \qquad (A16)$$

Also, upper limits for the total fluorescence quantum yields are given by

$$\Phi_{rad} \le \Phi_{MG} + \Phi_{MD} \cdot \Phi_{DG} \cdot \qquad (A17)$$

Equations A16 and A17 yield $\Phi_{T1} = 0.25$ and $\Phi_{rad} \le 0.75$ for pyrene and $\Phi_{T1} = 0.22$ and $\Phi_{rad} \le 0.78$ for PY11-C3.

A4 Pyrene Anion and Cation Spectra

The pyrene anion spectrum in Fig. 4.42 was obtained via reductive quenching of pyrene by N,N-dimethylaniline (DMA) in acetonitrile (ACN) [Rei14]. This quenching method was first reported by Aalbersberg et. al. [Aal59]. A mixture of 0.4 mM DMA and 0.022 mM pyrene was selectively excited at the pyrene S_2 maximum (334 nm), where DMA has no appreciable absorption (cf. Fig. A1a). The resulting transient absorption dataset is shown in Fig. A1c. In addition to the known pyrene S_1 (blue cursor) and triplet ESA (red cursor), a strong feature appears at 495 nm (green cursor), featuring a distinct time evolution (right panel). It grows with a rate close to the observed S_1 decay, and decays significantly faster than the triplet. Variation of the DMA concentration (cf. Fig. A1e) indicates this contribution is due to the diffusion controlled quenching of singlet excited pyrene molecules by DMA with a quenching rate $k_{Q,anion} = 3.1 \cdot 10^{10}\ mol^{-1}s^{-1}$. The increasing deviation from the S_1 decay rate could be due to the transient contribution to the rate of diffusion (cf. Section 4.6.2). In MeOH a weaker ion signal was detected, while in cyclohexane no ion signal was found. A higher solvent dipole moment is probably favorable as solvent molecules can effectively screen the DMA cation and the pyrene anion from one another, preventing prolonged inter-action and allowing them to separate. The nonpolar environment may also be affecting the energies of the involved states such that charge transfer is inhibited. The anion SAS retrieved from global analysis (cf. Fig. A2) is in agreement with prior results [Aal59, Sch73].

The pyrene cation spectrum was obtained via oxidative quenching using the salt 4,4'-bipyridinium chloride, a.k.a. 'methyl viologen' and 'paraquat' (PQ), which is somewhat more complex [Rei14]. In solution the PQ cation can accept an electron and form a PQ radical. PQ cations interact both with singlet as well as triplet pyrene. Quenching via the triplet state has been studied before [Das83, Nak99]. A mixture of 0.7 mM DMA and 0.026 mM pyrene in MeOH was selectively excited at the pyrene S_2 maximum (334 nm), where PQ has no appreciable absorption (cf. Fig. A1b). The resulting TA dataset is shown in Fig. A1d. Pyrene's triplet signature is hardly noticeable (red cursor), while strong long-lived features emerge after ca. 100 ns (green cursor). Variation of the PQ concentration results in three different quenching rates (cf. Fig. A1f). For the singlet and triplet decays $k_{S1} = 1.57 \cdot 10^{10}\ mol^{-1}s^{-1}$ and $k_{T1} = 4.43 \cdot 10^{9}\ mol^{-1}s^{-1}$. The cation signal grows with a slightly faster rate $k_{cat} = 6.11 \cdot 10^{9}\ mol^{-1}s^{-1}$, which is close to the value reported in [Das83].

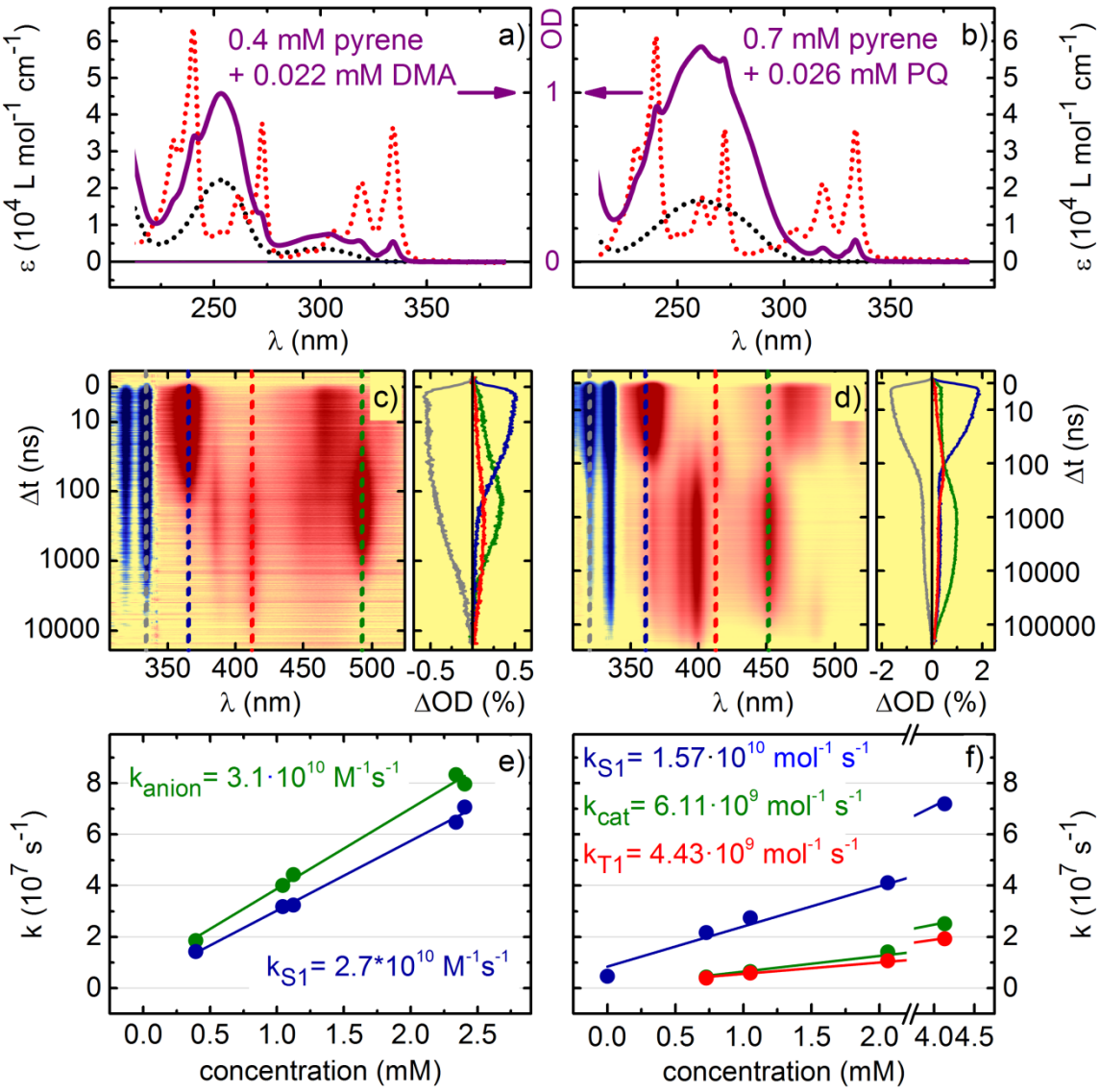

Fig. A1: (a,b) absorption spectra of pyrene, DMA and PQ and the mixtures used in TA. (c,d) TA datasets of pyene+DMA and pyrene+PQ in false color representation, riht panels indicate time traces at positions marked by color coded cursors. (e,f) concentration dependence of the respective ions growth rate (green) as well as singlet (blue) and triplet decay (red) with linear fits.

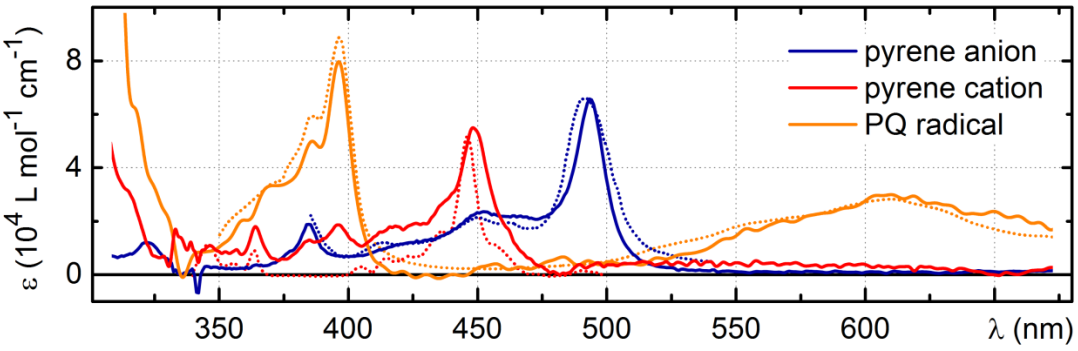

Fig. A2: Retrieved spectra of pyrene anion (solid blue), cation (solid red) and PQ radical (solid yellow) compared to scaled spectra reported in [Sch73], [Bou09] and [Far73], respectively (dots).

Such a detailed analysis is only possible in TA, since only the fast quenching of the singlet state is observable in commonly employed fluorescence quenching experiments. As in reductive quenching, the increasing deviation from the triplet decay rate could be due to the transient contribution to the rate of diffusion (cf. Section 4.6.2). In [Rei14] the dynamics are interpreted such that the product of the singlet quenching quickly relaxes to the GS and does not contribute significantly to the TA. Only ISC prior to the electron transfer makes detection of the ions possible, since the long lifetime of the resulting triplet complex allows the ions to drift apart. Both the PQ radical and the pyrene cation contribute to the observed ESA. Their lifetimes are similar, but can be disentangled via global analysis. The retrieved SAS of the PQ radical agrees well with the literature [Far73, Wat82] (cf. Fig. A2, orange line). The obtained pyrene cation SAS (red line) is quite similar to a spectrum reported in H_2O ice [Bou09], where the authors assign the strongest peaks between 420 nm and 460 nm as well as the weaker bands below 375 nm to the pyrene cation. Additional features are found between 375 nm and 400 nm. Here the perfect baseline reported in [Bou09] could not be reproduced without incurring negative signal above 500 nm. This as well as the broadened main peak may be due to the different environment, yet a product formed by the PQ radical and oxygen also absorbs in this range [Shi66, Pat77, Rei14].

B – Relevant Mathcad Code

B1 Development of the combined Gaussian/ $cos\left(B\cdot\left(t-t_0\right)^2+\phi\right)$ Model "Fcos"

Bastian Baudisch (05.09.16)

This is to document the steps taken in the development of the combined Gaussian/ $cos\left(B\cdot\left(t-t_0\right)^2+\phi\right)$ fit function for coherent artifacts induced by two photon absorption (TPA) and cross phase modulation (XPM). It does not include effects induced by group velocity mismatch (GVM) of pump w.r.t. probe.

The function was devised in analogy to the papers Lor02_ApplPhysB_74_019_2002 and Wah16_JOSAB_33_1476_2016. The resulting formulas for the signals are tested for typical datasets.

$fs := 10^{-15}\ s$ **ORIGIN** $:= 1$

Definition of Fitfunctions: 4 fitfunctions are investigated below:

Combination of Gaussian & Derivatives:

A simple fitting model is to use a Gaussian to describe the TPA contribution and the first two derivatives to deal with asymmetries and small wings overshooting into the negative on the sides of the artifact:

$$Gauss\left(A_0,t,t_0,\tau\right) := A_0\cdot\exp\left(\frac{-4\cdot\ln(2)\cdot\left(t-t_0\right)^2}{\tau^2}\right) \qquad Gauss1\left(A_0,t,t_0,\tau\right) := \frac{\mathrm{d}}{\mathrm{d}t}Gauss\left(A_0,t,t_0,\tau\right) \rightarrow -\frac{4\cdot A_0\cdot e^{-\frac{4\cdot\ln(2)\cdot\left(t-t_0\right)^2}{\tau^2}}\cdot\ln(2)\cdot\left(2\cdot t-2\cdot t_0\right)}{\tau^2}$$

$$Gauss2\left(A_0,t,t_0,\tau\right) := \frac{\mathrm{d}^2}{\mathrm{d}t^2}Gauss\left(A_0,t,t_0,\tau\right) \rightarrow \frac{16\cdot A_0\cdot e^{-\frac{4\cdot\ln(2)\cdot\left(t-t_0\right)^2}{\tau^2}}\cdot\ln(2)^2\cdot\left(2\cdot t-2\cdot t_0\right)^2}{\tau^4} - \frac{8\cdot A_0\cdot e^{-\frac{4\cdot\ln(2)\cdot\left(t-t_0\right)^2}{\tau^2}}\cdot\ln(2)}{\tau^2}$$

$$FGauss\left(A_0,A_1,A_2,t_0,\tau,t\right) := A_0\cdot\exp\left(\frac{-4\cdot\ln(2)\cdot\left(t-t_0\right)^2}{\tau^2}\right) + -\frac{4\cdot A_1\cdot e^{-\frac{4\cdot\ln(2)\cdot\left(t-t_0\right)^2}{\tau^2}}\cdot\ln(2)\cdot\left(2\cdot t-2\cdot t_0\right)}{\tau^2} + \frac{16\cdot A_2\cdot e^{-\frac{4\cdot\ln(2)\cdot\left(t-t_0\right)^2}{\tau^2}}\cdot\ln(2)^2\cdot\left(2\cdot t-2\cdot t_0\right)^2}{\tau^4} - \frac{8\cdot A_2\cdot e^{-\frac{4\cdot\ln(2)\cdot\left(t-t_0\right)^2}{\tau^2}}\cdot\ln(2)}{\tau^2}$$

Signal according to Lor02:

Lor02 predicts a Gaussian shaped signal from TPA + a XPM term S(t).

S(t) is derived via $\omega_{probe}(t) := \omega_0 + \beta \cdot t + \Delta\omega(t)$ with $\Delta\omega(t) := -2\, n2 \cdot \omega_0 \cdot \frac{d}{c} \cdot \frac{\mathrm{d}}{\mathrm{d}t} Gauss(A_{pump}, t, t_0, w)$, β being the linear probe chirp coefficient, $n2$ the nonlinear refractive index and d the thickness of the sample.

Defining a Density of modes proportional to $\left(\frac{\mathrm{d}}{\mathrm{d}t}\omega_{probe}(t)\right)^{-1}$ leads to the time dependent Signal $S(t) := 2 \log\left(\left(\frac{1}{\beta}\frac{\mathrm{d}}{\mathrm{d}t}\omega_{probe}(t)\right)\right)$.

Combining the constants $2\, n2 \cdot \omega_0$ into an Amplitude A_1', $\frac{\mathrm{d}}{\mathrm{d}t}\omega_{probe}(t) = \left(\beta + \frac{\mathrm{d}^2}{\mathrm{d}t^2} Gauss(A_0, t, t_0, w)\right)$, so S(t) becomes:

$$S(\beta, A_1', t_0, w, t) := 2 \log\left(1 - \frac{A_1' \cdot e^{-\frac{(t-t_0)^2}{w^2}} \cdot (2 \cdot t - 2 \cdot t_0)^2}{\beta \cdot w^4} + \frac{2 \cdot A_1' \cdot e^{-\frac{(t-t_0)^2}{w^2}}}{\beta \cdot w^2}\right)$$

Obviously, the constant β can also be included in the Amplitude. Adding a Gaussian for the TPA contribution yields the Fitfunction:

$$FLor02(A_0, A_1, t_0, \tau, t) := A_0 \cdot \exp\left(\frac{-4 \cdot \ln(2) \cdot (t - t_0)^2}{\tau^2}\right) + 2 \log\left(1 - \left(\frac{16 \cdot A_1 \cdot e^{-\frac{4 \cdot \ln(2) \cdot (t-t_0)^2}{\tau^2}} \cdot \ln(2)^2 \cdot (2 \cdot t - 2 \cdot t_0)^2}{\tau^4} - \frac{8 \cdot A_1 \cdot e^{-\frac{4 \cdot \ln(2) \cdot (t-t_0)^2}{\tau^2}} \cdot \ln(2)}{\tau^2}\right)\right)$$

This function is completely symmetric and can therefore not take into account asymmetries in the artifacts.

Signal according to Wah16:

The model described in Wah16 approximately describes the XPM induced probe phase shift as

$$\Delta\Phi(t) := \frac{4\,\pi \cdot n_2 \cdot L}{\lambda} \cdot I(t)$$

with $n2$ the nonlinear refractive index, L the thickness of the sample and $I(t)$ the Gaussian pump intensity profile. The resulting signal in the frequency domain is:

$$\Delta S_{pr}(\omega) := -\left|\Delta\Phi(\omega-\omega_0)\cdot\overline{E_{pr}}(\omega_0)\cdot E_{pr}(\omega)\right|\cdot\left[\pi\cdot\left|\beta(\omega_0)\right|\right]^{\frac{-1}{2}}\cdot cos\left(\Phi_S(\omega)-\Phi_S(\omega_0)+(\omega_0-\omega)\,t+\frac{\pi}{4}\right)$$

with E_{pr} ($\overline{E_{pr}}$)the unperturbed (unperturbed) Gaussian spectrum, β the second order supercontinuum chirp coefficient, t the pump probe delay and Φ_S the spectral phase, which contains terms of at least the order ω^2 :

$$\Phi_S(\omega) := \beta(\omega_{central})\cdot(\omega-\omega_{central})^2+\beta_2(\omega_{central})\cdot(\omega-\omega_{central})^3+\ldots$$

Hence, the fitfunction for the XPM induced artifact in the frequency domain should take the form $F(\omega) := E\cdot cos\left(C_1\cdot(\omega-\omega_{central})^2+C_2\right)$ with an Envelope E and fit paramters C_i.
As has been agrued in Lor02, for small perturbations of the linear chirp $\omega_{probe}(t) := \omega_0+\beta\cdot t$ the time dependence can be simply obtained via substitution:

$$t' \leftarrow \frac{(\omega-\omega_0)}{\beta}$$

Using a Gaussian envelope E , since $\Delta\Phi$, E_{pr} and $\overline{E_{pr}}$ are Gaussian, we arrive at the Fitfunction:

$$FWah16(A_0, t_0, w, B, \phi, t) := \overrightarrow{A_0\cdot\exp\left(-\frac{(t-t_0)^2}{w^2}\right)\cdot\cos\left(B\cdot(t-t_0)^2+\phi\right)}$$

With fit paramters A_0 , A_1 , t_0 , a width w that corrsponds to the width of the Envelope, not the IRF, a periodicity parameter B that parameterizes how fast the frequency of the fringes changes and a phase ϕ . This function is completely symmetric and can therefore not take into account asymmetries in the artifacts.

For illustration the graphs below show $\overrightarrow{E_0 \cdot cos\left(B \cdot t^2 + \phi\right)}$ for different ϕ:

$F\left(E_0, B, \phi, t\right) := \overrightarrow{E_0 \cdot \cos\left(B \cdot t^2 + \phi\right)}$ $\quad E_0 := 1$ $\quad B := 12 \cdot \frac{1}{s^2}$ $\quad t := -2\ s, -1.99\ s .. 2\ s$

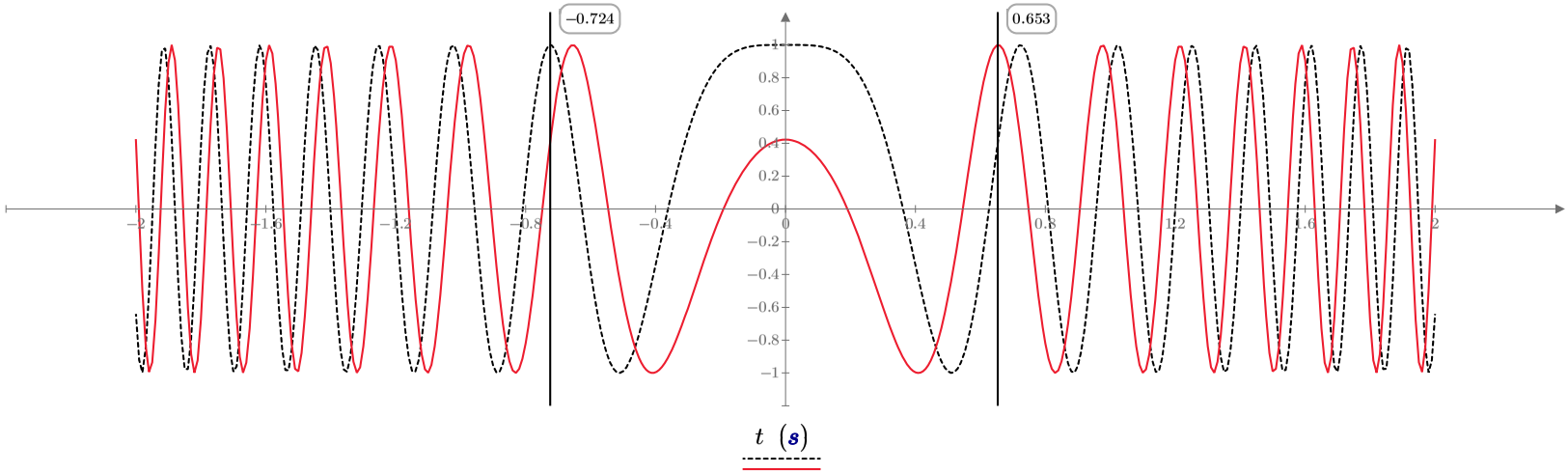

$F\left(E_0, B, 0°, t\right)$

$F\left(E_0, B, 65°, t\right)$

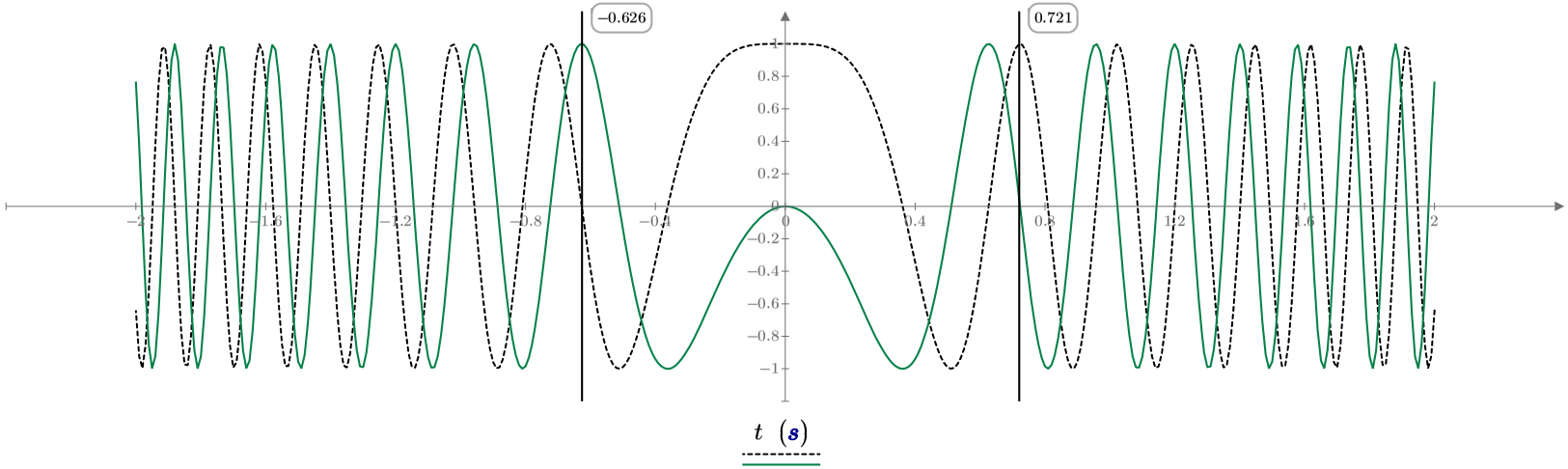

$F\left(E_0, B, 0°, t\right)$

$F\left(E_0, B, \frac{\pi}{2}, t\right)$

Signal according to Kov99:

The most general model neglecting GVD has been proposed by Kovalenko et al. See [Kov99]

Taking into account that in [Kov99] the white light is delayed, so the delay time goes backwards, the resulting signal in the frequency domain is (Kov99, Equation 25):

$$FKov(A_0, t_0, \tau_1, \tau_2, \beta, t) := -A_0 \cdot \mathrm{Im}\left(\sqrt{\exp\left(-\frac{8\ln(2)\,(t-t_0)^2}{\left(1+\left(\frac{1}{1-1\mathrm{i}\cdot\left(\beta\cdot\frac{\tau_2^2}{16\ln(2)}\right)}\right)\cdot 2\left(\frac{\tau_2}{\tau_1}\right)^2\right)\cdot\tau_1^2}+1\mathrm{i}\cdot\frac{-2\cdot t_0}{\beta\cdot\tau_2^2}\cdot\frac{(8\ln(2))^2\,(t-t_0)}{\left(1+\left(\frac{1}{1-1\mathrm{i}\cdot\left(\beta\cdot\frac{\tau_2^2}{16\ln(2)}\right)}\right)\cdot 2\left(\frac{\tau_2}{\tau_1}\right)^2\right)\cdot\tau_1^2}+\left(\frac{-8\ln(2)\,t_0}{\beta\cdot\tau_2^2}\right)^2\cdot\frac{8\ln(2)}{\tau_1^2\cdot\left(1+\left(\frac{1}{1-1\mathrm{i}\cdot\left(\beta\cdot\frac{\tau_2^2}{16\ln(2)}\right)}\right)\cdot 2\left(\frac{\tau_2}{\tau_1}\right)^2\right)}-\frac{1\mathrm{i}}{2}\cdot$$

$A_0 := 0.2$ $\quad t_0 := 0\ fs$ $\quad \tau_1 := 30\ fs$ $\quad \tau_2 := 1000\ fs$ $\quad \beta := 4\cdot 10^{-3}\cdot\frac{1}{fs^2}$

$t := -2\ ps, -1.999\ ps\,..\,2\ ps = \begin{bmatrix} -2\cdot 10^3 \\ \vdots \end{bmatrix} fs$

$minus(t) := FKov(A_0, t_0 - 0.5\ ps, \tau_1, \tau_2, \beta, t)$

$null(t) := FKov(A_0, t_0, \tau_1, \tau_2, \beta, t)$

$plus(t) := FKov(A_0, t_0 + 0.5\ ps, \tau_1, \tau_2, \beta, t)$

$\beta 1(t) := FKov(A_0, t_0, \tau_1, \tau_2, \beta, t) + 0.4$

$\beta 2(t) := FKov\left(A_0, t_0, \tau_1, \frac{\tau_2}{\sqrt{2}}, 2\,\beta, t\right) + 0.2$

$\beta 5(t) := FKov\left(A_0, t_0, \tau_1, \frac{\tau_2}{\sqrt{5}}, 5\,\beta, t\right)$

Term linear in t caries asymmetry.

Replacing ALL t_0 by $-t_0$ is a matter of definition. Kovalenko defines t_0 with opposite sign.

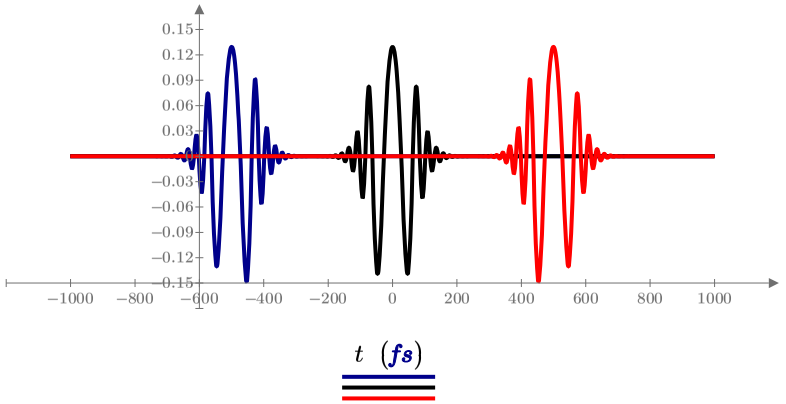

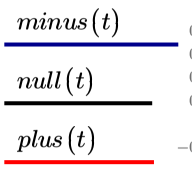

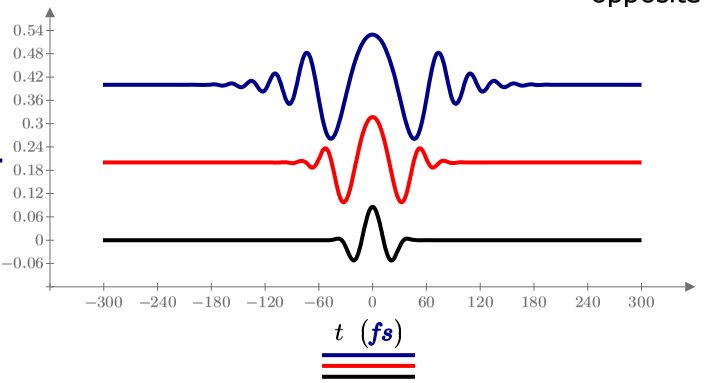

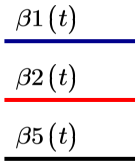

Trying a simplified model inspired by Kov99, Equation 26, which in the form presented in the paper doesn't apply in additionally chirpen white light due to the stretched envelope we observe.
Shift of t-axis results in symmetry about a point other than t=0.

$$FKov2\left(A_0, A_1, t_0, w, B, \phi, shift, t\right) := A_0 \cdot \exp\left(-\frac{\left(-t+shift+t_0\right)^2}{w^2}\right) \cdot \sin\left(B \cdot \left(-t+shift+t_0\right)^2 + A_1 \cdot \left(t_0\right) \cdot \left(-t+shift+t_0\right) + \phi\right)$$

$A_0 := 0.021$ $\quad A_1 := \frac{10}{ps^2}$ $\quad t_0 := -0\ ps$ $\quad w := 0.16\ ps$ $\quad \phi := 2.4$ $\quad B := \frac{120}{ps^2}$ $\quad shift := 0.8\ ps$

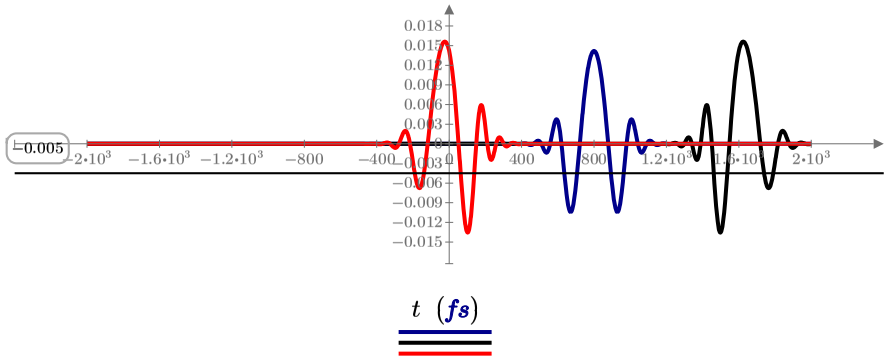

$FKov2\left(A_0, A_1, t_0, w, B, \phi, shift, t\right)$

$FKov2\left(A_0, A_1, t_0 + 0.8\ ps, w, B, \phi, shift, t\right)$

$FKov2\left(A_0, A_1, t_0 - 0.8\ ps, w, B, \phi, shift, t\right)$

New fitting model "Fcos": The Gaussian and Lor02 models cannot describe the increasingly large fringes in the artifacts produced in highly chirped supercontinua. The model derived from Wah16 describes the fringes very well, but due to its symmetry cannot reproduce asymmetric artifacts.
Therefore, as has been done in the Gauss–Model, a first derivative of the gaussian is artificially added to the envelope. This is meant to be only a small correction and its amplitude A_1 is restricted in the fitting algorithm to be at least one order of magnitude smaller than A_0.

$$Fcos\left(A_0, A_1, t_0, \tau, B, \phi, t\right) := \left(A_0 \cdot \exp\left(\frac{-4 \cdot \ln(2) \cdot \left(t-t_0\right)^2}{\tau^2}\right) + \frac{4 \cdot A_1 \cdot e^{-\frac{4 \cdot \ln(2) \cdot \left(t-t_0\right)^2}{\tau^2}} \cdot \ln(2) \cdot \left(2 \cdot t - 2 \cdot t_0\right)}{\tau^2}\right) \cdot \cos\left(B \cdot \left(t-t_0\right)^2 + \phi\right)$$

In this formula A_1 carries the unit seconds. It has to be scaled by $\frac{2}{\tau} \cdot \sqrt{\frac{ln(4)}{e}}$ in order to be directly comparable to A_0.

Testing the Fitfunctions

Define Residual for more illustrative Plotting: $Res(Data, Fit) := (Data - Fit) - 1.2 \cdot \max(Data)$

Step one: (Nearly) Symmetric Artifacts

Read a file with typical symmetric artifacts, $SymArt$ from a supercontinuum without additional chirp and $SymArt\_chirp$ from a supercontinuum with additional chirp:

$infile1 :=$ "testdata.txt"

Fitting with $FLor02$ and $FGauss$ in WL without additinal chirp: For a (nearly) symmetric artifact in unchirped WL, $FGauss$ yields (up to 1 fs) the same result for t_0 and w like $FLor02$. $FLor02$ uses one parameter less. Residuum is almost identical and resembles cosine.

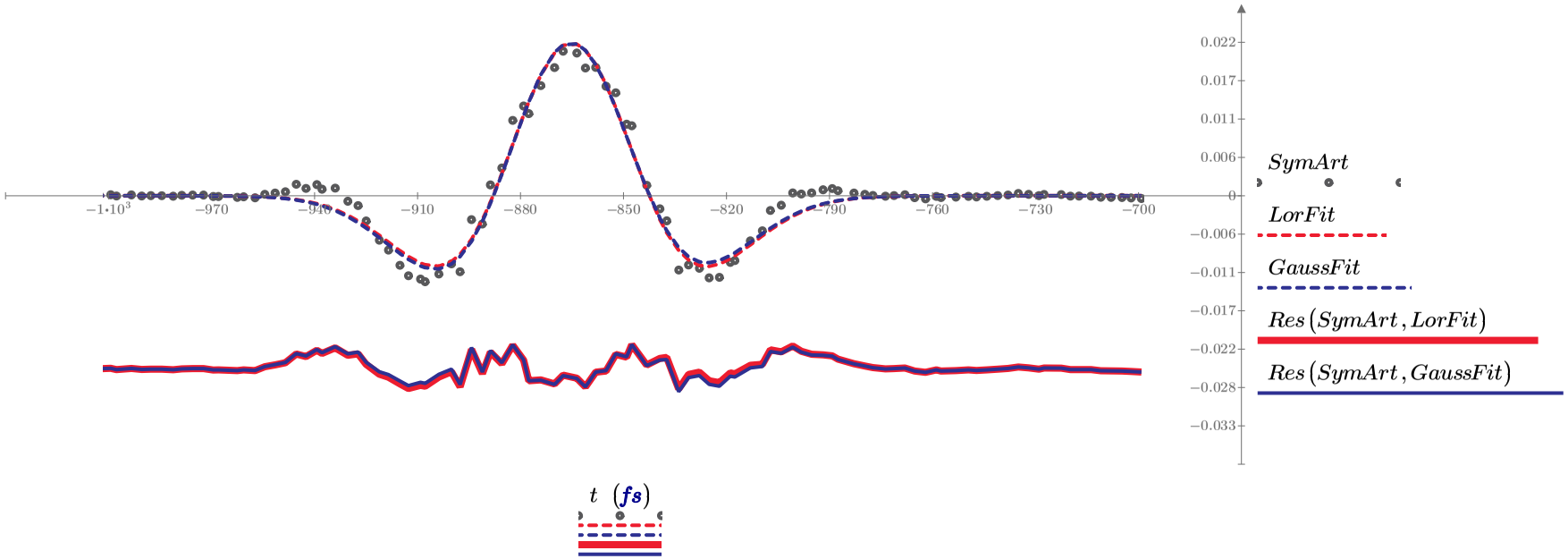

Fitting with $FLor02$ **and** $FGauss$ **in additionally chirped WL:** $FLor02$ and $FGauss$ cannot reproduce artifact in chirped WL. Residual looks like decaying cosine.

Solve Constraints Values

$w := 0.06\ ps \quad A_0 := 0.1 \quad t_0 := -0.5\ ps \quad A_1 := 10^{-5}\ ps^2$

$SymArt\_chirp = \overrightarrow{FLor02\left(A_0, A_1, t_0, w, t\right)}$

$Par3 := \mathbf{minerr}\left(A_0, A_1, t_0, w\right)$

$$Par3 = \begin{bmatrix} -0.0003 \\ (7.0609 \cdot 10^{-29})\ s^2 \\ -4.8419 \cdot 10^{-13}\ s \\ (1.1289 \cdot 10^{-13})\ s \end{bmatrix} \begin{matrix} A_0 \\ A_1 \\ t_0 \\ w \end{matrix}$$

$LorFit\_chirp := FLor02\left(Par3_1, Par3_2, Par3_3, Par3_4, t\right)$

Solve Constraints Values

$w := 0.1\ ps \quad A_0 := 0.1 \quad t_0 := -0.5\ ps \quad A_1 := 10^{-3}\ ps \quad A_2 := 10^{-5}\ ps^2$

$SymArt\_chirp = \overrightarrow{FGauss\left(A_0, A_1, A_2, t_0, w, t\right)}$

$Par4 := \mathbf{minerr}\left(A_0, A_1, A_2, t_0, w\right)$

$$Par4 = \begin{bmatrix} -0.0005 \\ -4.8239 \cdot 10^{-17}\ s \\ -6.1048 \cdot 10^{-29}\ s^2 \\ -4.8492 \cdot 10^{-13}\ s \\ (1.1302 \cdot 10^{-13})\ s \end{bmatrix} \begin{matrix} A_0 \\ A_1 \\ A_2 \\ t_0 \\ w \end{matrix}$$

$GaussFit\_chirp := FGauss\left(Par4_1, Par4_2, Par4_3, Par4_4, Par4_5, t\right)$

Shift in t_0 between models:

$t0shift := \left|Par3_3 - Par4_4\right| = 0.726\ fs$

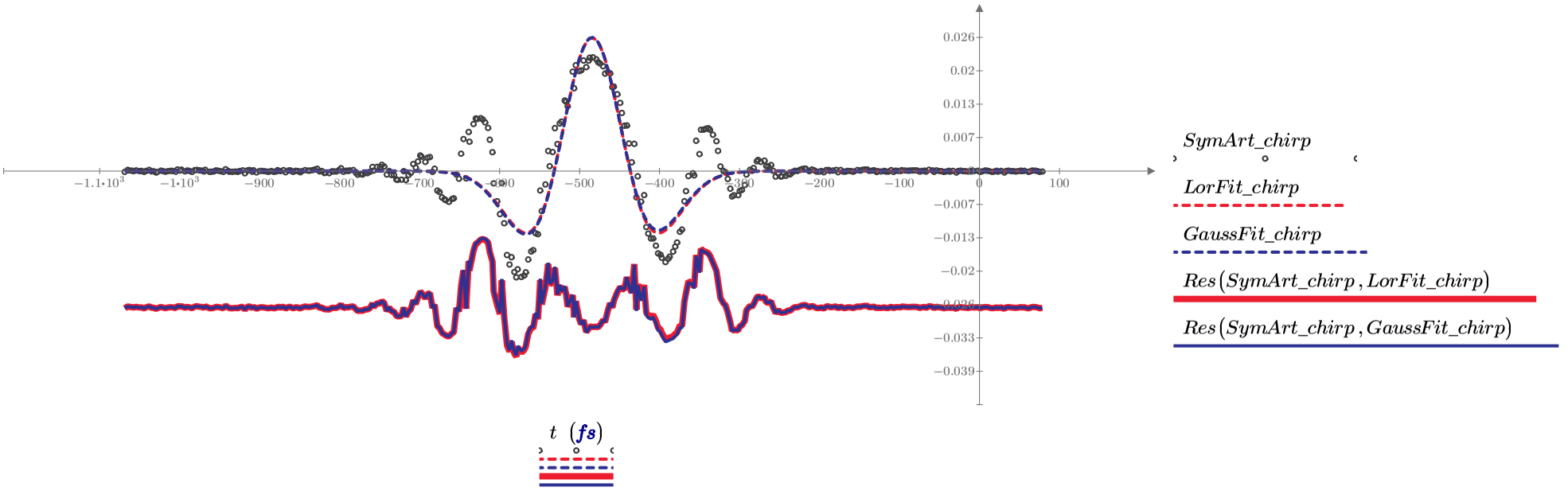

Fitting with $FWah16$ **in additionally chirped WL:** Wah16 model reproduces artifact fringes in chirped WL very well

Solver Constraints Guess Values

$w := 0.16 \quad A_0 := 0.02 \quad t_0 := -0.5 \quad \phi := 0.6$

$B := 200$

$SymArt\_chirp = \overrightarrow{FWah16\left(A_0, t_0, w, B, \phi, time\right)}$

$Par5 := \mathbf{minerr}\left(A_0, t_0, w, B, \phi\right)$

$$Par5 = \begin{bmatrix} 0.0309 \\ -0.4841 \\ 0.1334 \\ 258.4881 \\ 0.7979 \end{bmatrix} \quad \begin{matrix} A_0 \\ t_0 \\ w \\ B \\ \phi \end{matrix}$$

$WahFit\_chirp := FWah16\left(Par5_1, Par5_2, Par5_3, Par5_4, Par5_5, time\right)$

Shift in t_0 between models:

$t0shift := \left|Par5_2\ \mathbf{ps} - Par4_4\right| = 0.859\ \mathbf{fs}$

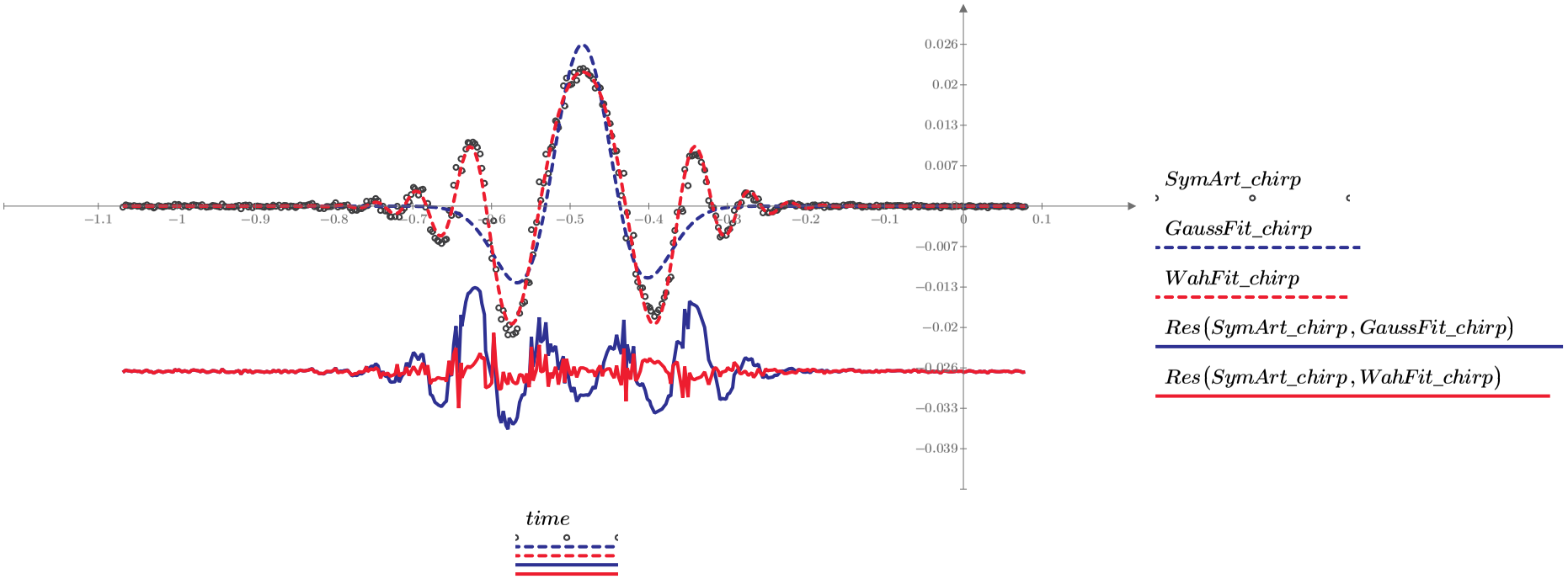

Can $FWah16$ **also be used in WL without additional chirp?:** $FWah16$ also reproduces artifact in WL without additional chirp - even better than $FGauss$**!**

Given

Guess Values

$w := 0.16 \qquad A_0 := 0.02 \qquad t_0 := -0.9 \qquad \phi := 0.6$

$B := 200$

Constraints

$SymArt = \overrightarrow{FWah16\left(A_0, t_0, w, B, \phi, time\right)}$

Solve

$Par5 := \mathbf{minerr}\left(A_0, t_0, w, B, \phi\right)$

$$Par5 = \begin{bmatrix} 0.0429 \\ -0.8654 \\ 0.04 \\ 848.9709 \\ 1.0777 \end{bmatrix} \begin{matrix} A_0 \\ t_0 \\ w \\ B \\ \phi \end{matrix}$$

$WahFit := FWah16\left(Par5_1, Par5_2, Par5_3, Par5_4, Par5_5, time\right)$

Shift in t_0 between models:

$t0shift := \left|Par5_2\ \mathit{ps} - Par2_4\right| = 0.346\ \mathit{fs}$

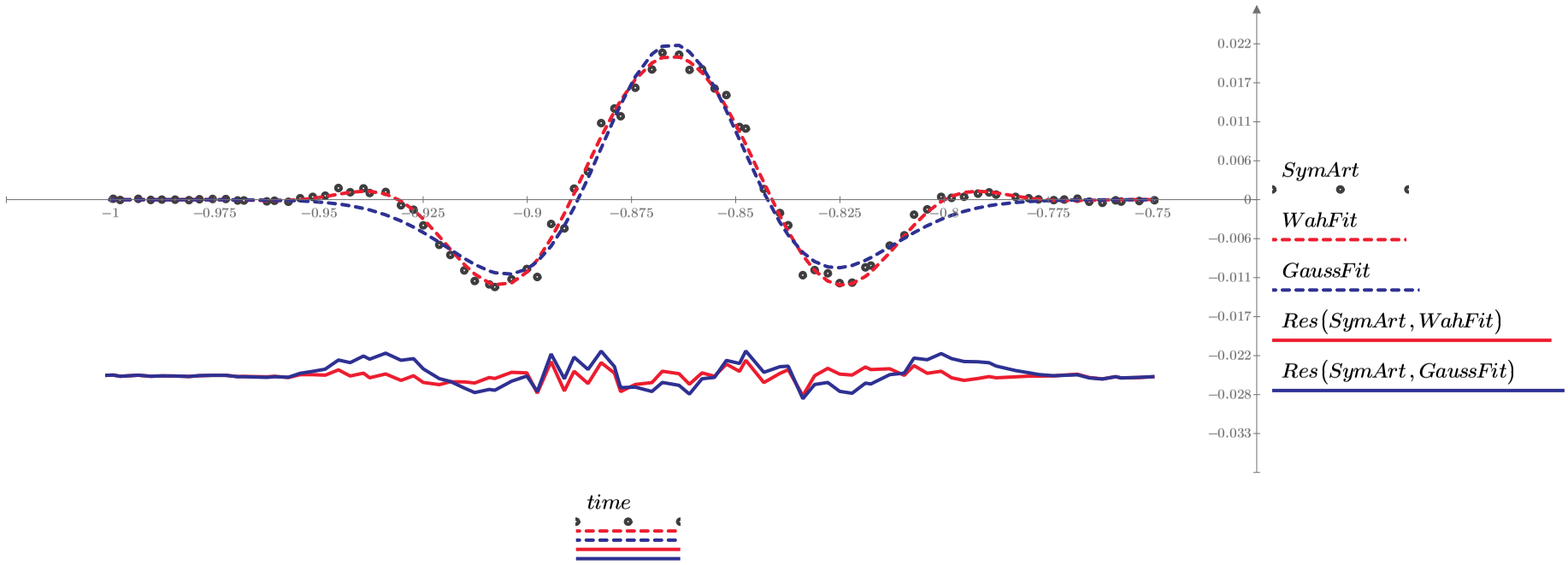

Step two: Asymmetric Artifacts: Asymmeric artifacts can not be modeled with the totally symmetric $FWah16$. Slight asymmetries can be dealt with by adding an asymmetric envelope. Including the first derivative of a Gaussian yields $Fcos$.

Read a file with typical asymmetric artifacts, $AsymArt$ from a WL without additional chirp and $AsymArt\_chirp$ from a WL with additional chirp:

$infile := \text{“testdata\_asym.txt”}$

Compare fit with $FWah16$ to fit using $Fcos$ and $FKov$:

Solver Constraints Guess Values

$w := 0.16 \quad A_0 := 1 \quad t_0 := -1.25 \quad \phi := 0.6$
$B := 200$

$AsymArt\_chirp = \overrightarrow{FWah16\left(A_0, t_0, w, B, \phi, time2\right)}$

$Par6 := \mathbf{minerr}\left(A_0, t_0, w, B, \phi\right)$

$$Par6 = \begin{bmatrix} 0.0188 \\ -1.2368 \\ 0.0918 \\ 318.3197 \\ 0.9138 \end{bmatrix} \begin{matrix} A_0 \\ t_0 \\ w \\ B \\ \phi \end{matrix}$$

$WahFit\_achirp := FWah16\left(Par6_1, Par6_2, Par6_3, Par6_4, Par6_5, time2\right)$

Solver Constraints Guess Values

$w := 0.15 \quad A_0 := 0.02 \quad t_0 := -1.24$
$B := 300 \quad A_1 := 0.0001$
$\phi := 0.6$

$AsymArt\_chirp = \overrightarrow{Fcos\left(A_0, A_1, t_0, w, B, \phi, time2\right)}$

$Par7 := \mathbf{minerr}\left(A_0, A_1, t_0, w, B, \phi\right)$

$$Par7 = \begin{bmatrix} 0.0187 \\ 0.0002 \\ -1.2363 \\ 0.1531 \\ 320.2588 \\ 0.9081 \end{bmatrix} \begin{matrix} A_0 \\ A_1 \\ t_0 \\ w \\ B \\ \phi \end{matrix}$$

Shift in t_0 between models:

$t0shift := \left|Par6_2\ ps - Par7_3\ ps\right| = 0.47\ fs$

$FcosFit\_achirp := Fcos\left(Par7_1, Par7_2, Par7_3, Par7_4, Par7_5, Par7_6, time2\right)$

Note that adding the asymmetry changes the fitted t_0 by 0.5 fs. Here, $A_1 << A_0$ was not explicitly enforced as a constraint. This only becomes necessary when the asymmetry becomes large.

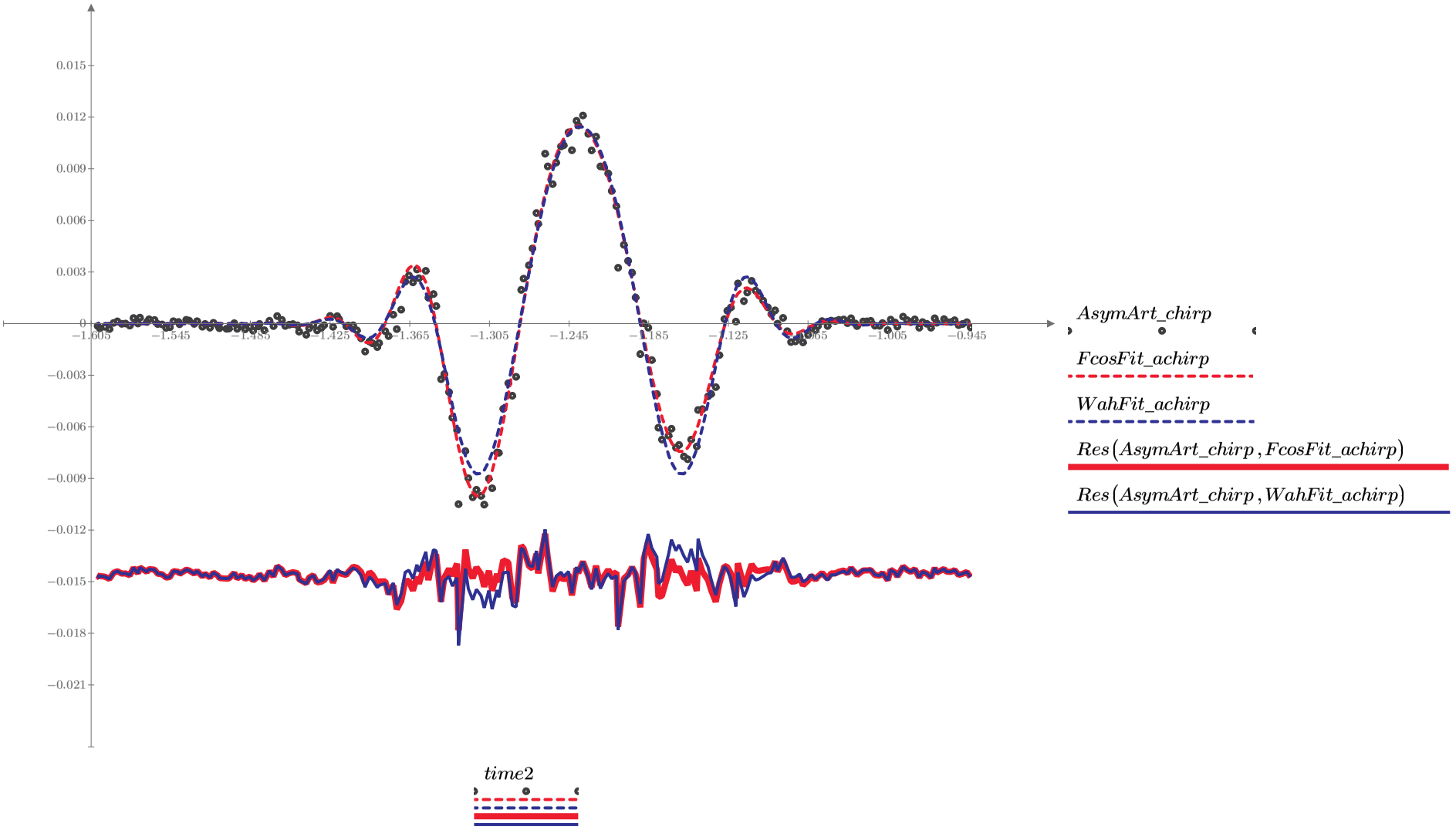

$t := time \cdot ps$

Solver Constraints Guess Values

$w := 0.026\ ps \quad A_0 := 0.02 \quad t_0 := -0.5\ ps$

$B := \frac{700}{ps^2} \quad A_1 := 0.00001\ ps \quad \phi := 0.26$

$SymArt\_chirp = \overrightarrow{Fcos\left(A_0, A_1, t_0, w, B, \phi, t\right)}$

$Par8 := \mathbf{minerr}\left(A_0, A_1, t_0, w, B, \phi\right)$

$$Par8 = \begin{bmatrix} 0.0309 \\ (2.0928 \cdot 10^{-16})\ s \\ -4.8386 \cdot 10^{-13}\ s \\ (2.223 \cdot 10^{-13})\ s \\ -2.5845 \cdot 10^{26}\ \frac{1}{s^2} \\ -0.7975 \end{bmatrix} \begin{matrix} A_0 \\ A_1 \\ t_0 \\ w \\ B \\ \phi \end{matrix}$$

$FcosFit\_AA1 := Fcos\left(Par8_1, Par8_2, Par8_3, Par8_4, Par8_5, Par8_6, t\right)$

Solver Constraints Guess Values

$w := 0.1\ ps \quad A_0 := 0.1 \quad t_0 := -0.9\ ps$

$A_2 := 10^{-5}\ ps^2$

$SymArt\_chirp = \overrightarrow{FGauss\left(A_0, A_1, A_2, t_0, w, t\right)}$

$A_1 := 10^{-3}\ ps$

$Par9 := \mathbf{minerr}\left(A_0, A_1, A_2, t_0, w\right)$

$$Par9 = \begin{bmatrix} -0.0108 \\ (4.9283 \cdot 10^{-16})\ s \\ -1.1364 \cdot 10^{-29}\ s^2 \\ -6.1267 \cdot 10^{-13}\ s \\ (5.9466 \cdot 10^{-14})\ s \end{bmatrix} \begin{matrix} A_0 \\ A_1 \\ A_2 \\ t_0 \\ w \end{matrix}$$

$GaussFit\_AA1 := FGauss\left(Par9_1, Par9_2, Par9_3, Par9_4, Par9_5, t\right)$

Shift in t_0 between models:

$t0shift1 := \left|Par8_3\ ps - Par9_4\ ps\right| = (1.288 \cdot 10^{-10})\ s \cdot fs$

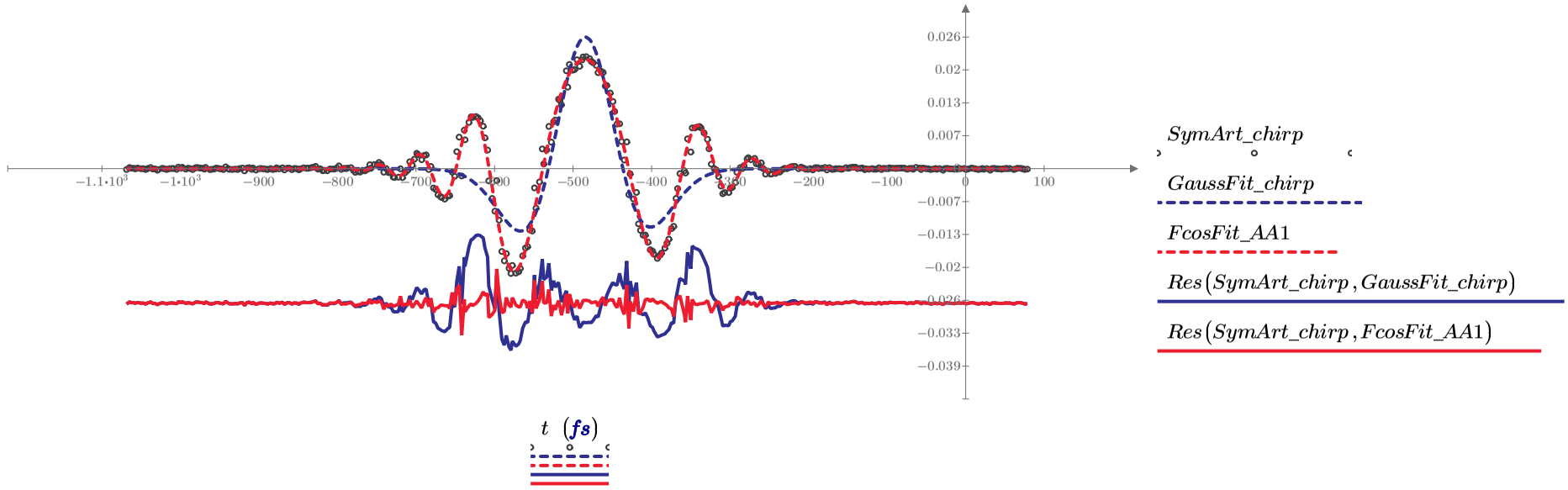

Can $Fcos$ still compete with $FGauss$ for asymmetric artifacts in WL without additional chirp?

Guess Values

$w := 0.009 \quad A_0 := 1 \quad t_0 := -0.352$

$B := 50 \quad A_1 := 0.02$

$\phi := 0.16 \quad A_2 := 0.001$

Constraints

$AsymArt2 = \overrightarrow{Fcos\left(A_0, A_1, t_0, w, B, \phi, time2\right)}$

Solver

$Par10 := \mathbf{minerr}\left(A_0, A_1, t_0, w, B, \phi\right)$

$FcosFit\_AA2 := Fcos\left(Par10_1, Par10_2, Par10_3, Par10_4, Par10_5, Par10_6, time2\right)$

Guess Values

$w := 0.1 \quad A_0 := 0.1 \quad t_0 := -0.3$

$A_1 := 10^{-3}$

$A_2 := 10^{-5}$

Constraints

$AsymArt2 = \overrightarrow{FGauss\left(A_0, A_1, A_2, t_0, w, time2\right)}$

Solver

$Par12 := \mathbf{minerr}\left(A_0, A_1, A_2, t_0, w\right)$

$GaussFit\_AA2 := FGauss\left(Par12_1, Par12_2, Par12_3, Par12_4, Par12_5, time2\right)$

Shift in t_0 between models:

$t0shift2 := \left|Par10_3\ ps - Par12_4\ ps\right| = 1.026\ fs$

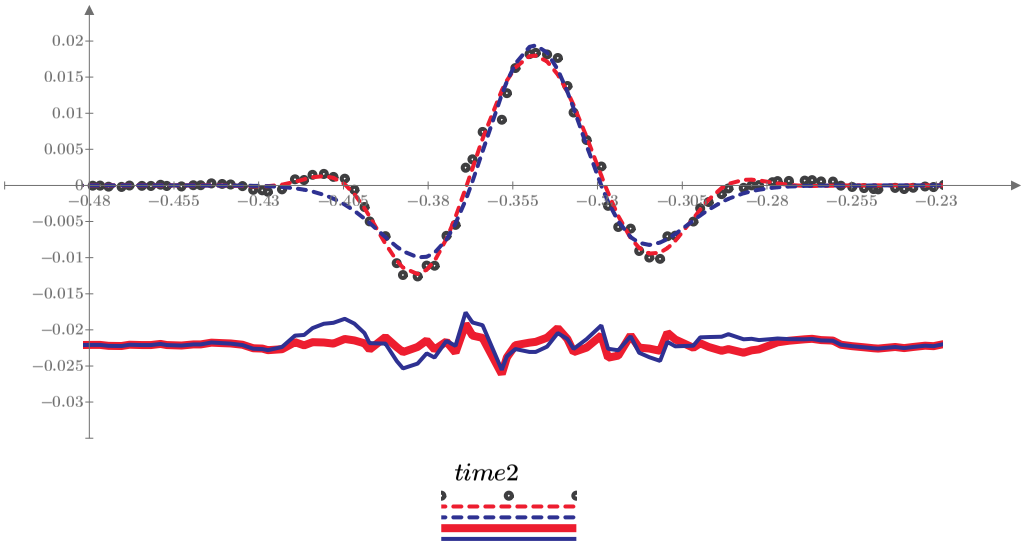

$AsymArt2$

$FcosFit\_AA2$

$GaussFit\_AA2$

$Res\left(AsymArt2, FcosFit\_AA2\right)$

$Res\left(AsymArt2, GaussFit\_AA2\right)$

Guess Values

$w := 0.16\ ps \quad A_0 := 1 \quad t_0 := -0.87\ ps$

$B := \frac{250}{ps^2} \quad A_1 := 0.01\ ps$

$A_2 := 0.001\ ps^2$

$\phi := 0.6$

Constraints

$SymArt = \overrightarrow{Fcos\left(A_0, A_1, t_0, w, B, \phi, t\right)}$

Solver

$Par11 := \mathbf{minerr}\left(A_0, A_1, t_0, w, B, \phi\right)$

$$Par11 = \begin{bmatrix} 0.043 \\ (3.311 \cdot 10^{-17})\ s \\ -8.653 \cdot 10^{-13}\ s \\ (6.664 \cdot 10^{-14})\ s \\ (8.469 \cdot 10^{26})\ \frac{1}{s^2} \\ 1.079 \end{bmatrix}$$

Constraints Guess Values

$w := 0.1\ ps \quad A_0 := 0.1 \quad t_0 := -0.87\ ps$

$A_1 := 10^{-3}\ ps$

$A_2 := 10^{-5}\ ps^2$

$SymArt = \overrightarrow{FGauss\left(A_0, A_1, A_2, t_0, w, t\right)}$

Solver

$Par13 := \mathbf{minerr}\left(A_0, A_1, A_2, t_0, w\right)$

$$Par13 = \begin{bmatrix} -4.054 \cdot 10^{-4} \\ -2.702 \cdot 10^{-17}\ s \\ -1.175 \cdot 10^{-29}\ s^2 \\ -8.657 \cdot 10^{-13}\ s \\ (5.398 \cdot 10^{-14})\ s \end{bmatrix}$$

$FcosFit\_SymArt := Fcos\left(Par11_1, Par11_2, Par11_3, Par11_4, Par11_5, Par11_6, t\right)$

$GaussFit\_SymArt := FGauss\left(Par13_1, Par13_2, Par13_3, Par13_4, Par13_5, t\right)$

Shift in t_0 between models:

$t0shift3 := \left|Par11_3 - Par13_4\right| = 0.445\ fs$

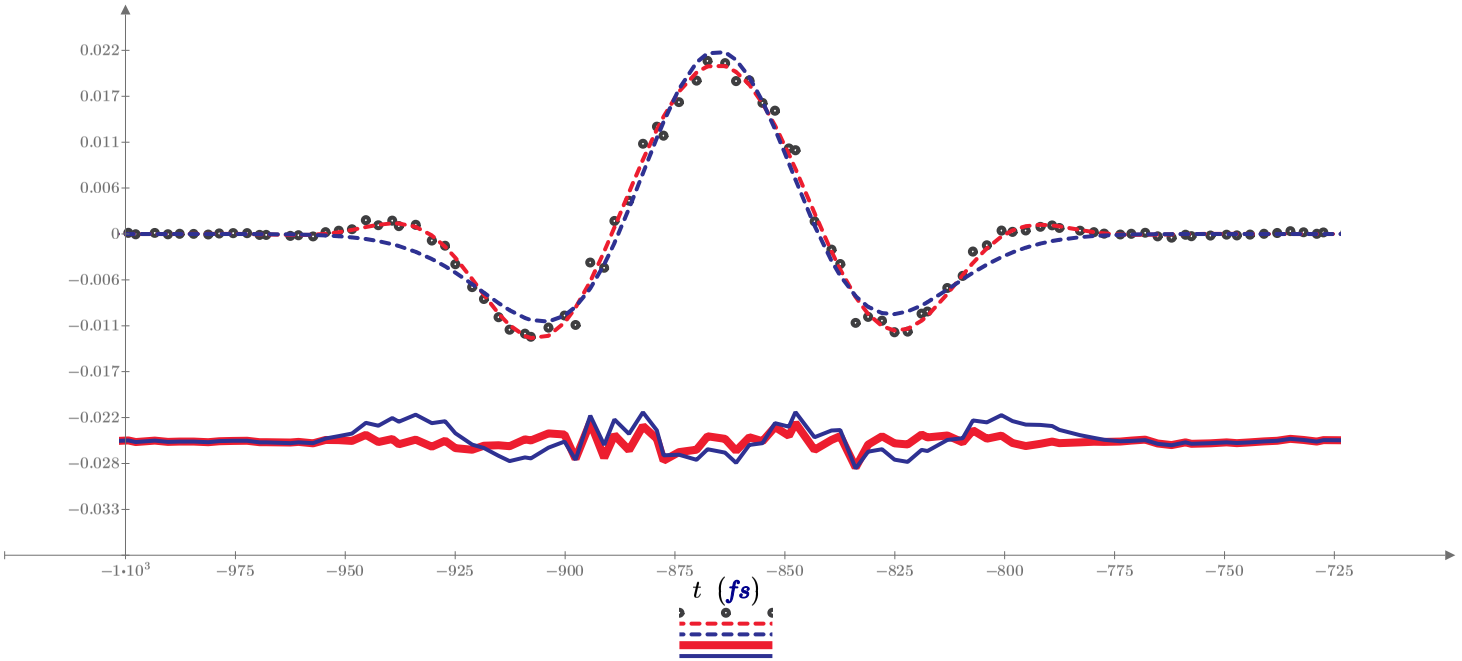

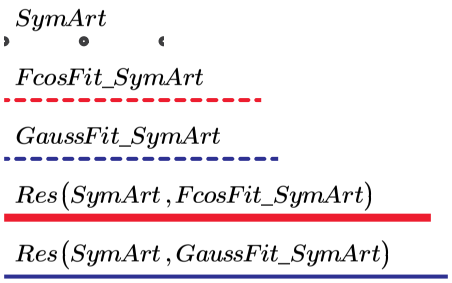

Even in WL without additional chirp, $Fcos$ yields a better fit to the signal than $FGauss$. Note that in this (for mirror measurements) extremely unsymmetric case the t_0 is shifted by >1 fs compared to the Gauss model, so significant improvement in the determination of t_0 can be gained by applying the more appropriate model.

$Fcos$ in all cases yields a fit better or at least as good as $FGauss$!!!

What about $Fcos$ vs the exact solution $FKov$? t asymmetry doesnt fit data, because t is negative in this example and asymmetry has the wrong "sign" for negative t. If reversed t Kov99 fits just as good as $Fcos$

$$FKov(A_0,t_0,\tau_1,\tau_2,\beta,t) := -A_0 \cdot \mathrm{Im}\left(\exp\left(-\frac{8\ln(2)\,(t-t_0)^2}{\left(1+\left(\frac{1}{1-1\mathrm{i}\cdot\left(\beta\cdot\frac{\tau_2^2}{16\ln(2)}\right)}\right)\cdot 2\left(\frac{\tau_2}{\tau_1}\right)^2\right)\cdot\tau_1^2} + 1\mathrm{i}\cdot\frac{2\cdot t_0}{\beta\cdot\tau_2^2}\cdot\frac{(8\ln(2))^2\,(t-t_0)}{\left(1+\left(\frac{1}{1-1\mathrm{i}\cdot\left(\beta\cdot\frac{\tau_2^2}{16\ln(2)}\right)}\right)\cdot 2\left(\frac{\tau_2}{\tau_1}\right)^2\right)\cdot\tau_1^2} + \left(\frac{-8\ln(2)\,t_0}{\beta\cdot\tau_2^2}\right)^2\cdot\frac{8\ln(2)}{\tau_1^2\cdot\left(1+\left(\frac{1}{1-1\mathrm{i}\cdot\left(\beta\cdot\frac{\tau_2^2}{16\ln(2)}\right)}\right)\cdot 2\left(\frac{\tau_2}{\tau_1}\right)^2\right)} - \frac{1\mathrm{i}}{2}\cdot$$

(!) Asymmetry: To reproduce asymmetry FKov must be multiplied by *-1 for fit!

Solver Constraints Guess Values

$\tau_1 := 0.03\ ps$ $\quad A_0 := 0.03$ $\quad t_0 := -0.5\ ps$

$\tau_2 := 1\ ps$ $\quad \beta := 4\cdot 10^{-3}\cdot\frac{1}{fs^2}$

$SymArt\_chirp = \overrightarrow{FKov(A_0,t_0,\tau_1,\tau_2,\beta,t)}$

$Par10 := \mathbf{minerr}(A_0,t_0,\tau_1,\tau_2,\beta)$

$$Par10 = \begin{bmatrix} 0.0328 \\ -4.8418\cdot 10^{-13}\ s \\ (6.9234\cdot 10^{-14})\ s \\ (1.3584\cdot 10^{-12})\ s \\ (1.0563\cdot 10^{27})\ \frac{1}{s^2} \end{bmatrix} \begin{matrix} A_0 \\ t_0 \\ \tau_1 \\ \tau_2 \\ beta \end{matrix}$$

$FKovFit\_chirp := FKov(Par10_1, Par10_2, Par10_3, Par10_4, Par10_5, t)$

Shift in t_0 between models:

$t0shift := |Par10_2 - Par8_3| = 0.323\ fs$

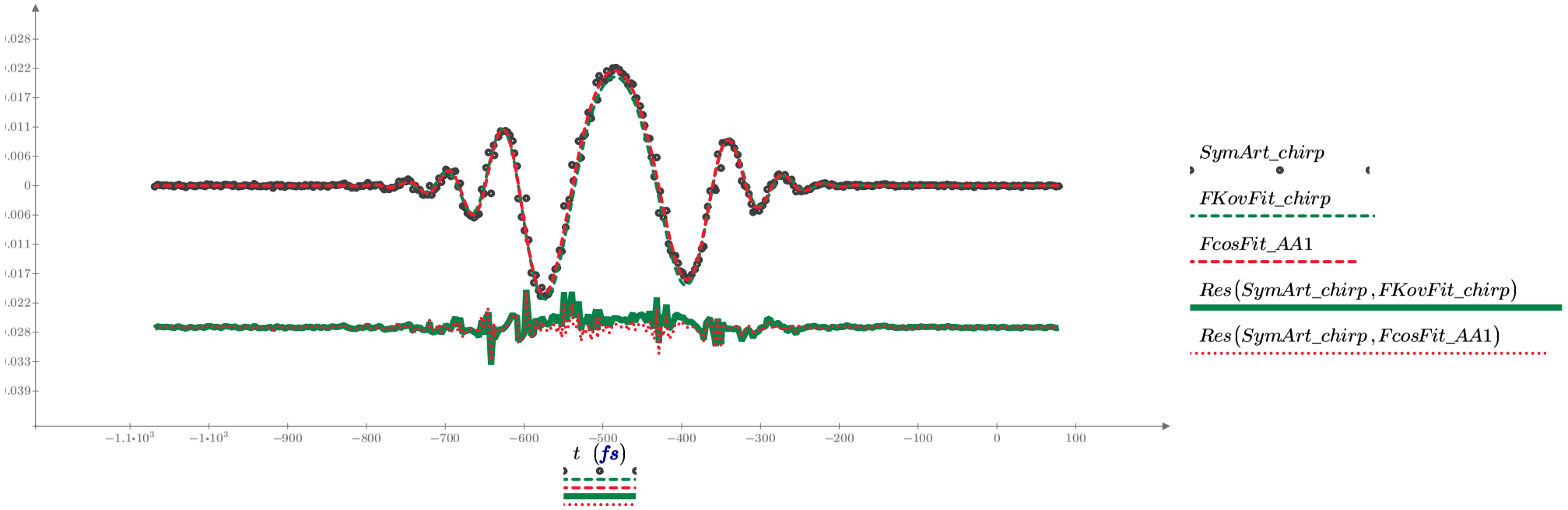

Solve Constraints Guess Values

$\tau_1 := 0.03\ ps \qquad A_0 := 0.03 \qquad t_0 := -1.25\ ps$

$\tau_2 := 1\ ps \qquad \beta := 4 \cdot 10^{-3} \cdot \frac{1}{fs^2}$

$AsymArt\_chirp = \overrightarrow{FKov\left(A_0, t_0, \tau_1, \tau_2, \beta, t\right)}$

$Par10 := \mathbf{minerr}\left(A_0, t_0, \tau_1, \tau_2, \beta\right)$

$$Par10 = \begin{bmatrix} 0.0198 \\ -1.2374 \cdot 10^{-12}\ s \\ \left(7.8358 \cdot 10^{-14}\right) s \\ \left(1.3682 \cdot 10^{-12}\right) s \\ \left(1.432 \cdot 10^{27}\right) \frac{1}{s^2} \end{bmatrix} \begin{matrix} A_0 \\ t_0 \\ \tau_1 \\ \tau_2 \\ beta \end{matrix}$$

$FKovFit\_chirp := FKov\left(Par10_1, Par10_2, Par10_3, Par10_4, Par10_5, t\right)$

Shift in t_0 between models:

$t0shift := \left|Par10_2 - Par7_3\ ps\right| = 1.089\ fs$

$FcosFit\_chirp := FcosFit\_achirp$

$Residual\_Fkov := Res(AsymArt\_chirp, FKovFit\_chirp)$ $Residual\_Fcos := Res(AsymArt\_chirp, FcosFit\_achirp)$

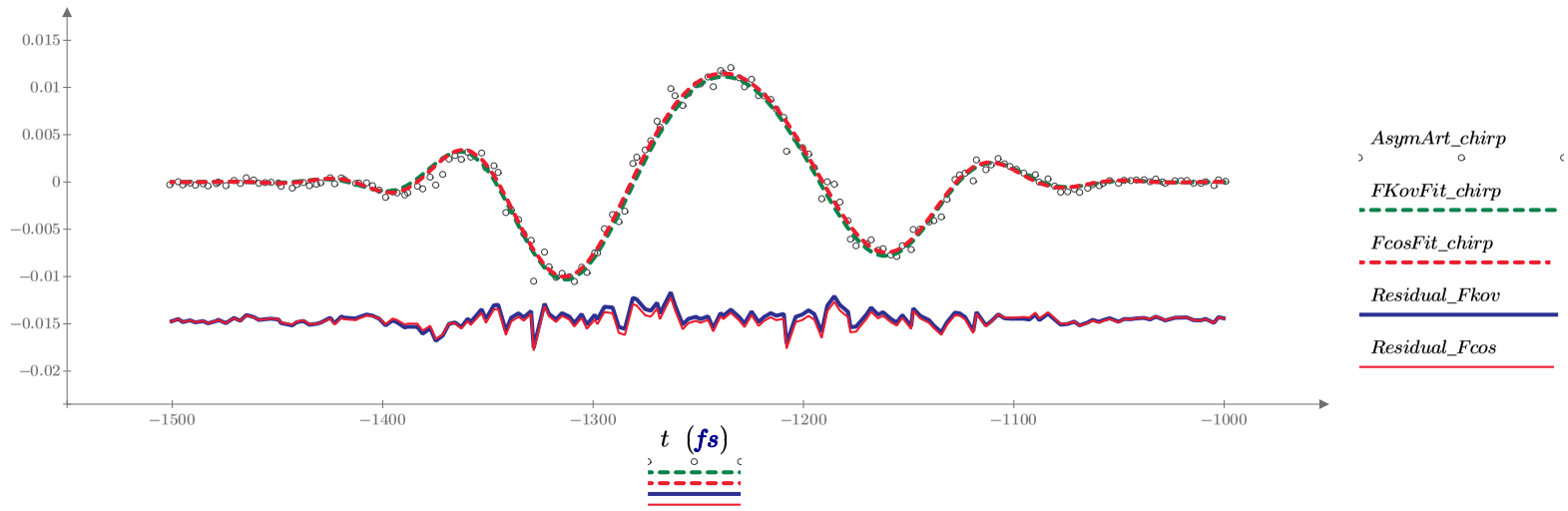

Guess Values

$w := 0.01\ ps \quad A_0 := 1 \quad t_0 := -0.35\ ps$

$B := \frac{50}{ps^2} \quad A_1 := 0.01\ ps$

$\phi := 0.6$

Constraints

$AsymArt2 = \overrightarrow{Fcos(A_0, A_1, t_0, w, B, \phi, t)}$

Solver

$Par10 := \mathbf{minerr}(A_0, A_1, t_0, w, B, \phi)$

Guess Values

$\tau_1 := 0.02\ ps \quad A_0 := 0.02 \quad t_0 := -0.35\ ps$

$\tau_2 := 0.3\ ps \quad beta := 1000 \frac{1}{ps^2}$

Constraints

$AsymArt2 = \overrightarrow{FKov(A_0, t_0, \tau_1, \tau_2, beta, t)}$

Solver

$Par14 := \mathbf{minerr}(A_0, t_0, \tau_1, \tau_2, beta)$

$KovFit\_AA2 := FKov(Par14_1, Par14_2, Par14_3, Par14_4, Par14_5, t)$

$FcosFit\_AA2 := Fcos(Par10_1, Par10_2, Par10_3, Par10_4, Par10_5, Par10_6, t)$

$$Par10 = \begin{bmatrix} -0.0388 \\ -8.2257 \cdot 10^{-17}\ s \\ -3.4819 \cdot 10^{-13}\ s \\ (5.6832 \cdot 10^{-14})\ s \\ (1.1554 \cdot 10^{27})\ \frac{1}{s^2} \\ 4.2301 \end{bmatrix}$$

$$Par14 = \begin{bmatrix} 0.0405 \\ -3.4896 \cdot 10^{-13}\ s \\ (4.8856 \cdot 10^{-14})\ s \\ (5.24 \cdot 10^{-13})\ s \\ (7.1993 \cdot 10^{27})\ \frac{1}{s^2} \end{bmatrix} \begin{matrix} A_0 \\ t_0 \\ \tau_1 \\ \tau_2 \\ beta \end{matrix}$$

$Par14 = 0.007\ \frac{1}{\quad}$ $t0shift := |Par10 - Par14| = 0.765\ fs$

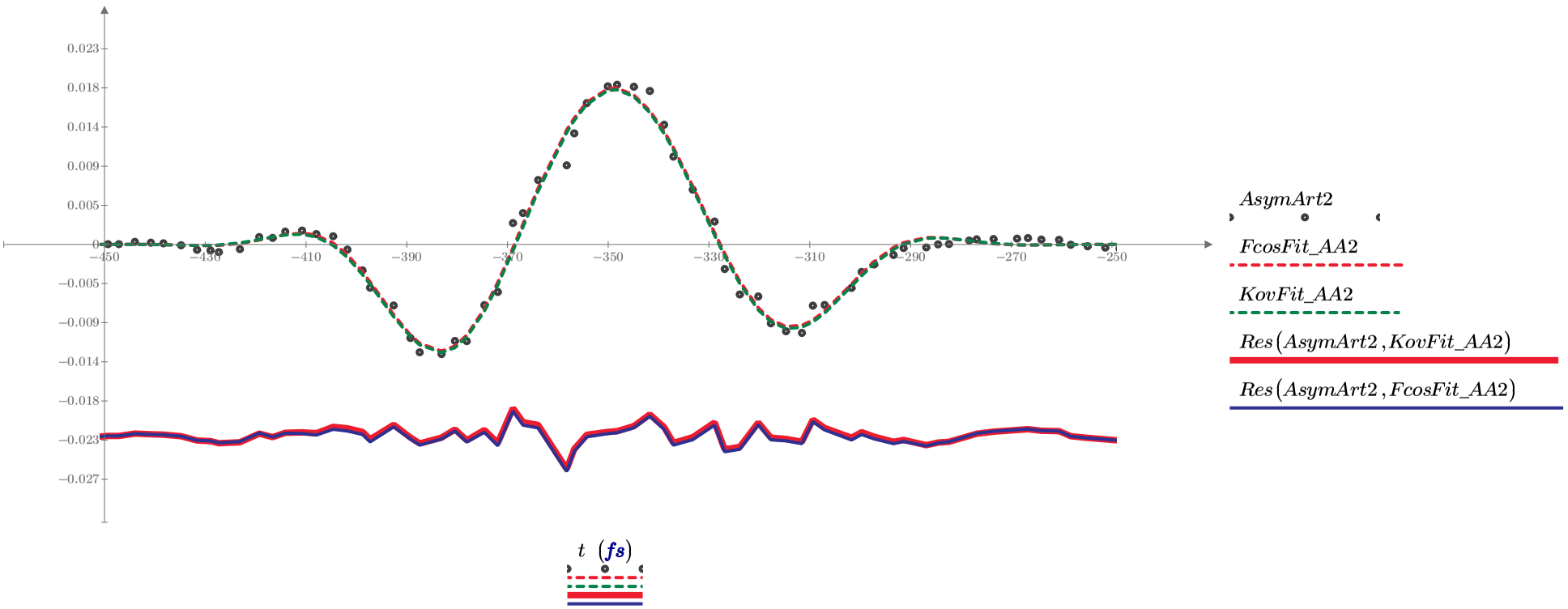

$Fcos$ in all cases yields a fit better than $FKov$!!!

B2 Trace by Trace Fitting of the Coherent Artifact Using Fcos

Bastian Baudisch (05.09.16)

$ORIGIN := 1$

$fs := 10^{-15}\ s$

This program evaluates transient GD measurements. It fits transient data one time trace at a time to obtain the Reference and Sample $t_0(\lambda)$ curves from the coherent artifact using the fitfunction specified. The Sample's GD is then calculated by subtraction of a polynomial fitted to the reference $t_0(\lambda)$ from the sample $t_0(\lambda)$ curve.

Read Reference and Sample Data:

Read Reference Measurement: $infile\_Ref := \text{“80\_B270\_1uJ\_RalUV\_BK7\_flip\_001\_WL\_OD.dat”}$

$DATA\_Ref := \text{READFILE}(infile\_Ref, \text{“delimited”})$

Read Sample Measurement: $infile\_Sample := \text{“80\_B270\_1uJ\_Df350−1100\_BK7\_flip\_001\_WL\_OD.dat”}$

$DATA\_S := \text{READFILE}(infile\_Sample, \text{“delimited”})$

Split DATA into a matrix of traces (remove axes):

$M\_Ref := \text{submatrix}(DATA\_Ref, 2, \text{rows}(DATA\_Ref), 2, \text{cols}(DATA\_Ref))$ $\quad \text{rows}(M\_Ref) = 2.968 \cdot 10^3$

$M\_S := \text{submatrix}(DATA\_S, 2, \text{rows}(DATA\_S), 2, \text{cols}(DATA\_S))$ $\quad \text{rows}(M\_S) = 2.999 \cdot 10^3$

Set limits for fit (by index) and obtain time and wavelength axes:

Set wavelength range: $i\lambda\_min := 16$ $\quad i\lambda\_max := 350$ $\quad$ Set time range: $it\_min := 40$ $\quad it\_max := 2500$

Specified range is used for reference and sample measurements:

$\lambda_R := \text{submatrix}(DATA\_Ref, 1, 1, i\lambda\_min, i\lambda\_max)^{\text{T}}\ nm$ $\quad \text{rows}(\lambda_R) = 335$ $\quad \lambda_S := \text{submatrix}(DATA\_S, 1, 1, i\lambda\_min, i\lambda\_max)^{\text{T}}\ nm$

$t_R := \text{submatrix}(DATA\_Ref, it\_min, it\_max, 1, 1)\ ps$ $\quad \text{rows}(t_R) = 2.461 \cdot 10^3$ $\quad t_S := \text{submatrix}(DATA\_S, it\_min, it\_max, 1, 1)\ ps$

Corresponding wavelength range:

$\lambda_{min} := \lambda_{R_1} = 308.235\ nm$

$\lambda_{max} := \lambda_{R_{i\lambda\_max - i\lambda\_min}} = 500.028\ nm$

Corresponding time range:

$t_{min} := t_{R_1} = -5.384\ ps$

$t_{max} := t_{R_{it\_max - it\_min}} = 2.089\ ps$

View time traces to be fitted:

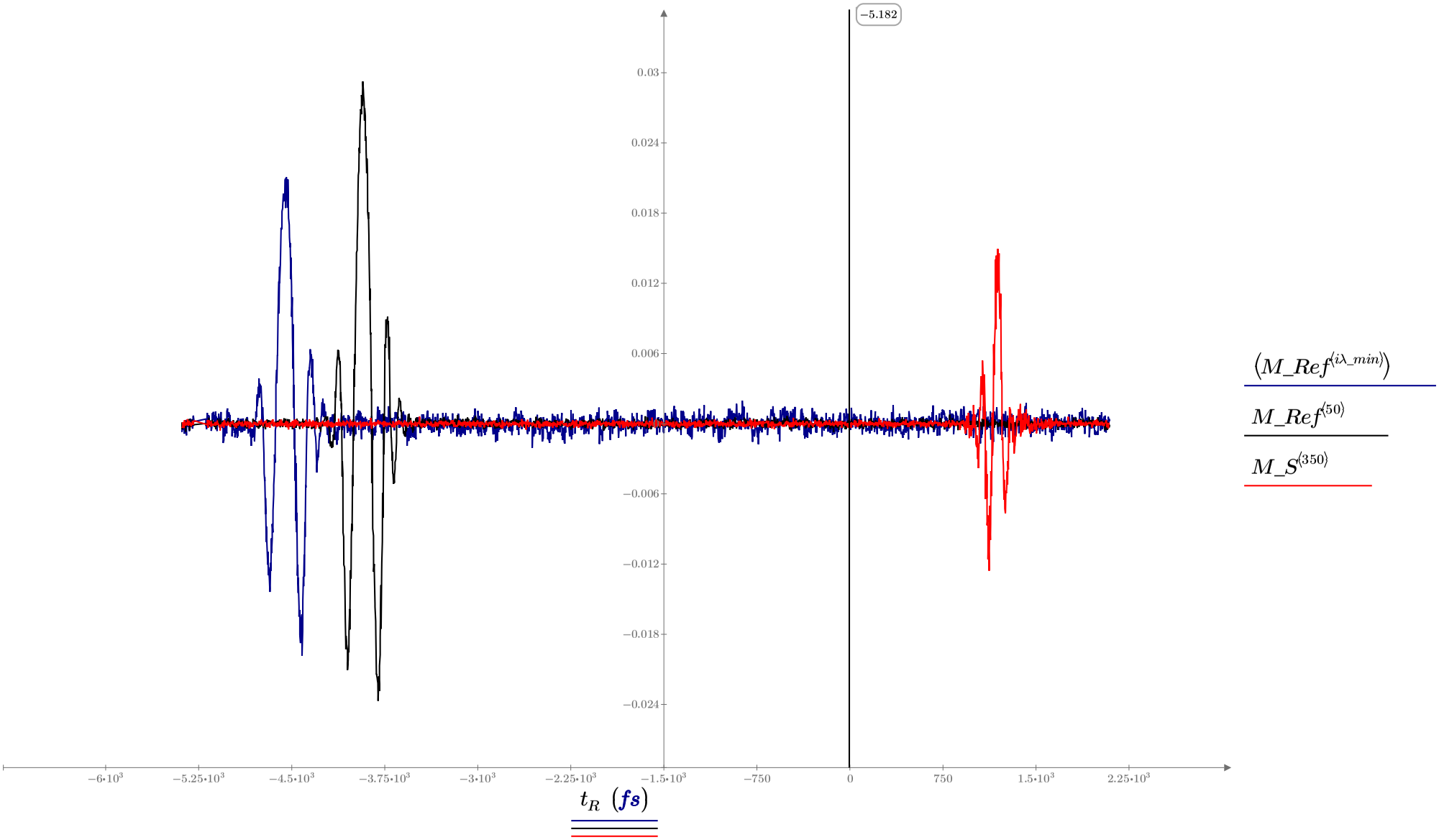

Fitfunction: Combining results from Lor02 and Wah16, the following fit model was obtained:

$$Fcos\left(A_0, A_1, t_0, FWHM, B, \phi, t\right) := \left(A_0 \cdot \exp\left(-\frac{\left(t-t_0\right)^2}{FWHM^2}\right) + \frac{A_1 \cdot e^{-\frac{\left(t-t_0\right)^2}{2\cdot FWHM^2}} \cdot \left(2\cdot t - 2\cdot t_0\right)}{FWHM^2}\right) \cdot \cos\left(B \cdot \left(t-t_0\right)^2 + \phi\right)$$

Using 6 independent paramters: Amplitudes A_0 and A_1, delay t_0, width $FWHM$, perdiodicity paramter B and phase ϕ.

Initial guess values for fit: Give an initial guess for the parameters of the first fit iteration (fit of the first trace). Use the graph below as a guide.

$t_{0Sample} := -4500\ fs$ $t_{0Ref} := -4600\ fs$ $A_{0S} := 0.02$ $A_{1S} := -0.1\ fs$ $FWHM_S := 140\ fs$ $B_S := 1.5 \cdot 10^{-4} \cdot \frac{1}{fs^2}$ $\phi_S := 0.8\ rad$

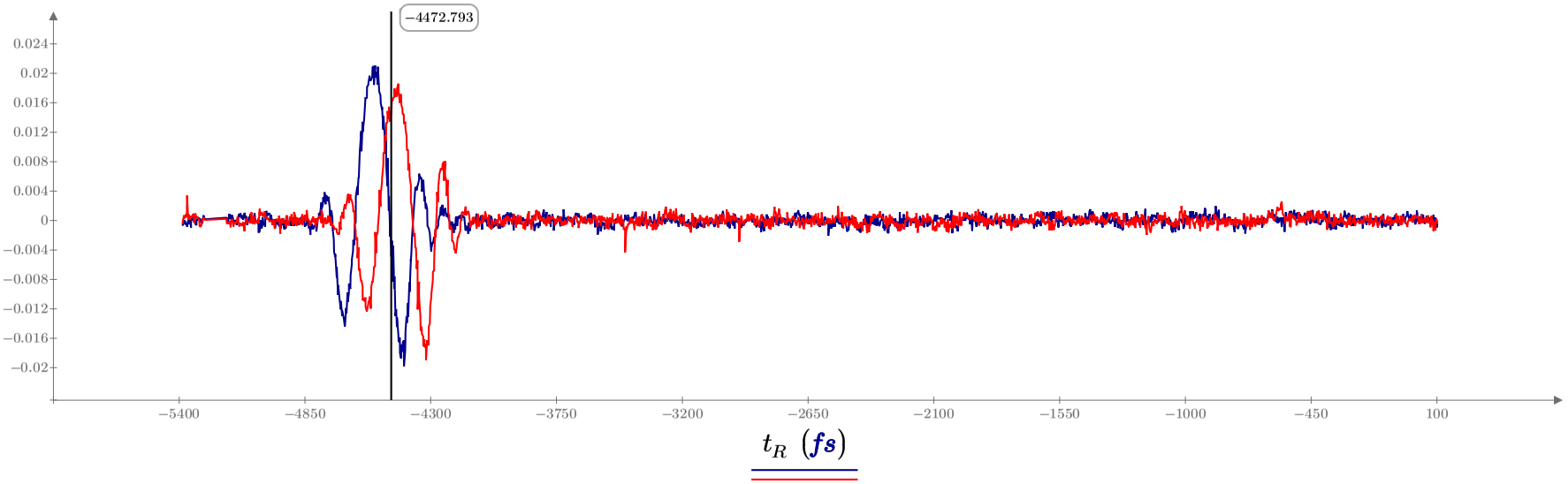

$\langle M\_Ref^{\langle i\lambda\_min\rangle}\rangle$

$M\_S^{\langle i\lambda\_min\rangle}$

Fit window: The signal occupies only a small portion of the trace. To reduce fitting time and increase accuracy the trace is truncated at +/- $window$ datapoints before/after the signal maximum for fitting. Choose window such that the signal occupies about 1/3 of the truncated trace.

$window := 180$

Trace by trace fitting: Fit by including the solver in a for loop.

Values

$Trace = \overrightarrow{Fcos\left(A_0, A_1, t_0, FWHM, B, \phi, t_{mov}\right)}$

Constraints

$0 < A_0 < 0.1 \quad |A_1| < 1\ fs \quad FWHM > 0\ fs \quad B > 0.1 \cdot 10^{-4} \cdot \frac{1}{fs^2} \quad \phi > 0\ rad$

Solver

$Out\left(Trace, A_0, A_1, t_0, FWHM, B, \phi, t_{mov}\right) := \mathbf{minerr}\left(A_0, A_1, t_0, FWHM, B, \phi\right)$

The for loop below can be used for reference & signal measurements, using the respective matrix of traces M, time axis and t_{0start} for each measurement. All other initial guess values are used for both datasets. Constraints were chosen to obtain the best possible fit.

t_{mov} is the truncated time axis for each step as set via $window$ moving with the coherent artifact.

$Fit\left(M, t, t_{0start}\right) :=$

$i \leftarrow 1$

$it_0 \leftarrow \left(\text{match}\left(\max\left(M^{\langle i\lambda\_min \rangle}\right), \left(M^{\langle i\lambda\_min \rangle}\right)\right)\right)_1$

$SigSel \leftarrow \text{submatrix}\left(M^{\langle i\lambda\_min \rangle}, it_0 - window, it_0 + window, 1, 1\right)$

$t_{mov} \leftarrow \text{submatrix}\left(t, it_0 - window, it_0 + window, 1, 1\right)$

$t_{0S} \leftarrow t_{0start}$

$Par1 \leftarrow Out\left(SigSel, A_{0S}, A_{1S}, t_{0S}, FWHM_S, B_S, \phi_S, t_{mov}\right)$

for $j \in 1, 2..6$

$\quad Fit_{i,j} \leftarrow Par1_j$

$Fit_{i,7} \leftarrow it_0$

for $i \in 2, 3..i\lambda\_max - i\lambda\_min + 1$

$\quad it_0\_i \leftarrow \left(\text{match}\left(\max\left(M^{\langle i\lambda\_min + i - 1 \rangle}\right), \left(M^{\langle i\lambda\_min + i - 1 \rangle}\right)\right)\right)_1$

$\quad t_{mov}\_i \leftarrow \text{submatrix}\left(t, it_0\_i - window, it_0\_i + window, 1, 1\right)$

$\quad SigSel \leftarrow \text{submatrix}\left(M^{\langle i\lambda\_min + i - 1 \rangle}, it_0\_i - window, it_0\_i + window, 1, 1\right)$

$\quad Par\_i \leftarrow Out\left(SigSel, Fit_{i-1,1}, A_{1S}, Fit_{i-1,3}, Fit_{i-1,4}, B_S, Fit_{i-1,6}, t_{mov}\_i\right)$

$\quad$ for $j \in 1, 2..6$

$\quad\quad Fit_{i,j} \leftarrow Par\_i_j$

$\quad Fit_{i,7} \leftarrow it_0\_i$

Fit

Find index of trace maximum it_0. Truncate trace and time axis around it_0 at +/- $window$.

Fit 1st trace using initial guess values & insert fitted parameters into the first row of the matrix Fit.

Add it_0 into Fit as 7th element.

Iterate the above procedure via for loop, using appropriate it_0_i and $window$ for each step.

Take fitted parameters from last step as initial guess for the next step. (Except A_{1S} and B_S, which are used in every step)

For each trace, insert fitted parameters and it_0_i into the respective row of the matrix Fit.

View Data & Fit - Select index: $ii := 200$ Corresponding wavelength: $\lambda_{R_{ii}} = 384.961\ nm$ Residual: $Res(Data, Fit) := (Data - Fit) - 1.5 \cdot \max(Data)$

The lines of the matrix Fit contain the fit parameters for each trace. Looking at a given column yields the wavelength dependence of the given parameter.

$Par\_R := Fit(M\_Ref, t_R, t_{0Ref})$ $A_{0R} := Par\_R^{\langle 1 \rangle}$ $A_{1R} := Par\_R^{\langle 2 \rangle}$ $t_{0R} := Par\_R^{\langle 3 \rangle}$ $FWHM_R := Par\_R^{\langle 4 \rangle}$ $B_R := Par\_R^{\langle 5 \rangle}$ $\phi_R := Par\_R^{\langle 6 \rangle}$

Graphs below show only the fitted window with the corresponding datapoints. Time axis moves along as index ii is increased!

$$Par\_R = \begin{bmatrix} 0.032 & (2.749 \cdot 10^{-16})\ s & -4.554 \cdot 10^{-12}\ s & (1.547 \cdot 10^{-13})\ s & (1.207 \cdot 10^{26})\ \frac{1}{s^2} & 0.869 & 250 \\ \vdots & & & & & & \end{bmatrix}$$

$$it_0R := Par\_R^{\langle 7 \rangle} = \begin{bmatrix} 250 \\ 250 \\ 266 \\ 266 \\ \vdots \end{bmatrix}$$

indt0 should rise monotonically if moving window has worked

$t_{windowR} := \text{submatrix}(t_R, it_0R_{ii} - window, it_0R_{ii} + window, 1, 1)$

$Ref(ii) := \text{submatrix}(M\_Ref^{\langle ii + i\lambda\_min - 1 \rangle}, (it_0R_{ii} - window), it_0R_{ii} + window, 1, 1)$

$FitRef(ii) := \text{submatrix}(Fcos(A_{0R_{ii}}, A_{1R_{ii}}, t_{0R_{ii}}, FWHM_{R_{ii}}, B_{R_{ii}}, \phi_{R_{ii}}, t_R), it_0R_{ii} - window, it_0R_{ii} + window, 1, 1)$

Reference Data & Fit:

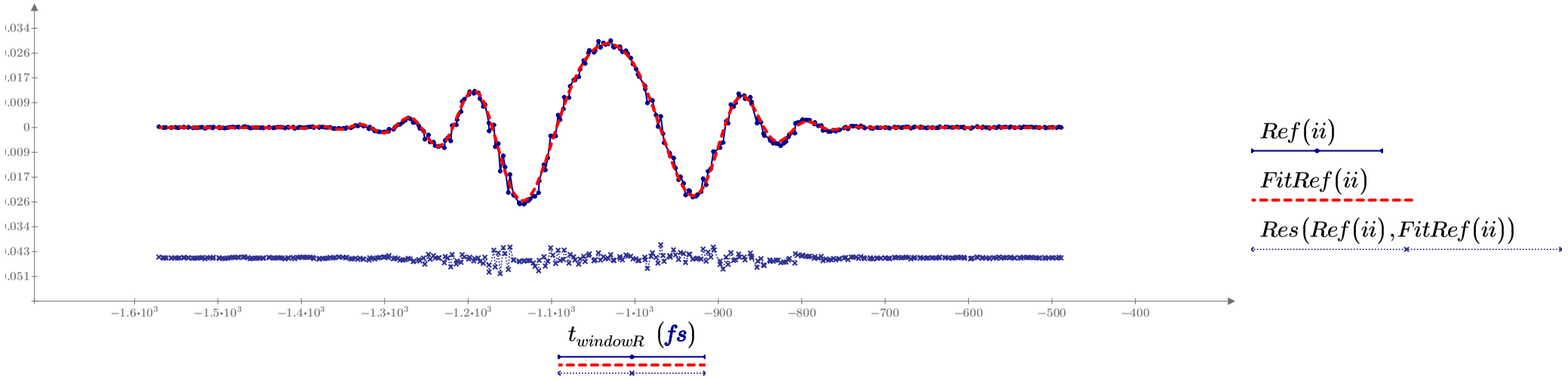

Sample Mirror Data & Fit: Corresponding wavelength: $\lambda_{S_{ii}} = 385.206\ nm$

$Par\_S := Fit\left(M\_S, t_S, t_{0Sample}\right)$ $A_{0S} := Par\_S^{\langle 1 \rangle}$ $A_{1S} := Par\_S^{\langle 2 \rangle}$ $t_{0S} := Par\_S^{\langle 3 \rangle}$ $FWHM_S := Par\_S^{\langle 4 \rangle}$ $B_S := Par\_S^{\langle 5 \rangle}$ $\phi_S := Par\_S^{\langle 6 \rangle}$

$$Par\_S = \begin{bmatrix} 0.027 & \left(3.116 \cdot 10^{-16}\right) s & -4.547 \cdot 10^{-12}\ s & \left(1.661 \cdot 10^{-13}\right) s & \left(1.225 \cdot 10^{26}\right) \frac{1}{s^2} & 0.858 & 284 \\ 0.028 & \left(3.437 \cdot 10^{-16}\right) s & -4.527 \cdot 10^{-12}\ s & \left(1.656 \cdot 10^{-13}\right) s & \left(1.223 \cdot 10^{26}\right) \frac{1}{s^2} & 0.839 & 287 \\ & & & & & & \vdots \end{bmatrix}$$

$$it_0S := Par\_S^{\langle 7 \rangle} = \begin{bmatrix} 284 \\ 287 \\ 290 \\ 303 \\ \vdots \end{bmatrix}$$

indt0 should rise monotonically if moving window has worked

$t_{windowS} := \text{submatrix}\left(t_S, it_0S_{ii} - window, it_0S_{ii} + window, 1, 1\right)$

$Sample(ii) := \text{submatrix}\left(M\_S^{\langle ii + i\lambda\_min - 1 \rangle}, \left(it_0S_{ii} - window\right), it_0S_{ii} + window, 1, 1\right)$

$FitS(ii) := \text{submatrix}\left(Fcos\left(A_{0S_{ii}}, A_{1S_{ii}}, t_{0S_{ii}}, FWHM_{S_{ii}}, B_{S_{ii}}, \phi_{S_{ii}}, t_S\right), it_0S_{ii} - window, it_0S_{ii} + window, 1, 1\right)$

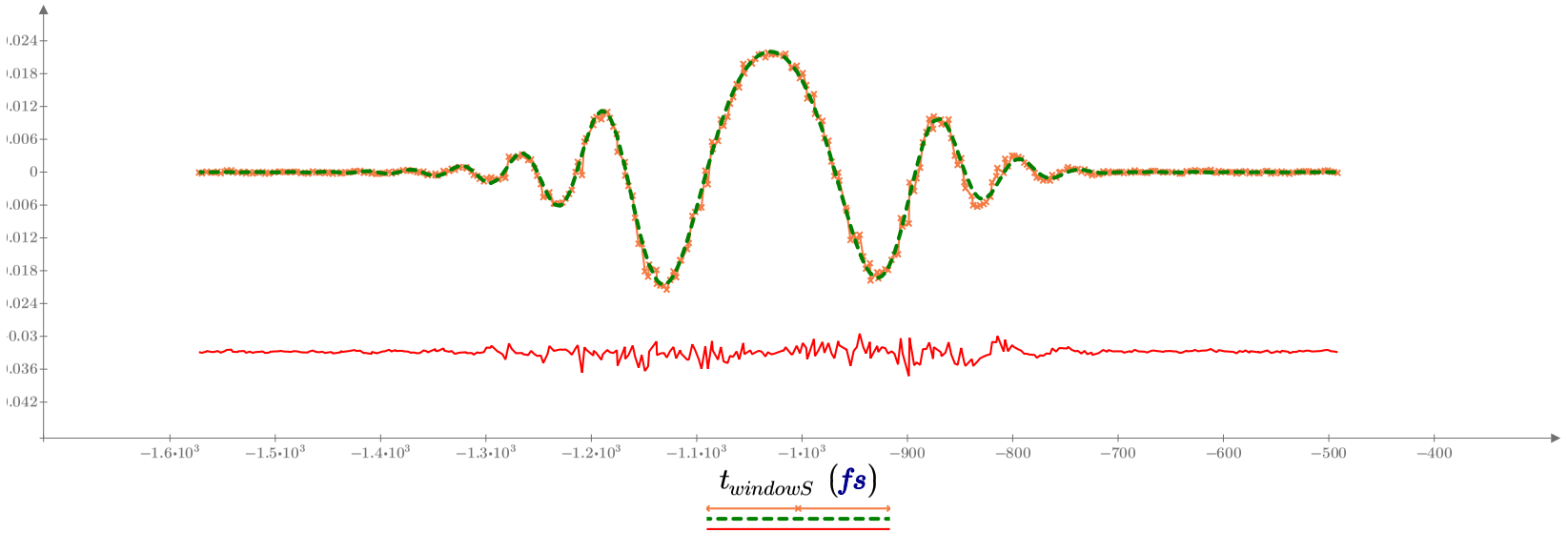

$Sample(ii)$

$FitS(ii)$

$Res(Sample(ii), FitS(ii))$

Quality of fit: Compute the RMS of the residual to quantify the fit quality Q1 inside and Q2 outside the fitted window. $iii := 1,2..i\lambda\_max - i\lambda\_min + 1$

$$Variance(V) := \frac{1}{\text{rows}(V)-1} \cdot \left(\sum_{i=1}^{\text{rows}(V)-1} \left(V_i - \text{mean}(V) \right)^2 \right) \qquad Stdev(V) := \sqrt[2]{Variance(V)}$$

Q1: RMS of Residual within fitted window divided by RMS of Signal within fitted window:

$$\text{Q1\_Ref}_{iii} := \frac{\text{Stdev}(Ref(iii) - FitRef(iii))}{\text{Stdev}(Ref(iii))} \qquad \text{Q1\_Sample}_{iii} := \frac{\text{Stdev}(Sample(iii) - FitS(iii))}{\text{Stdev}(Sample(iii))}$$

Q2: RMS outside (one $window$-length to the right) of fitted window divided by RMS of Signal within fitted window:

$$Q2\_Ref_{iii} := \frac{\text{Stdev}\left(\text{submatrix}\left(M\_Ref^{\langle iii \rangle}, \left(it_0R_{iii} + 1\ window\right), it_0R_{iii} + 2\ window, 1, 1\right)\right)}{\text{Stdev}(Ref(iii))} \qquad Q2\_Sample_{iii} := \frac{\text{Stdev}\left(\text{submatrix}\left(M\_S^{\langle iii \rangle}, \left(it_0S_{iii} + 1\ window\right), it_0S_{iii} + 2\ window, 1, 1\right)\right)}{\text{Stdev}(Sample(iii))}$$

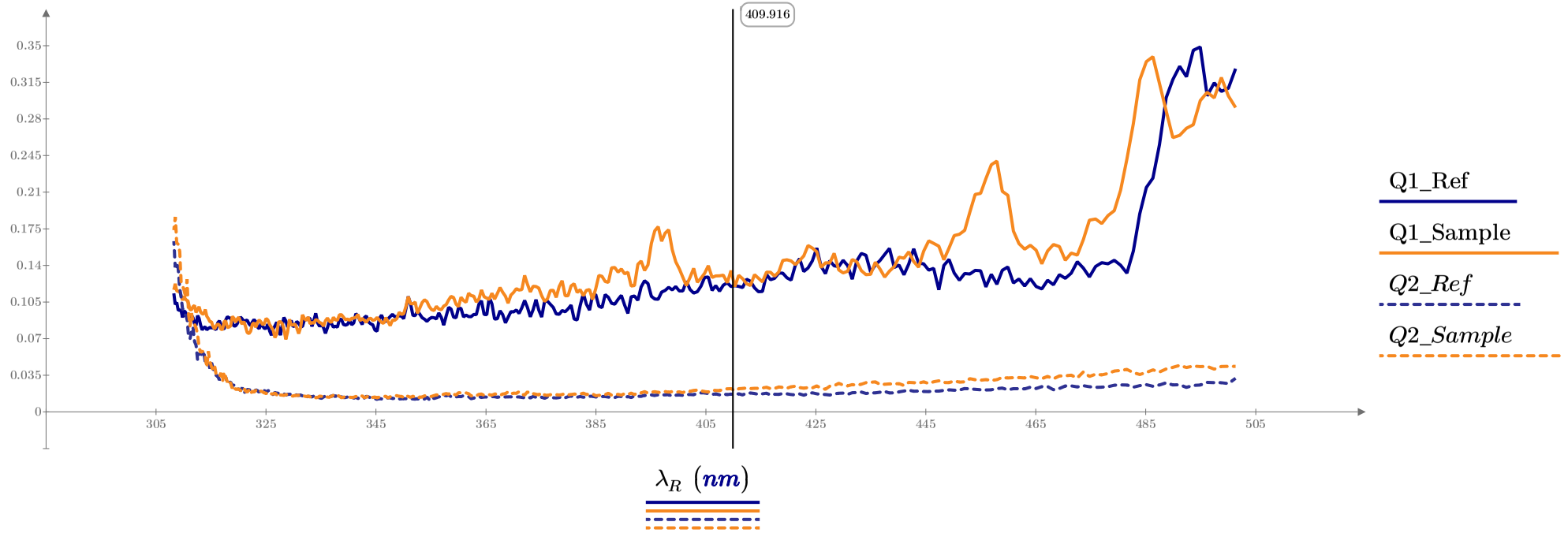

Wavelength dependence of fit parameters for reference and signal mesaurements

Gauss Amplitude A_0:

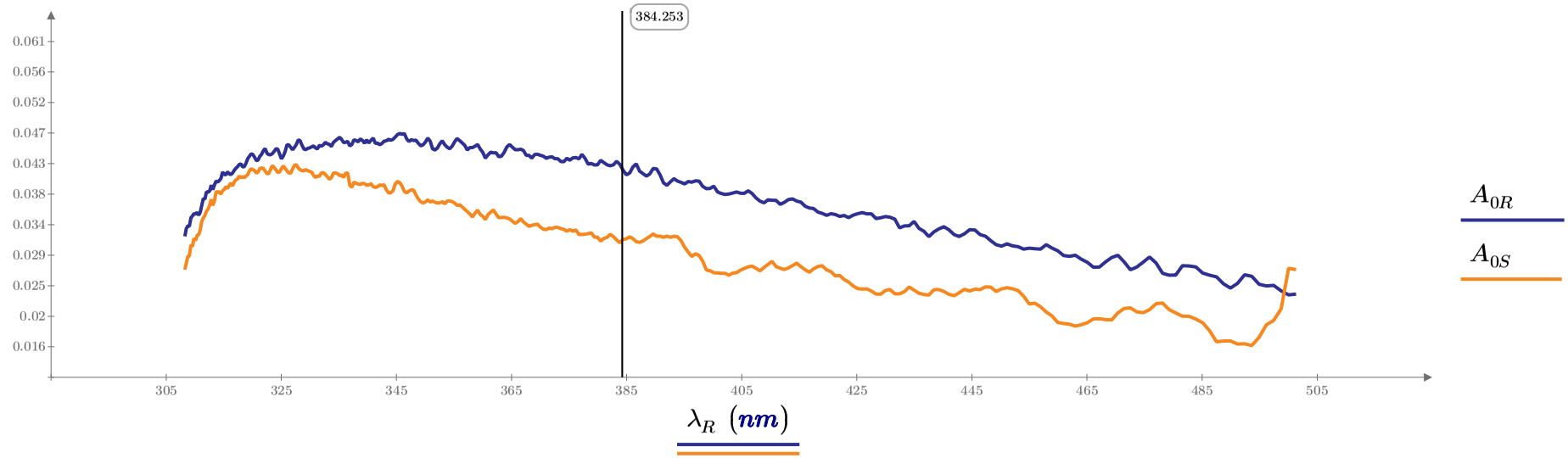

Amplitude of Gauss first derivative:

A_1 carries the unit ps and is not directly comparable to A_0. To obtain a meaningful Amplitude it is scaled accordingly.

$$A_{1R\_sc} := \frac{2 \cdot A_{1R} \cdot \sqrt{2 \cdot \ln(2)}}{\sqrt{e} \cdot FWHM_R}$$

$$A_{1S\_sc} := \frac{2 \cdot A_{1R} \cdot \sqrt{2 \cdot \ln(2)}}{\sqrt{e} \cdot FWHM_S}$$

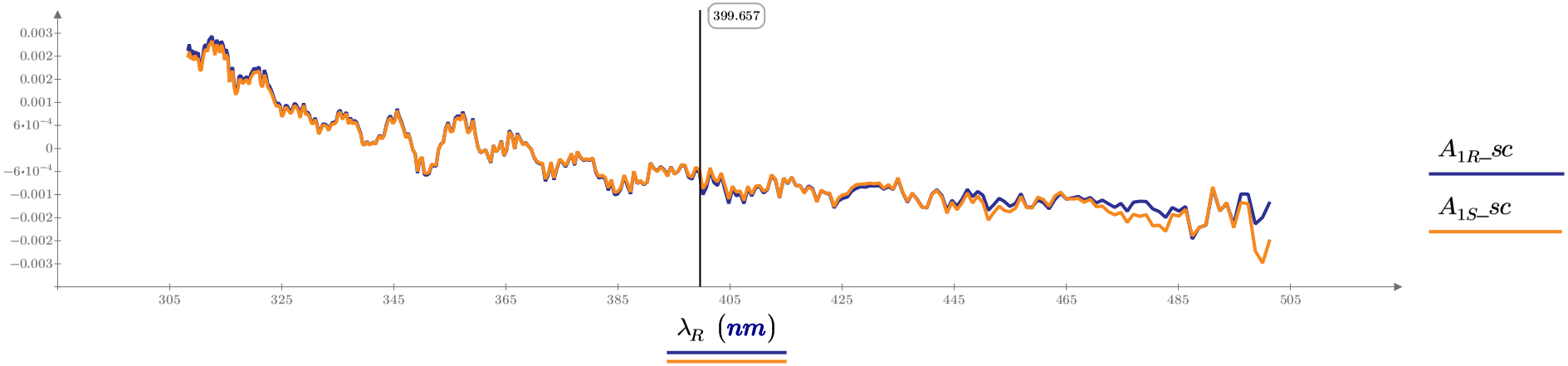

Width $FWHM$: $FWHM$ represents the width of the Gaussian envelope. It is not always a direct gauge for the IRF, since artifact fringes can effectively broaden the signal.

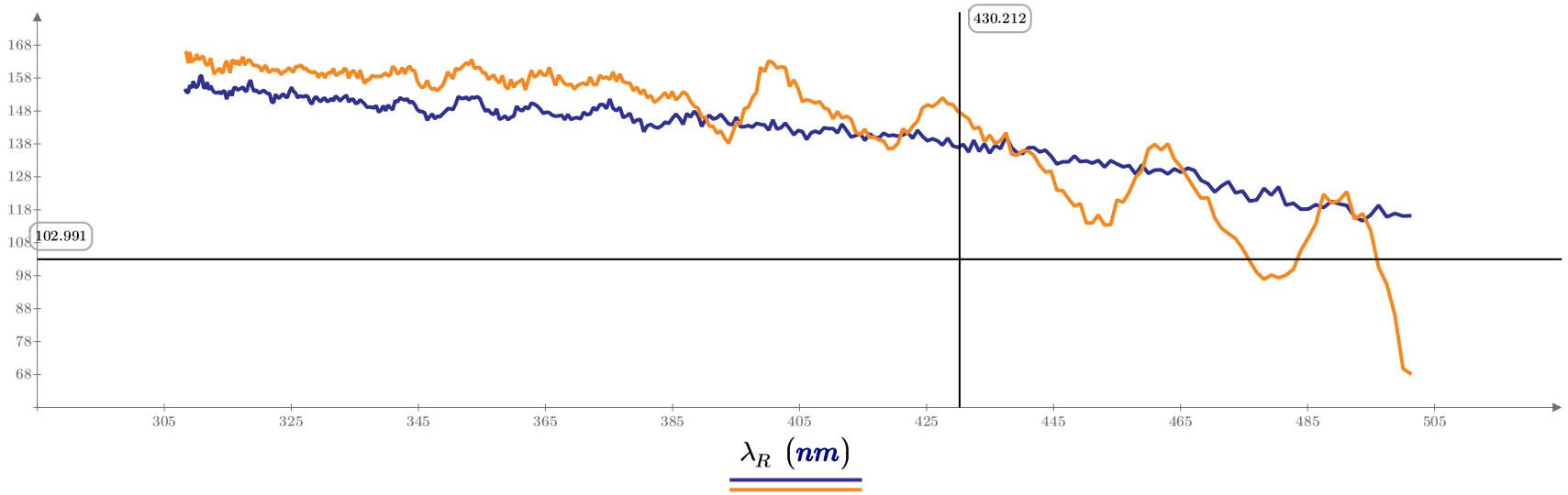

Periodicity Parameter B: B is a measure for the periodicity of the artifact fringes. It is not simply a frequency since their frequency increases linearly with time ($cos(\omega t \cdot t)$), so B carries the unit $\frac{1}{fs^2}$.

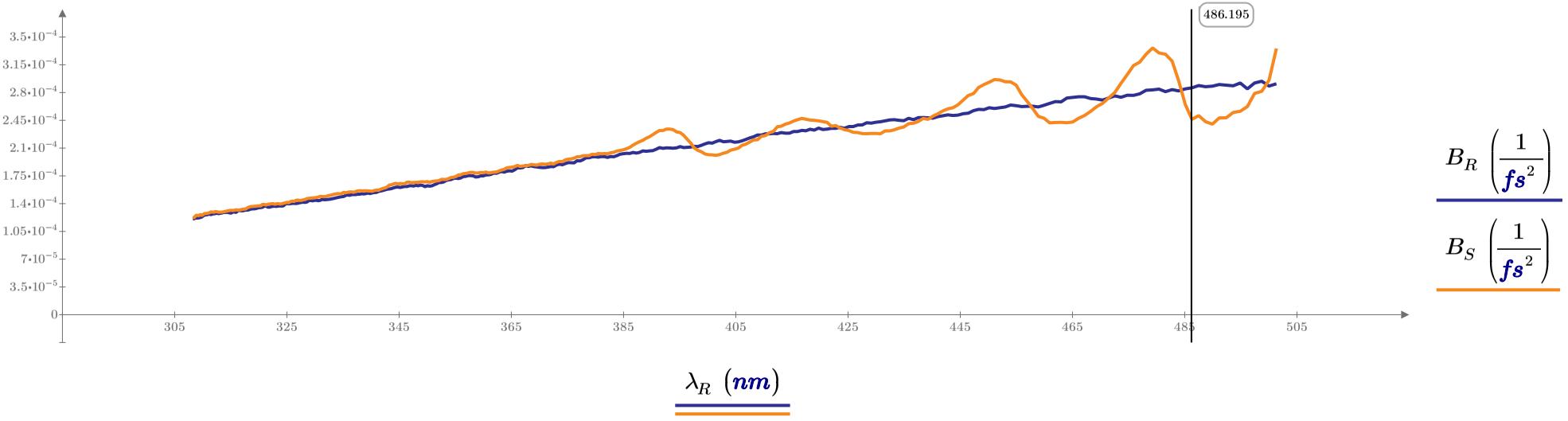

Phase ϕ: ϕ is the phase of the fitted cosine function.

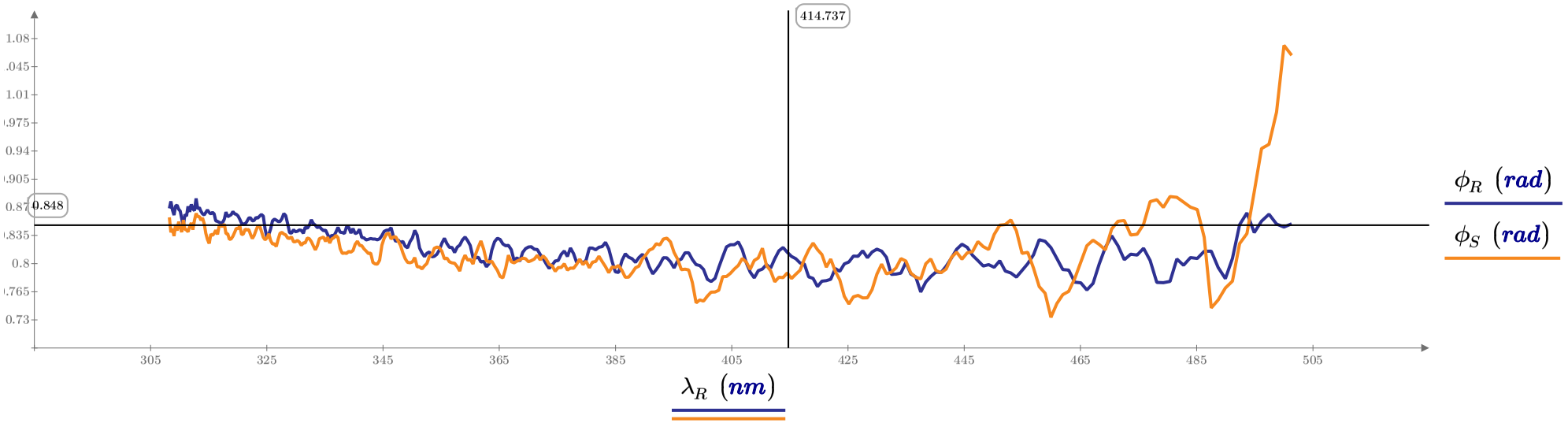

Intrpolate Reference t_0 by 9th order polynomial fit:

t_0 represents the time of perfect overlap between the pump and a chosen probe wavelength. The sample imprints its GD into the probe chirp and therefore the sample GD can be calculated by subtracting the reference t_0. The reference t_0 curve is fitted by a 9th order polynmial before subtraction:

$$Pol(\lambda, G_1, G_2, G_3, G_4, G_5, G_6, G_7, G_8, G_9) := \left(G_1 \cdot ps + \frac{G_2 \cdot ps}{nm} \cdot \lambda + \frac{G_3 \cdot ps}{nm^2} \cdot \lambda^2 + \frac{G_4 \cdot ps}{nm^3} \cdot \lambda^3 + \frac{G_5 \cdot ps}{nm^4} \cdot \lambda^4 + \frac{G_6 \cdot ps}{nm^5} \cdot \lambda^5 + \frac{G_7 \cdot ps}{nm^6} \cdot \lambda^6 + \frac{G_8 \cdot ps}{nm^7} \cdot \lambda^7 + \frac{G_9 \cdot ps}{nm^8} \cdot \lambda^8\right)$$

$\lambda_1 := \lambda_R - 500\ nm$ Shift wavelength for fit to avoid large numbers when computing higher orders of λ.

Given

$G_1 := -42$ $G_3 := 0.1$ $G_5 := 10^{-4}$ $G_7 := 10^{-8}$ $G_9 := 10^{-13}$

$G_2 := 1$ $G_4 := 10^{-3}$ $G_6 := 10^{-6}$ $G_8 := 10^{-10}$

Constraints

Solve Guess Values

$t_{0R} = Pol(\lambda_1, G_1, G_2, G_3, G_4, G_5, G_6, G_7, G_8, G_9)$

$Par := \mathbf{minerr}(G_1, G_2, G_3, G_4, G_5, G_6, G_7, G_8, G_9)$

$$Par = \begin{bmatrix} 1.105 \\ 0.012 \\ -2.761 \cdot 10^{-5} \\ 5.242 \cdot 10^{-7} \\ 6 \cdot 10^{-9} \\ 5.64 \cdot 10^{-11} \\ 2.674 \cdot 10^{-13} \\ 7.043 \cdot 10^{-16} \\ 6.667 \cdot 10^{-19} \end{bmatrix}$$

Fitted polynomial: $PFit\_Ref := Pol(\lambda_1, Par_1, Par_2, Par_3, Par_4, Par_5, Par_6, Par_7, Par_8, Par_9)$

$t_0(\lambda)$ for sample and reference traces and polynomial fit to the reference $t_0(\lambda)$:

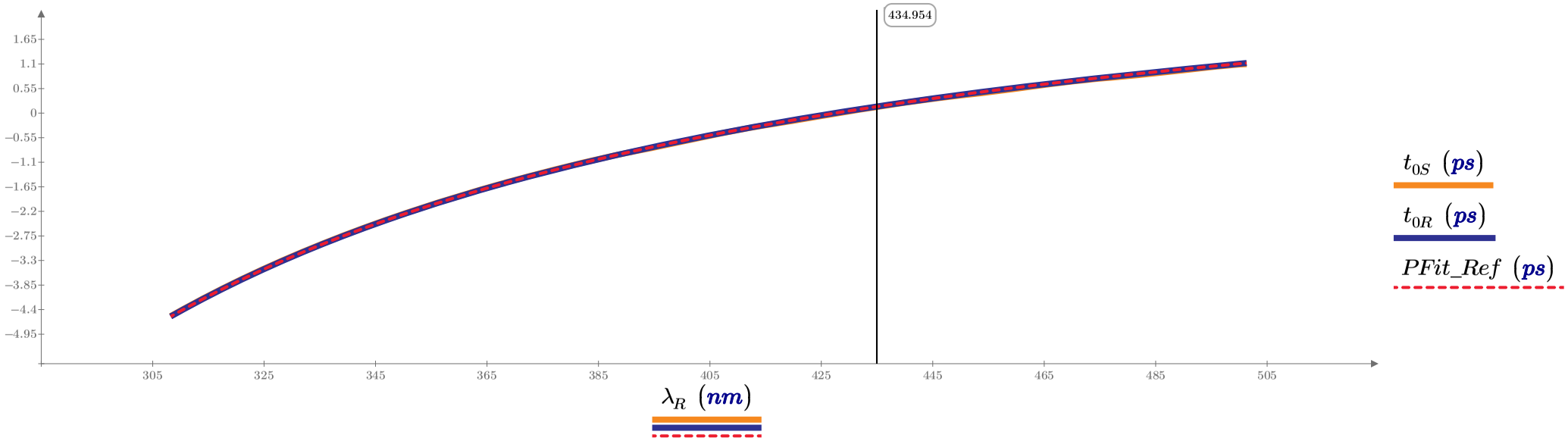

Residual of polynomial fit to reference: The standard deviation is < 0.5 fs and represents a measure for the accuracy in the determination of $t_0(\lambda)$

$$Stdev\left(t_{0R} - PFit\_Ref\right) = 0.401 \text{ fs}$$

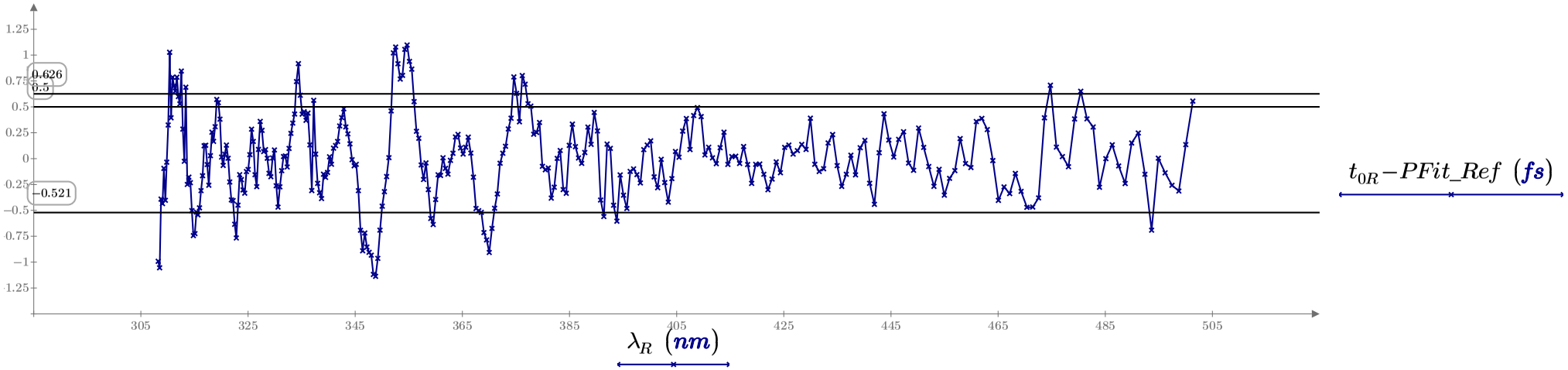

Sample GD: The sample's GD is calculated by linearly interpolating the sample axis λ_S onto the reference axis λ_R and subsequently subtracting the interpolated reference t_{0R} from the sample t_{0S}. The t_0 curves are not directly subtracted because the wavelength axis for reference and sample can differ slightly. Since GD is a relative quantity, it is ok to add a constant offset to the GD curve.

$li := 1,2..\text{rows}\left(t_{0R}\right)$ $t_{0S\_interp_{li}} := \text{linterp}\left(\lambda_S, t_{0S}, \lambda_{R_{li}}\right) = \begin{bmatrix} -4.555 \cdot 10^3 \\ \vdots \end{bmatrix}$ *fs* $offset := -0$ *fs* $GD := t_{0R} - t_{0S\_interp} + offset$

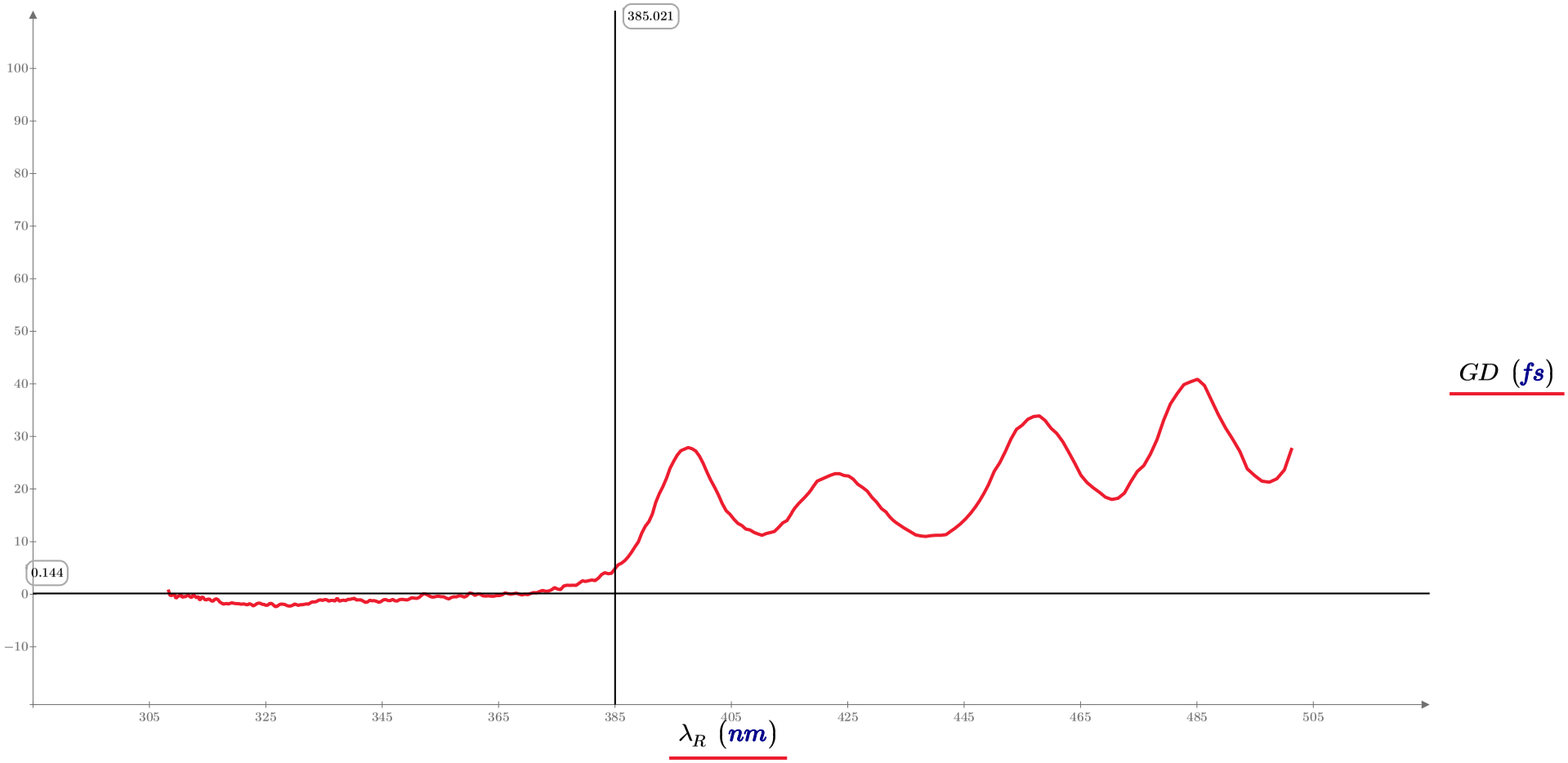

Output: The GD data and fit are written into an external text file. Note that units need to be stripped for writing. Units in the textfile are reciprocal to the factors shown in $data$.

$haeder := \text{augment}(\text{“lambda\_s (nm)”}, \text{“t0s (fs)”}, \text{“A0s”}, \text{“A1s\_sc”}, \text{“FWHMs (fs)”}, \text{“Bs (1/fs^2)”}, \text{“Phi\_s (rad)”}, \text{“lambda\_r (nm)”}, \text{“t0r (fs)”}, \text{“A0r”}, \text{“A1r\_sc”}, \text{“F}$

$$data := \text{augment}\left(\frac{\lambda_S}{nm}, \frac{t_{0S}}{fs}, A_{0S}, A_{1S\_}sc, \frac{FWHM_S}{fs}, B_S \cdot fs^2, \phi_S, \frac{\lambda_R}{nm}, \frac{t_{0R}}{fs}, A_{0R}, A_{1R\_}sc, \frac{FWHM_R}{fs}, B_R \cdot fs^2, \phi_R, \frac{GD}{fs}\right)$$

$OUT := \text{stack}(haeder, data) =$

“lambda_s (nm)”	“t0s (fs)”	“A0s”	“A1s_sc”	“FWHMs (fs)”	“Bs (1/fs^2)”	“Phi_s (rad)”	“lambda_r (nm)”
308.348	$-4.547 \cdot 10^3$	0.027	0.002	166.063	$1.225 \cdot 10^{-4}$	0.858	308.235
308.611	$-4.527 \cdot 10^3$	0.028	0.003	165.589	$1.223 \cdot 10^{-4}$	0.839	308.498
308.876	$-4.508 \cdot 10^3$	0.029	0.002	162.51	$1.249 \cdot 10^{-4}$	0.843	308.762
309.141	$-4.49 \cdot 10^3$	0.029	0.002	165.887	$1.252 \cdot 10^{-4}$	0.834	309.027
309.408	$-4.471 \cdot 10^3$	0.031	0.002	162.766	$1.246 \cdot 10^{-4}$	0.848	309.293
309.675	$-4.452 \cdot 10^3$	0.03	0.002	163.73	$1.263 \cdot 10^{-4}$	0.841	309.56
309.943	$-4.434 \cdot 10^3$	0.031	0.002	163.45	$1.249 \cdot 10^{-4}$	0.852	309.827
310.211	$-4.415 \cdot 10^3$	0.031	0.002	165.204	$1.263 \cdot 10^{-4}$	0.845	310.096
310.481	$-4.396 \cdot 10^3$	0.032	0.002	163.785	$1.275 \cdot 10^{-4}$	0.839	310.365
310.752	$-4.378 \cdot 10^3$	0.032	0.002	163.683	$1.274 \cdot 10^{-4}$	0.854	310.635
311.023	$-4.359 \cdot 10^3$	0.033	0.002	164.547	$1.279 \cdot 10^{-4}$	0.843	310.906
311.295	$-4.341 \cdot 10^3$	0.034	0.003	164.411	$1.284 \cdot 10^{-4}$	0.842	311.178
311.568	$-4.323 \cdot 10^3$	0.034	0.003	162.448	$1.295 \cdot 10^{-4}$	0.839	311.451
311.842	$-4.304 \cdot 10^3$	0.035	0.003	161.829	$1.294 \cdot 10^{-4}$	0.846	311.724
							⋱

$name := \text{concat}(\text{substr}(infile\_Sample, 3, \text{strlen}(infile\_Sample) - 7), \text{“\_FIT”}, \text{“.dat”})$

$x := \text{WRITETEXT}(name, OUT)$ $name = \text{“B270\_1uJ\_Df350−1100\_BK7\_flip\_001\_WL\_OD\_FIT.dat”}$

B3 Artifact Simulation 5 - including Mirror GD and Fit using FCos

Bastian Baudisch, März 2017

This program comuptes time domain pulse shapes via dft from an input probe pulse spectrum and a group delay (GD) curve.
Optionally reflection of the pulse on a mirror with known GD can be included.
Secondly the XPM induced TA signals that would be observed in transmission are computed and fitted using different fitfunctions, reproducing the input GD.

$ORIGIN := 1$
$fs := 10^{-15}\ s$
$THz := 10^{12}\ Hz$
$GW := 10^{9}\ W$

Create equally spaced frequency axis:

$\omega_{min} := 2300\ THz$ $\omega_{max} := 6500\ THz$ $\Delta\omega := 0.25\ THz$

$2 \cdot \pi \cdot c \cdot \omega_{max}^{-1} = 289.793\ nm$ $\omega := \omega_{min}, \omega_{min} + \Delta\omega .. \omega_{max} = \begin{bmatrix} \vdots \\ 3324.75 \\ \vdots \end{bmatrix} THz$ $\mathrm{rows}(\omega) = 16801$ $\lambda := \frac{2 \cdot \pi \cdot c}{\omega}$

Create/Read probe spectrum:

$\lambda_{0probe} := 480\ nm$ $FWHM_{probe} := 240\ nm$ $\omega_{0probe} := 2 \cdot \pi \cdot c \cdot \lambda_{0probe}^{-1} = 3924\ THz$

$$w_{probe} := \left(\frac{2 \cdot \pi \cdot c}{\left(\lambda_{0probe} - \frac{FWHM_{probe}}{4 \cdot \sqrt{\ln(2)}} \right)} - \frac{2 \cdot \pi \cdot c}{\left(\lambda_{0probe} + \frac{FWHM_{probe}}{4 \cdot \sqrt{\ln(2)}} \right)} \right) = \left(1.206 \cdot 10^{3}\right) THz$$

$$Spec_{\omega} := 1 \cdot e^{-\frac{\left(\omega - \omega_{0probe}\right)^{2 \cdot 3}}{\left(w_{probe}\right)^{2 \cdot 3}}}$$

$realspec := \mathrm{submatrix}(\mathrm{READFILE}(\text{“real\_probespec\_160314.txt”}, \text{“delimited”}), 1, 523, 1, 2)$ $Spec_{real} := \mathrm{linterp}\left(realspec^{\langle 1 \rangle} \cdot nm, \frac{2 \cdot realspec^{\langle 2 \rangle}}{\max\left(realspec^{\langle 2 \rangle}\right)}, \lambda \right)$

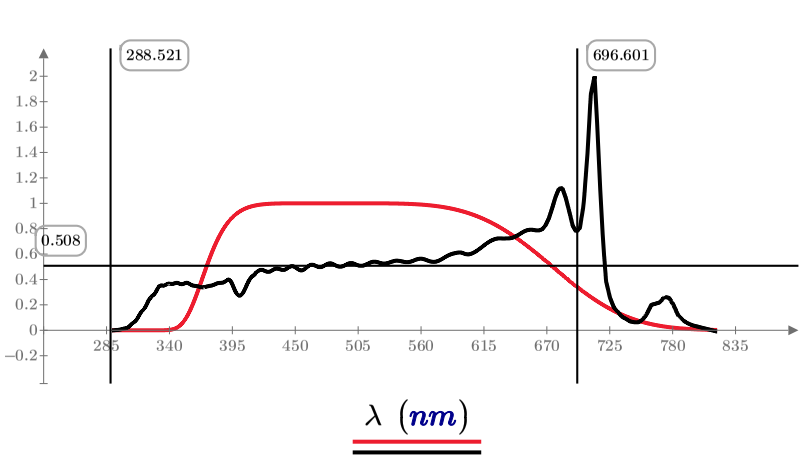

$Spec_{\omega}$
$Spec_{real}$

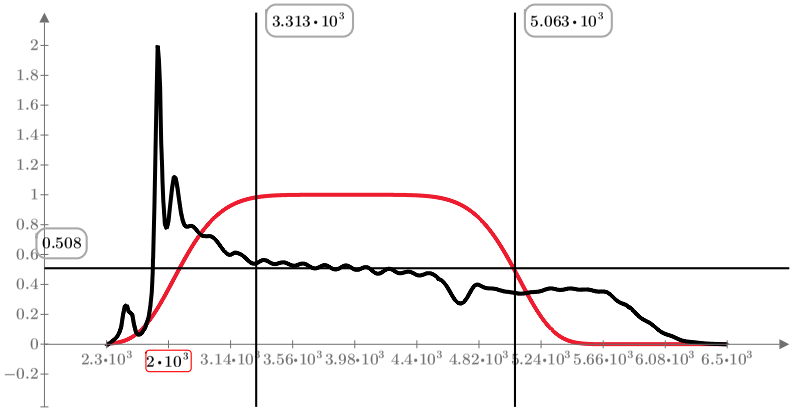

$Spec_{\omega}$
$Spec_{real}$

$Spec := Spec_{real}$

Fourier Limit estimated from Spectrum:

$FWHM_{THz} := 2 \cdot \sqrt{\ln(2)} \cdot w_{probe} = (2.007 \cdot 10^3)\ THz$ $\Delta\nu_{FWHM} := \frac{FWHM_{THz}}{2\ \pi}$ $\tau_{FL} := \frac{0.441}{\Delta\nu_{FWHM}} = 1.38\ fs$

Define Probe Phase (Linear Chirp β): $\beta := 10 \cdot 10^{-3}\ \frac{1}{fs^2}$ $\beta_\omega := \frac{1}{\beta}$ (similarity theorem..) $\phi_{probeLC} := \frac{1}{2} \cdot \beta_\omega \cdot (\omega - \omega_{0probe})^2$

$n := 1, 2 .. \text{rows}(\omega)$ $E_{FL_n} := \sqrt{Spec_n} \cdot 1$ $E_{LC_n} := \sqrt{Spec_n} \cdot e^{1i \cdot \phi_{probeLC_n}}$

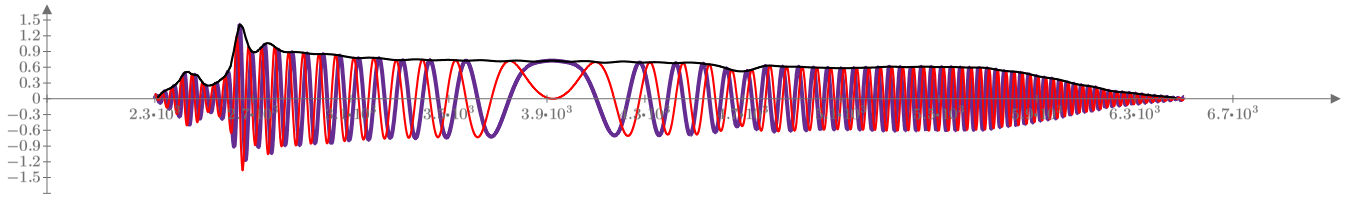

$\omega_n\ (THz)$ $\text{Re}(E_{LC_n})$ $\text{Im}(E_{LC_n})$ $\sqrt{Spec_n}$

Alterative: Read real Probe GD (fs) vs λ from file: $probeGD := \text{READFILE}(\text{“real\_wlgd\_160314.dat”}, \text{“delimited”})$

$GD_{probe} := \text{linterp}(GD\_data^{(1)}\ nm, -GD\_data^{(2)} \cdot fs, \lambda) = ?\ fs$ $GD_{probe_n} := 0\ fs$

Model Mirror Reflection:
Create/Read Mirror GD (fs) vs λ from file:

$GD_{mirror} := 10 \sin\left(0.04 \frac{\lambda}{nm} + 1.75\right) \cdot fs$ No. of Reflections on Mirror: $N_{refl} := 1$

$mirrorGD := submatrix(READFILE(\text{“GD\_Diflex1100\_extrapolated.txt”}, \text{“delimited”}), 230, rows(mirrorGD\_data) - 2000, 1, 2)$

$GDoffset := 55\ fs$ $GD_{mirror} := (\text{linterp}(mirrorGD\_trunc^{(1)} \cdot nm, mirrorGD\_trunc^{(2)} \cdot fs, \lambda_{GD})) + GDoffset$

$$GD := \overrightarrow{GD_{mirror} + GD_{probe}}$$

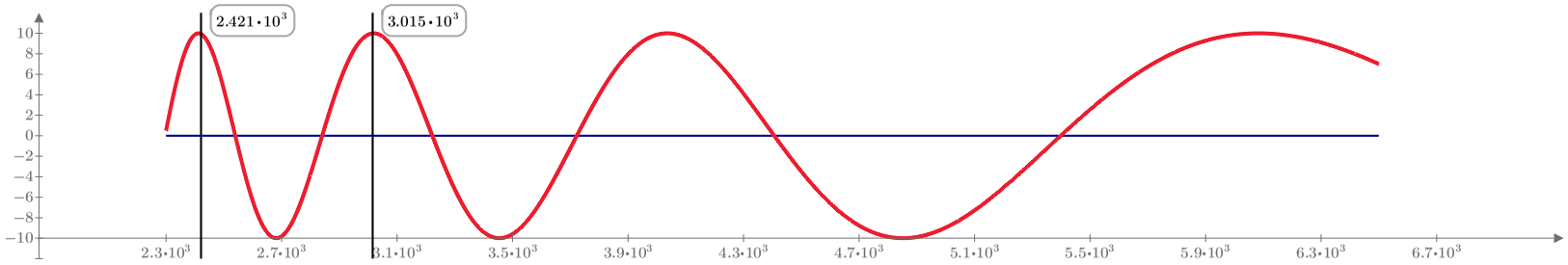

$\omega \ (THz)$

$GD_{probe} \ (fs)$

$GD_{mirror} \ (fs)$

Numerically integrate Spectral Phase from GD:

$$\phi(GD) := \left\| \begin{array}{l} \phi_1 \leftarrow 0 \\ \text{for } q \in 2,3..\text{rows}(\omega) \\ \quad \left\| \phi_q \leftarrow \phi_{q-1} + (GD)_q \cdot (\omega_q - \omega_{q-1}) \right. \\ \phi \end{array} \right.$$

$$\phi_{mirror} := \phi(GD_{mirror}) = \begin{bmatrix} \vdots \\ ? \\ ? \\ 5.17 \end{bmatrix}$$

$$\phi_{probeReal} := \phi(GD_{probe})$$

Total Spectral Phase:

$$\phi_S := \phi_{probeLC} + \phi_{probeReal} + N_{refl} \cdot \phi_{mirror}$$

$$E_n := \sqrt{Spec_n} \cdot e^{1i \cdot \phi_{S_n}}$$

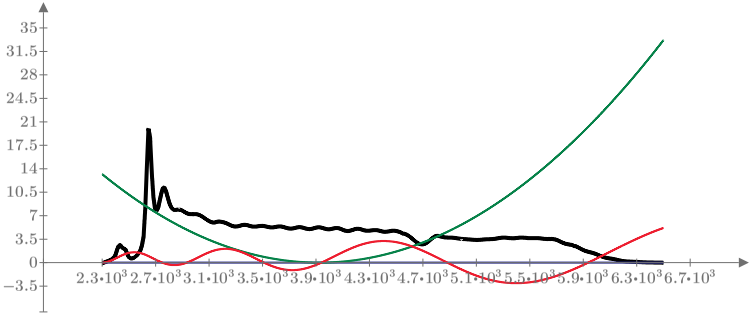

$\omega \ (THz)$

$10 \ Spec$

$\phi_{probeReal}$

$0.1 \ \phi_{probeLC}$

ϕ_{mirror}

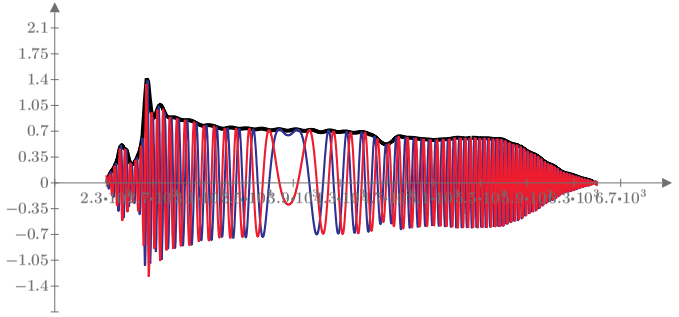

$\omega_n \ (THz)$

$\sqrt{Spec_n}$

$\text{Re}(E_n)$

$\text{Im}(E_n)$

Fourier Trafo mittels dft:

$E_t := \text{center}(\text{dft}(E))$ $\quad \text{rows}(E_t) = 1.68 \cdot 10^4$

$\Delta t := \dfrac{2\,\pi}{\max(\omega) - min(\omega)} = 1.495997\ fs$

$t := \left(\dfrac{\omega - min(\omega)}{\Delta\omega} - \dfrac{\text{rows}(E) - 1}{2}\right) \cdot \Delta t = \begin{bmatrix} -12566.371 \\ \vdots \end{bmatrix} fs$

$E_{LCt} := \text{center}\left(\text{dft}\left(E_{LC}\right)\right)$

$$I_t := \frac{\overrightarrow{|E_t|^2}}{\max\left(\overrightarrow{|E_t|^2}\right)} \qquad I_{LCt} := \frac{\overrightarrow{|E_{LCt}|^2}}{\max\left(\overrightarrow{|E_{LCt}|^2}\right)} \qquad Pump := 1 \cdot e^{-\left(\frac{t}{\frac{25\ fs}{2\cdot\sqrt{\ln(2)}}}\right)^2}$$

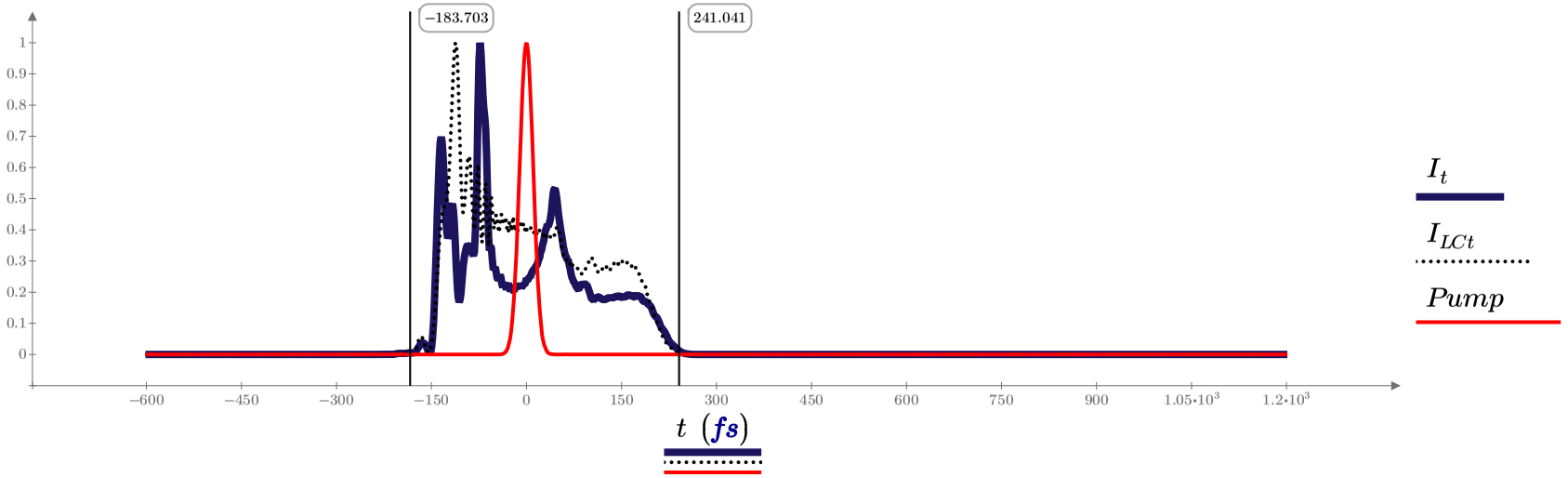

Timedomain Pulse Duration for Distorted Pulse:

$$imin := \text{for } i \in 1,2..\text{rows}(t) \quad \left\| \begin{array}{l} \text{if } I_{t_i} > 0.5 \cdot \max(I_t) \\ \quad \text{return } i \end{array} \right. = 8308$$

$$imax := \text{for } i \in imin+1, imin+2..\text{rows}(t) \quad \left\| \begin{array}{l} \text{if } I_{t_i} < 0.5 \cdot \max(I_t) \\ \quad \text{return } i \end{array} \right. = 8315$$

$FWHM_t := t_{imax} - t_{imin} = 10.472\ fs$

XPM : $I_{pump0} := 300\ \frac{GW}{cm^2}$ $\tau_{FWHM} := 25\ fs$ $n2 := 2.06 \cdot 10^{-7}\ \frac{cm^2}{GW}$ $L := 200\ \mu m$ Delay Time Achse: $\Delta t_{min} := -300\ fs$ $\Delta t_{max} := 200\ fs$ $\Delta\Delta t := 3\ fs$

$$I_{pump}(t, \Delta t) := I_{pump0} \cdot e^{-\left(\frac{t + \Delta t}{\frac{\tau_{FWHM}}{2 \cdot \sqrt{\ln(2)}}}\right)^2}$$

$$\phi_{XPMmax} := \frac{2 \cdot \omega_{0probe} \cdot L}{c} \cdot n2 \cdot I_{pump0} = 0.324$$

$$\Delta t := \Delta t_{min}, \Delta t_{min} + \Delta\Delta t .. \Delta t_{max} = \begin{bmatrix} \vdots \\ 198 \end{bmatrix} fs$$

$$E_{XPM} := \left\| \begin{array}{l} j \leftarrow 1 \\ \text{for } \Delta t \in \Delta t_{min}, \Delta t_{min} + \Delta\Delta t .. \Delta t_{max} \\ \quad \left\| \begin{array}{l} \text{for } n \in 1,2 .. \text{rows}(t) \\ \quad \left\| \begin{array}{l} \phi_{XPM_n} \leftarrow \frac{2 \cdot \omega_{0probe} \cdot L}{c} \cdot n2 \cdot I_{pump}(t_n, \Delta t) \\ E_{XPMref_{n,j}} \leftarrow E_{t_n} \cdot e^{1i \cdot (\phi_{XPM_n})} \end{array} \right. \\ j \leftarrow j + 1 \end{array} \right. \\ E_{XPMref} \end{array} \right.$$

$$T0 := \text{idft}(E_t)$$

$$S_{XPM} := \left\| \begin{array}{l} k \leftarrow 1 \\ \text{for } k \in 1,2 .. \text{cols}(E_{XPM}) \\ \quad \left\| \begin{array}{l} T_{XPMref}^{\langle k \rangle} \leftarrow \left(\text{idft}\left(E_{XPM}^{\langle k \rangle}\right)\right) \\ Sig^{\langle k \rangle} \leftarrow -\log\left(\frac{\left|\left(T_{XPMref}^{\langle k \rangle}\right)\right|^2 + 0.001}{|(T0)|^2 + 0.001}\right) \end{array} \right. \\ \begin{bmatrix} T_{XPMref} \\ Sig \end{bmatrix} \end{array} \right.$$

$$S_{XPMref} := S_{XPM_1} \qquad Signal := S_{XPM_2}$$

Double check frequency axis (should reproduce initially defined ω):

$$\Delta\omega := \frac{2\ \pi}{\max(t) - min(t)} = 0.25\ THz \qquad k := 1,2 .. \text{rows}(t) = \begin{bmatrix} 1 \\ 2 \\ \vdots \end{bmatrix} \qquad \omega := (k-1) \cdot \Delta\omega + \omega_{min} = \begin{bmatrix} 2300 \\ \vdots \end{bmatrix} THz \qquad \lambda := 2\ \pi \cdot \frac{c}{\omega} = \begin{bmatrix} 818.979 \\ \vdots \end{bmatrix} nm$$

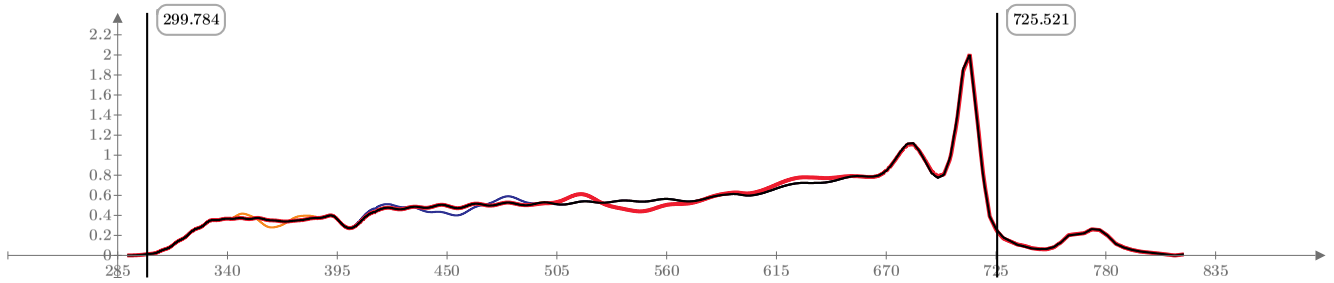

$\left|\left(S_{XPMref}^{\langle 60 \rangle}\right)\right|^2$

$\left|\left(S_{XPMref}^{\langle 90 \rangle}\right)\right|^2$

$\left|\left(S_{XPMref}^{\langle 120 \rangle}\right)\right|^2$

$|(T0)|^2$

Thin Out Spectral Axis (to speed up fitting, reduce very dense ω axis to about 524 points, equal to the no. of pixels on the CCD camera)**:**

$\mathrm{rows}(Signal) = 1.68 \cdot 10^4$ $\mathrm{rows}(\omega) = 1.68 \cdot 10^4$ retain every fac datapoint: $fac := 30$ $\omega_{full} := \omega$

$\frac{\mathrm{rows}(Signal)}{fac} = 560.033$

$k := 1,2..\frac{\mathrm{rows}(Signal)}{fac} = \begin{bmatrix} \vdots \\ 559 \\ 560 \end{bmatrix}$

$S_{thin} := \left\| \begin{array}{l} \text{for } k \in 1,2..\frac{\mathrm{rows}(Signal)}{fac} \\ \quad \left\| \begin{array}{l} S_{thin}^{\widehat{k}} \leftarrow \left(Signal^{\widehat{1+fac\cdot(k-1)}}\right) \\ \omega_{thin_k} \leftarrow \omega_{1+fac\cdot(k-1)} \end{array} \right. \\ \begin{bmatrix} S_{thin} \\ \omega_{thin} \end{bmatrix} \end{array} \right.$

$Signal := S_{thin_1}$ $\omega := S_{thin_2}$ $\lambda := 2\,\pi \cdot \frac{c}{\omega} = \begin{bmatrix} \vdots \\ 290.127 \end{bmatrix}$ *nm* $\mathrm{rows}(Signal) = 560$ $\mathrm{rows}(\omega) = 560$

Lineouts in spectral domain: $Spectrum(i) := Signal^{\langle i \rangle}$

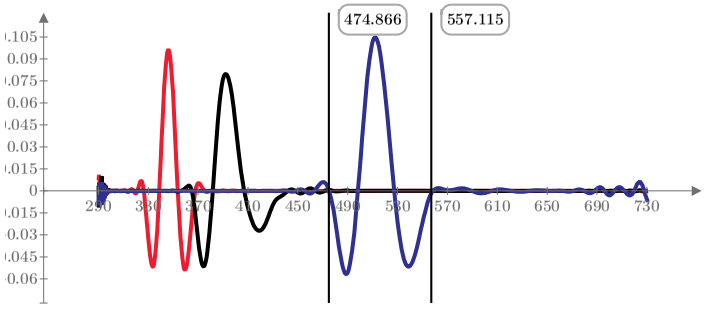

$\lambda\ (nm)$

$Spectrum(50)$

$Spectrum(75)$

$Spectrum(110)$

Lineouts in delay time domain: $tTrace(i) := \left(Signal^{\widehat{i}}\right)^{\mathrm{T}}$

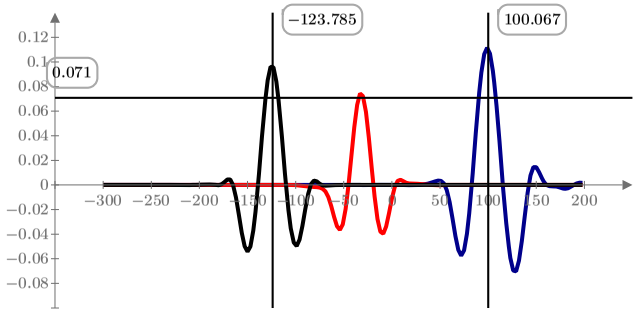

$\Delta t\ (fs)$

$tTrace(80)$

$tTrace(250)$

$tTrace(390)$

$M := \mathrm{reverse}(Signal)^{\mathrm{T}}$ $\mathrm{rows}(M) = 167$ $\mathrm{cols}(M) = 560$

DO NOT ATTEMPT TO VIEW M IN MATHCAD! It will take forever to caculate or crash the program. **Use Labview instead!**

Fit Routine:

In the following M will be fitted using different fitting models to retrieve the input GD. The fit routine is identical to the one used for the experimental data.

Define Fitfunctions:

$$Fcos\left(A_0, A_1, t_0, FWHM, B, \phi, t\right) := \left(A_0 \cdot \exp\left(\frac{-4\cdot\ln(2)\cdot\left(t-t_0\right)^2}{FWHM^2}\right) + -\frac{4\cdot A_1 \cdot e^{-\frac{4\cdot\ln(2)\cdot\left(t-t_0\right)^2}{FWHM^2}} \cdot \ln(2)\cdot\left(2\cdot t - 2\cdot t_0\right)}{FWHM^2}\right)\cdot\cos\left(B\cdot\left(t-t_0\right)^2 + \phi\right)$$

$$FGauss\left(A_0, A_1, t_0, FWHM, A_2, t\right) := A_0 \cdot \exp\left(\frac{-4\cdot\ln(2)\cdot\left(t-t_0\right)^2}{FWHM^2}\right) + -\frac{4\cdot A_1 \cdot e^{-\frac{4\cdot\ln(2)\cdot\left(t-t_0\right)^2}{FWHM^2}} \cdot \ln(2)\cdot\left(2\cdot t - 2\cdot t_0\right)}{FWHM^2} + \frac{16\cdot A_2 \cdot e^{-\frac{4\cdot\ln(2)\cdot\left(t-t_0\right)^2}{FWHM^2}} \cdot \ln(2)^2\cdot\left(2\cdot t - 2\cdot t_0\right)^2}{FWHM^4} - \frac{8\cdot A_2 \cdot e^{-\frac{4\cdot\ln(2)\cdot\left(t-t_0\right)^2}{FWHM^2}} \cdot \ln(2)}{FWHM^2}$$

$$Gauss\left(A_0, t_0, FWHM, t\right) := A_0 \cdot \exp\left(\frac{-4\cdot\ln(2)\cdot\left(t-t_0\right)^2}{FWHM^2}\right)$$

Define Spectral Interval to be Fitted:

$i\lambda\_min := 40$ $\quad$ $i\lambda\_max := 480$

$$\lambda\_min := 2\,\pi\cdot\frac{c}{\omega_{i\lambda\_max}} = 319.669\ nm \qquad \lambda\_max := 2\,\pi\cdot\frac{c}{\omega_{i\lambda\_min}} = 726.577\ nm$$

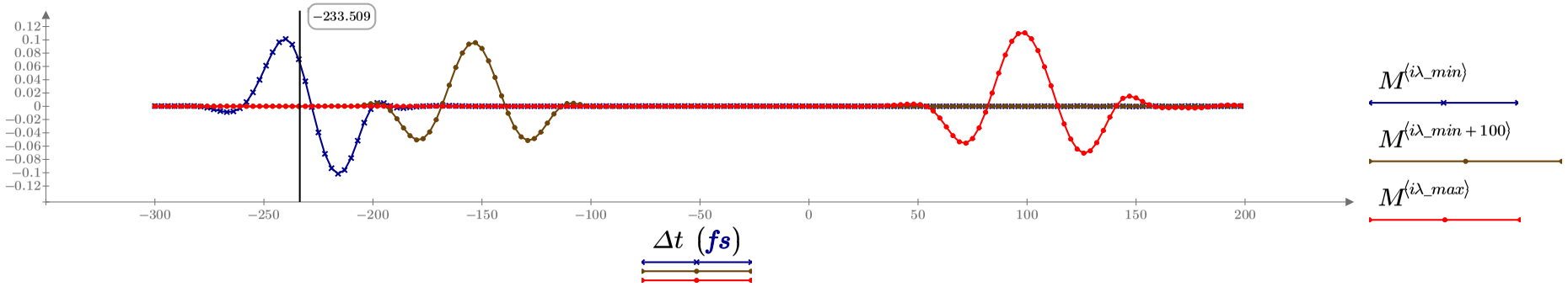

Initial guess values for fit: Give an initial guess for the parameters of the first fit iteration (fit of the first trace). Use the graph below as a guide.

$t_0 := \Delta t_{\text{match}\left(\max\left(M^{\langle i\lambda\_min\rangle}\right), M^{\langle i\lambda\_min\rangle}\right)_1} = -240\ fs$ $A_{0S} := 0.1$ $A_{1S} := -0.001\ fs$ $A_{2S} := 0.1\ fs^2$ $FWHM_S := 80\ fs$ $B_S := 15 \cdot 10^{-4} \cdot \frac{1}{fs^2}$ $\phi_S := 0.81\ rad$

Fit window: The signal occupies only a small portion of the trace. To reduce fitting time and increase accuracy the trace is truncated at +/- $window$ datapoints before/after the signal maximum for fitting. Choose window such that the signal occupies about 1/3 of the truncated trace.

$window := 20$

Trace by trace fitting: Fit by including the solver in a for loop. The lines of the matrix Fit contain the fit parameters for each trace. Looking at a given column yields the wavelength dependence of the given parameter. Analogous to the *"Trace by Trace Fitting of the Coherent Artifact"* Program shown before.

$Par\_Fcos := Fit\left(M, \Delta t, t_0\right)$ $A_{0C} := Par\_Fcos^{\langle 1\rangle}$ $A_{1C} := Par\_Fcos^{\langle 2\rangle}$ $t_{0C} := Par\_Fcos^{\langle 3\rangle}$ $FWHM_C := Par\_Fcos^{\langle 4\rangle}$ $B_C := Par\_Fcos^{\langle 5\rangle}$ $\phi_C := Par\_Fcos^{\langle 6\rangle}$

$Par\_FGauss := FitG\left(M, \Delta t, t_0\right)$ $A_{0G} := Par\_FGauss^{\langle 1\rangle}$ $A_{1G} := Par\_FGauss^{\langle 2\rangle}$ $t_{0G} := Par\_FGauss^{\langle 3\rangle}$ $FWHM_G := Par\_FGauss^{\langle 4\rangle}$ $A_{2G} := Par\_FGauss^{\langle 5\rangle}$

$Par\_FG2 := FitG2\left(M, \Delta t, t_0\right)$ $A_{0G2} := Par\_FG2^{\langle 1\rangle}$ $t_{0G2} := Par\_FG2^{\langle 2\rangle}$ $FWHM_{G2} := Par\_FG2^{\langle 3\rangle}$

View Data & Fit:
Select index: $ii := 100$ corresponding WL: $2\,\pi \cdot \frac{c}{\text{reverse}\left(\omega\right)_{ii + i\lambda\_min - 1}} = 345.149\ nm$ Def. Residual: $Res\left(Data, Fit\right) := \left(Data - Fit\right) - 1.5 \cdot \max\left(Data\right)$

Graphs below show only the fitted window with the corresponding datapoints. Time axis moves along as index ii is increased.

$$Par\_Fcos = \begin{bmatrix} \vdots & & & & \\ 0.214 & -1.12 \cdot 10^{-16}\ s & \left(7.652 \cdot 10^{-15}\right)\ s & \left(4.19 \cdot 10^{-14}\right)\ s & \left(2.053 \cdot 10^{27}\right) \frac{1}{s^2} \quad 1.08 \\ 0.212 & -1.036 \cdot 10^{-16}\ s & \left(8.73 \cdot 10^{-15}\right)\ s & \left(4.207 \cdot 10^{-14}\right)\ s & \left(2.059 \cdot 10^{27}\right) \frac{1}{s^2} \quad 1.076 \\ & & & & \ddots \end{bmatrix}$$

$$it_0S := Par\_Fcos^{\langle 7\rangle} = \begin{bmatrix} 21 \\ 21 \\ 21 \\ 22 \\ \vdots \end{bmatrix}$$

indt0 should rise monotonically if moving window has worked

$$\Delta t_{windowR} := \text{submatrix}\left(\Delta t, it_0S_{ii} - window, it_0S_{ii} + window, 1, 1\right)$$

$$Sam(ii) := \text{submatrix}\left(M^{\langle ii + i\lambda\_min - 1\rangle}, \left(it_0S_{ii} - window\right), it_0S_{ii} + window, 1, 1\right)$$

$$FitFcos(ii) := \text{submatrix}\left(\overrightarrow{Fcos\left(A_{0C_{ii}}, A_{1C_{ii}}, t_{0C_{ii}}, FWHM_{C_{ii}}, B_{C_{ii}}, \phi_{C_{ii}}, \Delta t\right)}, it_0S_{ii} - window, it_0S_{ii} + window, 1, 1\right)$$

$$FitFGauss(ii) := \text{submatrix}\left(\overrightarrow{FGauss\left(A_{0G_{ii}}, A_{1G_{ii}}, t_{0G_{ii}}, FWHM_{G_{ii}}, A_{2G_{ii}}, \Delta t\right)}, it_0S_{ii} - window, it_0S_{ii} + window, 1, 1\right)$$

$$FitGauss(ii) := \text{submatrix}\left(\overrightarrow{Gauss\left(A_{0G2_{ii}}, t_{0G2_{ii}}, FWHM_{G2_{ii}}, \Delta t\right)}, it_0S_{ii} - window, it_0S_{ii} + window, 1, 1\right)$$

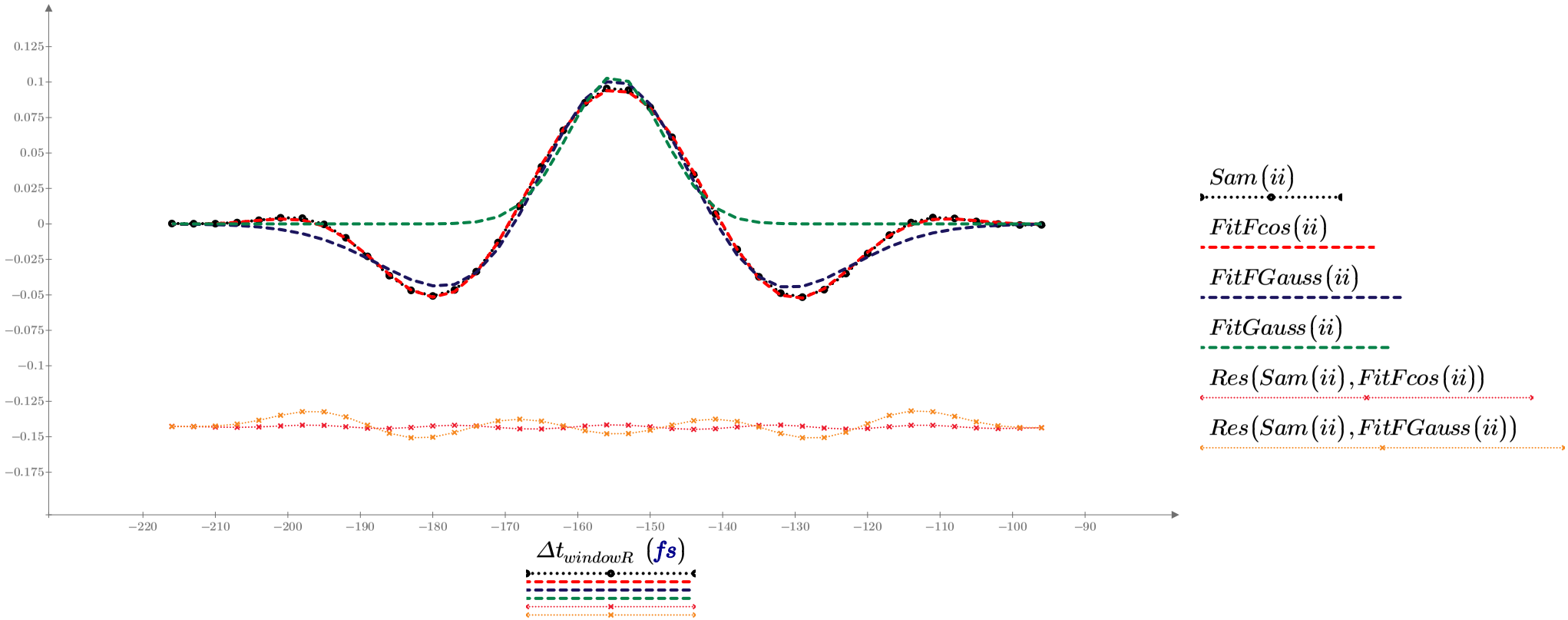

Spectral evolution of Fit Parameters and GD:

$\omega_{GD} := \text{submatrix}\left(\text{reverse}\left(\omega\right), i\lambda\_min, i\lambda\_max, 1, 1\right)$

$MirrorGD := \text{linterp}\left(\omega_{full}, GD, \omega_{GD}\right)$ Linear chirp used yes/no: $LC := 1$

$\lambda_{GD} := 2 \cdot \pi \cdot c \cdot \omega_{GD}^{-1}$

$RealGD := -\left(MirrorGD + LC \cdot \text{linterp}\left(\omega_{full}, \beta_{\omega} \cdot \left(\omega_{full} - \omega_{0probe}\right), \omega_{GD}\right)\right)$

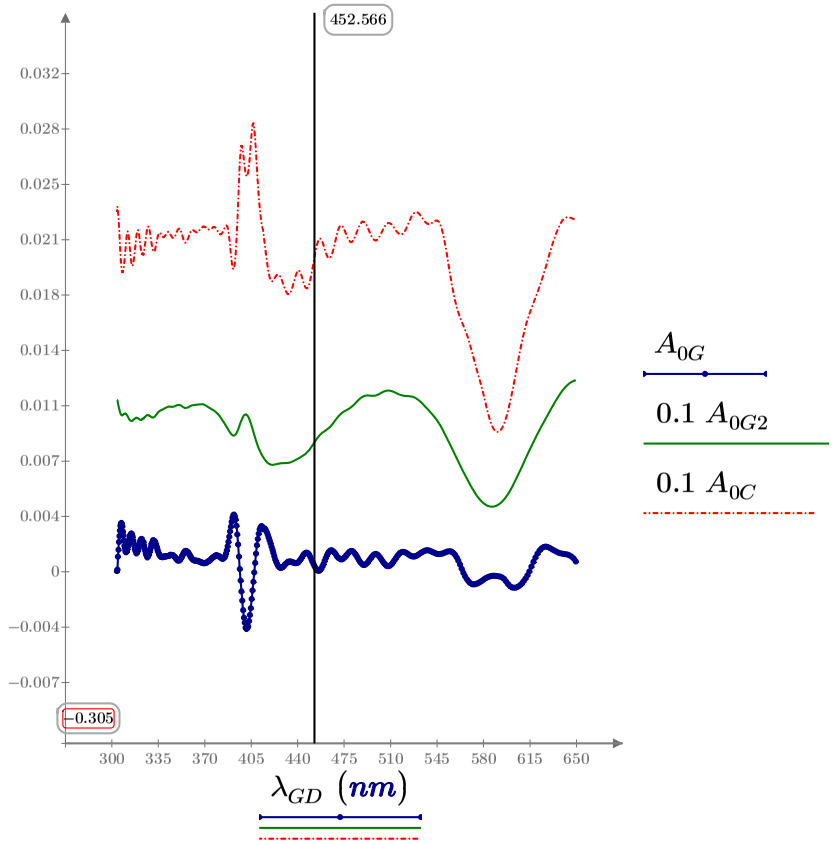

A_{0G}

$0.1\ A_{0G2}$

$0.1\ A_{0C}$

$A_{1C\_sc} := \dfrac{2 \cdot A_{1C} \cdot \sqrt{2 \cdot \ln(2)}}{\sqrt{e} \cdot FWHM_C}$ $A_{1G\_sc} := \dfrac{2 \cdot A_{1G} \cdot \sqrt{2 \cdot \ln(2)}}{\sqrt{e} \cdot FWHM_G}$ $\max\left(A_{1C\_sc}\right) = 0.032$

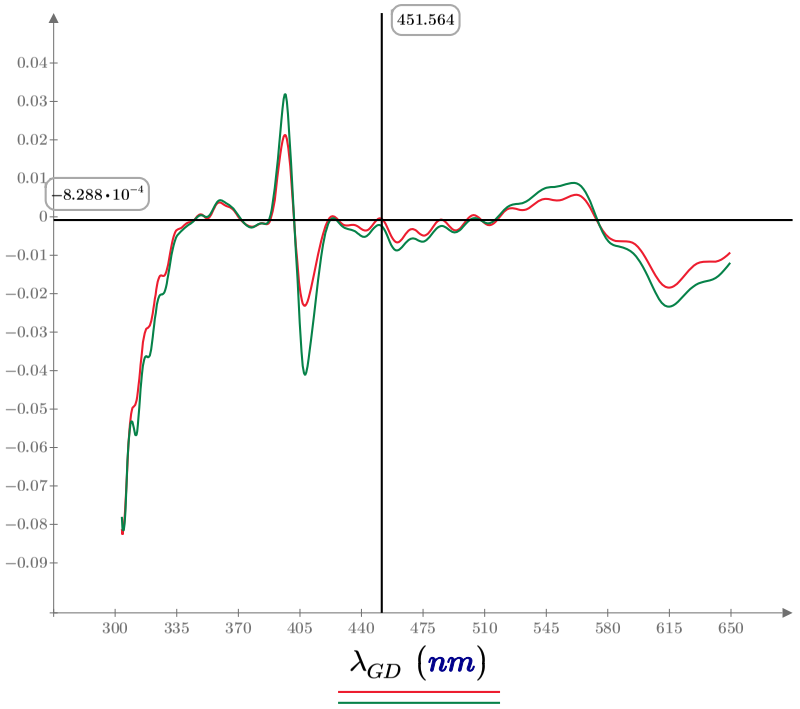

$-1 \cdot A_{1G\_sc}$

A_{1C_sc}

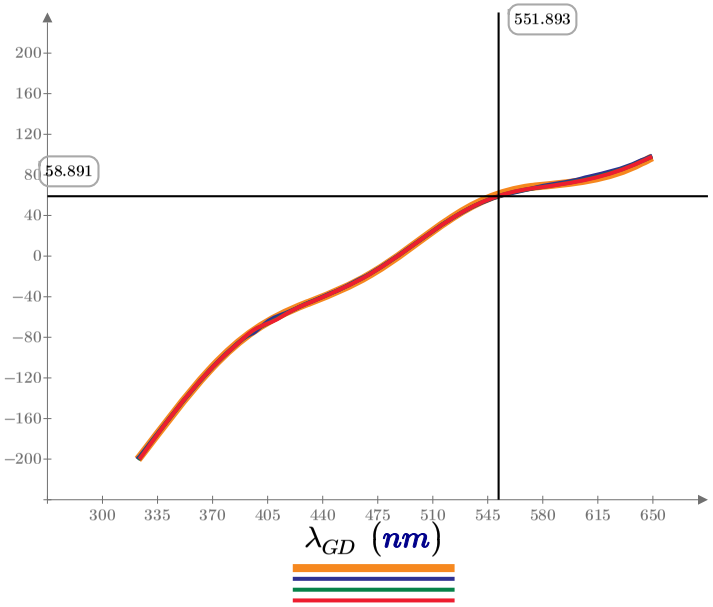

$RealGD$ (fs)

t_{0G} (fs)

t_{0G2} (fs)

t_{0C} (fs)

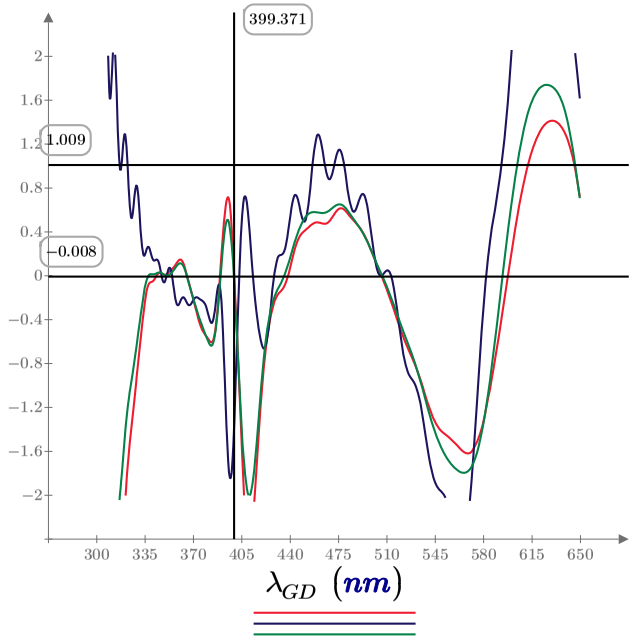

$(t_{0C} - RealGD)$ (fs)

$(t_{0G} - RealGD)$ (fs)

$(t_{0G2} - RealGD)$ (fs)

Rsulting GD:

$$fittedGD(t_{0Fit}) := -(t_{0Fit} + LC \cdot \text{linterp}(\omega_{full}, \beta_\omega \cdot (\omega_{full} - \omega_{0probe}), \omega_{GD}))$$

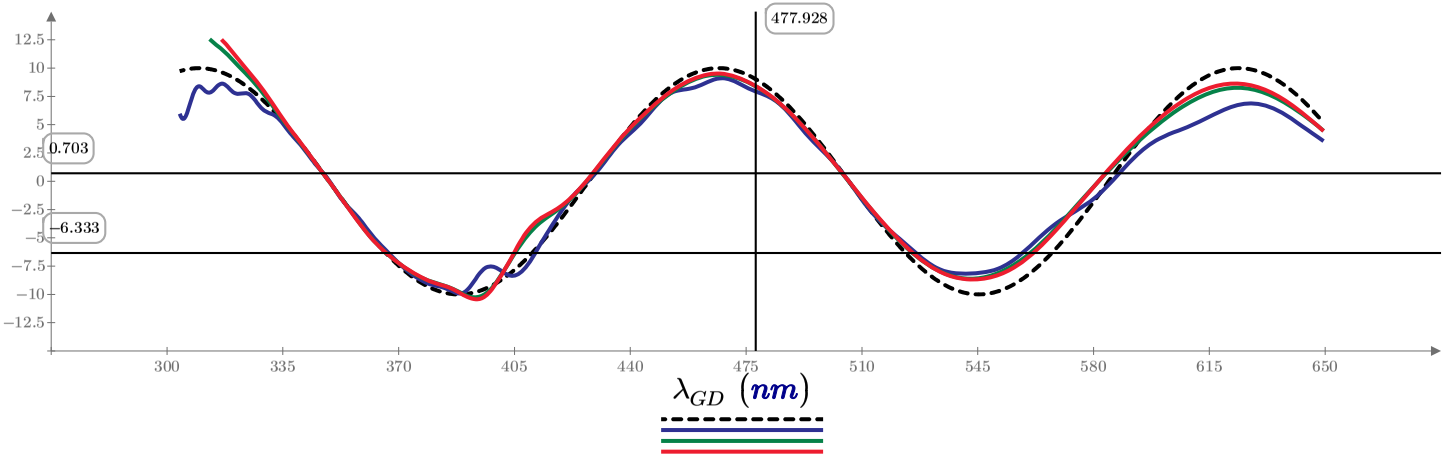

$MirrorGD$ (fs)

$fittedGD(t_{0G})$ (fs)

$fittedGD(t_{0G2})$ (fs)

$fittedGD(t_{0C})$ (fs)

Outputs: The data are written into external text files. Note that units need to be stripped for writing.

Build Fit and Residual Matrices plus a Data matrix truncated to the fitted range

$$FitRes := \left\| \begin{array}{l} \text{for } ii \in 1,2..i\lambda\_max - i\lambda\_min + 1 \\ \quad \left\| \begin{array}{l} Fit^{\langle ii \rangle} \leftarrow Fcos\left(A_{0C_{ii}}, A_{1C_{ii}}, t_{0C_{ii}}, FWHM_{C_{ii}}, B_{C_{ii}}, \phi_{C_{ii}}, \Delta t\right) \\ Res^{\langle ii \rangle} \leftarrow Fit^{\langle ii \rangle} - M^{\langle ii + i\lambda\_min - 1 \rangle} \end{array} \right. \\ \begin{bmatrix} Fit \\ Res \end{bmatrix} \end{array} \right.$$

$$M_{trunc} := \text{submatrix}\left(M, 1, \text{rows}(M), i\lambda\_min, i\lambda\_max\right)$$

$$BB1 := FitRes_1 \qquad BB2 := FitRes_2 \qquad FitRef := BB1 \qquad ResRef := BB2$$

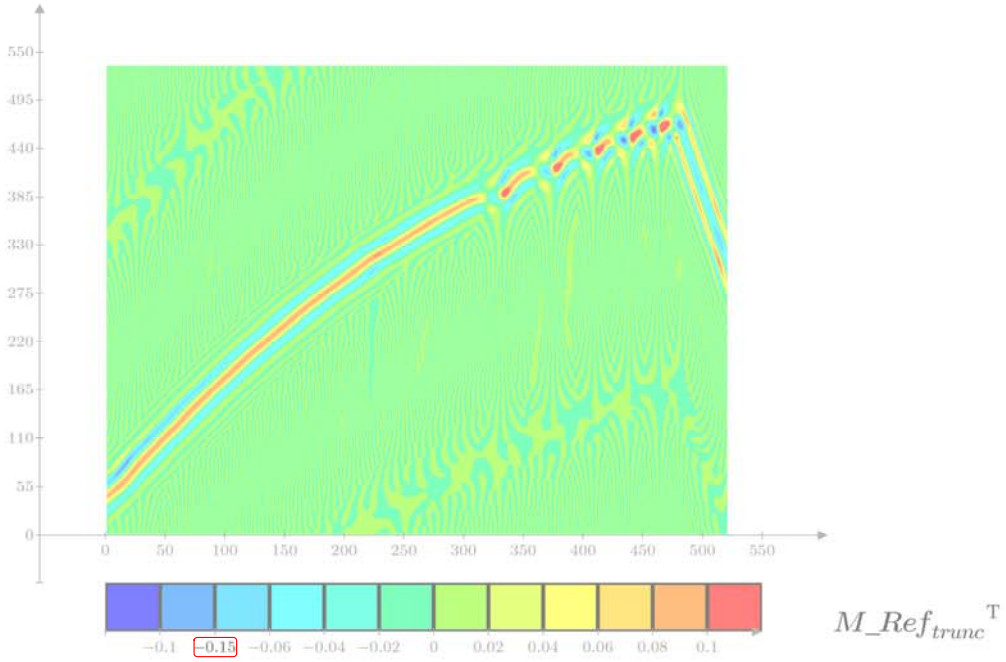

$M\_Ref_{trunc}{}^{T}$

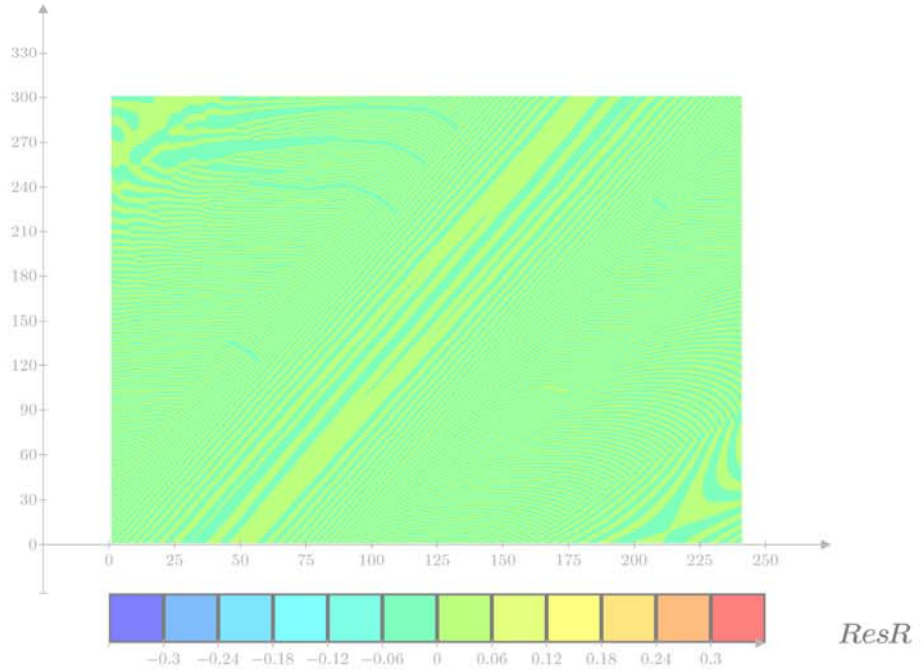

$ResR$

Output Simulated Data:

$name := \text{concat}(\text{“ArtSim\_SimData.txt”})$ $data := \text{stack}\left(\text{augment}\left(0, \frac{\text{reverse}(\lambda)^{\mathrm{T}}}{nm}\right), \text{augment}\left(\frac{\Delta t}{fs}, M\right)\right)$ $OUT\_SIM\_REF := \text{WRITETEXT}(name, data)$

Output Simulation Parameters:

$name := \text{concat}(\text{“ArtSim\_SimParameters.txt”})$

$params1 := \text{stack}(\text{“PROBE:”}, \text{“Number of reflections”}, \text{“lambda\_probe”}, \text{“FWHM\_probe”}, \text{“chirp\_beta”}, \text{“XPM \& PUMP:”}, \text{“I\_pump”}, \text{“FWHM\_pump”}, \text{“n2”}, \text{“}$

$params2 := \text{stack}\left(0, N_{refl}, \frac{\lambda_{0probe}}{nm}, \frac{FWHM_{probe}}{nm}, \beta \cdot fs^2, 0, I_{pump0} \cdot \frac{cm^2}{GW}, \frac{\tau_{FWHM}}{fs}, n2 \cdot \frac{GW}{cm^2}, \frac{L}{\mu m}, \frac{\Delta t_{min}}{fs}, \frac{\Delta\Delta t}{fs}\right)$

$data := \text{augment}(params1, params2)$ $OUT\_SIMPARAMS := \text{WRITETEXT}(name, data)$

Output Fits:

$name := \text{concat}(\text{“ArtSim\_Fit.txt”})$ $data := \text{stack}\left(\text{augment}\left(0, \frac{\lambda_{GD}{}^{\mathrm{T}}}{nm}\right), \text{augment}\left(\frac{\Delta t}{fs}, FitRef\right)\right)$ $OUT\_SIM\_REF := \text{WRITETEXT}(name, data)$

Output Fit Parameters:

$name := \text{“ArtSim\_FitParameters.txt”}$

$params1 := \text{augment}(\text{“lambda\_ (nm)”}, \text{“t0c (fs)”}, \text{“A0c”}, \text{“A1c\_sc”}, \text{“FWHMc (fs)”}, \text{“Bc (1/fs\^2)”}, \text{“Phi\_c (rad)”}, \text{“Fitted GD (fs) Fcos”}, \text{“lambda\_ (nm)”}, \text{“t0g (f}$

$params2 := \text{augment}\left(\frac{\lambda_{GD}}{nm}, \frac{t_{0C}}{fs}, A_{0C}, A_{1C\_}sc, \frac{FWHM_C}{fs}, B_C \cdot fs^2, \phi_C, \frac{fittedGD(t_{0C})}{fs}, \frac{\lambda_{GD}}{nm}, \frac{t_{0G}}{fs}, A_{0G}, A_{1G\_}sc, \frac{FWHM_G}{fs}, \frac{fittedGD(t_{0G})}{fs}, \frac{MirrorGD}{fs}\right)$

$data := \text{stack}(params1, params2)$ $OUT\_FITPARAMS := \text{WRITETEXT}(name, data)$

B4 Subtract CA from Pyrene TA Data using Fcos

Bastian Baudisch (13.03.16)

$fs := 10^{-15}\ s$ **ORIGIN** $:= 1$

Read Reference and Sample Data:

Read Reference Measurement: $infile\_Ref := ".\80\_Pyrene\_1mM\_CHex\_S3ex273nm\_100nJ\_mag\_av13\_WL\_OD.dat"$

$DATA\_Ref := \mathrm{READFILE}(infile\_Ref, "\mathrm{delimited}")$

Split DATA into matrix of traces (remove axes): $M\_Ref := \mathrm{submatrix}(DATA\_Ref, 2, \mathrm{rows}(DATA\_Ref), 2, \mathrm{cols}(DATA\_Ref))$ $\mathrm{rows}(M\_Ref) = 360$ $\mathrm{cols}(M\_Ref) = 524$

Set limits for fit (by index) and obtain time and wavelength axes:

Set wavelength range: $i\lambda\_min := 2$ $i\lambda\_max := 120$

Set time range: $it\_min := 2$ $it\_max := 300$

Specified range is used for reference and sample measurements:

$\lambda_R := \mathrm{submatrix}(DATA\_Ref, 1, 1, i\lambda\_min, i\lambda\_max)^{\mathrm{T}}\ nm$ $\mathrm{rows}(\lambda_R) = 119$

$t_R := \mathrm{submatrix}(DATA\_Ref, it\_min, it\_max, 1, 1)\ ps$ $\mathrm{rows}(t_R) = 299$

Corresponding wavelength range: $\lambda_{min} := \lambda_{R_1} = 287.774\ nm$ $\lambda_{max} := \lambda_{R_{i\lambda\_max - i\lambda\_min}} = 317.028\ nm$

Corresponding time range: $t_{min} := t_{R_1} = -2.001\ ps$ $t_{max} := \max(t_R) = 1.95\ ps$

View time traces to be fitted:

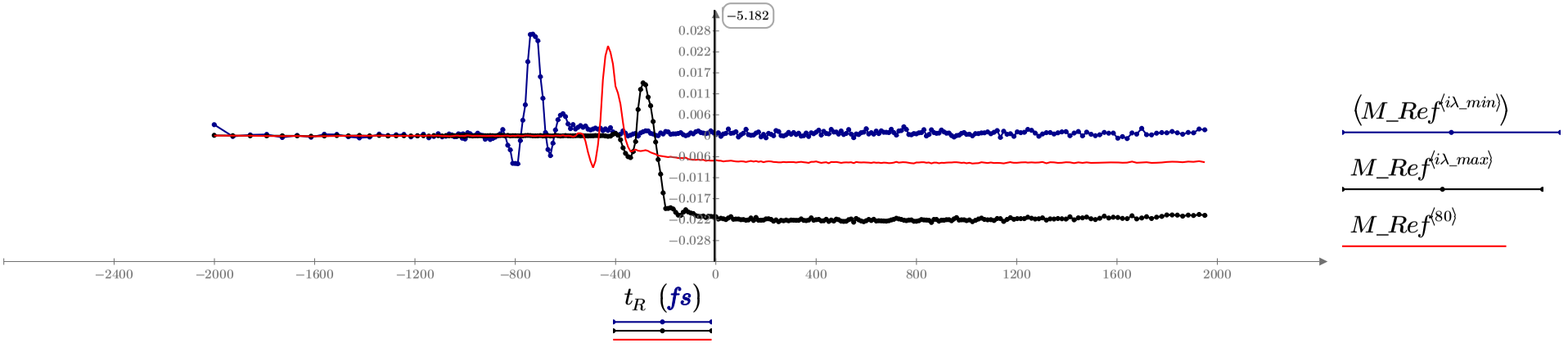

Fitfunctions:

$$Fcos\left(A_0, A_1, t_0, FWHM, B, \phi, t\right) := \left(A_0 \cdot \exp\left(-\frac{\left(t-t_0\right)^2}{FWHM^2}\right) + \frac{A_1 \cdot e^{-\frac{\left(t-t_0\right)^2}{2\cdot FWHM^2}} \cdot \left(2\cdot t - 2\cdot t_0\right)}{FWHM^2}\right) \cdot \cos\left(B\cdot\left(t-t_0\right)^2 + \phi\right)$$

$$Fmol\left(A_{1m}, A_{2m}, \tau_{1m}, \tau_{2m}, \tau_{CC}, t_0, t\right) := A_{1m} \cdot \exp\left(\left(\frac{\tau_{CC}}{4\cdot\sqrt{\ln(2)}\ \tau_{1m}}\right)^2 - \frac{\left(t-t_0\right)}{\tau_{1m}}\right) \cdot \left(\frac{1}{2}\left(1 - \operatorname{erf}\left(\frac{\tau_{CC}}{4\cdot\sqrt{\ln(2)}\ \tau_{1m}} - \frac{2\cdot\sqrt{\ln(2)}\cdot\left(t-t_0\right)}{\tau_{CC}}\right)\right)\right) + A_{2m} \cdot \exp\left(\left(\frac{\tau_{CC}}{4\cdot\sqrt{\ln(2)}\ \tau_{2m}}\right)^2 - \frac{\left(t-t_0\right)}{\tau_{2m}}\right) \cdot \left(\frac{1}{2}\left(1 - \operatorname{erf}\left(\frac{\tau_{CC}}{4\cdot\sqrt{\ln(2)}\ \tau_{2m}} - \frac{2\cdot\sqrt{\ln(2)}}{\tau_{CC}}\right)\right)\right)$$

Initial guess values for fit: Give an initial guess for the parameters of the first fit iteration (fit of the first trace). Use the graph below as a guide.

$t_{0Ref} := t_{R_{\text{match}\left(\max\left(M\_Ref^{\langle i\lambda\_min\rangle}\right),\ M\_Ref^{\langle i\lambda\_min\rangle}\right)_1}} = -739.859\ fs$

$A_{0S} := 0.005$ $A_{1S} := -0.0001\ fs$ $FWHM_S := 50\ fs$ $B_S := 10\cdot 10^{-4}\cdot\frac{1}{fs^2}$ $\phi_S := 0.8$

$A_{1mS} := -0.01$ $\tau_{1mS} := 130\ fs$ $A_{2mS} := 0.01$ $\tau_{2mS} := 10^5\ fs$ $\tau_{CCS} := 50\ fs$

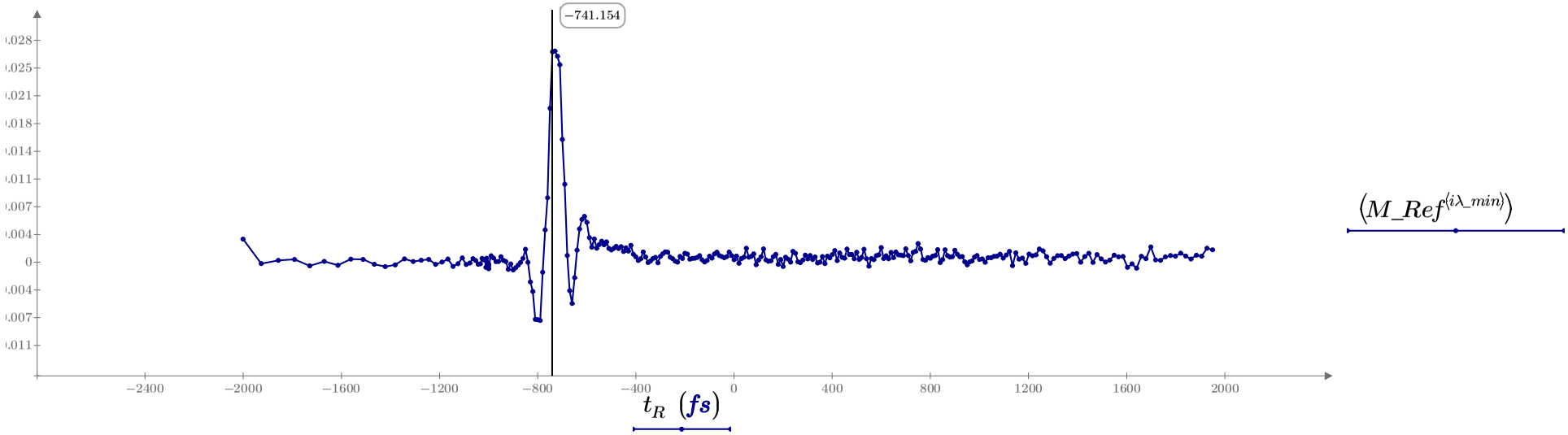

Fit window: The signal occupies only a small portion of the trace. To reduce fitting time and increase accuracy the trace is truncated at +/- $window$ datapoints before/after the signal maximum for fitting. Choose window such that the signal occupies about 1/3 of the truncated trace.

$window := 20$

Trace by trace fitting: Fit by including the solver in a for loop. Analogous to the *"Trace by Trace Fitting of the Coherent Artifact"* Program shown before.

View Data & Fit - Select index: $ii := 114$ Corresponding wavelength: $\lambda_{R_{ii}} = 315.839\ nm$ Residual: $Res(Data, Fit) := (Data - Fit) - 1.5 \cdot \max(Data)$

The lines of the matrix Fit contain the fit parameters for each trace. Looking at a given column yields the wavelength dependence of the given parameter.

$Par\_R := Fit(M\_Ref, t_R, t_{0Ref})$ $A_{0R} := Par\_R^{\langle 1 \rangle}$ $A_{1R} := Par\_R^{\langle 2 \rangle}$ $t_{0R} := Par\_R^{\langle 3 \rangle}$ $FWHM_R := Par\_R^{\langle 4 \rangle}$ $B_R := Par\_R^{\langle 5 \rangle}$ $\phi_R := Par\_R^{\langle 6 \rangle}$

$A_{1m} := Par\_R^{\langle 7 \rangle}$ $A_{2m} := Par\_R^{\langle 8 \rangle}$ $\tau_{1m} := Par\_R^{\langle 9 \rangle}$ $\tau_{2m} := Par\_R^{\langle 10 \rangle}$ $\tau_{CC} := Par\_R^{\langle 4 \rangle}$

Graphs below show only the fitted window with the corresponding datapoints. Time axis moves along as index ii is increased!

Reference Data & Fit:

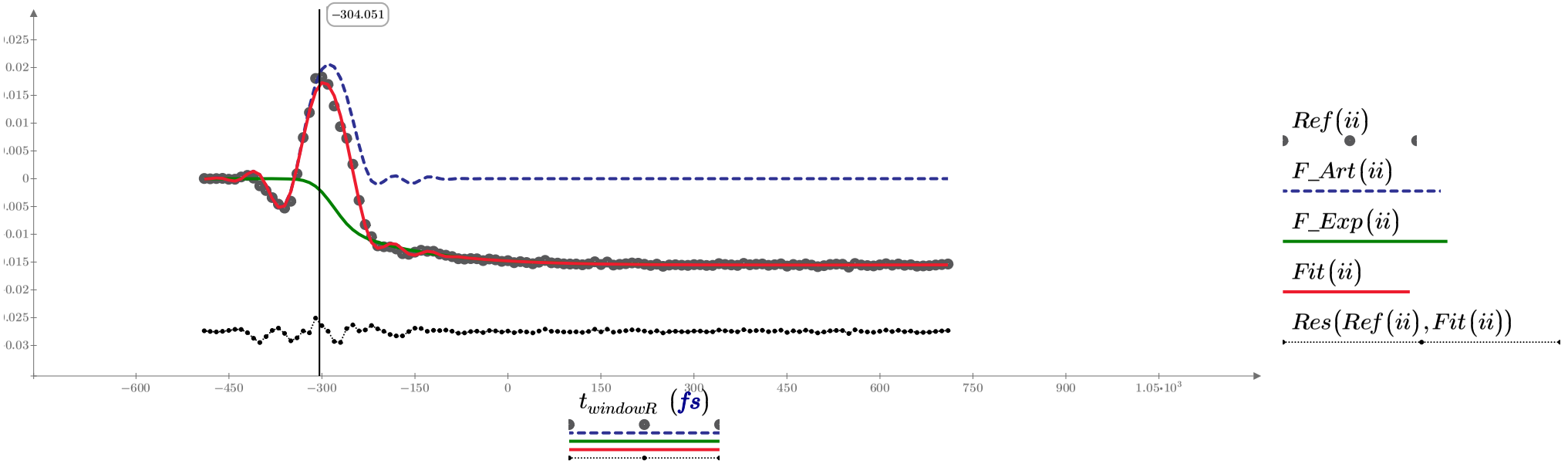

B5 Modeling Diffusion of Pyrene in Cyclohexane

Baudisch, Sep.2017

$ORIGIN := 1$

$ps := 10^{-12}\ s$

$mM := 1 \cdot 10^{-3}\ \frac{mol}{l}$

Stokes-Einstein-Beziehung

Die Stokes-Einstein-Beziehung beschreibt die Diffusion eines Moleküls in einer Newton'schen Flüssigkeit. Sie stellt einen Zusammenhang zwischen Größe und Dichte der (als kugelförmig betrachteten) Teilchen und ihrer Sinkgeschwindigkeit her. Durch die Stokes-Einstein-Beziehung lässt sich damit der **Diffusionskoeffizient** ausdrücken:

$$D = \frac{kT}{6\pi\eta r}$$

D= Diffusionskoeffizient
k= Boltzmannkonstante
T= absolute Temperatur
η= dynamische Viskosität des Lösemittels
r= Partikelradius

$k_B := 1.38064853 \cdot 10^{-23}\ \frac{J}{K}$

$T := 295\ K$

$\eta := 0.941 \cdot 10^{-3}\ \frac{kg}{m \cdot s}$

(CycHex at 22°C [http://ddbonline.ddbst.de/VogelCalculation/VogelCalculationCGI.exe])

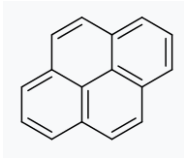

$r := 8.9\ Angstrom$

Sphere with same Volume:
(Lange Achse 9.2
kurze Achse 7.2 (Chemdraw)
breite carbon Monolayer

Scalene ellipsoid

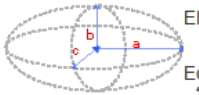

Ellipsoid is a sphere-like surface for which all cross-sections are ellipses.

Equation of standard ellipsoid body in xyz coordinate system is

$$\frac{x^2}{a^2} + \frac{y^2}{b^2} + \frac{z^2}{c^2} = 1.$$

where a - radius along x axis, b - radius along y axis, c - radius along z axis.

The volume of an ellipsoid is given by the following formula: $\frac{4}{3}\pi abc$

$$D := \frac{k_B \cdot T}{6 \cdot \pi \cdot \eta \cdot r} = 25.8\ \frac{Angstrom^2}{ns}$$

Wikipedia: For biological molecules the diffusion coefficients normally range from 10-11 to 10-10 m2/s.

$\Delta x := 5.5\ nm$ $\quad v_{diff} := \frac{2\ D}{\Delta x} = 0.094\ \frac{nm}{ns}$

$\Delta t := 10\ ns$ $\quad \Delta x_{diff} := v_{diff} \cdot \Delta t = 0.938\ nm$

Quelle: http://www.chemgapedia.de/vsengine/vlu/vsc/de/ch/8/bc/vlu/transport/pass_transport.vlu/Page/vsc/de/ch/8/bc/transport/diffusion1.vscml.html

Approximation of the time dependent rate via Einstein-Smoluchowski (Birks Eq.7.55, Mar87):

WARNING: Birks divides by 1000 in Bir69 due to differeing units (cm^3 vs. m^3)

WARNING 2: For k(t) the **SUM** of the radii of the two partners and the **SUM** of the Diffusionsconstants must be used --> For "Pyrene with Pyrene" 2x factor 2

$r_{sum} := 2\ r$ $D_{sum} := 2\ D$ $p := 0.82$

$$k(t) := 4\ \pi \cdot r_{sum} \cdot D_{sum} \cdot p \cdot \left(1 + \frac{p \cdot r_{sum}}{\sqrt{\pi \cdot D_{sum} \cdot t}}\right)$$

$t := 100\ ps, 200\ ps .. 300\ ns = \begin{bmatrix} 100 \\ \vdots \end{bmatrix} ps$

$$\tau(t, c_{Pyrene}) := \left(k(t) \cdot N_A \cdot c_{Pyrene}\right)^{-1}$$

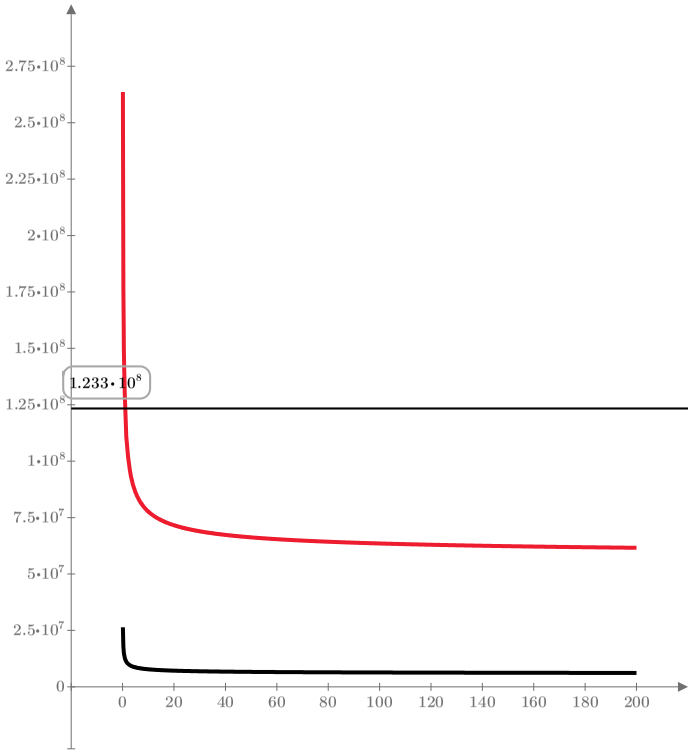

$t\ (ns)$

$$\frac{k(t) \cdot N_A \cdot 10\ mM\ \left(\frac{1}{s}\right)}{k(t) \cdot N_A \cdot 1\ mM\ \left(\frac{1}{s}\right)}$$

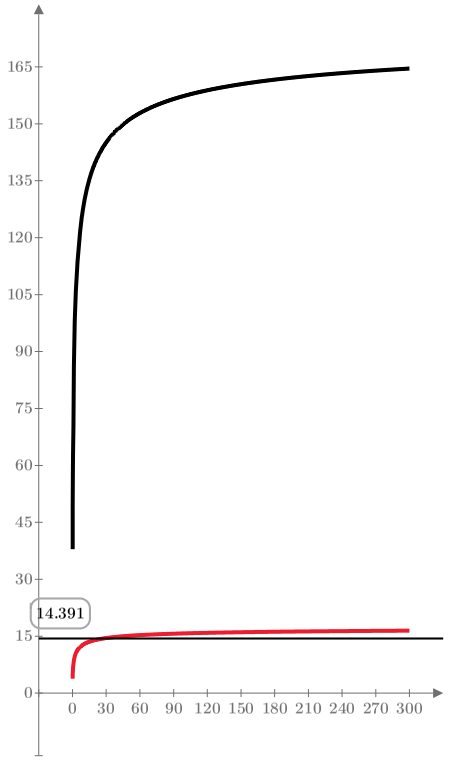

$t\ (ns)$

$$\frac{\tau(t, 10\ mM)\ (ns)}{\tau(t, 1\ mM)\ (ns)}$$

Limits:

$k_{lim} := 4\ \pi \cdot p \cdot r_{sum} \cdot D_{sum} = (9.465 \cdot 10^{-18})\ \frac{m^3}{s}$ $\quad k_{lim} \cdot N_A \cdot 10\ mM = (5.7 \cdot 10^{7})\ \frac{1}{s}$ $\quad N_A = (6.022 \cdot 10^{23})\ \frac{1}{mol}$

rearranged as in Birks 7.58: $R = 8.314\ \frac{kg \cdot m^2}{s^2 \cdot K \cdot mol}$ $\quad \frac{8 \cdot R \cdot 293\ K}{3 \cdot \eta} \cdot 10\ mM = (6.904 \cdot 10^{7})\ \frac{1}{s}$ $\quad k_{lim} \cdot N_A = (5.7 \cdot 10^{9})\ \frac{l}{s \cdot mol}$

$\tau_{lim}(c_{Pyrene}) := \frac{1}{k_{lim} \cdot N_A \cdot c_{Pyrene}}$

$\tau_{lim}(10\ mM) = 17.545\ ns$ $\quad \tau_{lim}(2\ mM) = 87.725\ ns$ $\quad \tau_{lim}(0.1\ mM) = (1.754 \cdot 10^{3})\ ns$

$\tau_{lim}(5\ mM) = 35.09\ ns$ $\quad \tau_{lim}(1\ mM) = 175.449\ ns$ $\quad \tau_{lim}(0.01\ mM) = (1.754 \cdot 10^{4})\ ns$

Time at which the rate has stabilized to within 10% (indepenedent of conc.):

$ind10 := \text{match}(1.1 \cdot k_{lim} \cdot 10^{19}, k(t) \cdot 10^{19}, \text{“near”})_1$ $\quad t_{ind10} = 131.4\ ns$

Time at which the decay time has stabilized to within 10% (indepenedent of conc.):

$ind10\tau := \text{match}(0.9 \cdot (\tau_{lim}(10\ mM)) \cdot 10^{9}, (\tau(t, 10\ mM)) \cdot 10^{9}, \text{“near”})_1$ $\quad t_{ind10\tau} = 106.3\ ns$

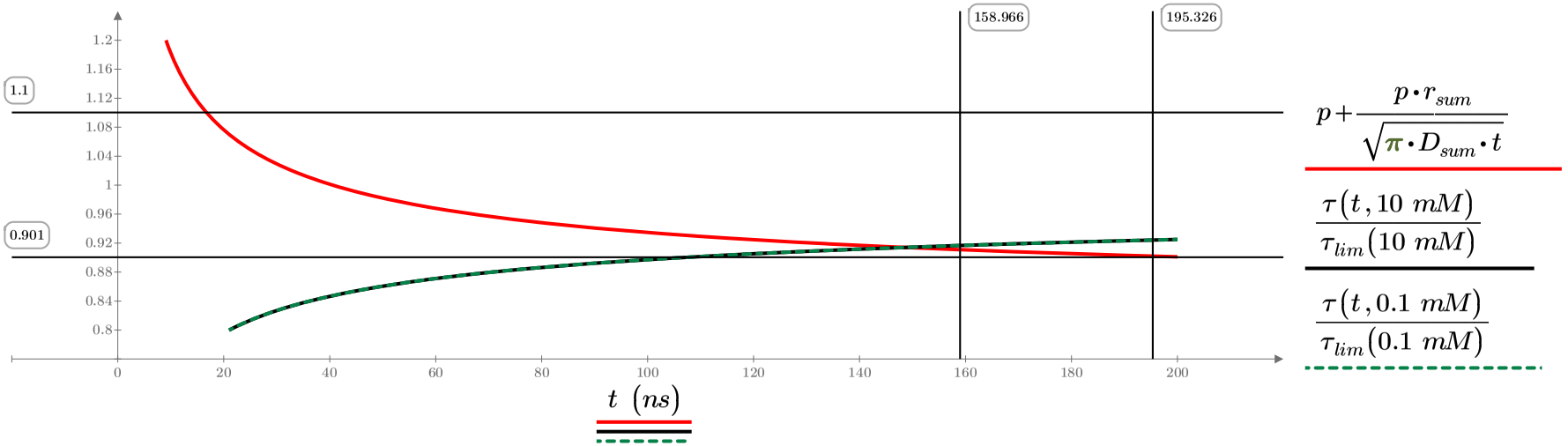

Populations:

Definition of rates:

$k_M := \frac{1}{565\ ns} = (1.77 \cdot 10^6)\ \frac{1}{s}$ $k_D := \frac{1}{61\ ns} = (1.639 \cdot 10^7)\ \frac{1}{s}$

Guess Values

$n1(100\ ps) = 0.01\ conc$ $n2(100\ ps) = 0\ mM$ $n3(100\ ps) = conc - 0.01\ conc$

Constraints

$\frac{d}{dt} n1(t) = -k(t) \cdot N_A \cdot n3(t) \cdot n1(t) - k_M \cdot n1(t)$

$\frac{d}{dt} n2(t) = k(t) \cdot N_A \cdot n3(t) \cdot n1(t) - k_D \cdot n2(t)$

$\frac{d}{dt} n3(t) = 0$

Solver

$F(conc) := \text{odesolve}\left(\begin{bmatrix} n1(t) \\ n2(t) \\ n3(t) \end{bmatrix}, 300\ ns\right)$

$exp\left(\frac{-}{\tau_{ri}}\right.$

Populations without transient contribution (k_{lim} instead of k(t))

Calculate Populations for several conc.:

$f10 := F(10\ mM)$ $f5 := F(5\ mM)$ $f4 := F(4\ mM)$ $f3 := F(3\ mM)$ $f2.5 := F(2.5\ mM)$ $f2 := F(2\ mM)$ $f1 := F(1\ mM)$

$f_{lim}10 := G(10\ mM)$ $f_{lim}5 := G(5\ mM)$ $f_{lim}4 := G(4\ mM)$ $f_{lim}3 := G(3\ mM)$ $f_{lim}2.5 := G(2.5\ mM)$ $f_{lim}2 := G(2\ mM)$ $f_{lim}1 := G(1\ mM)$

$f01 := F(0.1\ mM)$ $f_{lim}01 := G(0.1\ mM)$ $f001 := F(0.01\ mM)$ $f_{lim}001 := G(0.01\ mM)$

Populations for c=10mM: index 1 = S1, index 2 = Excimer, index 3 = Ground State

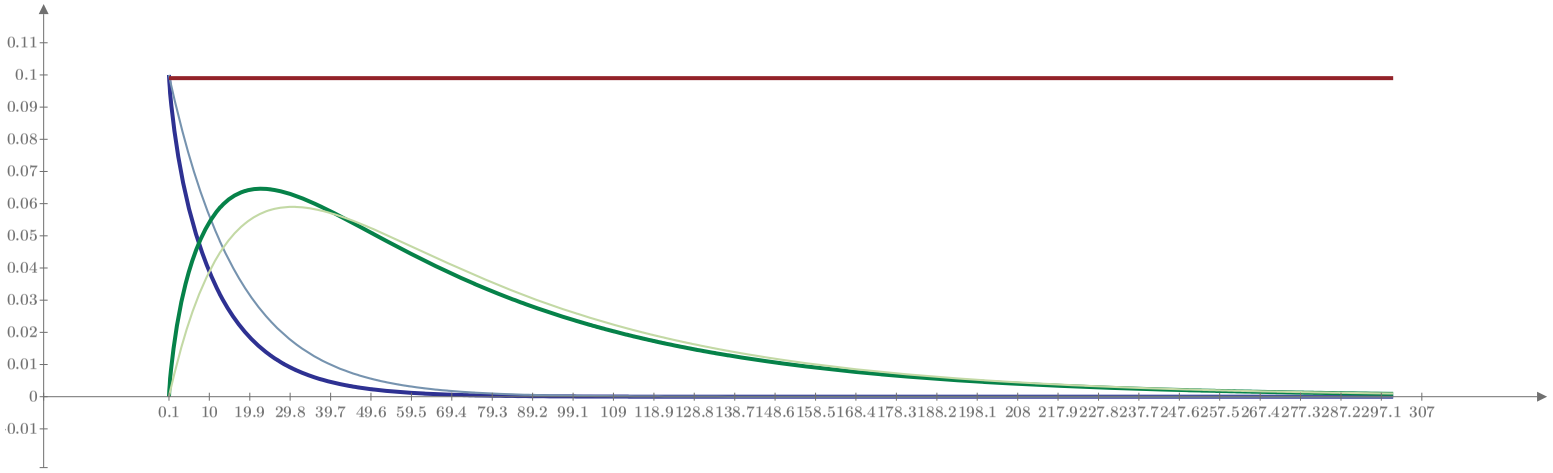

$t\ (ns)$

$\overrightarrow{f10_1(t)}\ \left(\frac{mol}{m^3}\right)$

$\overrightarrow{f_{lim}10_1(t)}\ \left(\frac{mol}{m^3}\right)$

$\overrightarrow{f10_2(t)}\ \left(\frac{mol}{m^3}\right)$

$\overrightarrow{f_{lim}10_2(t)}\ \left(\frac{mol}{m^3}\right)$

$\frac{1}{100}\ \overrightarrow{f10_3(t)}\ \left(\frac{mol}{m^3}\right)$

Zoom: Transient Contribution yields Increased slope in first 0.6 ns (Left Monomer-Decay, right Excimer-Rise)

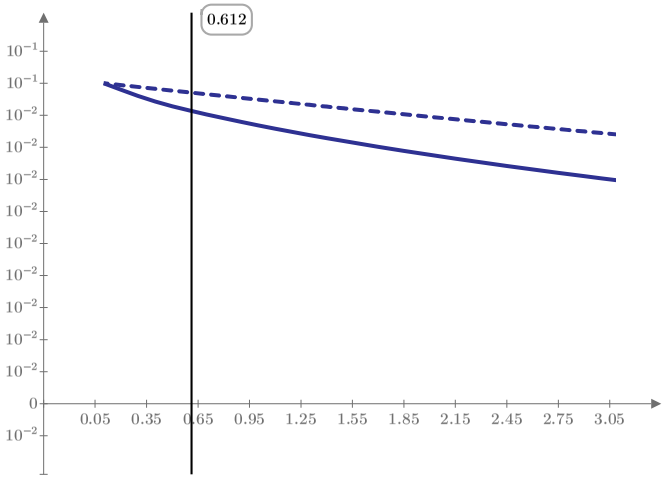

$t\ (ns)$

$\overrightarrow{f10_1(t)}\ \left(\frac{mol}{m^3}\right)$

$\overrightarrow{f_{lim}10_1(t)}\ \left(\frac{mol}{m^3}\right)$

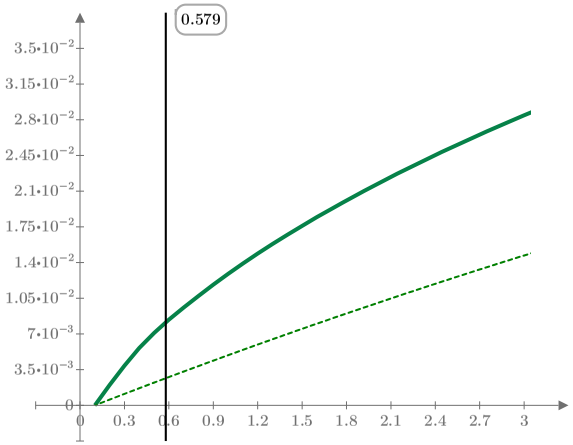

$t\ (ns)$

$\overrightarrow{f10_2(t)}\ \left(\frac{mol}{m^3}\right)$

$\overrightarrow{f_{lim}10_2(t)}\ \left(\frac{mol}{m^3}\right)$

Populationen für conc = 10, 1, 0.1 mM:

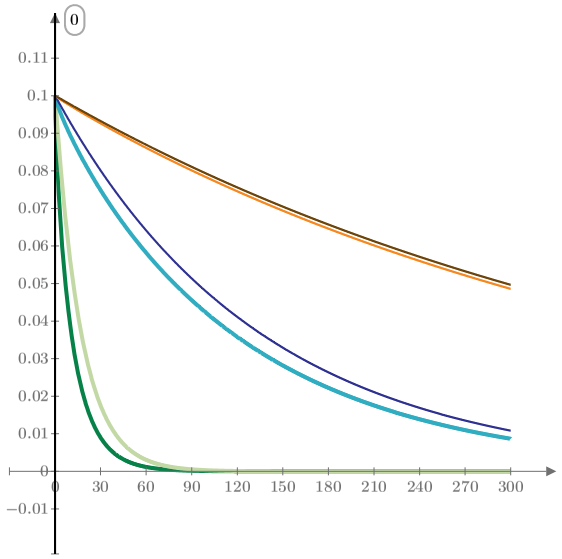

$t \ (ns)$

$\overrightarrow{f10_1(t)} \ \left(\frac{mol}{m^3}\right)$

$\overrightarrow{f_{lim}10_1(t)} \ \left(\frac{mol}{m^3}\right)$

$\overrightarrow{10 \cdot f1_1(t)} \ \left(\frac{mol}{m^3}\right)$

$\overrightarrow{10 \cdot f_{lim}1_1(t)} \ \left(\frac{mol}{m^3}\right)$

$\overrightarrow{100 \cdot f01_1(t)} \ \left(\frac{mol}{m^3}\right)$

$\overrightarrow{100 \cdot f_{lim}01_1(t)} \ \left(\frac{mol}{m^3}\right)$

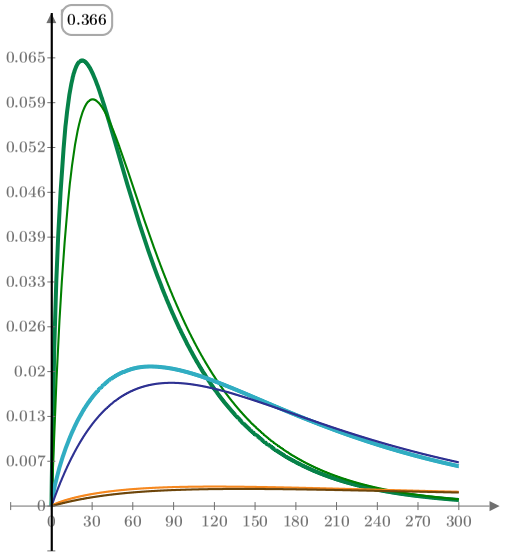

$t \ (ns)$

$\overrightarrow{f10_2(t)} \ \left(\frac{mol}{m^3}\right)$

$\overrightarrow{f_{lim}10_2(t)} \ \left(\frac{mol}{m^3}\right)$

$\overrightarrow{10 \cdot f1_2(t)} \ \left(\frac{mol}{m^3}\right)$

$\overrightarrow{10 \cdot f_{lim}1_2(t)} \ \left(\frac{mol}{m^3}\right)$

$100 \ \overrightarrow{f01_2(t)} \ \left(\frac{mol}{m^3}\right)$

$100 \ \overrightarrow{f_{lim}01_2(t)} \ \left(\frac{mol}{m^3}\right)$

Exponential Fits for k(t)= k_{lim} and with transient contribution k(t):

$$C(t, A_2, A_3, \tau_1, \tau_2, t0) := \overrightarrow{\left(A_2 \cdot \exp\left(-\frac{1}{\tau_1} \cdot (t - t0)\right) + A_3 \cdot \exp\left(-\frac{1}{\tau_2} \cdot (t - t0)\right)\right)} \quad n := 1, 2 .. \text{rows}(t)$$

$simdata_n := \overrightarrow{f2_1(t)}_n$

$simlim_n := \overrightarrow{f_{lim}2_1(t)}_n$

Fit of Monomer Population:

Guess Values

$A_{2M} := 0 \ mM \qquad A_{3M} := 0.1 \ mM$

$\tau_1 := 0.01 \ ns \quad \tau_2 := 60 \ ns \qquad t0 := 0.1 \ ns$

straints

$simdata = C(t, 0 \ mM, A_{3M}, \tau_1, \tau_2, 0.1 \ ns)$

Guess Values

$A_{2M} := 0 \ mM \qquad A_{3M} := 0.1 \ mM$

$\tau_1 := 0.01 \ ns \quad \tau_2 := 60 \ ns \qquad t0 := 0.1 \ ns$

straints

$simlim = C(t, 0 \ mM, A_{3M}, \tau_1, \tau_2, 0.1 \ ns)$

SolveCo

$Par := \mathbf{minerr}\left(A_{2M}, A_{3M}, \tau_1, \tau_2, \mathbf{t0}\right)$

SolveCo

$Palim := \mathbf{minerr}\left(A_{2M}, A_{3M}, \tau_1, \tau_2, \mathbf{t0}\right)$

$Fit := C\left(t, Par_1, Par_2, Par_3, Par_4, Par_5\right)$

$FitLim := C\left(t, Palim_1, Palim_2, Palim_3, Palim_4, Palim_5\right)$

$A_1 := Par_1 = 0 \ \frac{mol}{m^3}$ $A_2 := Par_2 = 0.019 \ \frac{mol}{m^3}$ $\tau_1 := Par_3 = 0.01 \ ns$ $\tau_2 := Par_4 = 66.478 \ ns$ $t0_1 := Par_5 = 0.1 \ ns$

$A_1 := Palim_1 = 0 \ \frac{mol}{m^3}$ $A_2 := Palim_2 = 0.02 \ \frac{mol}{m^3}$ $\tau_1 := Palim_3 = 0.01 \ ns$ $\tau_2 := Palim_4 = 76.592 \ ns$ $t0_2 := Palim_5 = 0.1 \ ns$

Compare Fits: shortened decay time when k(t) is active $Res(X, Y) := X - Y$ $ResMon := Res(simdata, Fit)$

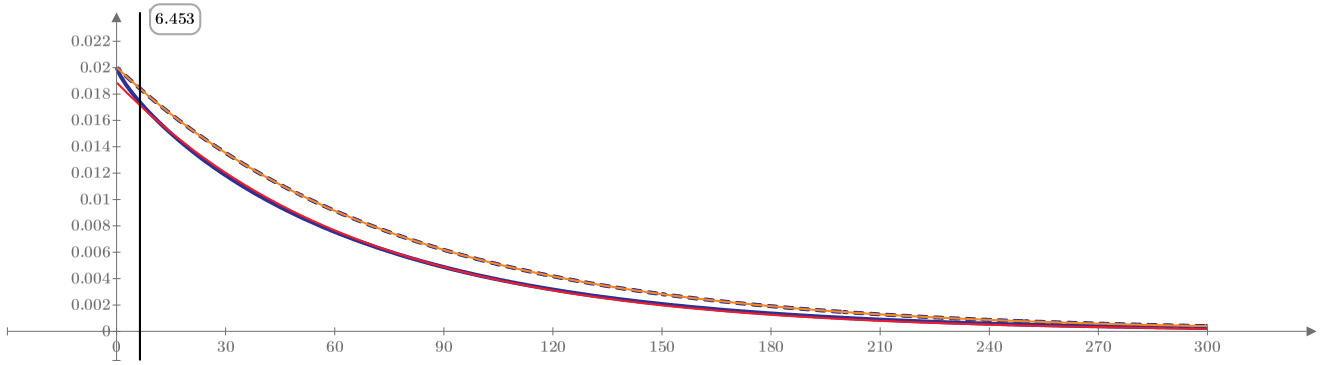

$simdata \left(\frac{mol}{m^3}\right)$

$Fit \left(\frac{mol}{m^3}\right)$

$simlim \left(\frac{mol}{m^3}\right)$

$FitLim \left(\frac{mol}{m^3}\right)$

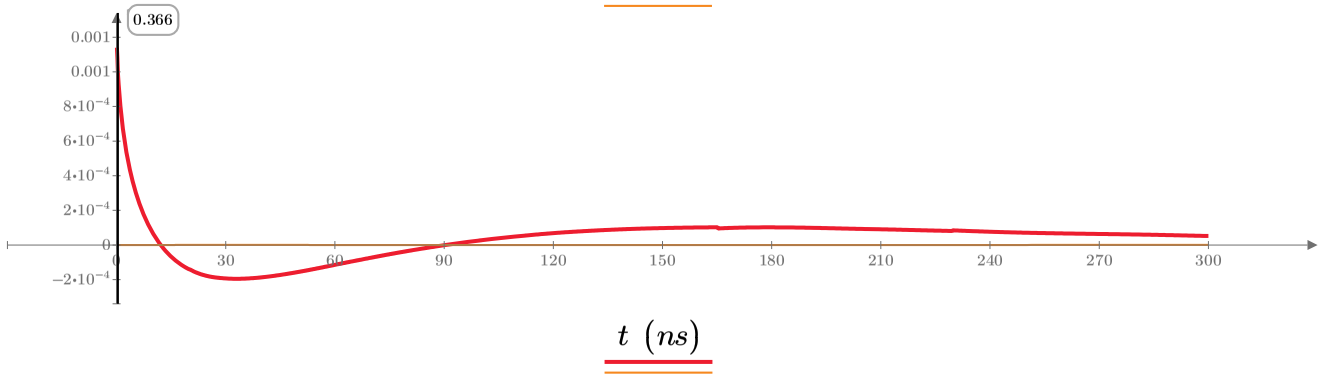

$Res(simdata, Fit) \left(\frac{mol}{m^3}\right)$

$Res(simlim, FitLim) \left(\frac{mol}{m^3}\right)$

Fit of Excimer Population:

$simdata_n := \overrightarrow{f2_2(t)}_n$

Guess Values

$A_{2M} := -0.1\ mM \quad A_{3M} := 0.1\ mM$

$\tau_1 := 30\ ns \quad \tau_2 := 160\ ns \quad t0 := 0.1\ ns$

Constraints

$simdata = C(t, A_{2M}, A_{3M}, \tau_1, \tau_2, 0.1\ ns)$

Solve

$Par := \mathbf{minerr}(A_{2M}, A_{3M}, \tau_1, \tau_2, t0)$

$simlim_n := \overrightarrow{f_{lim}2_2(t)}_n$

Guess Values

$A_{2M} := -0.1\ mM \quad A_{3M} := 0.1\ mM$

$\tau_1 := 30\ ns \quad \tau_2 := 160\ ns \quad t0 := 0.1\ ns$

Constraints

$simlim = C(t, A_{2M}, A_{3M}, \tau_1, \tau_2, 0.1\ ns)$

Solve

$Palim := \mathbf{minerr}(A_{2M}, A_{3M}, \tau_1, \tau_2, \mathbf{t0})$

$Fit2 := C(t, Par_1, Par_2, Par_3, Par_4, Par_5)$

$A_1 := Par_1 = -0.0215\ \frac{mol}{m^3} \quad A_2 := Par_2 = 0.0221\ \frac{mol}{m^3}$

$A_1 := Palim_1 = -0.0689\ \frac{mol}{m^3} \quad A_2 := Palim_2 = 0.0689\ \frac{mol}{m^3}$

$FitLim2 := C(t, Palim_1, Palim_2, Palim_3, Palim_4, Palim_5)$

$\tau_1 := Par_3 = 40.225\ ns \quad \tau_2 := Par_4 = 88.586\ ns \quad t0_1 := Par_5 = 0.1\ ns$

$\tau_1 := Palim_3 = 61.11\ ns \quad \tau_2 := Palim_4 = 76.41\ ns \quad t0_2 := Palim_5 = 0.1\ ns$

Compare Fits:

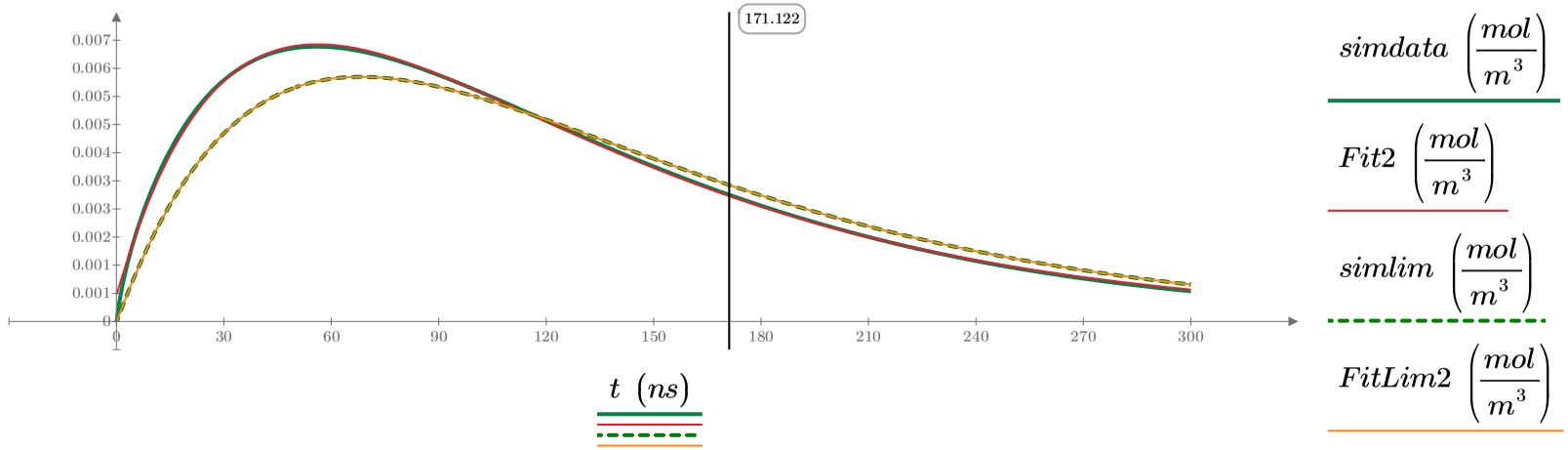

Compare Residuals:

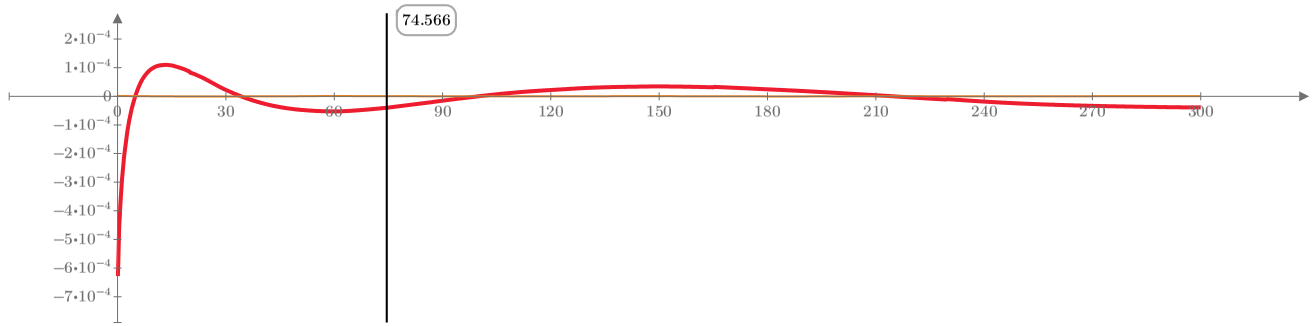

$t\ (ns)$

$Res(simdata, Fit2)\ \left(\frac{mol}{m^3}\right)$

$Res(simlim, FitLim2)\ \left(\frac{mol}{m^3}\right)$

$ResExc := Res(simdata, Fit2)$ $\sum\sqrt{(ResMon)^2} = 0.29\ mM$ $\sum\sqrt{(ResExc)^2} = 0.097\ mM$

Output: $version :=$ "_p085_km565"

Output of fitted spectra, parameters and separated functions:

$u := \frac{mol}{m^3}$ $Res1 := Res\left(\overrightarrow{f10_1(t)}, Fit\right)$ $ResLim1 := Res\left(\overrightarrow{f_{lim}10_1(t)}, FitLim\right)$ $Res2 := Res\left(\overrightarrow{f10_2(t)}, Fit2\right)$ $ResLim2 := Res\left(\overrightarrow{f_{li}$

simulated time traces:

$legend1 := \text{augment}(\text{"time(ns)"}, \text{"0.1mM Mon"}, \text{"0.1mM Exc"}, \text{"1mM Mon"}, \text{"1mM Ecx"}, \text{"2mM Mon"}, \text{"2mM Exc"}, \text{"5mM Mon"}, \text{"5mM Exc"}, \text{"10mM Mon"}$

$Concs\_kt\_out := \text{stack}\left(legend1, \left(\text{augment}\left(\frac{t}{ns}, \overrightarrow{f01_1(t)\ \frac{1}{u}}, \overrightarrow{f01_2(t)\ \frac{1}{u}}, \overrightarrow{f1_1(t)\ \frac{1}{u}}, \overrightarrow{f1_2(t)\ \frac{1}{u}}, \overrightarrow{f2_1(t)\ \frac{1}{u}}, \overrightarrow{f2_2(t)\ \frac{1}{u}}, \overrightarrow{f5_1(t)\ \frac{1}{u}}, \overrightarrow{f5_2(t)\ \frac{1}{u}}, \overrightarrow{f10_1(t)\ \frac{1}{u}}, \overrightarrow{f10_2(t)\ \frac{1}{u}}\right)\right)\right)$

$Concs\_lim\_out := \text{stack}\left(legend1, \left(\text{augment}\left(\frac{t}{ns}, \overrightarrow{f_{lim}01_1(t)\ \frac{1}{u}}, \overrightarrow{f_{lim}01_2(t)\ \frac{1}{u}}, \overrightarrow{f_{lim}1_1(t)\ \frac{1}{u}}, \overrightarrow{f_{lim}1_2(t)\ \frac{1}{u}}, \overrightarrow{f_{lim}2_1(t)\ \frac{1}{u}}, \overrightarrow{f_{lim}2_2(t)\ \frac{1}{u}}, \overrightarrow{f_{lim}5_1(t)\ \frac{1}{u}}, \overrightarrow{f_{lim}5_2(t)\ \frac{1}{u}}, \overrightarrow{f_{lim}10$

fits :

$legend2 := \text{augment}(\text{"time(ns)"}, \text{"Fit Mon"}, \text{"Fit Exc"}, \text{"Fit Lim Mon"}, \text{"Fit Lim Exc"}, \text{"Res Mon"}, \text{"Res Lim Mon"}, \text{"Res Exc"}, \text{"Res Lim Exc"})$

Acknowledgements

A significant number of people have helped me survive this chapter of my life and I'd like to acknowledge them below.

First of all I thank **Prof. Dr. Eberhard Riedle** for his supervision and for providing ideas, valuable contacts as well as the financial and technical resources for this work. I am aware that some of our interactions must have put unnecessary stress on the both of us. I'd like to thank you for your patience and for not giving up on me when I was ready to quit.

Other people who provided guidance and scientific advice include **Dr. Igor Pugliesi** who co-supervised the early stages of my stay, as well as **Dr. Roger-Jan Kutta**, whose engagement evolved from answering a question about a technical matter to an almost year-long intensive collaboration on the pyrene project. His contribution of the streak measurements at the University of Regensburg proved to be the decisive missing link.

I'd like to thank our collaborators on the mirror project **Dr. Florian Habel** and **Dr. Vladimir Pervak**, who not only provided several mirrors but also gave us a tour of their facilities and were always open to discussions about coating design and interferometry.

Pyrene dimers and oligomers were synthesized by **Dr. Ashok Keerthi** from the group of **Prof. Dr. Klaus Müllen**, at the Max Planck Institute of Polymer Research, Mainz, Germany. I also received active support from **Matthias Roos** and **Sebastian Reiter** in the group of **Prof. Dr. de Vivie-Riedle** in the form of theoretical calculations and from **Dr. Anne Rainer** from the group of **Prof. Dr. Wolfgang Zinth**, who dedicated a significant amount of her time to our streak measurements here at BMO.

There are also collaborators whose work is not directly represented in this thesis, but who nonetheless contributed positive and valuable interactions. These include **Prof. Dr. Jürgen Hauer**, **Dr. Uli Schmidhammer** and **Prof. Dr. Stephen Bradforth**, who was also kind enough to welcome me to his labs at USC in Los Angeles for a little while.

Technical support was provided by **Gerald Jung** and **Dr. Hans-Erik Swoboda** from Horiba Jobin Yvon, who not only helped keep the CPA in Munich running, but also supported me in carrying out an installation of a NOPA in Switzerland. In-house IT support was provided by **Dr. Karlheinz Mantel** and **Dr. Florian Trommer**. The friendly and extremely supportive atmosphere at BMO was completed by **Rudi Schwarz**, **Alfons Stork**, **Christian Hausmann** and **Harald Hoppe** at the BMO workshop.

I'd further like to acknowledge the work of my very diligent bachelor students **Alexander Richter** (pyrene), **Jonathan Reschauer** (pyrene dimers) and **Konstantin Büttner** (mirrors), whom I wish the best of luck in their future endeavours.

Prof. Dr. Matthias Kling, **Dr. Hanieh Fattahi**, **Dr. Nick Karpowicz** and **Mrs. Monika Wild** at the IMPRS APS graduate school far exceeded their task of providing an external framework and making sure I attended the required lectures. I very much value their input and support. Regular interactions with Ph.D. students from other groups at the school's annual seminars at Ringberg Castle and Vienna were crucial in helping me put things into perspective and stay sane. If not for the people at IMPRS, this work would have remained unfinished.

The same goes for my present and past colleagues in the Riedle group **Emanuel Wittmann**, **Qi Hu**, **Roland Wilcken**, **Matthias Block**, **Dr. Richard Ciesielski**, **Dr. Max Bradler**, **Dr. Nils Krebs**, **Cristina Leonardo**, **Henrieta Volfova**, **Philipp Neumann, Rudolf Reiel** and **Sebastian Wiegner**, who had to put up with me on a daily basis and provided camaraderie and cousel on scientific as well as other matters. I also learned a great deal from you guys and the extremely supportive atmosphere amongst my colleagues is the one thing that I am certainly going to miss. I'm looking forward to seeing all of you on the other side.

Finally and most importantly I'd like to thank the many friends and family who provided emotional support throughout this challenging time, most outstandingly my mother **Gabi Genisser-Baudisch** and **Dr. Linda Isa Eva Sfia Forster**, who has been my steadfast companion since the start of our master's theses.